

博士學位論文

Doctoral Thesis

論文題目

Thesis Title

Unified Crack Phase-Field Model Enhanced

by Diffusive-Discrete Crack Transition

for Brittle, Dynamic, and Ductile Fractures

(拡散-離散き裂遷移手法を導入した一般化フェーズフィールド
き裂モデルの定式化と脆性, 動的, 延性破壊への適用)

東北大学大学院工学研究科

Graduate School of Engineering,

TOHOKU UNIVERSITY

専攻/Department: Civil and Environmental Engineering

学籍番号/ ID No: C1TD6006

氏名/Name: Jike HAN

Copyright © 2023 by Jike HAN

Prof. Kenjiro Terada
(Principal Advisor)

Prof. Yuki Yamakawa

Assoc. prof. Isao Saiki

Assoc. prof. Shuji Moriguchi

Unified Crack Phase-Field Model Enhanced by Diffusive-Discrete Crack Transition for Brittle, Dynamic, and Ductile Fractures

ABSTRACT : This study aims to pave the road toward the comprehensive evaluation and prediction of the multistage and multiscale failure events of infrastructure facilities. To realize the purpose, a novel crack phase-field model is proposed, and a diffusive-discrete crack transition scheme is developed.

For predicting the damage evolution occurring in infrastructure facilities, the "crack phase-field model (CPFM)" is studied. The CPFM has recently received attention, which enables us to consider crack initiation, propagation, and bifurcation in materials as solutions to an energy minimization problem of potential energy based on Griffith's theory. Since the origin of the CPFM, it has been enhanced to describe brittle, dynamic, ductile, cohesive, fatigue, multifield fractures, and so on. In particular, when the failure phenomena of elastoplastic materials are targeted, several ingredients, such as the plasticity-induced degradation function, the plastic damage driving force, and the degrading fracture toughness, have been introduced into the original CPFM. Additionally, thresholds and coefficients have been employed by researchers for controlling the effect of the above-suggested ingredients and for pursuing better realizations of actual failure phenomena. Indeed, these treatments have shown the richness of capturing ductile fracture responses, but on the other hand, eventually, vitiate the variational consistency that is one of the beauties equipped to CPFMs. In the literature, this issue was recognized as a dilemma of the CPFMs for ductile fracture.

To address the issue, we propose a variationally and thermodynamically consistent CPFM for ductile fracture. Prior to the formulation, we review the distinctive features of the existing CPFMs for ductile fracture in terms of how ductile fracture is realized in previous studies. Based on the discussion, we propose a new model for ductile fracture equipped with two separate damage variables for elasticity and plasticity. Beginning with the introduction of a constitutive work density functional consisting of elastic, plastic hardening, and damage hardening components, we derive variationally and thermodynamically consistent evolution laws for plasticity and damage. The mathematical form describing the evolution laws of damage has been overlooked or not considered in previous studies and therefore deserves particular emphasis. The evolution laws for plasticity are coupled with damage, so the accumulation of plastic strain is ceased in the severely damaged region. Also, the proposed model is equipped with thresholds and coefficients to control the amount of damage driving force and thus is useful to reproduce actual failure events. Additionally, thanks to the introduction of both the plastic driving force and degrading fracture toughness, the formulation realizes both the plastic deformation-induced and negative hydrostatic pressure-induced damage evolutions. Therefore, the formulation unifies several of the existing CPFMs for ductile fracture proposed to date, including a few proposed by the authors.

Meanwhile, to realize explicit crack propagation, division of a base structure into multiple portions, and independent motions of the divided portions, a diffusive-discrete crack transition scheme is developed. The proposed scheme realizes the discontinuity of a state variable enjoying the feature of a meshfree method, the "finite cover method". Specifically, we determine explicit crack tips and paths by referring to the distribution of damage variables, which is apart from several conventional approaches

using the mechanical properties or the geometric information to determine crack tips and paths. Also, since the given crack topology is updated from diffusive to discrete intermittently during the course of the staggered iterative procedure in a single time step, even a curved crack path that evolves significantly within a single time increment can be explicitly captured. In addition, to stably update an explicit crack tip within the finite strain framework, we devise two stabilization techniques. Specifically, pseudo-stiffness is introduced to severely damaged elements around the discrete crack path for the quasi-static system to prevent excessively large deformations, and the damage and volume fraction-induced numerical damping is introduced for the dynamic problem to maintain computational stability and avoid distortion of the physical mesh due to the effects of stress wave propagation. Additionally, the corrector of the displacement increment is intentionally modified so that NR computations successfully converge, and the discrete crack opens in a gradual and stable manner.

The CPFM accommodating two damage variables for elasticity and plasticity is incorporated into the developed diffusive-discrete crack transition scheme, and we coin the name "Crack phase-field enhanced finite cover method (CPFFCM)" for the proposed method. The proposed method uses the derived CPFM as the damage computation tool to predict the crack initiation, propagation, and bifurcation, and the obtained diffusive crack path is transformed into the strong discontinuous representation by the developed diffusive-discrete crack transition scheme. Enjoying this combination, a series of failure events from the damage initiation to the post-failure phase, occurring in brittle and ductile materials under quasi-static and dynamic conditions, can be simulated. Based on the numerical simulation methods, we argue several advantages over previous studies:

1. The proposed method can simulate failure phenomena more stably than the standard FEM with the conventional CPFM since the damaged elements are less subjected to the extremely large deformation and rotation that lead to the mesh distortion.
2. The proposed method is developed within the finite strain framework, so the fracture events involving arbitrary crack initiation, propagation, bifurcation, division of the original object into multiple portions, and subsequent independent motions of the divided portions can be properly simulated.
3. Thanks to the introduction of discrete crack surfaces, the crack paths and crack surfaces obtained by different sets of parameters can be compared to each other, which can be helpful in understanding the contribution of provided parameters to the fracture behavior.

ACKNOWLEDGMENT

This dissertation is a record of my challenge at Tohoku University from 2019 to 2023. I show my appreciation to all those who helped in working on this dissertation, as well as those who supported me in my life.

First and foremost, I would like to express my sincere gratitude to Professor Kenjiro Terada, who has fully supported me throughout my research voyage from the undergraduate to doctoral programs. He gave me opportunities to study in Germany and acquire state-of-the-art international perspectives. Without his guidance, I would never choose to challenge myself in this academic field.

Next, I am thankful for my research supervisors, Assistant Professor Yuichi Shintaku and Assistant Professor Seishiro Matsubara, and the committee members of my dissertation, Professor Yuki Yamakawa, Associate Professor Isao Saiki, and Associate Professor Shuji Moriguchi. Their valuable comments helped me to improve the quality of my research.

In addition, I would also like to thank my colleagues at Computational Safety Engineering Lab. for their technical discussion and support. Their attitudes to conducting research inspired and disciplined me every day.

Finally, I would like to give my gratitude to my parents, who gave me health and education and allowed me to keep going on the seaway that I have wanted to sail. Also, the superlative appreciation is dedicated to my wife, Keina, for her patiently emotional support.

Although this dissertation is a milestone in my research, it is not the end. My voyage continues, and let me try to struggle in the dramatically changing world with the memory of studying at Tohoku University.

Contents

1	Introduction	1
1.1	Research Background	1
1.2	Previous studies for fracture simulation	3
1.2.1	Diffusive approach	3
1.2.2	Discrete approach	6
1.3	Purpose of this study	9
1.4	Outline of this dissertation	12
2	Crack phase-field model: CPFEM	15
2.1	Kinematics	15
2.2	Phase-field approximation	16
2.3	CPFEM for quasi-static and dynamic brittle fractures	18
2.4	Review of distinctive features in CPFEM for ductile fracture	21
2.4.1	Concise summary of CPFEM for brittle fracture	22
2.4.2	Issue inherent in conventional CPFEM for brittle fracture	22
2.4.3	Plastic driving force for damage computation	25
2.4.4	Degrading fracture toughness for damage computation	27
2.4.5	Yield function for CPFEM with plastic damage driving force	30
2.4.6	Yield function for CPFEM without plastic damage driving force	32
2.5	Proposed model	38
2.5.1	Constitutive work density functional	38

2.5.2	Thermodynamic consistency	41
2.5.3	Verification of the positivity of λ^p and λ^f	47
2.5.4	Governing equations	49
2.5.5	Equivalence and novelty	52
2.6	Numerical implementation of the proposed model	53
2.6.1	Return mapping algorithm for internal variables	54
2.6.2	Spatial discretization	56
3	Numerical simulations by CPFIGA	59
3.1	Exmaple 3-1: Tensile failure of a square element	59
3.1.1	Parameter study for plastic damage threshold Ψ_{cr}^p	60
3.1.2	Parameter study for plastic damage coefficient ζ^p	62
3.1.3	Comparison of evolution laws	64
3.2	Exmaple 3-2: Tensile failure of symmetrically notched specimen	66
3.3	Exmaple 3-3: Cup-cone failure of notched round bar	71
3.4	Exmaple 3-4: Tensile failure of notched specimens (AHSS sheet)	77
3.4.1	Experimental setup and classification of crack growth behavior . . .	78
3.4.2	Experimental result	81
3.4.3	Exemplification	85
4	Crack phase-field enhanced finite cover method: CPFFCM	95
4.1	Finite cover method	95
4.1.1	Mathematical and physical covers	95
4.1.2	Finite cover approximation	96
4.2	Spatial discretization by FCM	98
4.3	Temporal discretization by Newton method	101
4.4	Numerical algorithm	104
4.5	Transition scheme from diffusive to discrete crack topologies	105
4.5.1	Explicit crack tip determination technique	106

4.5.2	Crack opening stabilization technique	108
4.6	Similarities and differences between previous studies and this study	111
5	Numerical simulations by CPFFCM	113
5.1	Quasi-static brittle fracture	113
5.1.1	Example 5-1-1: Tensile failure of single-edge notched specimen . .	114
5.1.2	Example 5-1-2: Shear failure of single-edge notched specimen . . .	119
5.1.3	Example 5-1-3: Tensile failure of double-edge notched asymmetric specimen	122
5.1.4	Example 5-1-4: Tensile failure of multiholed specimen	127
5.2	Dynamic brittle fracture	131
5.2.1	Example 5-2-1: Vibration test of cantilever beam	134
5.2.2	Example 5-2-2: Rotation test of hollow square plate	139
5.2.3	Example 5-2-3: Three-point bending test of notched beam (John- Shah test)	144
5.2.4	Example 5-2-4: Impact failure of L-shaped plate	147
5.3	Ductile fracture	152
5.3.1	Example 5-3-1: Tensile failure of I-shaped specimen	153
5.3.2	Example 5-3-2: Tensile failure of asymmetrically notched specimen	158
5.3.3	Example 5-3-3: Cup-cone failure of smooth/notched round bars . .	163
6	Conclusion	173
6.1	Regarding the enhancement of crack phase-field modeling	173
6.2	Regarding the enhancement of numerical simulation method	174
6.3	Future works	175
Appendix A	Supplements for CPFM	178
A.1	Original motivation to introduce two damage variables d^e and d^p	178
A.2	Confirmation of $\mathcal{K}_{22} > 0$	179

A.3	Components accounting for global tangent matrix	182
Appendix B	Supplements for CPFFCM	186
B.1	Numerical error caused by rearrangement of finite covers	186
REFERENCES		189

List of Tables

1.1	Several CPFMs combined with strong discontinuity approaches.	8
2.1	Geometric setup and material parameters for the one-dimensional bar. . . .	23
2.2	Unified nature of the proposed model by reference to several recently developed CPFMs.	53
3.1	Material parameters for the square element.	60
3.2	Material parameters for the symmetrically notched specimen.	67
3.3	Five cases under consideration for the symmetrically notched specimen. . .	68
3.4	Material parameters for the notched round bar.	72
3.5	Three cases under consideration for the notched round bar.	73
3.6	Material parameters for single notched specimens.	86
3.7	Two cases under consideration for single notched specimens.	87
4.1	Similarities and differences between previous studies and this study.	111
5.1	Material parameters for numerical simulations in Section 5.1.1 ~ Section 5.1.4.	113
5.2	Material parameters for Example 5-2-1.	134
5.3	Numerical simulation cases for Example 5-2-1.	134
5.4	Material parameters for Example 5-2-2.	139
5.5	Numerical simulation cases for Example 5-2-2.	140
5.6	Material parameters for Example 5-2-3.	144
5.7	Numerical simulation cases, crack initiation time, point, and propagation angle for Example 5-2-3.	145

5.8	Material parameters for Example 5-2-4.	148
5.9	Material parameters for Example 5-3-1.	153
5.10	Numerical simulation cases for Example 5-3-1.	154
5.11	Material parameters for Example 5-3-2.	161
5.12	Numerical simulation cases for Example 5-3-2.	162
5.13	Material parameters for Example 5-3-3.	168

List of Figures

1.1	Classification of failures in an infrastructure facility.	2
1.2	The outline of this dissertation.	12
2.1	Diffusive crack topology in CPF modeling.	16
2.2	Stress–total strain curves for the incorporation of the elastoplastic constitutive law and conventional CPF brittle modeling.	24
2.3	Stress–total strain curves with plastic driving force.	27
2.4	Micro-mechanisms of ductile fracture and its numerical approximation. . .	28
2.5	Stress–total strain curves with degrading fracture toughness.	29
2.6	Stress, elastic strain, plastic strain and crack phase-field variable–total strain curves with effective/nominal stress (“effective” and “nominal (m)” are equivalent to Setup A and Setup B).	35
2.7	Surfaces of plastic strain determined by crack phase-field variable and total strain.	36
3.1	Stress, damage variables, and hardening variable–total strain curves for the single square element: Comparisons of the value of threshold Ψ_{cr}^p	61
3.2	Stress, damage variables, and hardening variable–total strain curves for the single square element: Comparisons of the value of coefficient ζ^p	63
3.3	Stress, damage variables, and hardening variable–total strain curves for the single square element: Comparisons of the evolution laws.	65
3.4	Geometry and boundary conditions for the symmetrically notched specimen.	67
3.5	Load-displacement curves for the symmetrically notched specimen.	68

3.6	Detailed evolution of elastic & plastic damage variables and degrading fracture toughness: Case I.	70
3.7	Detailed evolution of elastic & plastic damage variables and degrading fracture toughness: Case II.	71
3.8	Detailed evolution of elastic & plastic damage variables and degrading fracture toughness: Case III.	72
3.9	Detailed evolution of parameters, $\beta_{G2}\tau_p^*$ and $\beta_{G1}\alpha^*$, in degrading fracture toughness: Case II and Case III.	73
3.10	Detailed evolution of elastic & plastic damage variables and degrading fracture toughness: Case IV.	74
3.11	Detailed evolution of elastic & plastic damage variables and degrading fracture toughness: Case V.	75
3.12	Geometry and boundary conditions for the notched round bar.	75
3.13	Load-displacement curves for the notched round bar.	76
3.14	Detailed evolutions of elastic & plastic damage variables, degrading fracture toughness, and two cosine functions: Case I.	77
3.15	Detailed evolutions of elastic & plastic damage variables, degrading fracture toughness, and two cosine functions: Case II.	78
3.16	Detailed evolutions of elastic & plastic damage variables, degrading fracture toughness, and two cosine functions: Case III.	79
3.17	Crack propagation of the NRB: Case II (The region having $d^e \leq 0.99$ is removed, and only the 3/4 crack surface is shown).	80
3.18	Experimental setup for single notched specimen.	80
3.19	Experimental results for JSC1180.	82
3.20	Experimental results for JSC980.	83
3.21	Various crack initiation positions depending on different tensile strength and notch geometry.	84
3.22	Numerical setups for single notched specimens.	88

3.23	Numerical results for JSC1180.	89
3.24	Numerical results for JSC980.	90
3.25	Various crack initiation positions (left: before crack initiation, right: after crack initiation) depending on the degradation of degrading fracture toughness for $R = 5.0$ [mm].	91
3.26	Various crack initiation positions (left: before crack initiation, right: after crack initiation) depending on the degradation of degrading fracture toughness for $R = 0.5$ [mm].	91
4.1	Definitions of mathematical and physical covers.	96
4.2	Definition of a mathematical element and weight functions for PU approximation.	96
4.3	Definition of physical elements.	97
4.4	Drawings of the pseudo damping function.	102
4.5	Example of updating discrete crack surfaces: comparison between previous studies and this study.	111
5.1	Geometry with boundary conditions and mesh distribution for Example 5-1-1.	114
5.2	Load-displacement curves obtained for Example 5-1-1.	115
5.3	Snapshots of the crack evolutions obtained for Example 5-1-1 (Cases Q1 and Q2).	115
5.4	Snapshots of the crack evolutions obtained for Example 5-1-1 (Cases C1 and C2).	116
5.5	Relationships between the number of iterations and residuals obtained for Example 5-1-1 (without/with the stabilization technique in Algorithm 4). . .	117
5.6	Snapshots of the crack openings obtained for Example 5-1-1 (without/with the stabilization technique) (Algorithm 4).	118
5.7	Geometry with boundary conditions and mesh distribution for Example 5-1-2.	120
5.8	Load-displacement curves obtained for Example 5-1-2.	120

5.9	Snapshots of the crack evolutions obtained for Example 5-1-2.	121
5.10	Overlay of a diffuse crack obtained by CPFFEM on a discrete crack provided by CPFFCM for Example 5-1-2 (the dotted lines indicate $d \approx 0.95$).	121
5.11	Illustration of the moving circle algorithm (the dotted lines indicate $d \approx 0.60$).	122
5.12	Geometry with boundary conditions and mesh distribution for Example 5-1-3.	122
5.13	Load-displacement curves obtained for Example 5-1-3.	123
5.14	Snapshots of the crack evolutions obtained for Example 5-1-3: Case D1 and Case D2.	124
5.15	Snapshots of the crack evolutions obtained for Example 5-1-3: Case D3 and Case D4.	124
5.16	Snapshots of the crack evolutions obtained for Example 5-1-3: Case D5 and Case D6.	125
5.17	Illustration of the collapsed element group when the global NR computation diverges in CPFFEM: Case D1 in Example 5-1-3.	125
5.18	Illustrations of different scenarios involving two crack connections with three geometries in Example 5-1-3.	126
5.19	Geometry with boundary conditions and mesh distributions for Example 5-1-4.	128
5.20	Load-displacement curves obtained for Example 5-1-4.	128
5.21	Snapshots of the crack evolutions obtained for Example 5-1-4.	129
5.22	Illustration of severely damaged elements involving oscillatory displacements and collapsed element groups when the global NR computation diverges in CPFFEM: 5-hole & 7-hole specimens in Example 5-1-4.	129
5.23	Snapshots of the crack evolutions obtained for Example 5-1-4 (Case H1).	131
5.24	Snapshots of the crack evolutions obtained for Example 5-1-4 (Case H2).	132
5.25	Geometry with boundary conditions for Example 5-2-1.	134

5.26	Transition trends of energy components for Example 5-2-1. Ela: elastic strain energy; Kin: kinetic energy; Dis: dissipation energy; Bod: external energy of body force; Tra: external energy of traction force (Tra=Ela+Kin+Dis-Bod).	136
5.27	Energy states for Example 5-2-1: Case cb1. Elastic strain energy density in tension Ψ^{e+} and kinetic energy density K in order from the top.	137
5.28	Energy states for Example 5-2-1: Case cb2. Elastic strain energy density in tension Ψ^{e+} , kinetic energy density K , dissipation energy density D , and external energy density of body force P^b in order from the top.	137
5.29	Trajectories of motion for Example 5-2-1: Case cb3 and Case cb4.	138
5.30	Geometry with boundary conditions for Example 5-2-2.	139
5.31	Transition trends of all energy components for Example 5-2-2. Ela: elastic strain energy; Fra: crack generation energy; Kin: kinetic energy; Dis: dissipation energy; Tra: external energy of initial traction force (Tra=Ela+Fra+Kin+Dis).	141
5.32	Trajectories of motion for Example 5-2-2.	142
5.33	Geometry with boundary conditions for Example 5-2-3.	144
5.34	Reaction force-displacement curves for Example 5-2-3.	146
5.35	Comparison of crack paths for Example 5-2-3. Deformation magnitude: 50 times.	146
5.36	Experiment results ¹⁸⁴⁾ for Example 5-2-3.	146
5.37	Geometry with boundary conditions for Example 5-2-4.	148
5.38	Transition trends of all energy components for Example 5-2-4. Ela: elastic strain energy; Fra: crack generation energy; Kin: kinetic energy; Dis: dissipation energy; Bod: external energy of body force; Tra: external energy of traction force (Tra=Ela+Fra+Kin+Dis-Ext).	149
5.39	Snapshots of crack propagations for Example 5-2-4.	150
5.40	Displacement-time curves for Example 5-2-4.	151
5.41	Trajectory of motion for Example 5-2-4.	152

5.42	Geometry with boundary conditions for Example 5-3-1.	153
5.43	Load-displacement curves for Example 5-3-1.	154
5.44	Snapshots of deformation and detailed evolution of elastic damage variable d^e for Example 5-3-1: Case i1. The top row shows the vertical displacement, and the bottom row shows the elastic damage variable.	155
5.45	Snapshots of deformation and detailed evolution of elastic damage variable d^e for Example 5-3-1: Case i2. The top row shows the vertical displacement, and the bottom row shows the elastic damage variable.	156
5.46	Snapshots of the localization of global hardening variable α immediately before crack initiation for Example 5-3-1. The maximum value in each snapshot is shown in red and the minimum value in blue.	157
5.47	Snapshots of deformation and detailed evolution of elastic damage variable d^e for Example 5-3-1: Case i3. The top row shows the vertical displacement, and the bottom row shows the elastic damage variable.	158
5.48	Snapshots of deformation and detailed evolution of elastic damage variable d^e for Example 5-3-1: Case i4. The top row shows the vertical displacement, and the bottom row shows the elastic damage variable.	159
5.49	Snapshots of deformation and detailed evolution of elastic damage variable d^e for Example 5-3-1: Case i5. The top row shows the vertical displacement, and the bottom row shows the elastic damage variable.	160
5.50	Geometry with boundary conditions for Example 5-3-2.	161
5.51	Load-displacement curves for Example 5-3-2.	162
5.52	Detailed evolution of elastic damage variable d^e and two degradation functions, $\cos^{p_1}(\beta_{G1}\alpha^*/2)$ & $\cos^{p_2}(\beta_{G2}\tau_p^*/2)$, for degradaing fracture toughness in Eq. (3.1): Case h1.	163
5.53	Detailed evolution of elastic damage variable d^e and two degradation functions, $\cos^{p_1}(\beta_{G1}\alpha^*/2)$ & $\cos^{p_2}(\beta_{G2}\tau_p^*/2)$, for degradaing fracture toughness in Eq. (3.1): Case h2.	164

5.54	Detailed evolution of elastic damage variable d^e and two degradation functions, $\cos^{p_1}(\beta_{G1}\alpha^*/2)$ & $\cos^{p_2}(\beta_{G2}\tau_p^*/2)$, for degrading fracture toughness in Eq. (3.1): Case h3.	165
5.55	Detailed evolution of elastic damage variable d^e and two degradation functions, $\cos^{p_1}(\beta_{G1}\alpha^*/2)$ & $\cos^{p_2}(\beta_{G2}\tau_p^*/2)$, for degrading fracture toughness in Eq. (3.1): Case h4.	166
5.56	Crack path in initial configuration for Example 5-3-2.	166
5.57	Detailed evolution of elastic damage variable d^e : Brittle fracture.	167
5.58	Geometry with boundary conditions for Example 5-3-3.	167
5.59	Load-gauge displacement curves for Example 5-3-3.	169
5.60	Detailed evolution of discrete crack surfaces, elastic damage variable d^e and two degradation functions, $\cos^{p_1}(\beta_{G1}\alpha^*/2)$ & $\cos^{p_2}(\beta_{G2}\tau_p^*/2)$, for degrading fracture toughness in Eq. (3.1): SRB. (Only 1/4 of the round bar is shown.)	170
5.61	Detailed evolution of discrete crack surfaces, elastic damage variable d^e and two degradation functions, $\cos^{p_1}(\beta_{G1}\alpha^*/2)$ & $\cos^{p_2}(\beta_{G2}\tau_p^*/2)$, for degrading fracture toughness in Eq. (3.1): NRB. (Only 1/4 of the round bar is shown.)	171
5.62	Crack surfaces of the cup-cone failure.	172
B.1	Enlarged views of Fig. 5.31(b) along with data plots of FC-based staggered iterations.	186
B.2	Distributions of the history variable \mathcal{H}^e and damage variable d in order from the top in the initial configuration.	187

1 Introduction

1.1 Research Background

Natural disasters, such as earthquakes, hurricanes, and floods, bring devastating effects on local and global communities all over the world. They cause not only immediate damage and loss of human life but also lead to long-term aftershocks such as infective disease ^{1),2)}, logistics disruption ^{3),4)}, and environmental pollution ⁵⁾. These problems often result from the destruction of infrastructure facilities. That is, roads, bridges, and buildings are destroyed, making it difficult or impossible for people to access essential services such as food, medication, and energy. From this perspective, a framework is needed that can evaluate or predict how infrastructure facilities are damaged and destroyed in the event of a natural disaster. With such a framework, proactive procedures, such as reinforcement and repair, can be adequately performed, which can mitigate the degree of damage to infrastructure facilities caused by natural disasters and, consequently, shorten post-disaster economic stagnation.

An infrastructure facility, which is called “a structure” hereafter, experiences several “failures” before losing its functionality, as illustrated in Fig. 1.1. If the external forces acting on the structure are small, or if the structure has been repeatedly subjected to these forces for a long period of time, the structure experiences microscale damage. The damaged region is often small compared with the size of the whole structure and may not be visible. Also, the structure does not immediately lose its functionality. We call this type of failure “segment-level fracture”. Meanwhile, if the external forces are sufficiently large to cause the structure to lose its functionality, “structural level fracture” occurs. At this stage, the crack

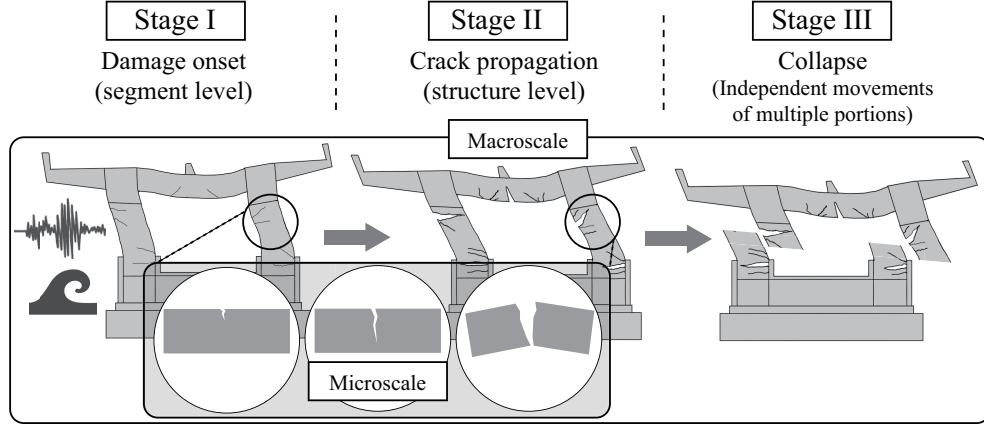


Fig. 1.1: Classification of failures in an infrastructure facility.

propagations occurring in the structure are visible macroscopically, and the recovery of the structure is often impossible. Also, the structural level fracture may endanger human lives. Additionally, if the external forces are extremely large, some segments may be separated from the base structure and fall to the ground, or the structure itself may be collapsed. This stage is called “collapse”, in which the structure not only loses its functionality but also drives the secondary destruction of other structures and also becomes the obstacle to evacuation.

While several types of failures are explained above, they are all derived from the simplest one, i.e., brittle fracture. As represented by brittle fracture, originating from the pioneering study conducted by Griffith ⁶⁾, a vast number of experimental and theoretical studies have been dedicated to understanding failure phenomena. In a fracture process causing failure, it is commonly understood that a set of new crack surfaces is generated if a crack opening condition is satisfied. To be specific, if an instantaneous energy release rate \mathcal{G}^* is equal to or larger than its critical value (i.e., $\mathcal{G}^* \geq \mathcal{G}_c$) inherent in the material under consideration, cracks initiate brittle fracture. Meanwhile, in the case of ductile materials such as aluminum or steel, since plastic deformation accompanied by hardening occurs before crack initiation, another portion of energy must be dissipated by the inelastic (plastic) deformation. Accordingly, the critical value \mathcal{G}_c of elastoplastic materials is known to be larger than that of brittle materials; see, e.g., References ^{7),8)} for more detailed discussions.

In time with the experimental and theoretical developments, numerical simulations have

gained popularity in predicting crack propagations or understanding the mechanisms and physics of fracture phenomena. Today, the finite element method (FEM) is definitely the most well-known and reliable simulation tool, which has been mainly developed in the mechanical and civil engineering fields. In fact, the research using the FEM has contributed greatly to understanding the fracture behavior of materials at the specimen level geometry. At the practical level, commercial software, such as Abaqus ⁹⁾, Ansys ¹⁰⁾, COMSOL ¹¹⁾, DIANA ¹²⁾, and Nastran ¹³⁾ is known as reliable tools employing implicit schemes, which allows engineers without advanced academic knowledge to conduct numerical simulations. However, at the current stage, a numerical simulation method (or framework) that can describe multiple fracture scales and stages in a large structure, from the microscale crack initiation to the final macroscale collapse, does not exist.

1.2 Previous studies for fracture simulation

In general, techniques within the FE framework to represent crack propagations are classified into two major groups, i.e., diffusive and discrete approaches. In what follows, representative previous studies of the two approaches, their advantages and disadvantages, and the methods chosen in this thesis are discussed.

1.2.1 Diffusive approach

The diffusive approach, which is known collectively as the “continuum damage model (CDM) ^{14),15),16),17)}”, pursues constitutive modeling to replace the discrete expression of fracture by strain-softening behavior of finite elements. In the process of the replacement of the crack representation, the “damage variable” was introduced, which is usually a scalar quantity to represent how much of the original mechanical ability of the material has been lost due to damage. Some of the CDMs have long histories: the Gurson-Tvergaard-Needleman (GTN) model ^{18),19)}, the Lemaitre model ²⁰⁾ and the Microplane damage model ²¹⁾ were first reported in the 1980s. Today, most CDMs can be categorized into one of them.

The CDM was originally developed as a “local approach”, in which the damage evolution was computed locally, i.e., at each Gaussian point of a finite element, and the damage variable was defined as an internal variable. However, this local approach is known to suffer from unstable numerical solutions caused by the ill-posedness of the underlying partial differential equation ²²⁾. This deficit eventually leads to pathological mesh-dependent solutions and even results in divergence immediately after the onset of damage evolution. Thus, some sorts of regularization techniques are necessarily required to overcome this issue, which originated from non-local integral algorithms ²³⁾ and gradient-enhanced approximations ²⁴⁾. Accordingly, the non-local modeling becomes essential for properly describing damage evolution in materials without mesh-dependency, and a lot of advanced CDMs have been proposed in the last two or three decades, e.g. Bažant et al. ²⁵⁾, Peerlings et al. ²⁶⁾, Reusch et al. ²⁷⁾, Geers ²⁸⁾, Golshani et al. ²⁹⁾, Lyakhovsky et al. ³⁰⁾, Waffenschmidt et al. ³¹⁾, Thai et al. ³²⁾, Poh & Sun ³³⁾, and Kurumatani et al. ³⁴⁾ are relatively well known in the community of damage modeling.

Being independent of the main family of CDMs but having an equivalent concept to the gradient-enhanced approaches, the “crack phase-field model (CPFM)” has recently received attention. The model has a physical background inspired by Francfort & Marigo ³⁵⁾. That is, crack initiation, propagation, and bifurcation in brittle materials can be represented by solutions to an energy minimization problem of potential energy based on Griffith’s theory. The geometry representation of discrete crack surfaces was subsequently regularized by adopting a so-called phase-field approximation ^{36),37),38)}. Later, Miehe et al. ³⁹⁾ proposed a thermodynamically consistent formulation within the continuum mechanics framework and coined the term “crack phase-field” to describe diffusive crack representations. Also, Miehe et al. ⁴⁰⁾ introduced a history variable to represent the maximum elastic strain energy in tension ever experienced that ensures the irreversibility of crack propagation. Since then, the CPFM has become increasingly popular, and a great deal of effort has been made on its enhancements. For instance, the original CPFM has been enhanced to describe the dynamic fracture ^{41),42),43),44),45),46)}, cohesive fracture ^{47),48),49),50),51),52),53),54),55)}, fatigue fracture

56),57),58),59),60),61),62), multifield fracture^{63),64),65),66),67),68)} to name only a few. For the historical development and comprehensive understanding of the CPFEM, refer to Ambati et al.⁶⁹⁾ and Wu et al.⁷⁰⁾.

When particular attention is paid to the definition of the elastic damage driving force for the elastic system, several studies are available. Henry & Levine⁷¹⁾ identified the crack states by decomposing a strain tensor into tensile and compressive parts. Amor et al.⁷²⁾ proposed an energy split based on the volumetric-deviatoric decomposition. Miehe et al.³⁹⁾ defined the driving force based on the spectral split principle. Steinke & Kaliske⁷³⁾ proposed a split based on the directional stress decomposition. Storm et al.⁷⁴⁾ has introduced a homogenization-type approach by incorporating the concept of representative crack element (RCE) into the CPFEM.

To describe ductile fracture, the above elastic damage driving force is insufficient, and the plasticity-induced damage driving force should be adequately introduced in damage computation. Pioneering works for CPFEM of ductile fracture have been done by several different research groups. Alessi et al.^{75),76)} proposed a variational elastoplastic gradient damage model that introduces a “plastic-damage coupled dissipation potential” to realize plasticity-dependent damage evolution. Ambati et al.^{77),78)} proposed a “plasticity-induced degradation function” to represent ductile fracture. Since the degradation function is determined by both the crack phase-field variable and the plastic hardening variable relevant to plastic deformation, the degradation of material stiffness is realized only in the region where plastic deformation is concentrated. Also, Miehe et al.^{79),80)} introduced “plastic damage driving force” into damage computation within the gradient plasticity framework^{81),82)}. Similarly, Borden et al.⁸³⁾ introduced the effect of stress triaxiality on the plastic strain energy as a parameter to control the damage evolution. In general, under plastic deformation, the amount of plastic work due to hardening is considerably larger than that of elastic strain energy, resulting in crack initiation in a plastic-deformation dominant region. As an alternative concept, Dittmann et al.⁸⁴⁾ and Yin & Kaliske⁸⁵⁾ have proposed a different “degrading fracture toughness”, which is degraded with the accumulation of plastic strain. This concept can

be phenomenologically regarded as fatigue damage, although only the monocycle failure is considered. Meanwhile, as an example of rigorous mathematical descriptions, Dal Maso et al.⁸⁶⁾ discussed Γ -convergence properties associated with the fracture models for perfectly plastic materials subjected to antiplane shear. Additionally, among the other models reported are those by Kuhn et al.⁸⁷⁾, Alessi et al.⁸⁸⁾, Aldakheel et al.⁸⁹⁾, Dittmann et al.⁹⁰⁾, and Han et al.⁹¹⁾.

In a review by Alessi et al.⁹²⁾, some early CPFMs for ductile fracture are investigated regarding their responses to homogeneous and non-homogeneous deformations. In the study, a dilemma is pointed out: the introduction of thresholds and coefficients to control damage driving force improves the richness of capturing ductile fracture responses while vitiating variational consistency. In fact, several CPFMs^{83),93),94),91)} introduce thresholds and coefficients regarding damage in the numerical implementation stage or without driving variational consistent damage evolution law, which in nature, violates the variational structure of the original formulation. Additionally, these newly introduced thresholds and coefficients may lead to unreasonable mechanical responses of materials, which are not able to be explained by physics.

1.2.2 Discrete approach

Another approach is called the “discrete approach,” which probably has a little longer history than the diffusive approach, by which the discontinuous displacement field is incorporated into FE approximations. Note that the discrete approach is often called the “meshless method” or “meshfree method”. Strictly speaking, the two methods employ different computational techniques, i.e., the meshless method does not require finite elements and only uses nodes to solve governing equations, whereas the meshfree method uses finite elements but relies on the partition of unity property to realize the strong discontinuity of a state variable. As representative FEMs combined with strong discontinuity approaches, the node-releasing FEM^{95),96)}, the element-free Galerkin FEM^{97),98)}, the embedded FEM⁹⁹⁾, the partition-of-unity-based FEM^{100),101),102)}, the generalized or extended FEM (GFEM or XFEM, respec-

tively)^{103),104),105),106)}, and the numerical manifold method or the finite cover method (NMM or FCM, respectively)^{107),108),109)} are well known in the field of computational mechanics.

Although the methods introduced above realize discontinuities, such as cracks, it is necessary to introduce a fracture criterion when there is a need to know the crack initiation position and its propagation direction. In many cases, the geometric information and mechanical properties around the crack tip are employed in the fracture criterion. For instance, within the framework of linear fracture mechanics, the stress intensity factor¹¹⁰⁾ and J-integral¹¹¹⁾ are commonly used; see Fleming et al.¹¹²⁾, Rao & Rahman¹¹³⁾, Liu et al.¹¹⁴⁾, Laborde et al.¹¹⁵⁾, Ghorashi et al.¹¹⁶⁾, Rao & Rahman¹¹⁷⁾, Bechet et al.¹¹⁸⁾, Belytschko & Gracie¹¹⁹⁾, and Duflo et al.¹²⁰⁾. While these methods represent discrete cracks with high accuracy, their abilities to trace complex crack propagations in three-dimensional cases are limited. Also, in some cases, the initial crack location or its propagation direction must be known in advance to obtain appropriate simulation results. To address the inconvenience of these incorporations and to describe an arbitrary crack propagation problem, diffusive-discrete crack transition techniques have been studied. They have the advantages of both diffusive and discrete approaches, i.e., arbitrary crack propagation problems are solved using CDMs, and the predicted crack paths are replaced by discrete representations. Among the diffusive-discrete crack transition techniques, Simone et al.¹²¹⁾, Areias & Belytschko¹²²⁾, Mediavilla et al.¹²³⁾, Comi et al.¹²⁴⁾, Moës et al.¹²⁵⁾, Roth et al.¹²⁶⁾, Wang et al.¹²⁷⁾, and Wu et al.¹²⁸⁾ are known as representative studies that succeeded in implementing CDMs in meshfree methods.

More recently, the candidate to be incorporated into diffusive-discrete crack transition techniques seems to be shifting from the CDM to the CPFM. The author considers that this trend is due to not only the popularity of the CPFM but also the origin of it. That is, the CPFM originally stems from fracture mechanics associated with discrete cracks or, equivalently, strong discontinuities. Nevertheless, the CPFM eventually performs equivalently to other gradient-enhanced damage models since the crack surfaces were regularized to be diffusive representations. Indeed, this approximation has facilitated the implementation of the CPFM into the standard FEM but has provoked several problems that CDMs usually

Table 1.1: Several CPFMs combined with strong discontinuity approaches.

Working group	Strain	2D/3D	Method	Crack tip	Targeting problem
	When and How crack paths or tips are updated				
Giovanardi et al. ¹²⁹⁾	Small	2D	XFEM	Implicit	Brittle fracture
	The regions outside of crack tips are updated at the end of each time step.				
Geelen et al. ¹³⁰⁾	Small	2D	XFEM	Explicit*	Brittle fracture
	Crack tips are updated by a switching criterion at the end of each time step.				
Muixí et al. ¹³¹⁾	Small	2D/3D	XFEM	Implicit	Brittle fracture
	The regions outside of crack tips are updated at the end of each time step.				
Sun et al. ¹³²⁾	Small	2D/3D	FEMM	Explicit*	Brittle fracture
	Crack tips are updated by a switching criterion ¹³⁰⁾ at the end of each time step.				
Hussein et al. ¹³³⁾	Small	2D	VEM	Explicit*	Brittle fracture
	Crack tips are updated by length minimization problems at the end of each time step.				
Yang et al. ¹³⁴⁾	Small	2D	NMM	Explicit*	Brittle fracture
	Crack tips are updated by finding the farthest damaged nodes at the end of each time step.				

face. For instance, severely damaged finite elements or mesh collapses cause the failure of global Newton-Raphson (NR) computations. Additionally, a discrete crack representation cannot be realized, so some subsequent phenomena, e.g., frictional contact between opposite crack surfaces, inflow/outflow of gases and liquids within a cracked region, independent movements of multiple portions separated by cracks, etc., are difficult to be described.

With regard to combining one of the aforementioned discrete approaches with the CPFM, several challenges have been addressed by different groups, as listed in Table 1.1. Giovanardi et al. ¹²⁹⁾ introduced a coupling method named “*Xfield*”. In this method, a discrete crack path is realized by the XFEM, while the damage computation is conducted only for a certain region around the crack tip, which is referred to as an overlapping subdomain. Geelen et al. ¹³⁰⁾ proposed a continuous-discontinuous crack transition method to simulate brittle fractures, in which a discrete crack path is represented by the XFEM when the increment of a diffusive crack, $\Delta\Gamma_t$, reaches a predefined threshold. Muixí et al. ¹³¹⁾ also proposed a coupling method between the XFEM and CPF modeling, but discrete and diffusive cracks do not overlap, unlike in the approach of Giovanardi et al. ¹²⁹⁾. Instead, a diffusive crack topology in the CPFM is placed only in the region around a crack tip, while the XFEM is utilized to

represent a discrete crack in the rest of the region. As a result, crack tip enrichment in the XFEM is not required in their method. Sun et al. ¹³²⁾ proposed a method called “FEMM-PF”, which combines the FE-meshfree method (FEMM) ¹³⁵⁾ with the CPFEM. Employing the same continuous-discontinuous switching criterion as that of Geelen et al. ¹³⁰⁾, they presented several three-dimensional (3D) numerical simulations to demonstrate the capability of their method. As an alternative concept, Hussein et al. ¹³³⁾ proposed a method of coupling the crack phase-field and a discrete cutting method to exploit the feature of the virtual element method (VEM) ^{136),137)}. More recently, Yang et al. ¹³⁴⁾ extended their previous work ¹³⁸⁾ to introduce explicit crack surfaces via the NMM.

At the current stage, several unresolved problems still remain. In particular, if a crack is supposed to propagate rapidly at once or while bending, the algorithms developed in most of the previous studies might lead to undesirable crack paths. This is because the explicit crack tip is updated only at the end of each pseudo-time interval in quasi-static analyses. As a result, the crack tip representation is considered semi-explicit and is marked by an asterisk * in Table 1.1 since the crack propagating during one loading step is represented implicitly from beginning to end. Also, all the previous methods were developed within the small strain framework, but the finite strain assumption is required to adequately capture the fracture problems affected by the geometrical nonlinearity, such as large deformation and rotation. Additionally, the enhancements of the previous studies to describe dynamic and ductile fracture have not been addressed, which are necessary to capture a series of failure events involving arbitrary crack initiation, propagation, bifurcation, division of a base structure into multiple portions, and independent motions of the divided portions.

1.3 Purpose of this study

Against the above-explained research background and academic agendas to be addressed, this study aims to pave the road toward the comprehensive evaluation and prediction of the multistage and multiscale failure events of a structure summarized in Fig. 1.1.

The first aim is to propose a variationally and thermodynamically consistent CPFM for ductile fracture. For the sake of formulation, we review the distinctive features of the existing CPFMs for ductile fracture in terms of how ductile fracture is realized in previous studies. The specific discussion is focused on the plastic driving force and degrading fracture toughness in damage evolution. Also, we investigate the damage evolution tendency in terms of the definition of yield function. Based on the discussion, we propose a new model for ductile fracture equipped with two separate damage variables for elasticity and plasticity. Beginning with the introduction of a constitutive work density functional consisting of elastic, plastic hardening, and damage hardening components, we derive variationally and thermodynamically consistent evolution laws for plasticity and damage. These evolution laws for plasticity and damage are derived by using separate threshold (yield) functions while having similar formats so that those for damage ensure variational and thermodynamic consistencies. The mathematical form describing the evolution laws of damage has been overlooked or not considered in previous studies and therefore deserves particular emphasis. The evolution laws for plasticity are coupled with damage, so the accumulation of plastic strain is lowered in the severely damaged region. Also, the proposed model is equipped with thresholds and coefficients to control the amount of damage driving force and thus is useful to reproduce actual failure events. Additionally, thanks to the introduction of both the plastic driving force and degrading fracture toughness, the formulation realizes both the plastic deformation-induced and negative hydrostatic pressure-induced damage evolution. Therefore, the formulation unifies several of the existing CPFMs for ductile fracture proposed to date, including a few proposed by the authors.

On the other hand, with almost the same mentality as the previous studies listed in Table 1.1, we propose a novel transition scheme from a diffusive crack topology in CPFM to a discrete crack represented by a strong discontinuity approach. Specifically, the crack initiation and propagation processes are determined from an energy minimization problem with respect to the CPF modeling, and the predicted path of a diffusive crack topology is replaced by a discrete topology by applying the FCM. The proposed scheme can trace an actual crack

path as closely as possible and stably update its explicit crack tip even in a large deformation regime. The features of the proposed scheme are summarized as follows:

- By developing a technique for determining explicit crack tips, the given crack topology is updated from diffusive to discrete intermittently during the course of a staggered iterative procedure in a single time step. This is realized by the moving circle algorithm, which is conceptually equivalent to the medial-axis-based algorithm proposed by Tamayo-Mas & Rodríguez-Ferran ¹³⁹⁾, thereby pursuing the evolution of explicit crack tips. Here, the physical quantities are transferred from old to new covers within the FCM framework during this evolution while satisfying the equilibrium condition. With this technique, even a curved crack path that evolves significantly within a single time increment can be explicitly captured.
- To stably update an explicit crack tip within the finite strain framework, we devise stabilization techniques. Specifically, a pseudo-stiffness is introduced to severely damaged elements around the discrete crack path for the quasi-static system to prevent excessively large deformations. On the other hand, the damage and volume fraction-induced numerical damping is introduced for the dynamic system to maintain computational stability and avoid distortion of the physical mesh due to the effects of stress wave propagation. Additionally, the corrector of the displacement increment is intentionally modified so that NR computations successfully converge, and the discrete crack opens in a gradual and stable manner.

The CPFEM accommodating two damage variables for elasticity and plasticity is incorporated into the developed diffusive-discrete crack transition scheme. Accordingly, a series of fracture events involving arbitrary crack initiation, propagation, bifurcation, division of an original object into multiple portions, and independent motions of the divided portions can be investigated in the numerical simulation.

1.4 Outline of this dissertation

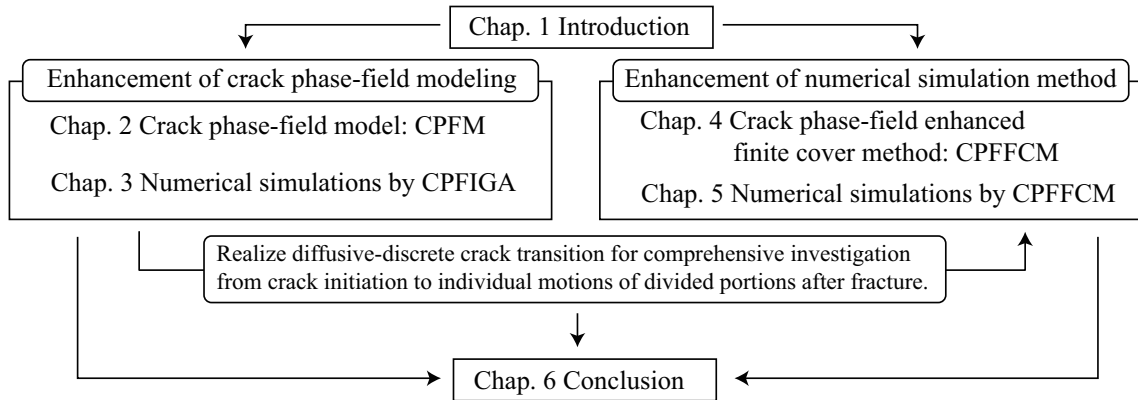


Fig. 1.2: The outline of this dissertation.

The outline of this dissertation is summarized in Fig. 1.2. This dissertation begins with the enhancement of CPFMs for ductile fracture in Chapter 2. After revisiting the fundamental description regarding the kinematics of continuum mechanics, the regularization of cracks in the CPF modeling, and the formulation of the conventional CPFM for brittle and dynamic fractures, the discussion is focused on the ingredients to realize ductile fracture in the CPF context. Based on the review of existing models, the proposed model that accommodates damage variables for elasticity and plasticity is derived, which is reasonable with respect to both the variational and thermodynamic arguments. In the end, the numerical implementation of the proposed model within the framework of the isogeometric analysis (IGA)¹⁴⁰⁾ is presented.

Chapter 3 is devoted to numerical simulations to verify the performance of the proposed model and demonstrate its ability to reproduce the typical ductile fracture behavior of elastoplastic materials. The first example shows the characteristic features of the proposed model by a uni-directional uniform deformation setup, and its performance is compared with the performance of the previous models in the literature. The second example demonstrates several different crack initiation and propagation scenarios by providing different sets of parameters concerning damage evolution. Several typical ductile fractures occurring in notched specimens are simulated here. In the third example, the cup-cone fracture is simulated,

in which the plastic deformation-induced and negative hydrostatic pressure-induced crack initiation and the plastic deformation-induced crack propagation around the surface of the specimen are demonstrated. In the last example, the characteristic crack initiation and propagation trends of advanced high strength steel materials are simulated, where the role of the degrading fracture toughness is reconsidered by reference to simulation results.

To realize a series of fracture events involving crack initiation at an arbitrary location, propagation, and bifurcation in arbitrary directions, arbitrary divisions of an original object into multiple portions, and independent motions of divided portions, the numerical algorithm for realizing the diffusive-discrete crack topological transition is presented in Chapter 4. The proposed scheme determines the crack initiation, propagation, and bifurcation processes of brittle, dynamic, and ductile fractures from an energy minimization problem relevant to the CPF theory. Additionally, the predicted path in a diffusive crack topology is replaced by its discrete representation by the application of the finite cover method (FCM). Several algorithms to realize the diffusive-discrete crack topological transition, as well as the spatial and temporal discretizations, are explained step by step by reference to graphical explanations.

Chapter 5 proposes a novel simulation method called “Crack phase-field enhanced finite cover method (CPFFCM)”. The proposed method uses the derived CPFM in Chapter 2 as the damage computation tool to predict the crack initiation, propagation, and bifurcation, and the obtained diffusive crack path is replaced by the developed diffusive-discrete crack transition scheme in Chapter 4. Enjoying this combination, a series of failure events from the damage initiation to the post-failure phase, occurring in brittle and ductile materials under quasi-static and dynamic conditions, can be simulated. In the first section regarding brittle fracture, the basic performance of the CPFFCM is investigated. In particular, for comparison, we conduct simulations using the CPFFCM and the standard FEM with the conventional CPFM. The following section demonstrates the dynamic fractures involving arbitrary crack initiation, propagation, bifurcation, division of the original object into multiple portions, and subsequent independent motions of the divided portions. In the last section, several ductile fracture patterns involving the negative hydrostatic pressure-induced damage are computed

by the CPFFCM. Specifically, as a three dimensional example, the cup-cone failure simulation is conducted to reproduce the explicit cup-cone crack surfaces.

In Chapter 6, the implications of the obtained research outcomes are analyzed, and the future direction of research is discussed.

2 Crack phase-field model: CPFM

This chapter summarizes the fundamentals of the CPFM and presents a novel model for ductile fracture. The basic descriptions regarding the kinematics of continuum mechanics are first presented and followed by the regularization of cracks in the CPF modeling and the formulation of the conventional CPFM for brittle and dynamic fractures. Subsequently, the several ingredients to realize ductile fracture in the CPFM are summarized, where the discussion is focused on the plastic driving force, degrading fracture toughness, and yield function. Based on the discussion, the proposed model that accommodates damage variables for elasticity and plasticity is derived. In the end, the numerical implementation of the proposed model within the framework of the isogeometric analysis (IGA) ¹⁴⁰⁾ is presented.

2.1 Kinematics

Let us consider an arbitrary continuum body within the finite deformation framework. The initial and current configurations are denoted by $\mathcal{B}_0 \subset \mathbb{R}^s$ and $\mathcal{B}_t \subset \mathbb{R}^s$ with dimension $s \in \{2, 3\}$, and their boundaries are denoted by $\partial\mathcal{B}_0 \subset \mathbb{R}^{s-1}$ and $\partial\mathcal{B}_t \subset \mathbb{R}^{s-1}$, respectively. Here, the boundary is a set of two types of partial boundaries, i.e., the Neumann and Dirichlet boundaries ($\partial\mathcal{B}_0 = \partial\mathcal{B}_0^N \cup \partial\mathcal{B}_0^D$ and $\partial\mathcal{B}_t = \partial\mathcal{B}_t^N \cup \partial\mathcal{B}_t^D$).

At time $t \in \mathcal{T} = [0, T]$, points denoted by $\mathbf{X} \in \mathcal{B}_0$ are mapped onto $\mathbf{x} \in \mathcal{B}_t$ by the mapping function $\mathbf{x} = \boldsymbol{\varphi}(\mathbf{X}, t) : \mathcal{B}_0 \times \mathcal{T} \rightarrow \mathbb{R}^s$. Here, $\mathbf{u} = \mathbf{x} - \mathbf{X}$ denotes the total displacement. To describe the deformation of the body, the deformation gradient $\mathbf{F} := \nabla \boldsymbol{\varphi} = \partial \mathbf{x} / \partial \mathbf{X}$ is introduced, which is decomposed into the elastic and plastic parts, \mathbf{F}^e and \mathbf{F}^p , so that $\mathbf{F} = \mathbf{F}^e \cdot \mathbf{F}^p$. Hereafter, the operators ∇ and $\nabla_{\mathbf{x}}$ denote, respectively, the spatial gradients

with respect to the initial configuration \mathcal{B}_0 and the current configuration \mathcal{B}_t .

Meanwhile, to describe the hardening caused by plastic deformation, the local and global plastic hardening variables, $\bar{\alpha} : \mathcal{B}_0 \times \mathcal{T} \rightarrow \mathbb{R}$ and $\alpha : \mathcal{B}_0 \times \mathcal{T} \rightarrow \mathbb{R}$, are introduced within the framework of micromorphic plasticity ^{141),142)}.

In addition, to regularize the crack surfaces, the crack phase-field (CPF) variable $d : \mathcal{B}_0 \times \mathcal{T} \rightarrow \mathbb{R}$ is introduced. Similarly to the concept of continuum damage mechanics (CDM) ¹⁷⁾, $d = 1$ indicates the fully broken state, whereas the sound state corresponds to $d = 0$. Additionally, we postulate the irreversible condition $\dot{d} > 0$ for damage evolution.

2.2 Phase-field approximation

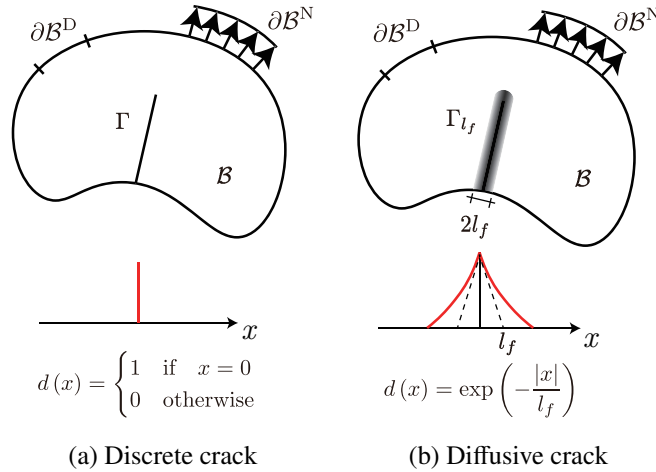


Fig. 2.1: Diffusive crack topology in CPF modeling.

Francfort and Marigo ³⁵⁾ first derived the crack initiation followed by propagation as an optimization problem of the energy function, which consists of the elastic strain energy and the energy needed for crack surface generation. Their formulation was subsequently regularized by adopting a diffusive topological approximation by Bourdin et al. ³⁸⁾, and the initial CPF model was born. In the last one or two decades, the crack phase-field model has gained popularity in the community of computational mechanics.

In the CPF modeling, the discrete crack surfaces Γ in a continuum body are numerically

approximated as a diffusive crack topology Γ_{l_f} by introducing a phase-field approximation as shown in Fig. 2.1. As mentioned above, a scalar-valued variable d , called the “crack phase-field (CPF) variable”, is introduced as a damage variable to connect two physical states of the material smoothly; intact state $d = 0$ and fully broken state $d = 1$. To briefly review the phase-field approximation for discrete crack surfaces, let us take a one-dimensional bar in tension as an example, which is assumed to have an infinite length $L \in [-\infty, +\infty]$ and discrete crack surfaces at $x = 0$.

The diffusive crack distribution in second-order phase-field approximation theory is given as

$$d(x) = \exp\left(-\frac{|x|}{l_f}\right), \quad (2.1)$$

where l_f is the crack length scale parameter to represent the width of the diffusive crack. By taking the limit $l_f \rightarrow 0$, the diffuse crack converges to the original discrete crack, as illustrated in Fig. 2.1(a). On the other hand, the exponential function in Eq. (2.1) is known to be a solution to the following differential equation:

$$d - l_f^2 \frac{d^2 d}{dx^2} = 0, \quad (2.2)$$

which is also identified with the Euler equation of the following variational problem:

$$\begin{aligned} d &= \arg \left\{ \inf_{d \in W} I(d) \right\} \\ \text{with } I(d) &:= \frac{1}{2} \int_{\mathbb{B}_0} \{d^2 + l_f^2 d'^2\} dV, \quad W := \{d \mid d(0) = 1, d(\pm\infty) = 0\}. \end{aligned} \quad (2.3)$$

Under the one-dimensional setup, the volume integration is equivalent to $dV = \Gamma dx$, so that the substitution of Eq. (2.1) into Eq. (2.3) yields $I(d) = \Gamma l_f$. Here, the discrete crack Γ is found to be approximately equivalent to Γ_{l_f} , i.e.,

$$\Gamma \approx \Gamma_{l_f} := \frac{I(d)}{l_f} = \int_{\mathbb{B}_0} \frac{1}{2l_f} \{d^2 + l_f^2 d'^2\} dV, \quad (2.4)$$

where the integrand is identified with the crack surface density and expressed as

$$\gamma_{l_f}(d, d') = \frac{1}{2l_f} (d^2 + l_f^2 d'^2). \quad (2.5)$$

The multi-dimensional extension of this crack surface density straightforwardly reads

$$\gamma_{l_f}(d, \nabla d) = \frac{1}{2l_f} (d^2 + l_f^2 |\nabla d|^2). \quad (2.6)$$

Here, for the details concerning the phase-field approximation, refer to Bourdin et al. ³⁸⁾, Miehe et al. ³⁹⁾, and Borden et al. ¹⁴³⁾ to name a few. It is worth mentioning that Eq. (2.6) is well-known as the crack surface density of the “AT2 model”, which is probably the most used in the community of CPFEM. Also, other CPFEMs are available, but let us ask readers to refer to Reference ⁷⁰⁾.

2.3 CPFEM for quasi-static and dynamic brittle fractures

Before presenting the proposed model for ductile fracture, let us revisit the conventional CPFEM for quasi-static and dynamic brittle fractures. Based on the first law of thermodynamics, the following energy conservation relation holds for the motion of the continuum body:

$$\mathcal{E} + \mathcal{K} + \mathcal{D} = \mathcal{P} \quad , \quad (2.7)$$

where \mathcal{E} , \mathcal{K} , \mathcal{D} , and \mathcal{P} denote the constitutive work, kinetic energy, dissipation energy due to numerical damping, and external work, respectively. Here, these energy terms are defined as follows:

$$\mathcal{E} = \int_{\mathcal{B}_0} \Psi dV = \int_{\mathcal{B}_0} \left\{ \Psi^e(\mathbf{F}, d) + \Psi^f(d, \nabla d) \right\} dV \quad , \quad (2.8)$$

$$\mathcal{K} = \int_{\mathcal{B}_0} K dV = \int_{\mathcal{B}_0} \frac{1}{2} \rho_0 \|\dot{\mathbf{u}}\|^2 dV \quad , \quad (2.9)$$

$$\mathcal{D} = \int_{\mathcal{B}_0} D dV = \int_{\mathcal{B}_0} \int_t (\underline{\underline{C}} : \dot{\mathbf{F}}) : \dot{\mathbf{F}} dt dV, \quad (2.10)$$

and

$$\mathcal{P} = \int_{\mathcal{B}_0} P^b dV + \int_{\partial \mathcal{B}_0} P^t dA = \int_{\mathcal{B}_0} \int_t \mathbf{B} \cdot \dot{\mathbf{u}} dt dV + \int_{\partial \mathcal{B}_0} \int_t \mathbf{T} \cdot \dot{\mathbf{u}} dt dA \quad , \quad (2.11)$$

where Ψ , K , D , P^b , and P^t are the constitutive work density, kinetic energy density, dissipation energy density due to numerical damping, and external work densities of the body and traction forces, \mathbf{B} and \mathbf{T} , respectively.

The constitutive work density Ψ is further decomposed into the elastic strain energy density Ψ^e and the crack generation energy density Ψ^f , whose specific forms are given as, respectively,

$$\Psi^e = \begin{cases} g(d) \left(\underbrace{\Psi_{0,\text{dev}}^e + \Psi_{0,\text{vol}}^e}_{\Psi_0^{e+}} \right) + \underbrace{0}_{\Psi_0^{e-}} & \text{for } J \geq 1 \\ g(d) \underbrace{\Psi_{0,\text{dev}}^e}_{\Psi_0^{e+}} + \underbrace{\Psi_{0,\text{vol}}^e}_{\Psi_0^{e-}} & \text{for } J < 1 \end{cases} \quad \text{with} \quad \begin{cases} \Psi_{0,\text{vol}}^e = \frac{\kappa}{2} \left(\frac{J^2 - 1}{2} - \ln J \right) \\ \Psi_{0,\text{dev}}^e = \frac{\mu}{2} (I_{\bar{\mathbf{b}}} - 3) \end{cases} \quad (2.12)$$

and

$$\Psi^f = G_c \gamma_{l_f} = G_c \frac{d^2 + l_f \|\nabla d\|^2}{2l_f}. \quad (2.13)$$

Here, $J = \det[\mathbf{F}]$ denotes the determinant of the deformation gradient \mathbf{F} , $I_{\bar{\mathbf{b}}}$ is the first invariant of the second-order tensor defined as $\bar{\mathbf{b}} = J^{-2/3} \mathbf{b}$ with $\mathbf{b} = \mathbf{F} \cdot \mathbf{F}^T$ being the left Cauchy-Green tensor, and μ & κ are the shear and bulk elastic moduli, respectively. Also, $\Psi_{0,\text{dev}}^e$ & $\Psi_{0,\text{vol}}^e$ are the deviatoric and volumetric components of the elastic strain energy, and Ψ_0^{e+} & Ψ_0^{e-} denote the damage driving part and the remaining part that does not contribute to damage evolution. In addition, $g(d)$ is the degradation function used to represent the deterioration of the material, for which the following two forms are employed in this study:

$$\begin{aligned} \text{Quadratic form: } g(d) &= (1 - d)^2 \\ \text{Cubic form: } g(d) &= (s - 2)(1 - d)^3 + (3 - s)(1 - d)^2, \end{aligned} \quad (2.14)$$

where s is a constant to ensure the condition $\partial_d g(d)|_{d=0} < 0$, whose value is fixed at $s = 0.1$ in this study. Furthermore, G_c and l_f are the fracture toughness and the crack length scale parameter.

Meanwhile, the kinetic energy density K is computed from the mass density ρ_0 and the velocity vector $\dot{\mathbf{u}}$. The dissipation energy density due to numerical damping, D , is supposed

to be a material-specific quantity but is introduced for numerical damping to ensure computational stability in this study. The fourth-order damping tensor \underline{C} will be explained later. In addition, the external work densities, P^b and P^t , are computed from the body force \mathbf{B} and the traction force \mathbf{T} , respectively, the former of which is exclusively due to gravity. Note that the constitutive work density Ψ and the kinetic energy density K are state functions, so they are path-independent and can be computed only from the state variables, \mathbf{u} and d , at the current time. In contrast, the remaining two components, i.e., the dissipation energy density D and the external work densities P^b and P^t , are path-dependent quantities and are thus expressed in time-integral forms.

The time derivative of Eq. (2.7) leads to the following power balance equation:

$$\dot{\mathcal{E}} + \dot{\mathcal{K}} + \dot{\mathcal{D}} = \dot{\mathcal{P}} \quad , \quad (2.15)$$

where

$$\dot{\mathcal{E}} = \int_{\mathcal{B}_0} \dot{\Psi} dV = \int_{\mathcal{B}_0} \left(\frac{\partial \Psi^e}{\partial \mathbf{F}} : \dot{\mathbf{F}} + \frac{\partial \Psi^e}{\partial d} \dot{d} + \frac{\partial \Psi^f}{\partial d} \dot{d} + \frac{\partial \Psi^f}{\partial \nabla d} \cdot \nabla \dot{d} \right) dV \quad , \quad (2.16)$$

$$\dot{\mathcal{K}} = \int_{\mathcal{B}_0} \dot{K} dV = \int_{\mathcal{B}_0} \rho_0 \ddot{\mathbf{u}} \cdot \dot{\mathbf{u}} dV \quad , \quad (2.17)$$

$$\dot{\mathcal{D}} = \int_{\mathcal{B}_0} \dot{D} dV = \int_{\mathcal{B}_0} (\underline{C} : \dot{\mathbf{F}}) : \dot{\mathbf{F}} dV, \quad (2.18)$$

and

$$\dot{\mathcal{P}} = \int_{\mathcal{B}_0} \dot{P}^b dV + \int_{\partial \mathcal{B}_0} \dot{P}^t dA = \int_{\mathcal{B}_0} \mathbf{B} \cdot \dot{\mathbf{u}} dV + \int_{\partial \mathcal{B}_0} \mathbf{T} \cdot \dot{\mathbf{u}} dA \quad . \quad (2.19)$$

The substitution of Eqs. (2.16)–(2.19) into Eq. (2.15) yields

$$\begin{aligned} & - \int_{\mathcal{B}_0} \left(\nabla \cdot \mathbf{P} + \nabla \cdot (\underline{C} : \dot{\mathbf{F}}) + \mathbf{B} - \rho_0 \ddot{\mathbf{u}} \right) \cdot \dot{\mathbf{u}} dV - \int_{\mathcal{B}_0} \left(-\frac{\partial g(d)}{\partial d} \Psi_0^{e+} - \frac{G_c}{l_f} (d - l_f^2 \nabla^2 d) \right) \dot{d} dV \\ & + \int_{\partial \mathcal{B}_0^N} \left(\mathbf{P} \cdot \mathbf{N} + (\underline{C} : \dot{\mathbf{F}}) \cdot \mathbf{N} - \bar{\mathbf{T}} \right) \cdot \dot{\mathbf{u}} dA + \int_{\partial \mathcal{B}_0^D} \left(\mathbf{P} \cdot \mathbf{N} + (\underline{C} : \dot{\mathbf{F}}) \cdot \mathbf{N} - \mathbf{T} \right) \cdot \dot{\mathbf{u}} dA \\ & + \int_{\partial \mathcal{B}_0} G_c l_f \nabla d \cdot \mathbf{N} \dot{d} dA = 0. \end{aligned} \quad (2.20)$$

Similarly, the first-order stability condition for any possible admissible variations $\{\delta \mathbf{u}, \delta d\}$ is given as

$$\begin{aligned} & - \int_{\mathcal{B}_0} \left(\nabla \cdot \mathbf{P} + \nabla \cdot (\underline{\mathbf{C}} : \dot{\mathbf{F}}) + \mathbf{B} - \rho_0 \ddot{\mathbf{u}} \right) \cdot \delta \mathbf{u} dV - \int_{\mathcal{B}_0} \left(-\frac{\partial g(d)}{\partial d} \Psi_0^{e+} - \frac{G_c}{l_f} (d - l_f^2 \nabla^2 d) \right) \delta d dV \\ & + \int_{\partial \mathcal{B}_0^N} \left(\mathbf{P} \cdot \mathbf{N} + (\underline{\mathbf{C}} : \dot{\mathbf{F}}) \cdot \mathbf{N} - \bar{\mathbf{T}} \right) \cdot \delta \mathbf{u} dA + \int_{\partial \mathcal{B}_0} G_c l_f \nabla d \cdot \mathbf{N} \delta d dA \geq 0, \end{aligned} \quad (2.21)$$

in which the variation $\delta \mathbf{u}$ vanishes on the Dirichlet boundary $\partial \mathcal{B}_0^D$. From these equations and the prescribed condition $\dot{d} \geq 0$, the governing equations of the mechanical and damage fields are derived in strong form as follows:

- Equilibriums for the mechanical field:

$$\begin{aligned} \nabla \cdot \mathbf{P} + \nabla \cdot (\underline{\mathbf{C}} : \dot{\mathbf{F}}) + \mathbf{B} &= \rho_0 \ddot{\mathbf{u}} \quad \text{in } \mathcal{B}_0, \\ \mathbf{P} \cdot \mathbf{N} + (\underline{\mathbf{C}} : \dot{\mathbf{F}}) \cdot \mathbf{N} &= \bar{\mathbf{T}} \quad \text{on } \partial \mathcal{B}_0^N, \\ \mathbf{u} &= \bar{\mathbf{u}} \quad \text{on } \partial \mathcal{B}_0^D. \end{aligned} \quad (2.22)$$

- Threshold function for the crack phase-field with loading/unloading conditions:

$$\begin{aligned} \Phi^f &= -\frac{\partial g(d)}{\partial d} \Psi_0^{e+} - \frac{G_c}{l_f} (d - l_f^2 \nabla^2 d) \leq 0, \quad \dot{d} \geq 0, \quad \Phi^f \dot{d} = 0 \quad \text{in } \mathcal{B}_0, \\ G_c l_f \nabla d \cdot \mathbf{N} &= 0 \quad \text{on } \partial \mathcal{B}_0. \end{aligned} \quad (2.23)$$

2.4 Review of distinctive features in CPFEM for ductile fracture

This section presents a review of distinctive features in CPFEM for ductile fracture. Specifically, the emphasis is placed on the plastic driving force and degrading fracture toughness that enable CPFEM to represent damage evolution in elastoplastic materials. Attention is also paid to the damage evolution tendency in terms of the definition of the yield function.

2.4.1 Concise summary of CPFM for brittle fracture

Recently, the so-called “AT2 model” is widely used and known to correspond to an exponential diffusive crack topology expressed as $d = \exp(-|x|/l_f)$ in a one-dimensional case. As explained in Section 2.3, the constitutive work density Ψ in CPF modeling for brittle fracture consists of the elastic and damage contributions as follows:

$$\Psi = \Psi^e + \Psi^f, \quad \Psi^e = g(d) \Psi_0^{e+} + \Psi_0^{e-}, \quad \Psi^f = G_c \underbrace{\gamma_{l_f}}_{\text{Eq. (2.6)}}. \quad (2.24)$$

Based on the variational principle, two governing equations are derived as

$$\nabla \cdot \boldsymbol{\sigma} = \mathbf{0} \quad \text{and} \quad -\frac{\partial g(d)}{\partial d} \Psi_0^{e+} - \frac{G_c}{l_f} (d - l_f^2 \Delta d) = 0, \quad (2.25)$$

where $\boldsymbol{\sigma}$ is the stress tensor in general description, and $\Delta = \nabla^2$ denotes the Laplacian operator. Here, we have neglected the body and traction forces imposed on the continuum body for convenience. When a uniform deformation is considered ($\Delta d = 0$), an analytical solution for the crack phase-field variable is derived as follows:

$$d = \frac{2l_f \Psi_0^{e+}}{G_c + 2l_f \Psi_0^{e+}}, \quad (2.26)$$

in which we have assumed the quadratic form for the degradation function $g(d) = (1 - d)^2$. Eq. (2.26) eventually implies that the damage evolves along with the increase of the tensile component of the elastic strain energy Ψ_0^{e+} . In fact, this property holds regardless of the model type, such as AT1 and AT2 models, the function form of degradation function $g(d)$, and the values of material parameters, G_c & l_f .

2.4.2 Issue inherent in conventional CPFM for brittle fracture

When an elastoplastic material is targeted, damage evolution cannot be predicted by the straightforward incorporation of an elastoplastic constitutive law with conventional CPFM for brittle fracture. To clarify the issue inherent in the models, let us consider the one-dimensional problem of a uniformly deforming bar subjected to monotonic loading in its tensile direction, whose geometric setup and material parameters are provided in Table 2.1.

Table 2.1: Geometric setup and material parameters for the one-dimensional bar.

Parameter		Value	Unit
Length of one-dimensional bar	L	10	[mm]
Total displacement	u	-	[mm]
Young's modulus	E	200000	[MPa]
Initial yield stress	y_0	1000	[MPa]
Linear hardening parameter	h	1000 or 0	[MPa]
Fracture toughness	G_c	500	[N/mm]
Crack length scale parameter	l_f	1	[mm]

When linear elastoplasticity under the small strain assumption is assumed, the total strain ε , plastic strain ε^p and elastic strain ε^e can be written, respectively, as

$$\varepsilon = \frac{u}{L}, \quad \varepsilon^p = \frac{\langle E\varepsilon - y_0 \rangle}{E + h} \quad \text{and} \quad \varepsilon^e = \varepsilon - \varepsilon^p, \quad (2.27)$$

where $\langle \bullet \rangle = (\bullet + |\bullet|)/2$ is the Macaulay bracket. Here, E , y_0 , and h denote Young's modulus, initial yield stress, and linear hardening parameter. Assuming that $\dot{\varepsilon}^p = \dot{\alpha}$ in the one-dimensional setting, we will not make a distinction between the plastic strain ε^p and the plastic hardening variable (denoted by α) in the following description. Also, the constitutive work density functional, which consists of elastic, plastic, and damage parts, yields

$$\Psi = \Psi^e + \Psi^p + \underbrace{\Psi^f}_{\text{Eq. (2.24)}} \quad (2.28)$$

with $\Psi^e = g(d) \underbrace{\frac{1}{2} E \varepsilon^e{}^2}_{\Psi_0^e}, \quad \sigma = g(d) \underbrace{E \varepsilon^e}_{\sigma_0}, \quad \text{and} \quad \Psi^p = \underbrace{y_0 \alpha + \frac{1}{2} h \alpha^2}_{\Psi_0^p}.$

From this setup, the following governing equations are derived based on the variational principle:

$$\nabla \cdot \boldsymbol{\sigma} = \mathbf{0} \quad \text{and} \quad -\frac{\partial g(d)}{\partial d} \Psi_0^e - \frac{G_c}{l_f} (d - l_f^2 \Delta d) = 0. \quad (2.29)$$

Then, similar to Eq. (2.26), the damage variable d is given as

$$d = \frac{2l_f \Psi_0^e}{G_c + 2l_f \Psi_0^e}. \quad (2.30)$$

Here, the quadratic form $g(d) = (1 - d)^2$ introduced in the above equation allows softening behavior before reaching peak stress. To avoid such an undesirable response, we replace Ψ_0^e by $\langle \Psi_0^e - \Psi_{cr}^e \rangle$ as

$$d = \frac{2l_f \langle \Psi_0^e - \Psi_{cr}^e \rangle}{G_c + 2l_f \langle \Psi_0^e - \Psi_{cr}^e \rangle}, \quad (2.31)$$

where Ψ_{cr}^e is a threshold to activate the damage driving force, and $\Psi_{cr}^e \rightarrow \infty$ corresponds to an elastoplastic deformation without damage.

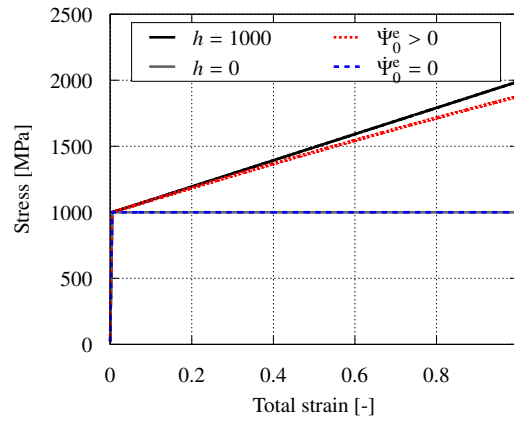


Fig. 2.2: Stress–total strain curves for the incorporation of the elastoplastic constitutive law and conventional CPF brittle modeling.

Using $\Psi_{cr}^e = 2.5$, we obtain the stress-total strain curves as shown in Fig. 2.2. The black and gray solid lines represent the elastoplastic responses without damage computation for linear hardening ($h = 1000$) and perfectly plastic ($h = 0$) cases, respectively. In contrast, the red and blue dashed lines represent those with damage. As can be seen in this figure, only a small reduction of material stiffness is seen in the linear hardening case, and no damage evolution is seen in the perfectly plastic case. This issue arises from the straightforward incorporation of an elastoplastic constitutive law with the conventional CPF modeling for brittle fracture. In fact, using Eq. (2.28), Eq. (2.29), and Eq. (2.31), the total strain $\varepsilon^{\text{quad}}$ at

peak stress reads

$$\begin{aligned}\varepsilon^{\text{quad}} &= \varepsilon^{\text{equad}} + \varepsilon^{\text{pquad}} = \sqrt{\frac{G_c}{3El_f} - \frac{2\Psi_{\text{cr}}^e}{3E}} + \frac{(E\varepsilon^{\text{quad}} - y_0)}{E + h} \\ \Rightarrow \varepsilon^{\text{quad}} &= \frac{E + h}{h} \left(\sqrt{\frac{G_c}{3El_f} - \frac{2\Psi_{\text{cr}}^e}{3E}} - \frac{y_0}{E + h} \right).\end{aligned}\quad (2.32)$$

Substituting the values for the linear hardening case in Table 2.1 into the last equation above, we have

$$\varepsilon^{\text{quad}} = \frac{E + h}{h} \left(\sqrt{\frac{G_c}{3El_f} - \frac{2\Psi_{\text{cr}}^e}{3E}} - \frac{y_0}{E + h} \right) \approx 4.7732.$$

This means that about 477% strain is required to reach peak stress with $(1 - d_{\text{cr}})^2 = 9/16$. From a common-sense standpoint, such an extremely large deformation with only 25% damage ($d_{\text{cr}} = 0.25$) is impossible, especially for metallic materials. While the amount of deformation at peak stress in the linear hardening case becomes smaller when the value of fracture toughness, G_c , is lower, this is unlikely in actual situations. More emphasis should be placed on the fact that damage evolution cannot be realized regardless of the material parameters used in the perfectly plastic case because the rate of change of elastic strain energy $\dot{\Psi}_0^e$ is zero during plastic deformation. In a similar model proposed by Duda et al. ¹⁴⁴⁾, an elastoplastic constitutive law was employed, but the damage computation only relied on the elastic response. From the above discussion, it is clear that an appropriate theory to describe the ductile fracture of elastoplastic materials by CPF modeling is needed.

2.4.3 Plastic driving force for damage computation

The first component is the plastic driving force introduced for damage computation. The original idea was proposed by Alessi et al. ^{75),76),88)} who introduced a plasticity-dependent damage dissipation potential for perfectly plasticity and Miehe et al. ^{79),80)} who assumed a pseudo plastic strain energy density. As is well known, the amount of plastic work due to hardening is larger than that of elastic strain energy under the plastic state. Hence, it is reasonably assumed that the increase in plastic work promotes damage evolution, and

the numerical simulation results are therefore expected to be consistent with actual failure phenomena to some extent. Some other models adopting the plastic driving force were proposed around the same time as the above groups. Among them, Kuhn et al.⁸⁷⁾ proposed a model in the small strain framework, and Borden et al.⁸³⁾ introduced two coefficients $\beta_e \in [0, 1]$ and $\beta_p \in [0, 1]$ to control the portion of thermodynamic force associated with damage evolution (damage driving force). Also, several models with a similar setup for the damage driving force were reported. Choo and Sun et al.¹⁴⁵⁾ developed a model for geological materials, and Rodriguez et al.¹⁴⁶⁾ proposed a model describing coupling with non-local plasticity. Huang and Gao et al.¹⁴⁷⁾ presented another model by introducing a plastic adjustment function for the damage driving force, and Fang et al.¹⁴⁸⁾ proposed a model to incorporate multi-surface plasticity.

Now, let us compare the models with and without a plastic driving force, as discussed in the previous subsection. Similarly to the setup in Section 2.4.1, we define the constitutive work density functional for the current case as

$$\Psi = \Psi^e + \Psi^p + \underbrace{\Psi^f}_{\text{Eq. (2.24)}} \quad (2.33)$$

with $\Psi^e = g(d) \underbrace{\frac{1}{2} E \varepsilon^2}_{\Psi_0^e}$ and $\Psi^p = g(d) \underbrace{\left(y_0 \alpha + \frac{1}{2} h \alpha^2 \right)}_{\Psi_0^p}$.

Then, the application of a variational statement to Eq. (2.33) provides the damage variable as

$$d = \frac{2l_f (\Psi_0^e + \Psi_0^p)}{G_c + 2l_f (\Psi_0^e + \Psi_0^p)}. \quad (2.34)$$

Similar to Eq. (2.31), we introduce another threshold Ψ_{cr}^p to activate the plastic driving force, so that Eq. (2.34) is modified as follows:

$$d = \frac{2l_f \left\{ \langle \Psi_0^e - \Psi_{cr}^e \rangle + \langle \Psi_0^p - \Psi_{cr}^p \rangle \right\}}{G_c + 2l_f \left\{ \langle \Psi_0^e - \Psi_{cr}^e \rangle + \langle \Psi_0^p - \Psi_{cr}^p \rangle \right\}}. \quad (2.35)$$

Here, along with the values of parameters provided in Table 2.1, $\Psi_{cr}^e = 2.5$ and $\Psi_{cr}^p = 500$ are given to avoid softening behavior in elastic and early plastic states.

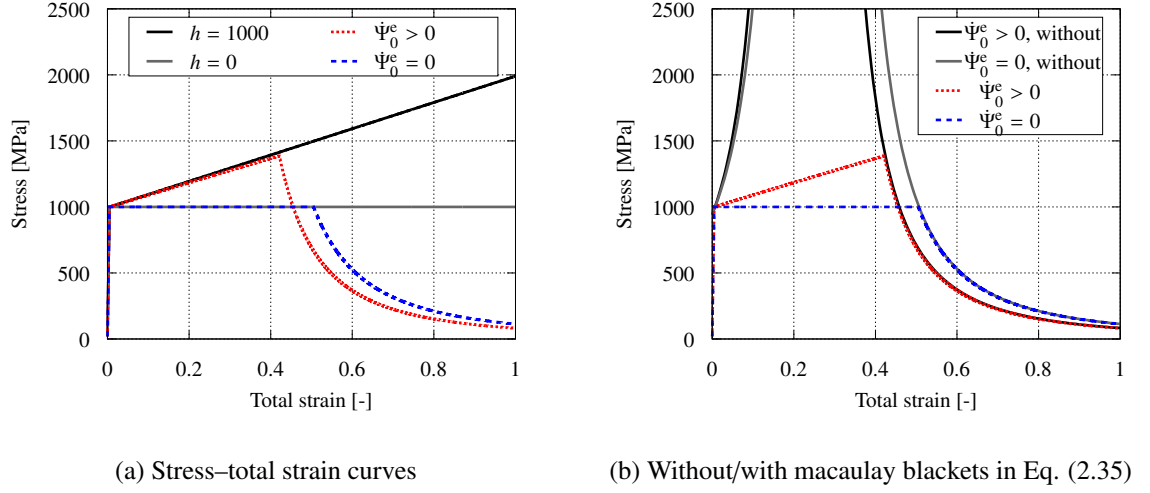


Fig. 2.3: Stress-total strain curves with plastic driving force.

Fig. 2.3 shows the stress-total strain curves for this setup. Here, the black and gray solid lines are the same as those in Fig. 2.2, which are the elastoplastic responses without damage computation for the linear hardening ($h = 1000$) and perfectly plastic ($h = 0$) cases, respectively. Also, the red and blue dashed lines show the corresponding responses when the plastic driving force is used. As can be seen from Fig. 2.3(a), damage evolutions are observed in both the linear hardening and perfectly plastic cases. It should be noted that stress is a monotonically decreasing function of plastic deformation, and its maximum appears as soon as the plastic driving force is activated. This fact can be better understood by neglecting Macaulay brackets in Eq. (2.35). That is, Fig. 2.3(b) shows the stress responses of the cases “ $\dot{\Psi}_0^e > 0$, without” and “ $\dot{\Psi}_0^e = 0$, without”, both of which represent the pure mathematical results without Macaulay brackets in Eq. (2.35), whereas the other two curves are the same as those in Fig. 2.3(a).

2.4.4 Degrading fracture toughness for damage computation

As an alternative concept for the CPF modeling for ductile fracture, degrading fracture toughness was introduced by several researchers to represent the deterioration of material due to plastic deformation; see, e.g., Dittmann et al. ⁸⁴⁾, Yin & Kaliske ⁸⁵⁾, Zhao et al. ¹⁴⁹⁾,

Hu et al.¹⁵⁰⁾, and Han et al.⁹¹⁾. Although the function forms of degrading fracture toughness in these studies differ from each other, the underlying concept is the same in that the amount of fracture toughness decreases with the accumulation of plastic deformation. Endowed with this property, the models enable us to realize crack initiation, propagation, and bifurcation in a region where plastic strain is severely accumulated.

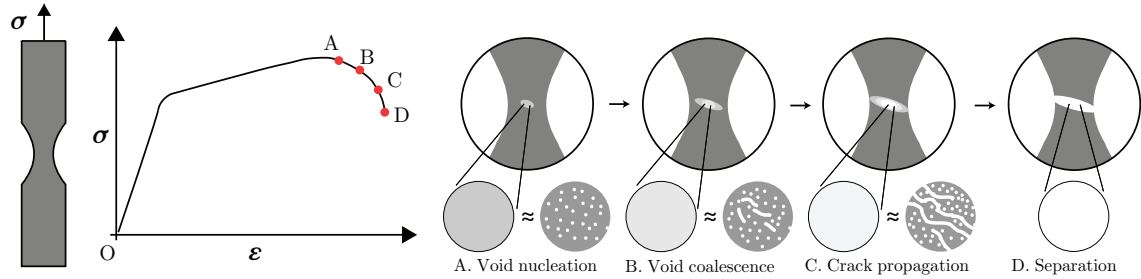


Fig. 2.4: Micro-mechanisms of ductile fracture and its numerical approximation.

It should be noted that introducing degrading fracture toughness in the CPF modeling is a phenomenological approach. As discussed in Han et al.⁹¹⁾, within the process zone, which is formed around the fracture surface due to plastic deformation, the apparent or macroscopic material properties gradually decrease due to void nucleation and evolution. The situation is schematically shown in Fig. 2.4. As can be seen from this figure, within the region of localized plastic deformation, the evolution of small defects causes a reduction in the effective surface at the micro-scale, which results in the corresponding reduction of macroscopic load-bearing capacity. This kind of phenomenon is commonly represented by the reduction of material properties according to the effective stress concept in conventional continuum damage mechanics (CDM)¹⁷⁾. A similar phenomenological description for degrading fracture toughness has been recently reported in Hu et al.¹⁵⁰⁾. It is, therefore, reasonable to assume that the fracture toughness also gradually decreases with the increase in accumulated plastic strain. However, it is well known that ductile failure involves the degradation of material stiffness not only as a result of plastic deformation but also owing to the negative hydrostatic pressure (mean stress) in the transitional process, whose fracture trend was indeed confirmed in recent experiments¹⁵¹⁾. Based on these observations and considerations,

our recent work ¹⁵²⁾ is the first to propose a degrading fracture toughness reflecting both the effects of the plastic deformation and the negative hydrostatic pressure.

To illustrate the effect of degrading fracture toughness, let us take the same setup as before. Assuming a linearly decreasing function such that $G_c = \langle G_{c0} - h_G \varepsilon^p \rangle$, the constitutive work density functional and damage variable can be expressed, respectively, as

$$\Psi = \Psi^e + \Psi^p + \Psi^f$$

$$\text{with } \Psi^e = g(d) \underbrace{\frac{1}{2} E \varepsilon^2}_{\Psi_0^e}, \quad \Psi^p = \underbrace{y_0 \alpha + \frac{1}{2} h \alpha^2}_{\Psi_0^p}, \quad \Psi^f = \int_0^t \langle G_{c0} - h_G \varepsilon^p \rangle \frac{d\dot{d} + l_f^2 \nabla d \cdot \nabla \dot{d}}{l_f} dt$$
(2.36)

and

$$d = \frac{2l_f \langle \Psi_0^e - \Psi_{cr}^e \rangle}{\left\langle G_{c0} - h_G \frac{\langle E \varepsilon - y_0 \rangle}{E + h} \right\rangle + 2l_f \langle \Psi_0^e - \Psi_{cr}^e \rangle},$$
(2.37)

where G_{c0} and h_G denote the initial fracture toughness and the linear degrading parameter, respectively. Note that the damage part Ψ^f has been modified in Eq. (2.36), reflecting a history-dependent property of the dissipated energy due to damage. This modification was utilized by Alessi et al. ⁵⁶⁾ and Carrara et al. ⁵⁸⁾ to describe fatigue problems, while not considered in Dittmann et al. ⁹⁰⁾ and Yin & Kaliske ⁸⁵⁾.

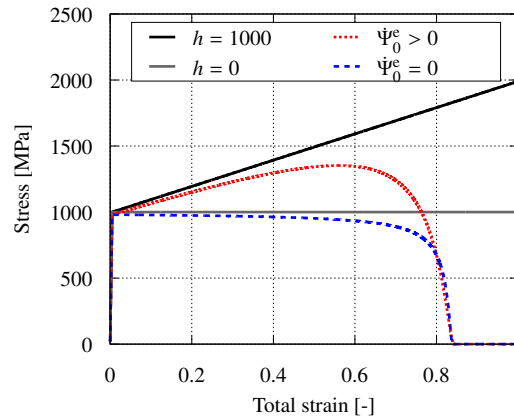


Fig. 2.5: Stress–total strain curves with degrading fracture toughness.

The red-colored and blue-colored curves in Fig. 2.5 correspond to the above setup, while the black and gray solid curves are the same as those in Fig. 2.2. Here, $G_{c0} = 500$, $h_G = 600$ and $\Psi_{cr}^e = 0$ have been used. As can be seen from this figure, damage evolutions are observed for both the linear hardening and perfectly plastic cases, $\dot{\Psi}_0^e > 0$ and $\dot{\Psi}_0^e = 0$. However, the decreasing trends of stress are quite different from the cases with a plastic driving force shown in Fig. 2.3. To be specific, while the stress does not reach the maximum for the perfect plastic case, there is a peak stress for the linear hardening case.

2.4.5 Yield function for CPFEM with plastic damage driving force

The third component in CPF modeling for ductile fracture is yield function. Although some early CPF ductile models have been investigated in a review by Alessi et al.⁹²⁾ in terms of their ability to represent homogeneous and non-homogeneous deformations, there is no elaborate study for the effect of defining yield criteria on the performance of the corresponding models. In what follows, we borrow the manner of verification presented by Grassl & Jirásek¹⁵³⁾ and investigate the responses obtained by different setups for yield function.

Generally, the form of a yield function coincides with the energetic ingredients in CPF modeling. For instance, when both the elastic and plastic damage driving forces are considered, the yield function is often defined by the nominal stress and nominal hardening force; see References^{80),83),91)}. An equivalent setup to these studies in a one-dimensional system is assumed as

$$\text{Setup A: } \left\{ \begin{array}{l} \phi^{Ap} = (1 - d)^2 \{E(\varepsilon - \varepsilon^p) - (y_0 + h\varepsilon^p)\} \\ \quad \text{with } \phi^{Ap} \leq 0, \quad \dot{\varepsilon}^p \geq 0 \quad \text{and} \quad \phi^{Ap}\dot{\varepsilon}^p = 0 \\ \phi^{Af} = 2(1 - d) \left(\left\langle \frac{1}{2}E(\varepsilon - \varepsilon^p)^2 - \Psi_{cr}^e \right\rangle + \left\langle y_0\varepsilon^p + \frac{1}{2}h\varepsilon^{p2} - \Psi_{cr}^p \right\rangle \right) - \frac{G_c}{l_f}d \\ \quad \text{with } \phi^{Af} \leq 0, \quad \dot{d} \geq 0 \quad \text{and} \quad \phi^{Af}\dot{d} = 0. \end{array} \right. \quad (2.38)$$

Here, ϕ^{Ap} is the yield function for plasticity, and linear hardening is employed for the sake of simplicity. Meanwhile, ϕ^{Af} is the yield function for damage, for which neither the plastic

driving force nor the degrading fracture toughness is introduced here ($\Psi_{\text{cr}}^p = +\infty$ and $G_c = \text{const.}$) to see the distinctive difference between the material responses realized by Setups A and B, the latter of which will be discussed in the next subsection. Note that \bullet indicates the material time derivative of \bullet . Then, the analytical solution for the damage variable is again expressed by Eq. (2.31).

Meanwhile, we make further reference to the loading/unloading conditions. If the yield function is negative at the current state, the deformation state is elastic, implying $\dot{\varepsilon}^p = 0$. On the other hand, if the yield function is zero, $\dot{\varepsilon}^p$ either becomes positive or remains zero for the plastic or elastic unloading states. Thus, if the current deformation state is plastic, the next state remains plastic or becomes elastic unloading. Exactly the same argument can be made for damage. Therefore, for Setup A defined by Eq. (2.38), the following conditions must be satisfied for the time rate of change of accumulated plastic strain (hardening variable) and the damage variable as well as those of the yield and threshold functions:

$$\begin{cases} \dot{\phi}^{\text{Ap}} \leq 0, & \dot{\varepsilon}^p \geq 0 \quad \text{and} \quad \dot{\phi}^{\text{Ap}} \dot{\varepsilon}^p = 0, \\ \dot{\phi}^{\text{Af}} \leq 0, & \dot{d} \geq 0 \quad \text{and} \quad \dot{\phi}^{\text{Af}} \dot{d} = 0. \end{cases} \quad (2.39)$$

Here, the material time derivatives of $\dot{\phi}^{\text{Ap}}$ and $\dot{\phi}^{\text{Af}}$ can be expressed in matrix notation as

$$\underbrace{\begin{pmatrix} \dot{\phi}^{\text{Ap}} \\ \dot{\phi}^{\text{Af}} \end{pmatrix}}_{\delta\phi^{\text{A}}} = \begin{pmatrix} \frac{\partial\phi^{\text{Ap}}}{\partial\varepsilon}\dot{\varepsilon} + \frac{\partial\phi^{\text{Ap}}}{\partial\varepsilon^p}\dot{\varepsilon}^p + \frac{\partial\phi^{\text{Ap}}}{\partial d}\dot{d} \\ \frac{\partial\phi^{\text{Af}}}{\partial\varepsilon}\dot{\varepsilon} + \frac{\partial\phi^{\text{Af}}}{\partial\varepsilon^p}\dot{\varepsilon}^p + \frac{\partial\phi^{\text{Af}}}{\partial d}\dot{d} \end{pmatrix} = \underbrace{\begin{pmatrix} \frac{\partial\phi^{\text{Ap}}}{\partial\varepsilon}\dot{\varepsilon} \\ \frac{\partial\phi^{\text{Af}}}{\partial\varepsilon}\dot{\varepsilon} \end{pmatrix}}_{\delta\varepsilon^{\text{A}}} - \underbrace{\begin{pmatrix} -\frac{\partial\phi^{\text{Ap}}}{\partial\varepsilon^p} & -\frac{\partial\phi^{\text{Ap}}}{\partial d} \\ -\frac{\partial\phi^{\text{Af}}}{\partial\varepsilon^p} & -\frac{\partial\phi^{\text{Af}}}{\partial d} \end{pmatrix}}_{\mathcal{K}^{\text{A}}} \cdot \underbrace{\begin{pmatrix} \dot{\varepsilon}^p \\ \dot{d} \end{pmatrix}}_{\delta\gamma^{\text{A}}}, \quad (2.40)$$

where

$$\begin{aligned} -\frac{\partial\phi^{\text{Ap}}}{\partial\varepsilon^p} &= (1-d)^2 (E+h), \quad -\frac{\partial\phi^{\text{Ap}}}{\partial d} = 2(1-d) \underbrace{\{E(\varepsilon - \varepsilon^p) - (y_0 + h\varepsilon^p)\}}_{=0 \text{ Eq. (2.38)}} \\ -\frac{\partial\phi^{\text{Af}}}{\partial\varepsilon^p} &= 2(1-d)E(\varepsilon - \varepsilon^p) \quad \text{and} \quad -\frac{\partial\phi^{\text{Af}}}{\partial d} = 2\left(\frac{1}{2}E(\varepsilon - \varepsilon^p)^2 - \Psi_{\text{cr}}^e\right) + \frac{G_c}{l_f}, \end{aligned} \quad (2.41)$$

in which we have assumed $\langle \bullet \rangle > 0$ in Eq. (2.38) because only the elastic driving force invokes damage evolution in this setup. Using the expressions in Eq. (2.40), we rewrite Eq.

(2.39) in direct notation as

$$\delta \varepsilon^A - \mathcal{K}^A \cdot \delta \gamma^A \leq 0, \quad \delta \gamma^A \geq 0 \quad \text{and} \quad \delta \gamma^{AT} \cdot (\delta \varepsilon^A - \mathcal{K}^A \cdot \delta \gamma^A) = 0. \quad (2.42)$$

This is the so-called linear complementarity problem as elaborated in References ^{154),155)}, for which the following conditions must be satisfied:

$$\mathcal{K}_{11}^A > 0, \quad \mathcal{K}_{22}^A > 0 \quad \text{and} \quad \mathcal{K}_{11}^A \mathcal{K}_{22}^A - \mathcal{K}_{12}^A \mathcal{K}_{21}^A > 0, \quad (2.43)$$

whose mathematical justification is discussed in Reference ¹⁵⁶⁾. Substituting Eq. (2.41) into Eq. (2.43), we find that Setup A with $0 \leq d < 1$ always fulfills the following conditions unless the unrealistic case $h \leq -E$ holds:

$$\begin{aligned} \mathcal{K}_{11}^A &= (1-d)^2 (E+h) > 0, \quad \mathcal{K}_{22}^A = 2 \left(\frac{1}{2} E (\varepsilon - \varepsilon^p)^2 - \Psi_{cr}^e \right) + \frac{G_c}{l_f} > 0, \\ \text{and} \quad \mathcal{K}_{11}^A \mathcal{K}_{22}^A - \mathcal{K}_{12}^A \mathcal{K}_{21}^A &> 0. \end{aligned} \quad (2.44)$$

Therefore, it is found that $\mathcal{K}_{12} = 0$ in Eq. (2.41) implies that the evolution of plastic strain is independent of the evolution of damage.

2.4.6 Yield function for CPFEM without plastic damage driving force

On the other hand, some studies ^{78),84),85),150),152)} have defined the yield function using nominal stress and effective hardening force because the plastic damage driving force is not considered. A one-dimensional setup equivalent to these studies is as follows:

$$\text{Setup B: } \left\{ \begin{array}{l} \phi^{Bp} = (1-d)^2 E (\varepsilon - \varepsilon^p) - (y_0 + h \varepsilon^p) \\ \quad \text{with } \phi^{Bp} \leq 0, \quad \dot{\varepsilon}^p \geq 0 \quad \text{and} \quad \phi^{Bp} \dot{\varepsilon}^p = 0 \\ \phi^{Bf} = 2(1-d) \left\langle \frac{1}{2} E (\varepsilon - \varepsilon^p)^2 - \Psi_{cr}^e \right\rangle - \frac{G_c}{l_f} d \\ \quad \text{with } \phi^{Bf} \leq 0, \quad \dot{d} \geq 0 \quad \text{and} \quad \phi^{Bf} \dot{d} = 0 \end{array} \right., \quad (2.45)$$

where ϕ^{Bp} and ϕ^{Bf} are the yield functions for plasticity and damage, respectively. As discussed in the previous subsection, the following conditions must be satisfied:

$$\left\{ \begin{array}{l} \dot{\phi}^{Bp} \leq 0, \quad \dot{\varepsilon}^p \geq 0 \quad \text{and} \quad \dot{\phi}^{Bp} \dot{\varepsilon}^p = 0 \\ \dot{\phi}^{Bf} \leq 0, \quad \dot{d} \geq 0 \quad \text{and} \quad \dot{\phi}^{Bf} \dot{d} = 0 \end{array} \right. . \quad (2.46)$$

Here, the material time derivatives, $\dot{\phi}^{\text{Bp}}$ and $\dot{\phi}^{\text{Bf}}$, can be written in matrix notation as

$$\underbrace{\begin{pmatrix} \dot{\phi}^{\text{Bp}} \\ \dot{\phi}^{\text{Bf}} \end{pmatrix}}_{\delta\phi^{\text{B}}} = \begin{pmatrix} \frac{\partial\phi^{\text{Bp}}}{\partial\varepsilon}\dot{\varepsilon} + \frac{\partial\phi^{\text{Bp}}}{\partial\varepsilon^{\text{p}}}\dot{\varepsilon}^{\text{p}} + \frac{\partial\phi^{\text{Bp}}}{\partial d}\dot{d} \\ \frac{\partial\phi^{\text{Bf}}}{\partial\varepsilon}\dot{\varepsilon} + \frac{\partial\phi^{\text{Bf}}}{\partial\varepsilon^{\text{p}}}\dot{\varepsilon}^{\text{p}} + \frac{\partial\phi^{\text{Bf}}}{\partial d}\dot{d} \end{pmatrix} = \underbrace{\begin{pmatrix} \frac{\partial\phi^{\text{Bp}}}{\partial\varepsilon}\dot{\varepsilon} \\ \frac{\partial\phi^{\text{Bf}}}{\partial\varepsilon}\dot{\varepsilon} \end{pmatrix}}_{\delta\varepsilon^{\text{B}}} - \underbrace{\begin{pmatrix} -\frac{\partial\phi^{\text{Bp}}}{\partial\varepsilon^{\text{p}}} & -\frac{\partial\phi^{\text{Bp}}}{\partial d} \\ -\frac{\partial\phi^{\text{Bf}}}{\partial\varepsilon^{\text{p}}} & -\frac{\partial\phi^{\text{Bf}}}{\partial d} \end{pmatrix}}_{\mathcal{K}^{\text{B}}} \cdot \underbrace{\begin{pmatrix} \dot{\varepsilon}^{\text{p}} \\ \dot{d} \end{pmatrix}}_{\delta\gamma^{\text{B}}}, \quad (2.47)$$

where

$$\begin{aligned} -\frac{\partial\phi^{\text{Bp}}}{\partial\varepsilon^{\text{p}}} &= (1-d)^2 E + h, & -\frac{\partial\phi^{\text{Bp}}}{\partial d} &= -\frac{\partial\phi^{\text{Bf}}}{\partial\varepsilon^{\text{p}}} = 2(1-d)E(\varepsilon - \varepsilon^{\text{p}}), \\ \text{and} \quad -\frac{\partial\phi^{\text{Bf}}}{\partial d} &= 2\left(\frac{1}{2}E(\varepsilon - \varepsilon^{\text{p}})^2 - \Psi_{\text{cr}}^{\text{e}}\right) + \frac{G_{\text{c}}}{l_{\text{f}}}. \end{aligned} \quad (2.48)$$

Here, we have assumed $\langle \bullet \rangle > 0$ for convenience. Using the expressions in Eq. (2.47), we rewrite Eq. (2.46) as

$$\delta\varepsilon^{\text{B}} - \mathcal{K}^{\text{B}} \cdot \delta\gamma^{\text{B}} \leq 0, \quad \delta\gamma^{\text{B}} \geq 0 \quad \text{and} \quad \delta\gamma^{\text{B}\text{T}} \cdot (\delta\varepsilon^{\text{B}} - \mathcal{K}^{\text{B}} \cdot \delta\gamma^{\text{B}}) = 0. \quad (2.49)$$

To fulfill the requirements for this linear complementarity problem with non-negative components in $\delta\gamma^{\text{B}}$, the following conditions must be satisfied:

$$\mathcal{K}_{11}^{\text{B}} > 0, \quad \mathcal{K}_{22}^{\text{B}} > 0 \quad \text{and} \quad \mathcal{K}_{11}^{\text{B}}\mathcal{K}_{22}^{\text{B}} - \mathcal{K}_{12}^{\text{B}}\mathcal{K}_{21}^{\text{B}} > 0. \quad (2.50)$$

The first and second conditions can easily be confirmed to hold for the hardening case ($h \geq 0$):

$$\mathcal{K}_{11}^{\text{B}} = (1-d)^2 E + h > 0 \quad \text{and} \quad \mathcal{K}_{22}^{\text{B}} = 2\left(\frac{1}{2}E(\varepsilon - \varepsilon^{\text{p}})^2 - \Psi_{\text{cr}}^{\text{e}}\right) + \frac{G_{\text{c}}}{l_{\text{f}}} > 0. \quad (2.51)$$

On the other hand, the third condition is expanded as

$$\begin{aligned} &\mathcal{K}_{11}^{\text{B}}\mathcal{K}_{22}^{\text{B}} - \mathcal{K}_{12}^{\text{B}}\mathcal{K}_{21}^{\text{B}} \\ &= \left\{(1-d)^2 E + h\right\} \left\{2\left(\frac{1}{2}E(\varepsilon - \varepsilon^{\text{p}})^2 - \Psi_{\text{cr}}^{\text{e}}\right) + \frac{G_{\text{c}}}{l_{\text{f}}}\right\} - \{2(1-d)E(\varepsilon - \varepsilon^{\text{p}})\}^2 > 0. \end{aligned} \quad (2.52)$$

Subsequently, after some mathematical manipulation, the following inequality is obtained:

$$(1-d)^2 > \frac{h \left\{E\varepsilon^{\text{e}2} - \left(2\Psi_{\text{cr}}^{\text{e}} - \frac{G_{\text{c}}}{l_{\text{f}}}\right)\right\}}{E \left\{3E\varepsilon^{\text{e}2} + \left(2\Psi_{\text{cr}}^{\text{e}} - \frac{G_{\text{c}}}{l_{\text{f}}}\right)\right\}}. \quad (2.53)$$

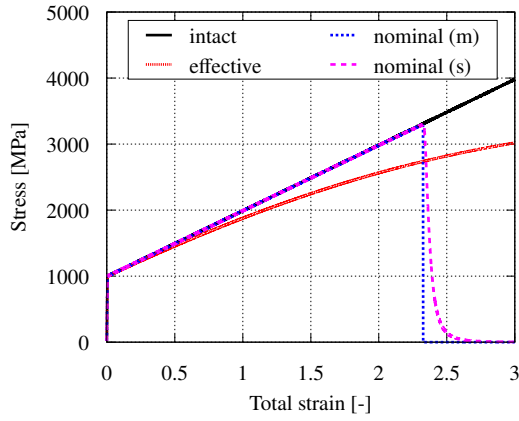
The left-hand side must be equal to or less than one for $d \in [0, 1]$, whereas the right-hand side becomes larger than one if the elastic strain satisfies the following condition:

$$\varepsilon^e > \underbrace{\sqrt{\frac{(E+h)}{E(h-3E)}} \left(2\Psi_{\text{cr}}^e - \frac{G_c}{l_f} \right)}_{\varepsilon_{\text{cr}}^e}. \quad (2.54)$$

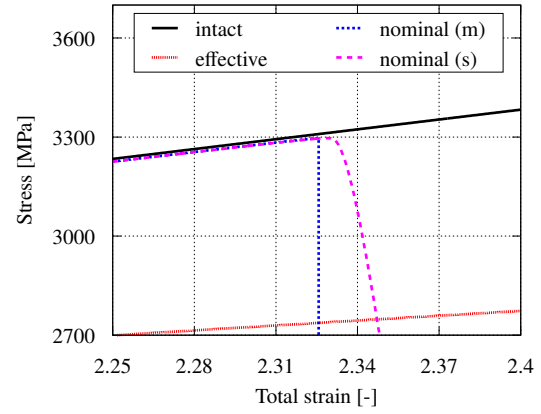
When this condition holds or, equivalently, when the elastic strain becomes larger than the critical value $\varepsilon_{\text{cr}}^e$, proper evolutions of the accumulated plastic strain and damage variable, $\delta\gamma^B \geq 0$, are not ensured. In addition, since the critical value is determined only by the material parameters, there is no way to avoid this issue.

Fig. 2.6 shows the variations of stress, elastic strain, plastic strain, and the crack phase-field variable with respect to the total strain for both Setups A and B, for which $\Psi_{\text{cr}}^e = 2.5$ is again given. Here, the black-colored solid line in each of the figures indicates the response of the “intact” state without damage evolutions, and the red dashed line indicated by “effective” represents the result of Setup A, in which the effective stress is employed in the yield function. Also, the blue and magenta dashed lines, indicated by “nominal (m)” and “nominal (s)”, correspond to the results of Setup B by using the monolithic and staggered algorithms, respectively, which adopt the nominal stress in the yield function. As can be seen from Fig. 2.6(a), the stress response of “effective” shows a gradual decrease but never declines drastically. In contrast, the stresses of “nominal (m)” and “nominal (s)” are almost the same as the “intact” state until reaching their peaks and exhibit different trends in the rapid drops immediately after the peaks. See also the enlarged view around the peak stresses in Fig. 2.6(b). As mentioned above, since the accumulation of plastic strain computed by the “effective” case equivalent to Setup A is independent of damage evolution, the evolution of elastic and plastic strains match those of the “intact” case; see Fig. 2.6(c)~(e), where the red dashed lines overlap with the black-colored solid lines, so the black-colored solid lines are barely visible.

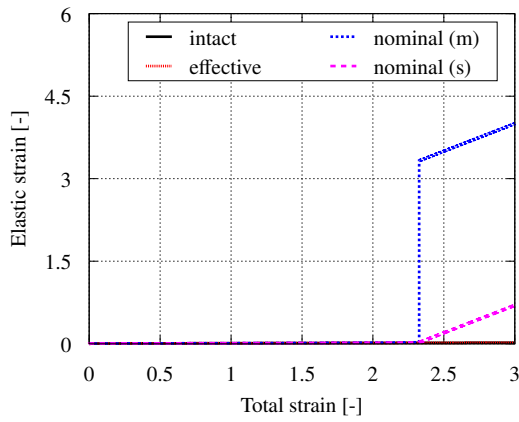
Meanwhile, in the “nominal (m)” case corresponding to Setup B, an abrupt increase in elastic strain and a sudden decrease of plastic strain are seen at $\varepsilon \approx 2.32$, which corresponds to the instance when the elastic strain reaches $\varepsilon_{\text{cr}}^e$. In fact, by using the parameters listed in



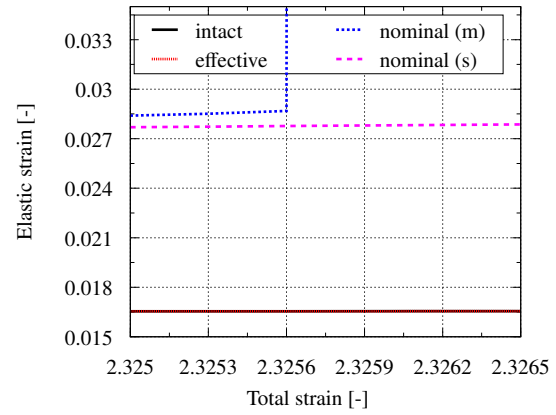
(a) Stress–total strain curves



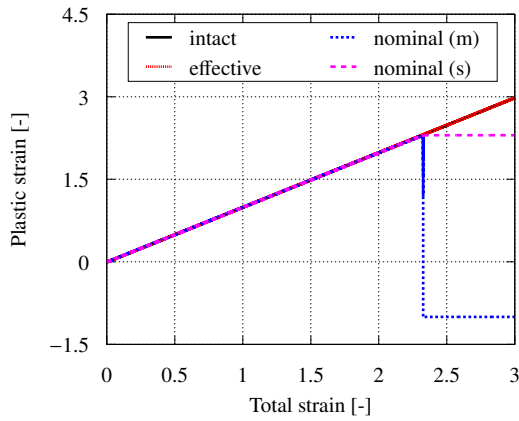
(b) Stress–total strain curves (enlarged view)



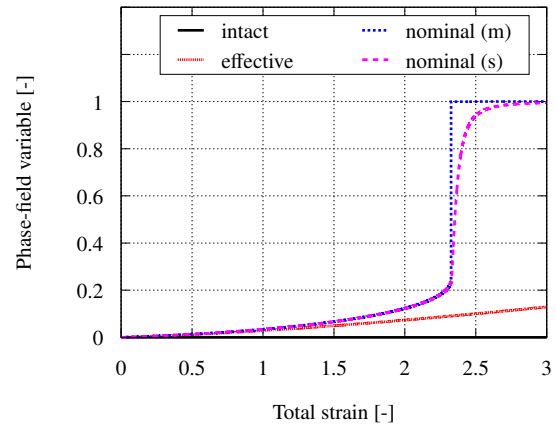
(c) Elastic strain–total strain curves



(d) Elastic strain–total strain curves (enlarged view)



(e) Plastic strain–total strain curves



(f) Phase-field variable–total strain curves

Fig. 2.6: Stress, elastic strain, plastic strain and crack phase-field variable–total strain curves with effective/nominal stress (“effective” and “nominal (m)” are equivalent to Setup A and Setup B).

Table 2.1 in Eq. (2.54), we can compute the critical value of elastic strain ε_{cr}^e as

$$\varepsilon_{cr}^e = \sqrt{\frac{(E + h)}{E(h - 3E)} \left(2\Psi_{cr}^e - \frac{G_c}{l_f} \right)} \approx 0.02882,$$

which is exactly the same amount of increase/decrease in elastic strain/plastic strain indicated by the blue dashed lines in Fig. 2.6(d) and (e). As a result, the damage variable instantly approaches to one due to the rapid increase in elastic strain energy, as shown in Fig. 2.6(f). Also, during this process, the plastic strain becomes negative, as can be seen from Fig. 2.6(e). The situations for Setups A and B can be adequately explained by depicting the plastic strain surfaces defined as functions of the total strain and crack phase-field variable, which are obtained, respectively, as

$$\varepsilon_{Setup A}^p = \frac{E\varepsilon - y_0}{E + h} \quad \text{and} \quad \varepsilon_{Setup B}^p = \frac{(1 - d)^2 E\varepsilon - y_0}{(1 - d)^2 E + h}. \quad (2.55)$$

Fig. 2.7 shows the corresponding surfaces. The plastic strain surface of Setup B exhibits

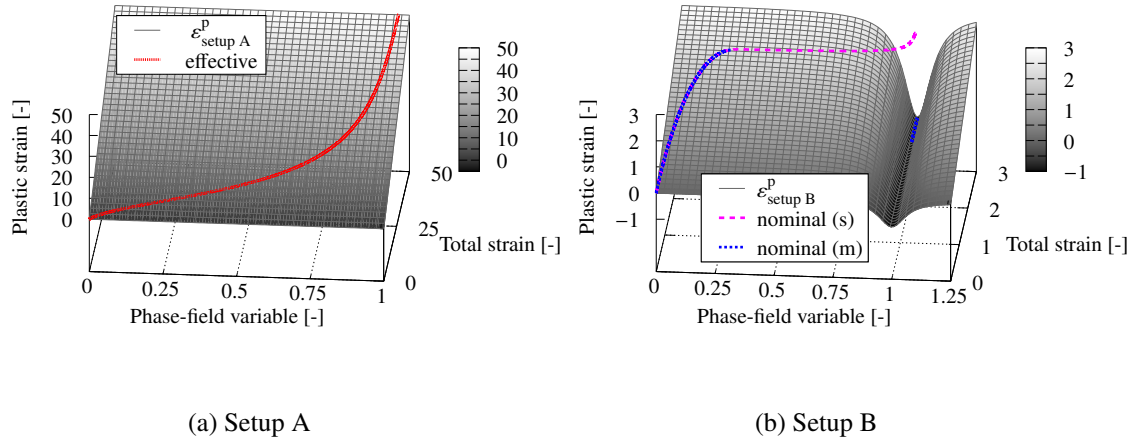


Fig. 2.7: Surfaces of plastic strain determined by crack phase-field variable and total strain.

a depression with minus values of plastic strain (Fig. 2.7(b)), whereas that of Setup A does not (Fig. 2.7(a)). Also, the three lines indicate the paths of the “effective”, “nominal (m)”, and “nominal (s)” cases. As can be seen from Fig. 2.7(a), the plastic strain is constant with respect to the crack phase-field variable, and the actual path indicated by the red line on

the surface monotonically increases. In contrast, as illustrated in Fig. 2.7(b), the plastic strain surface attains the minimum of $\varepsilon^p = -1$ at $d = 1$, and the blue line, representing the “nominal (m)” case, varies from the origin $(d, \varepsilon, \varepsilon^p) = (0, 0, 0)$ and moves in a single bound from a certain point to the minimum. Thus, it is concluded that the combined use of nominal quantities in the yield function and the monolithic algorithm (Setup B) leads to physically unacceptable updates of the state variables.

On the other hand, as can be seen from the magenta dashed line in Fig. 2.7(b), the staggered algorithm may be used to achieve physically acceptable constitutive updates. That is, at least, the values of plastic strain are kept positive. As suggested by Miehe et al.⁴⁰⁾ and Ambati et al.⁷⁷⁾, converged solutions can be obtained stably to some extent by the staggered algorithm even for unstable crack growths. We guess that this algorithm is also effective for stabilizing elastoplastic constitutive responses. In short, every time the mechanical field is solved, the deformation state must be determined by reference to the yield function. Since the equivalent stress is multiplied by the degradation function in the yield function, the deformation state inevitably becomes elastic when the damage variable d reaches a certain value. A comprehensive explanation of this situation can be found in ϕ^{Bp} of Eq. (2.45). Owing to this property, the magenta dashed line in Fig. 2.6(e), which represents the evolution of plastic strain for the “nominal (s)” case, does not exhibit negative values. Also, the damage variable gradually reaches one, as can be indicated by the blue dotted line in Fig. 2.6(f), while that of the “nominal (m)” case instantaneously becomes one. In addition, as can be seen from the magenta dashed line of Fig. 2.6(c) and (e), after the yield function returns to negative, the evolution of the plastic strain ceases, and any additional deformation is considered elastic deformation.

This transition in the deformation state from elastic to plastic and again to elastic states seems to be physically inappropriate, but it brings computational stability. That is, since the region with severe damage exhibits an elastic state, it is unnecessary to execute the return mapping calculations, which leads to computational instability caused by the excessive amount of softening of finite elements. However, it should be noted that the solution after the

cessation of plastic deformation is just “a solution of either the governing equations for displacement or damage variable” but does not necessarily satisfy both of them. In other words, the intermediate solution in the staggered algorithm does not represent an actual physical state. This can be visually understood from the magenta dashed line in Fig. 2.7(b), which deviates from the surface.

2.5 Proposed model

As suggested in the previous section, to describe ductile fracture by CPFM, the plasticity-induced damage driving force should be involved in the formulation. In this section, based on the study of characteristic features of existing CPFM for ductile fracture, we propose a new model¹⁵⁷⁾ endowed with elastic and plastic damage variables. Its constitutive work density consists of the elastic, plastic hardening, and damage hardening components. Evolution laws for plasticity and damage are derived by using separate threshold (yield) functions while having similar formats so that those for damage hold variational and thermodynamic consistencies. Also, the proposed model is equipped with thresholds and coefficients to control the amount of damage driving force.

2.5.1 Constitutive work density functional

In line with the previous studies^{142),91)}, we define the following constitutive work density functional to describe the energy state of the continuum body:

$$\Psi := \Psi^e(\mathbf{F}, \mathbf{F}^p, d^e) + \Psi^p(\bar{\alpha}, \alpha, \nabla \alpha, d^p) + \Psi^f(\mathbf{F}, \mathbf{F}^p, \alpha, d, \nabla d), \quad (2.56)$$

where Ψ^e , Ψ^p , and Ψ^f denote the elastic strain energy density, the plastic strain energy density (stored energy due to plastic hardening) and the energy density due to crack surface generation (stored energy due to damage hardening), respectively. Also, $d^e : \mathcal{B}_0 \times \mathcal{T} \rightarrow \mathbb{R}$ and $d^p : \mathcal{B}_0 \times \mathcal{T} \rightarrow \mathbb{R}$ are the elastic and plastic damage variables, whose evolution laws will be presented later. In the following, specific function forms of these energy density functionals are provided in order.

Similar to Eq. (2.12), we employ a Neo-Hookean hyperelastic constitutive law^{158),159)} with a volumetric-deviatoric split⁷²⁾ of the elastic strain energy density as

$$\Psi^e = \begin{cases} g(d^e) \underbrace{(\Psi_{0,\text{dev}}^e + \Psi_{0,\text{vol}}^e)}_{\Psi_0^{e+}} + \underbrace{0}_{\Psi_0^{e-}} & \text{for } J^e \geq 1 \\ g(d^e) \underbrace{\Psi_{0,\text{dev}}^e}_{\Psi_0^{e+}} + \underbrace{\Psi_{0,\text{vol}}^e}_{\Psi_0^{e-}} & \text{for } J^e < 1 \end{cases} \quad \text{with} \quad \begin{cases} \Psi_{0,\text{vol}}^e = \frac{\kappa}{2} \left(\frac{J^{e2} - 1}{2} - \ln J^e \right) \\ \Psi_{0,\text{dev}}^e = \frac{\mu}{2} (I_{\bar{\mathbf{b}}^e} - 3) \end{cases}, \quad (2.57)$$

where $I_{\bar{\mathbf{b}}^e}$ is the first invariant of the second-order tensor defined as $\bar{\mathbf{b}}^e = J^{e-2/3} \mathbf{b}^e$ with $\mathbf{b}^e = \mathbf{F}^e \cdot \mathbf{F}^{eT}$ being the elastic left Cauchy-Green tensor. Additionally, J^e denotes the Jacobian of the elastic deformation gradient \mathbf{F}^e . When the plastic incompressibility, namely $\det[\mathbf{F}^p] = 1$, is assumed, $J^e = J = \det[\mathbf{F}]$ is ensured. Moreover, $g(d^e)$ is an elastic degradation function to describe the degradation of material stiffness, for which the following two forms are employed:

$$\text{Quadratic form: } g(d^e) = (1 - d^e)^2 \quad (2.58)$$

$$\text{Cubic form: } g(d^e) = (s - 2)(1 - d^e)^3 + (3 - s)(1 - d^e)^2.$$

In a one-dimensional elastic case, the theoretical peak stress and strain for Eq. (2.58)₂ are given, respectively, as

$$\lim_{s \rightarrow 0} \sigma_{\text{cr}}^{\text{cubic}} = \frac{81}{50} \sqrt{\frac{2EG_c}{15l_f}} \quad \text{and} \quad \lim_{s \rightarrow 0} \varepsilon_{\text{cr}}^{\text{cubic}} = \sqrt{\frac{10G_c}{27El_f}}, \quad (2.59)$$

Using $\sigma_{\text{cr}}^{\text{cubic}} = g(d^e) E \varepsilon_{\text{cr}}^{\text{cubic}}$, we have $g(d^e) = 243/250$, which means only 2.8% of Young's modulus degrades before the stress attains its peak. Thus, one beauty of this function is that it provides an almost linear stress-strain response up to the peak stress.

Second, the plastic strain energy density (stored energy due to plastic hardening) is defined as

$$\Psi^p := g(d^p) \left\{ \int_0^{\bar{\alpha}} \hat{H}(\tilde{\alpha}) d\tilde{\alpha} + y_0 \frac{l_p^2}{2} \|\nabla \alpha\|^2 + \frac{p_p}{2} (\bar{\alpha} - \alpha)^2 \right\}, \quad (2.60)$$

where $\hat{H}(\bar{\alpha})$, y_0 , l_p and p_p are the plastic hardening function at material points, the initial yield stress, the plastic length scale parameter, and the penalty parameter to link $\bar{\alpha}$ to α in

the micromorphic regularization, respectively. Also, $g(d^p)$ is a plastic degradation function, which assumes the same function form as in Eq. (2.58). Here, the spatial gradient of the global hardening variable has been introduced to smooth the distribution of plastic hardening energy spatially. Without the spatial gradient term for damage computations, we may encounter strong nonuniform distribution of damage variables even in one element. This is an inappropriate situation because the fully damaged element still has resistance to loading. Note that if a large value of the penalty parameter p_p is taken, the connection between α and $\bar{\alpha}$ becomes stronger, but the convergence property of the Newton-Raphson procedure is reduced or lost. So, relatively small values of the penalty parameter will be used in our numerical examples, with priority given to ensuring convergence.

Lastly, we borrow the idea from References ^{56),58)} to define the energy density due to crack surface generation (stored energy due to damage hardening) as

$$\Psi^f := \int_0^t G_c(\alpha^*, \tau_p^*) \left(\frac{d\dot{d} + l_f^2 \nabla d \cdot \nabla \dot{d}}{l_f} \right) dt. \quad (2.61)$$

Here, G_c denotes the degrading fracture toughness and is defined in this study as

$$\frac{\partial G_c(\alpha^*, \tau_p^*)}{\partial \alpha^*} \leq 0, \quad \frac{\partial G_c(\alpha^*, \tau_p^*)}{\partial \tau_p^*} \leq 0 \quad \text{with} \quad \alpha^* = \langle \alpha - \alpha_{cr} \rangle, \quad \tau_p^* = \underbrace{\left\langle \frac{1}{3} \text{tr} [\boldsymbol{\tau}_0] \right\rangle}_{\tau_p} - \tau_{cr}, \quad (2.62)$$

in which the degradation effects are determined by both the plastic hardening variable α and the negative hydrostatic pressure τ_p . The concept of degrading fracture toughness stems from the macroscopic and phenomenological viewpoints for the failure of elastoplastic materials, as explained in References ^{91),152)}. Here, we have used two variables with different units (α^* & τ_p^*) to define the degrading fracture toughness by directly extending the previous studies ^{84),85),91)}. Nevertheless, another choice of arguments having the same unit can be taken for the degrading fracture toughness; for example, $G_c^*(\|\boldsymbol{\tau}_{0,dev}\|, \tau_p)$ or $G_c^*(\alpha, J^e)$ may be possible. Note that the degrading fracture toughness is introduced to describe monocyclic fracture in this study, though it can be extended to reproduce fatigue problems by introducing the kinematic hardening for plasticity and the cyclic history variable for degrading fracture toughness as proposed by Alessi et al. ⁵⁶⁾, Carrara et al. ⁵⁸⁾, and Ulloa et al. ⁶²⁾.

Remark 1 Since Eq. (2.61) is a time integral form, the constitutive work density functional Ψ is history-dependent with respect to α^* and τ_p^* . Then, Eq. (2.56) is no longer a state functional, and we thus proceed with our discussion by using the power density $\dot{\Psi}$ to circumvent this history-dependent problem in what follows. Note that Eq. (2.56) is a state functional only when the fracture toughness is assumed constant ($G_c = \text{const.}$) as to be done in general CPF brittle and ductile models.

Remark 2 One may argue that Eq. (2.56) is unacceptable in terms of the principle in physics because it is regarded as “free energy density” but involves plastic and damage dissipation terms Ψ^p and Ψ^f . However, such a manner of incorporating Ψ^p and Ψ^f into the free energy (or stored energy) density is widely accepted in the existing plasticity/damage modeling; see, for example, ^{(160), (158), (161), (17)}. Specifically, for the modeling in plasticity, the energy due to plastic hardening is commonly considered as a “pseudo” energetic component of free energy density. In this context, we are also able to assume the existence of pseudo energy due to damage hardening and consider it as a part of free energy. In short, the argument is whether or not possible to assume the dissipations relevant to plasticity and damage hardenings as energy components of the free energy (stored energy).

2.5.2 Thermodynamic consistency

Based on the first principle of thermodynamics, the energy conservation law is written as

$$\frac{dK}{dt} + \frac{dD}{dt} = \mathbf{f}_{\text{ext}} \cdot \dot{\mathbf{u}} - \mathbf{f}_{\text{int}} \cdot \dot{\mathbf{u}}, \quad (2.63)$$

where \mathbf{f}_{ext} and \mathbf{f}_{int} are the external and internal forces. Here, to confirm the thermodynamic consistency of the proposed model, we define the energy dissipation rate as

$$\mathbf{f}_{\text{ext}} \cdot \dot{\mathbf{u}} - \frac{d}{dt} (\Psi + K) = \mathbf{f}_{\text{int}} \cdot \dot{\mathbf{u}} - \dot{\Psi} \quad (2.64)$$

where

$$\begin{aligned} \mathbf{f}_{\text{int}} \cdot \dot{\mathbf{u}} &= \boldsymbol{\tau} : \mathbf{d}, \\ \dot{\Psi} &= \frac{\partial \Psi^e}{\partial \mathbf{b}^e} : \dot{\mathbf{b}}^e + \frac{\partial \Psi^e}{\partial d^e} \dot{d}^e + \frac{\partial \Psi^p}{\partial \bar{\alpha}} \dot{\bar{\alpha}} + \frac{\partial \Psi^p}{\partial \alpha} \dot{\alpha} + \frac{\partial \Psi^p}{\partial \nabla \alpha} \cdot \nabla \dot{\alpha} + \frac{\partial \Psi^p}{\partial d^p} \dot{d}^p + \frac{\partial \Psi^f}{\partial d} \dot{d} + \frac{\partial \Psi^f}{\partial \nabla d} \cdot \nabla \dot{d}. \end{aligned} \quad (2.65)$$

The rate of deformation tensor \mathbf{d} and the material time derivative of the elastic left Cauchy-Green tensor, $\dot{\mathbf{b}}^e$, are given, respectively, as

$$\mathbf{d} = \text{sym} [\mathbf{l}] = \frac{1}{2} (\mathbf{l} + \mathbf{l}^T) \quad \text{with} \quad \mathbf{l} = \dot{\mathbf{F}} \cdot \mathbf{F}^{-1} = \underbrace{\dot{\mathbf{F}}^e \cdot \mathbf{F}^{e-1}}_{\mathbf{l}^e} + \underbrace{\mathbf{F}^e \cdot \overbrace{\dot{\mathbf{F}}^p \cdot \mathbf{F}^{p-1}}^{L^p} \cdot \mathbf{F}^{e-1}}_{\mathbf{l}^p}, \quad (2.66)$$

and

$$\dot{\mathbf{b}}^e = \mathbf{l} \cdot \mathbf{b}^e + \mathbf{b}^e \cdot \mathbf{l}^T + \mathbf{F} \cdot \dot{\mathbf{C}}^{p-1} \cdot \mathbf{F}^T. \quad (2.67)$$

Thus, for a scalar quantity \bullet , the following relation holds:

$$\frac{\partial \bullet}{\partial \mathbf{b}^e} : \dot{\mathbf{b}}^e = \left(2 \frac{\partial \bullet}{\partial \mathbf{b}^e} \cdot \mathbf{b}^e \right) : (\mathbf{d} - \mathbf{d}^p), \quad (2.68)$$

where \mathbf{d}^p denotes the rate of plastic deformation tensor defined as

$$\mathbf{d}^p := \mathbf{F}^e \cdot \text{sym} [\mathbf{L}^p] \cdot \mathbf{F}^{e-1} = -\frac{1}{2} \mathbf{F} \cdot \dot{\mathbf{C}}^{p-1} \cdot \mathbf{C}^p \cdot \mathbf{F}^{-1}. \quad (2.69)$$

After some mathematical manipulation for Eq. (2.64), we obtain a more explicit form of the energy dissipation rate as

$$\boldsymbol{\tau} : \mathbf{d}^p - r^p \dot{\bar{\alpha}} + \tau^{fe} \dot{d}^e + \tau^{fp} \dot{d}^p - r^f \dot{d}, \quad (2.70)$$

where $\boldsymbol{\tau}$, r^p , τ^{fe} , τ^{fp} , and r^f are the driving force for plasticity conjugated to \mathbf{d}^p , plastic dissipative resistance force (plastic hardening force) associated with $\bar{\alpha}$, elastic damage driving force conjugated to d^e , plastic damage driving force conjugated to d^p , and damage dissipative resistance force (damage hardening force) associated with d , respectively. They are defined as

$$\boldsymbol{\tau} := 2 \frac{\partial \Psi^e}{\partial \mathbf{b}^e} \cdot \mathbf{b}^e = \begin{cases} g(d^e) \frac{\kappa}{2} (J^{e2} - 1) \mathbf{1} + g(d^e) \mu \text{dev} [\bar{\mathbf{b}}^e] & \text{for } J^e \geq 1 \\ \frac{\kappa}{2} (J^{e2} - 1) \mathbf{1} + g(d^e) \mu \text{dev} [\bar{\mathbf{b}}^e] & \text{for } J^e < 1 \end{cases}, \quad (2.71)$$

$$r^p := \frac{\partial \Psi^p}{\partial \bar{\alpha}} = g(d^p) \left\{ \hat{H}(\bar{\alpha}) + p_p(\bar{\alpha} - \alpha) \right\}, \quad (2.72)$$

$$\tau^{\text{fe}} := -\frac{\partial \Psi^{\text{e}}}{\partial d^{\text{e}}} = -\frac{\partial g(d^{\text{e}})}{\partial d^{\text{e}}} \Psi_0^{\text{e+}}, \quad (2.73)$$

$$\tau^{\text{fp}} := -\frac{\partial \Psi^{\text{p}}}{\partial d^{\text{p}}} = -\frac{\partial g(d^{\text{p}})}{\partial d^{\text{p}}} \Psi_0^{\text{p}}, \quad (2.74)$$

and

$$r^{\text{f}} := \frac{\partial \Psi^{\text{f}}}{\partial d} - \frac{d}{d\mathbf{X}} \cdot \frac{\partial \Psi^{\text{f}}}{\partial \nabla d} = G_{\text{c}}(\alpha^*, \tau_{\text{p}}^*) \left(\frac{d - l_{\text{f}}^2 \Delta d}{l_{\text{f}}} \right). \quad (2.75)$$

Note that during the derivation process from Eq. (2.64) to Eq. (2.70), we have assumed $\delta_{\alpha} \Psi = 0$ based on the micromorphic regularization. Thus, the terms involving α vanish. In addition, owing to the plastic incompressibility, i.e., $\det[\mathbf{F}^{\text{p}}] = 1$, assumed in this study, we have

$$\frac{d}{dt} \det[\mathbf{C}^{\text{p}}] = \frac{1}{2} \underbrace{\det[\mathbf{F}^{\text{p}}]}_{=1} \mathbf{C}^{\text{p-1}} : \left\{ \mathbf{F}^{\text{pT}} \cdot (\mathbf{L}^{\text{p}} + \mathbf{L}^{\text{pT}}) \cdot \mathbf{F}^{\text{p}} \right\} = 0 \Rightarrow \text{tr}[\text{sym}[\mathbf{L}^{\text{p}}]] = 0. \quad (2.76)$$

Considering this property, we can use the relation $\boldsymbol{\tau} : \mathbf{d}^{\text{p}} = \boldsymbol{\tau}_{\text{dev}} : \mathbf{d}^{\text{p}}$, and Eq. (2.70) eventually yields

$$\boldsymbol{\tau}_{\text{dev}} : \mathbf{d}^{\text{p}} - r^{\text{p}} \dot{\alpha} + \tau^{\text{fe}} \dot{d}^{\text{e}} + \tau^{\text{fp}} \dot{d}^{\text{p}} - r^{\text{f}} \dot{d}. \quad (2.77)$$

In order to prescribe the admissible stress field for plasticity, we define the threshold function (the yield function in J_2 plasticity) as

$$\Phi^{\text{p}}(\boldsymbol{\tau}_{\text{dev}}, r^{\text{p}}) := \frac{\|\boldsymbol{\tau}_{\text{dev}}\|}{g(d^{\text{e}})} - \sqrt{\frac{2}{3}} \frac{g(d^{\text{p}}) y_0 + r^{\text{p}}}{g(d^{\text{p}})} = \|\boldsymbol{\tau}_{0,\text{dev}}\| - \sqrt{\frac{2}{3}} (y_0 + r_0^{\text{p}}) \leq 0, \quad (2.78)$$

in which the effective stress $\boldsymbol{\tau}_0$ and effective hardening force r_0^{p} are used. Note that the set of $\boldsymbol{\tau}$ and r^{p} (or $\boldsymbol{\tau}_0$ and r_0^{p}) for the threshold function Eq. (2.78) is convex and define the admissible space such that $\mathbb{K}^{\text{p}} := \{\boldsymbol{\tau}_{\text{dev}}, r^{\text{p}} \mid \Phi^{\text{p}} \leq 0\}$. It should also be noted that Eq. (2.78) does not lead to the improper plasticity/damage responses as demonstrated in Section 2.4.5 and matches the concept of the effective area in CDM, as established by Kachanov¹⁶²⁾, Rabotnov¹⁶³⁾, and Murakami¹⁷⁾.

Similarly, to define the admissible stress field for damage, another threshold function is defined as

$$\begin{aligned} \Phi^f(\tau^{fe}, \tau^{fp}, r^f) &:= \tau^{fe*} + \tau^{fp*} - r^f \leq 0 \\ \text{with} \quad \tau^{fe*} &= -\frac{\partial g(d^e)}{\partial d^e} \langle \Psi_0^{e+} - \Psi_{cr}^e \rangle \zeta^e = \tau^{fe} \zeta^e \chi^e - \tau_{cr}^{fe} \zeta^e \chi^e, \\ \tau^{fp*} &= -\frac{\partial g(d^p)}{\partial d^p} \langle \Psi_0^p - \Psi_{cr}^p \rangle \zeta^p = \tau^{fp} \zeta^p \chi^p - \tau_{cr}^{fp} \zeta^p \chi^p, \end{aligned} \quad (2.79)$$

where τ^{fe*} and τ^{fp*} are the “modified” elastic and plastic damage driving forces. To activate these driving forces, two threshold parameters Ψ_{cr}^e and Ψ_{cr}^p have been introduced. Also, inspired by Borden¹⁶⁴⁾, two coefficients $\zeta^e \in [0, 1]$ and $\zeta^p \in [0, 1]$ have been introduced to control the contributions of elastic and plastic strain energies for damage evolution, respectively. From the phenomenological viewpoint for failure in elastoplastic materials, the two threshold parameters, Ψ_{cr}^e and Ψ_{cr}^p , realize the behavior such that “the deterioration of material initiates after experiencing a certain amount of elastic and/or plastic deformations”, while the two coefficients ζ^e and ζ^p realize the behavior such that “not all the portion of the thermodynamic forces τ^{fe} and τ^{fp} contribute to the damage evolution”. Similarly to plasticity, the set of τ^{fe} , τ^{fp} , and r^f (or τ^{fe*} , τ^{fp*} , and r^f) in the threshold function Eq. (2.79) is convex and define the admissible space such that $\mathbb{K}^f := \{\tau^{fe}, \tau^{fp}, r^f \mid \Phi^f \leq 0\}$. In addition, χ^e and χ^p are step functions defined as, respectively,

$$\chi^e = \begin{cases} 1 & \text{if } \Psi_0^{e+} - \Psi_{cr}^e > 0 \\ 0 & \text{otherwise} \end{cases} \quad \text{and} \quad \chi^p = \begin{cases} 1 & \text{if } \Psi_0^p - \Psi_{cr}^p > 0 \\ 0 & \text{otherwise} \end{cases}. \quad (2.80)$$

Now, for the given rates $\{\mathbf{d}^p, \dot{\alpha}, \dot{d}^e, \dot{d}^p, \dot{d}\}$, we postulate the dissipation potential Υ as

$$\Upsilon = \sup_{\{\tau_{dev}, r^p\} \in \mathbb{K}^p, \{\tau^{fe}, \tau^{fp}, r^f\} \in \mathbb{K}^f} \left[\tau_{dev} : \mathbf{d}^p - r^p \dot{\alpha} + \tau^{fe} \dot{d}^e + \tau^{fp} \dot{d}^p - r^f \dot{d} \right], \quad (2.81)$$

This optimization problem is a particular case of the principle of maximum dissipation and can be rewritten in an equivalent form:

$$\Upsilon = \sup_{\{\tau_{dev}, r^p, \tau^{fe}, \tau^{fp}, r^f\}} \sup_{\{\lambda^p, \lambda^f\}} \left[\tau_{dev} : \mathbf{d}^p - r^p \dot{\alpha} + \tau^{fe} \dot{d}^e + \tau^{fp} \dot{d}^p - r^f \dot{d} - \lambda^p \Phi^p - \lambda^f \Phi^f \right], \quad (2.82)$$

where $\lambda^p \geq 0$ and $\lambda^f \geq 0$ are Lagrange multipliers, i.e., the plastic multiplier in the theory of plasticity and the damage multiplier in the crack phase-field description. Then, we find the stationary conditions of the Lagrangian in Eq. (2.82) with respect to $\{\tau_{\text{dev}}, r^p, \tau^{\text{fe}}, \tau^{\text{fp}}, r^f\}$ and $\{\lambda^p, \lambda^f\}$ to derive the following five evolution laws accompanied by the corresponding loading/unloading conditions:

$$\left\{ \begin{array}{l} \mathbf{d}^p = \lambda^p \frac{\partial \Phi^p}{\partial \tau_{\text{dev}}} = \frac{\lambda^p}{g(d^e)} \frac{\tau_{0,\text{dev}}}{\|\tau_{0,\text{dev}}\|} \\ \dot{\alpha} = -\lambda^p \frac{\partial \Phi^p}{\partial r^p} = \sqrt{\frac{2}{3}} \frac{\lambda^p}{g(d^p)} \\ \dot{d}^e = \lambda^f \frac{\partial \Phi^f}{\partial \tau^{\text{fe}}} = \lambda^f \zeta^e \chi^e \\ \dot{d}^p = \lambda^f \frac{\partial \Phi^f}{\partial \tau^{\text{fp}}} = \lambda^f \zeta^p \chi^p \\ \dot{d} = -\lambda^f \frac{\partial \Phi^f}{\partial r^f} = \lambda^f \end{array} \right. \quad \text{with} \quad \left\{ \begin{array}{l} \lambda^p \geq 0, \quad \Phi^p \leq 0, \quad \text{and} \quad \lambda^p \Phi^p = 0 \\ \lambda^f \geq 0, \quad \Phi^f \leq 0, \quad \text{and} \quad \lambda^f \Phi^f = 0 \end{array} \right. \quad (2.83)$$

Since $\|\mathbf{d}^p\| = \lambda^p / g(d^e)$ and $\dot{d} = \lambda^f$, the second, third and fourth evolution laws in Eq. (2.83) yield, respectively,

$$\dot{\alpha} = \frac{g(d^e)}{g(d^p)} \sqrt{\frac{2}{3}} \|\mathbf{d}^p\|, \quad \dot{d}^e = \zeta^e \chi^e \dot{d}, \quad \dot{d}^p = \zeta^p \chi^p \dot{d}. \quad (2.84)$$

Following these relations, $\bar{\alpha}$ & b^e (or \mathbf{d}^p) are updated according to Algorithm 1 in Section 2.6.1, and d^e & d^p are updated by Eq. (2.122) in Section 2.6.2, respectively.

The thermodynamic consistency can be confirmed for all variations $\{\mathbf{d}^p, \dot{\alpha}, \dot{d}^e, \dot{d}^p, \dot{d}\}$ as follows:

$$\begin{aligned} \Upsilon &= \sup_{\{\tau_{\text{dev}}, r^p\} \in \mathbb{K}^p, \{\tau^{\text{fe}}, \tau^{\text{fp}}, r^f\} \in \mathbb{K}^f} \left[\tau_{\text{dev}} : \mathbf{d}^p - r^p \dot{\alpha} + \tau^{\text{fe}} \dot{d}^e + \tau^{\text{fp}} \dot{d}^p - r^f \dot{d} \right] \\ &= \sup_{\tau_{\text{dev}}, r^p, \tau^{\text{fe}}, \tau^{\text{fp}}, r^f} \left[\sqrt{\frac{2}{3}} g(d^e) y_0 \|\mathbf{d}^p\| + r^p \left(\frac{g(d^e)}{g(d^p)} \sqrt{\frac{2}{3}} \|\mathbf{d}^p\| - \dot{\alpha} \right) \right. \\ &\quad \left. - \frac{\partial g(d^e)}{\partial d^e} \Psi_{\text{cr}}^e \dot{d}^e - \frac{\partial g(d^p)}{\partial d^p} \Psi_{\text{cr}}^p \dot{d}^p + \frac{r^{\text{fe}}}{\zeta^e} (\dot{d}^e - \zeta^e \dot{d}) + \frac{r^{\text{fp}}}{\zeta^p} (\dot{d}^p - \zeta^p \dot{d}) \right], \end{aligned} \quad (2.85)$$

in which we have reflected the assumptions such that $\chi^e = \chi^p = 1$, $r^f = r^{\text{fe}} + r^{\text{fp}}$, $\tau^{\text{fe}*} \leq r^{\text{fe}}$, and $\tau^{\text{fp}*} \leq r^{\text{fp}}$ for convenience. For the hardening materials ($r^p \geq 0$), the dissipation potential

Eq. (2.85) eventually takes the closed form as follows:

$$\Upsilon = \begin{cases} \sqrt{\frac{2}{3}} g(d^e) y_0 \|d^p\| - \frac{\partial g(d^e)}{\partial d^e} \Psi_{cr}^e \dot{d}^e - \frac{\partial g(d^p)}{\partial d^p} \Psi_{cr}^p \dot{d}^p \\ \quad \text{if } \dot{\alpha} \geq \frac{g(d^e)}{g(d^p)} \sqrt{\frac{2}{3}} \|d^p\|, \quad d^e \leq \zeta^e d, \quad \text{and} \quad \dot{d}^p \leq \zeta^p \dot{d} \\ +\infty \quad \text{otherwise} \end{cases} \quad (2.86)$$

To the best of our knowledge, the present study is the first among the models equipped with the thresholds and coefficients used to control the damage driving forces to derive the variationally consistent evolution laws for damage variables (the third, fourth, and fifth equations in Eq. (2.83)) in CPF modeling. As mentioned in Section 2.4.3, while thresholds and coefficients to delay the activation or control the contribution of plastic driving forces have been introduced in earlier studies^{83),147),91)}, the variational structure of the evolution of the damage variable appears to have been overlooked. As a result, the damage variables, d^e , d^p , and d , have not been differentiated. For brittle fracture, d^p does not exist, and d^e is naturally equal to d . On the other hand, when the ductile fracture accompanied by plastic deformation is considered, the term τ^{fp*} in Eq. (2.79) has no effect until it is activated, and $\dot{d}^p = 0$ while $\dot{d}^e > 0$ with $\tau^{fe*} > 0$. Therefore, since the evolution tendencies in d^e and d^p are different, the evolution laws for plasticity (the first and second equations in Eq. (2.83)) are separately affected by $g(d^e)$ and $g(d^p)$. Further explanation about the motivation to introduce two damage variables is given in Appendix A.1.

Remark 3 As suggested by Miehe et al.⁸⁰⁾, as long as the same degradation function $g(d)$ acts on both the stress and hardening components, the evolution of plastic deformation is independent of that of damage. That is because of the relation $\phi^p = g(d) \phi_0^p$, and it is indeed demonstrated in Section 2.4.3. However, once the different forms of degradation function or evolution tendencies of damage variables are assumed, as discussed in this thesis, we may encounter improper plasticity/damage responses as shown in Section 2.4.6. For instance, if we assume the yield function as $\phi^p = g(d^e) \|\tau_{0,dev}\| - g(d^p) \left(\sqrt{2/3} (y_0 + r_0^p) \right)$, there exists a critical amount of elastic strain similar to Eq. (2.53).

Remark 4 *The plasticity modeling and damage modeling have similar mathematical structures, as recognized from Eq. (2.78), Eq. (2.79), Eq. (2.83), and Eq. (2.86). That is, each has a threshold function & appropriate loading/unloading conditions and eventually leads to a similar form of dissipation (initial yield value multiplied by a rate of the conjugating variable). This manner of formulation is sometimes called “two-surface formulation” as in Brepols et al.^{165),166)} and is commonly seen in Literature for CPF modeling.*

Remark 5 *Unlike some CPF ductile models introducing the plastic damage driving force^{80),83),91)}, the proposed model does not involve the damage driving force due to the initial yield stress ($-\partial g(d^p)/\partial d^p y_0 \bar{\alpha}$). In the case of perfectly plastic materials, this setup makes the damage driving force zero. In such a case, the degrading fracture toughness plays the role of promoting damage evolution.*

2.5.3 Verification of the positivity of λ^p and λ^f

The positivities of the Lagrange multipliers λ^p and λ^f for the novel evolution laws Eq. (2.83) are confirmed in this subsection. As discussed in Section 2.4.5 and Section 2.4.6, the following conditions must be satisfied under the plastic/damaged state in addition to the loading/unloading conditions in Eq. (2.83):

$$\begin{cases} \lambda^p \geq 0, & \dot{\Phi}^p \leq 0 & \text{and} & \lambda^p \dot{\Phi}^p = 0 \\ \lambda^f \geq 0, & \dot{\Phi}^f \leq 0 & \text{and} & \lambda^f \dot{\Phi}^f = 0 \end{cases}. \quad (2.87)$$

To simplify the discussion, both the elastic and plastic driving forces are inactivated in what follows. Then, $\dot{\Phi}^p$ and $\dot{\Phi}^f$ are expanded as, respectively,

$$\begin{aligned} \dot{\Phi}^p &= \frac{\partial \Phi^p}{\partial \mathbf{b}^e} : \dot{\mathbf{b}}^e + \frac{\partial \Phi^p}{\partial \bar{\alpha}} \dot{\alpha} + \frac{\partial \Phi^p}{\partial \bar{\alpha}} \dot{\bar{\alpha}} \\ &= \left(2 \frac{\partial \Phi^p}{\partial \mathbf{b}^e} \cdot \mathbf{b}^e \right) : \mathbf{d} + \frac{\partial \Phi^p}{\partial \alpha} \dot{\alpha} - \left\{ \frac{1}{g(d^e)} \left(2 \frac{\partial \Phi^p}{\partial \mathbf{b}^e} \cdot \mathbf{b}^e \right) : \frac{\boldsymbol{\tau}_{0,\text{dev}}}{\|\boldsymbol{\tau}_{0,\text{dev}}\|} - \sqrt{\frac{2}{3}} \frac{1}{g(d^p)} \frac{\partial \Phi^p}{\partial \bar{\alpha}} \right\} \lambda^p \end{aligned} \quad (2.88)$$

and

$$\begin{aligned}
\dot{\Phi}^f &= \frac{\partial \Phi^f}{\partial \mathbf{b}^e} : \dot{\mathbf{b}}^e + \frac{\partial \Phi^f}{\partial \alpha} \dot{\alpha} + \frac{\partial \Phi^f}{\partial \bar{\alpha}} \dot{\bar{\alpha}} + \frac{\partial \Phi^f}{\partial d^e} \dot{d}^e + \frac{\partial \Phi^f}{\partial d^p} \dot{d}^p + \frac{\partial \Phi^f}{\partial d} \dot{d} + \frac{\partial \Phi^f}{\partial \Delta d} \Delta \dot{d} \\
&= \left(2 \frac{\partial \Phi^f}{\partial \mathbf{b}^e} \cdot \mathbf{b}^e \right) : \mathbf{d} + \frac{\partial \Phi^f}{\partial \alpha} \dot{\alpha} - \left\{ \frac{1}{g(d^e)} \left(2 \frac{\partial \Phi^f}{\partial \mathbf{b}^e} \cdot \mathbf{b}^e \right) : \frac{\boldsymbol{\tau}_{0,\text{dev}}}{\|\boldsymbol{\tau}_{0,\text{dev}}\|} - \sqrt{\frac{2}{3}} \frac{1}{g(d^p)} \frac{\partial \Phi^f}{\partial \bar{\alpha}} \right\} \lambda^p \\
&\quad - \left(-\frac{\partial \Phi^f}{\partial d^e} \zeta^e - \frac{\partial \Phi^f}{\partial d^p} \zeta^p - \frac{\partial \Phi^f}{\partial d} - \frac{d^2}{d \mathbf{X}^2} \frac{\partial \Phi^f}{\partial \Delta d} \right) \lambda^f.
\end{aligned} \tag{2.89}$$

These expressions of the material time derivatives, $\dot{\Phi}^p$ and $\dot{\Phi}^f$, can be written in matrix notation as

$$\underbrace{\begin{pmatrix} \dot{\Phi}^p \\ \dot{\Phi}^f \end{pmatrix}}_{\delta \Phi} = \underbrace{\begin{pmatrix} \left(2 \frac{\partial \Phi^p}{\partial \mathbf{b}^e} \cdot \mathbf{b}^e \right) : \mathbf{d} + \frac{\partial \Phi^p}{\partial \alpha} \dot{\alpha} \\ \left(2 \frac{\partial \Phi^f}{\partial \mathbf{b}^e} \cdot \mathbf{b}^e \right) : \mathbf{d} + \frac{\partial \Phi^f}{\partial \alpha} \dot{\alpha} \end{pmatrix}}_{\delta \varepsilon} - \underbrace{\begin{pmatrix} \mathcal{K}_{11} & \mathcal{K}_{12} \\ \mathcal{K}_{21} & \mathcal{K}_{22} \end{pmatrix}}_{\mathcal{K}} \cdot \underbrace{\begin{pmatrix} \lambda^p \\ \lambda^f \end{pmatrix}}_{\delta \gamma}, \tag{2.90}$$

where we have defined

$$\begin{aligned}
\mathcal{K}_{11} &= \frac{1}{g(d^e)} \left(2 \frac{\partial \Phi^p}{\partial \mathbf{b}^e} \cdot \mathbf{b}^e \right) : \frac{\boldsymbol{\tau}_{0,\text{dev}}}{\|\boldsymbol{\tau}_{0,\text{dev}}\|} - \sqrt{\frac{2}{3}} \frac{1}{g(d^p)} \frac{\partial \Phi^p}{\partial \bar{\alpha}}, \\
\mathcal{K}_{12} &= 0, \\
\mathcal{K}_{21} &= \frac{1}{g(d^e)} \left(2 \frac{\partial \Phi^f}{\partial \mathbf{b}^e} \cdot \mathbf{b}^e \right) : \frac{\boldsymbol{\tau}_{0,\text{dev}}}{\|\boldsymbol{\tau}_{0,\text{dev}}\|} - \sqrt{\frac{2}{3}} \frac{1}{g(d^p)} \frac{\partial \Phi^f}{\partial \bar{\alpha}}, \\
\mathcal{K}_{22} &= -\frac{\partial \Phi^f}{\partial d^e} \zeta^e - \frac{\partial \Phi^f}{\partial d^p} \zeta^p - \frac{\partial \Phi^f}{\partial d} - \frac{d^2}{d \mathbf{X}^2} \frac{\partial \Phi^f}{\partial \Delta d}.
\end{aligned} \tag{2.91}$$

The substitution of Eq. (2.90) into Eq. (2.87) yields the following conditions:

$$\delta \varepsilon - \mathcal{K} \cdot \delta \gamma \leq 0, \quad \delta \gamma \geq 0 \quad \text{and} \quad \delta \gamma^T \cdot (\delta \varepsilon - \mathcal{K} \cdot \delta \gamma) = 0. \tag{2.92}$$

Similarly to the discussions in Section 2.4.5 and Section 2.4.6, we have the following conditions^{154),155)} to satisfy the positivity of Lagrange multipliers $\delta \gamma$:

$$\mathcal{K}_{11} > 0, \quad \mathcal{K}_{22} > 0 \quad \text{and} \quad \mathcal{K}_{11} \mathcal{K}_{22} - \mathcal{K}_{12} \mathcal{K}_{21} > 0. \tag{2.93}$$

The first condition is satisfied for an arbitrary material with hardening behavior ($\partial_{\bar{\alpha}} r_0^p \geq 0$).

That is,

$$\begin{aligned} \mathcal{K}_{11} &= \frac{1}{g(d^e)} \left(2 \frac{\partial \Phi^p}{\partial \mathbf{b}^e} \cdot \mathbf{b}^e \right) : \frac{\boldsymbol{\tau}_{0,\text{dev}}}{\|\boldsymbol{\tau}_{0,\text{dev}}\|} - \sqrt{\frac{2}{3}} \frac{1}{g(d^p)} \frac{\partial \Phi^p}{\partial \bar{\alpha}} \\ &= \underbrace{\frac{1}{g(d^e)} \left(2 \frac{\partial \|\boldsymbol{\tau}_{0,\text{dev}}\|}{\partial \mathbf{b}^e} \cdot \mathbf{b}^e \right) : \frac{\boldsymbol{\tau}_{0,\text{dev}}}{\|\boldsymbol{\tau}_{0,\text{dev}}\|}}_{>0} + \frac{2}{3} \frac{1}{g(d^p)} \underbrace{\frac{\partial r_0^p}{\partial \bar{\alpha}}}_{\geq 0} > 0. \end{aligned} \quad (2.94)$$

The component \mathcal{K}_{22} is rewritten as

$$\begin{aligned} \mathcal{K}_{22} &= -\frac{\partial \Phi^f}{\partial d^e} \zeta^e - \frac{\partial \Phi^f}{\partial d^p} \zeta^p - \frac{\partial \Phi^f}{\partial d} - \frac{d^2}{d\mathbf{X}^2} \frac{\partial \Phi^f}{\partial \Delta d} \\ &= \frac{\partial^2 g(d^e)}{\partial d^{e2}} (\Psi_0^{e+} - \Psi_{\text{cr}}^e) \zeta^{e2} + \frac{\partial^2 g(d^p)}{\partial d^{p2}} (\Psi_0^p - \Psi_{\text{cr}}^p) \zeta^{p2} + \frac{G_c}{l_f} - \frac{d^2}{d\mathbf{X}^2} \frac{\partial G_c l_f \Delta d}{\partial \Delta d} > 0. \end{aligned} \quad (2.95)$$

Here, the quadratic forms, $g(d^e) = (1 - d^e)^2$ and $g(d^p) = (1 - d^p)^2$, always guarantee the second condition in Eq. (2.93), namely $\mathcal{K}_{22} > 0$, because they are convex with respect to the damage variables, d^e and d^p . That is, both the second derivatives become $\partial_{d^{e2}}^2 g(d^e) = \partial_{d^{p2}}^2 g(d^p) = 2 > 0$. Nevertheless, if the cubic form is employed, $\partial_{d^{e2}}^2 g(d^e) = \partial_{d^{p2}}^2 g(d^p)$ may have negative values. To be precise, $\partial_{d^{e2}}^2 g(d^e) = (12 - 6s)d^e + 4s - 6$ and $\partial_{d^{p2}}^2 g(d^p) = (12 - 6s)d^p + 4s - 6$ are zero or positive only when $d^e \geq 0.5$ and $d^p \geq 0.5$ for any $s \geq 0$, so that $\mathcal{K}_{22} > 0$. If either $d^e < 0.5$ or $d^p < 0.5$, an additional procedure is necessary to confirm the inequality condition in Eq. (2.95), as explained in detail in Appendix A.2. Finally, from Eq. (2.94), Eq. (2.95), and $\mathcal{K}_{12} = 0$, the third condition is verified, which confirms that two Lagrange multipliers, λ^p and λ^f , are positive.

2.5.4 Governing equations

To derive governing equations, we consider the power balance equation such that

$$\dot{\mathcal{E}} + \dot{\mathcal{D}} = \dot{\mathcal{P}}, \quad (2.96)$$

where $\dot{\mathcal{E}}$, $\dot{\mathcal{D}}$, and $\dot{\mathcal{P}}$ are the internal power, dissipation power, and external power defined, respectively, as

$$\begin{aligned}\dot{\mathcal{E}} &= \int_{\mathcal{B}_0} \underbrace{\dot{\Psi}}_{\text{Eq. (2.65)}_2} dV, \quad \dot{\mathcal{D}} = \int_{\mathcal{B}_0} \underbrace{\Upsilon}_{\text{Eq. (2.86)}} dV, \\ \text{and } \dot{\mathcal{P}} &= \int_{\mathcal{B}_0} \mathbf{B} \cdot \dot{\mathbf{u}} dV + \int_{\partial\mathcal{B}_0^N} \mathbf{T}^N \cdot \dot{\mathbf{u}} dA + \int_{\partial\mathcal{B}_0^D} \mathbf{T}^D \cdot \dot{\mathbf{u}}^D dA.\end{aligned}\tag{2.97}$$

Here, \mathbf{B} is the body force in the initial configuration, and \mathbf{T}^N & \mathbf{T}^D denote the traction forces acting on the Neumann and Dirichlet boundaries, $\partial\mathcal{B}_0^N$ & $\partial\mathcal{B}_0^D$, in the initial configuration.

The substitution of Eq. (2.97) into Eq. (2.96) yields

$$\begin{aligned}& \int_{\mathcal{B}_0} \left(\frac{\partial\Psi^e}{\partial\mathbf{b}^e} : \dot{\mathbf{b}}^e + \frac{\partial\Psi^e}{\partial d^e} \dot{d}^e + \frac{\partial\Psi^p}{\partial\bar{\alpha}} \dot{\bar{\alpha}} + \frac{\partial\Psi^p}{\partial\alpha} \dot{\alpha} + \frac{\partial\Psi^p}{\partial\nabla\alpha} \cdot \nabla\dot{\alpha} + \frac{\partial\Psi^p}{\partial d^p} \dot{d}^p + \frac{\partial\Psi^f}{\partial d} \dot{d} + \frac{\partial\Psi^f}{\partial\nabla d} \cdot \nabla\dot{d} \right) dV \\& + \int_{\mathcal{B}_0} \left(\sqrt{\frac{2}{3}} g(d^e) y_0 \|\mathbf{d}^p\| - \frac{\partial g(d^e)}{\partial d^e} \Psi_{\text{cr}}^e \dot{d}^e - \frac{\partial g(d^p)}{\partial d^p} \Psi_{\text{cr}}^p \dot{d}^p \right) dV \\& - \int_{\mathcal{B}_0} \mathbf{B} \cdot \dot{\mathbf{u}} dV - \int_{\partial\mathcal{B}_0^N} \mathbf{T}^N \cdot \dot{\mathbf{u}} dA - \int_{\partial\mathcal{B}_0^D} \mathbf{T}^D \cdot \dot{\mathbf{u}}^D dA \\& = - \int_{\mathcal{B}_0} (\nabla \cdot \mathbf{P} + \mathbf{B}) \cdot \dot{\mathbf{u}} dV + \int_{\partial\mathcal{B}_0^N} (\mathbf{P} \cdot \mathbf{N} - \mathbf{T}^N) \cdot \dot{\mathbf{u}} dA + \int_{\partial\mathcal{B}_0^D} (\mathbf{P} \cdot \mathbf{N} - \mathbf{T}^D) \cdot \dot{\mathbf{u}}^D dA \\& - \int_{\mathcal{B}_0} \underbrace{\sqrt{\frac{3}{2}} g(d^p) \left(\|\boldsymbol{\tau}_{0,\text{dev}}\| - \sqrt{\frac{2}{3}} (y_0 + r_0^p) \right)}_{\Phi^p \leq 0} \dot{\bar{\alpha}} dV \\& + \int_{\mathcal{B}_0} (p_p (\alpha - \bar{\alpha}) - y_0 l_p^2 \Delta\alpha) \dot{\alpha} dV + \int_{\partial\mathcal{B}_0} (y_0 l_p^2 \nabla\alpha \cdot \mathbf{N}) \dot{\alpha} dA \\& - \int_{\mathcal{B}_0} \underbrace{\left(-\frac{\partial g(d^e)}{\partial d^e} \langle \Psi_0^{e+} - \Psi_{\text{cr}}^e \rangle \zeta^e - \frac{\partial g(d^p)}{\partial d^p} \langle \Psi_0^p - \Psi_{\text{cr}}^p \rangle \zeta^p - G_c (\alpha^*, \tau_p^*) \left(\frac{d - l_f^2 \Delta d}{l_f} \right) \right)}_{\Phi^f \leq 0} \dot{d} dV \\& + \int_{\partial\mathcal{B}_0} (G_c (\alpha^*, \tau_p^*) l_f \nabla d \cdot \mathbf{N}) \dot{d} dA = 0,\end{aligned}\tag{2.98}$$

in which we have used the relations in Eq. (2.66), Eq. (2.67), Eq. (2.68), Eq. (2.84) as well as $\mathbf{P} = \partial_{\mathbf{F}} \Psi^e$ and the Gaussian divergence theorem.

Meanwhile, the first-order stability condition for any possible variations $\{\delta\mathbf{u}, \delta\bar{\alpha}, \delta\alpha, \delta d\}$

can be written in a similar form as

$$\begin{aligned}
& - \int_{\mathcal{B}_0} (\nabla \cdot \mathbf{P} + \mathbf{B}) \cdot \delta \mathbf{u} dV + \int_{\partial \mathcal{B}_0^N} (\mathbf{P} \cdot \mathbf{N} - \mathbf{T}^N) \cdot \delta \mathbf{u} dA \\
& - \int_{\mathcal{B}_0} \underbrace{\sqrt{\frac{3}{2}} g(d^p) \left(\|\boldsymbol{\tau}_{0,\text{dev}}\| - \sqrt{\frac{2}{3}} (y_0 + r_0^p) \right)}_{\Phi^p \leq 0} \delta \bar{\alpha} dV \\
& + \int_{\mathcal{B}_0} (p_p (\alpha - \bar{\alpha}) - y_0 l_p^2 \Delta \alpha) \delta \alpha dV + \int_{\partial \mathcal{B}_0} (y_0 l_p^2 \nabla \alpha \cdot \mathbf{N}) \delta \alpha dA \\
& - \int_{\mathcal{B}_0} \underbrace{\left(-\frac{\partial g(d^e)}{\partial d^e} \langle \Psi_0^{e+} - \Psi_{\text{cr}}^e \rangle \zeta^e - \frac{\partial g(d^p)}{\partial d^p} \langle \Psi_0^p - \Psi_{\text{cr}}^p \rangle \zeta^p - G_c (\alpha^*, \tau_p^*) \left(\frac{d - l_f^2 \Delta d}{l_f} \right) \right)}_{\Phi^f \leq 0} \delta d dV \\
& + \int_{\partial \mathcal{B}_0} (G_c (\alpha^*, \tau_p^*) l_f \nabla d \cdot \mathbf{N}) \delta d dA \geq 0.
\end{aligned} \tag{2.99}$$

Finally, from Eq. (2.98) and Eq. (2.99), the governing equations of the proposed model are derived as follows:

- Equilibrium for mechanical field:

$$\nabla \cdot \mathbf{P} + \mathbf{B} = \mathbf{0} \quad \text{in } \mathcal{B}_0, \quad \mathbf{P} \cdot \mathbf{N} = \mathbf{T}^N \quad \text{on } \partial \mathcal{B}_0^N, \quad \mathbf{u} = \bar{\mathbf{u}} \quad \text{on } \partial \mathcal{B}_0^D, \tag{2.100}$$

- Equilibrium for micromorphic plastic field:

$$p_p (\alpha - \bar{\alpha}) - y_0 l_p^2 \Delta \alpha = 0 \quad \text{in } \mathcal{B}_0, \quad \nabla \alpha \cdot \mathbf{N} = 0 \quad \text{on } \partial \mathcal{B}_0, \tag{2.101}$$

- Threshold function for plasticity with loading/unloading conditions:

$$\Phi^p = \|\boldsymbol{\tau}_{0,\text{dev}}\| - \sqrt{\frac{2}{3}} (y_0 + r_0^p) \leq 0, \quad \dot{\alpha} \geq 0, \quad \Phi^p \dot{\alpha} = 0 \quad \text{in } \mathcal{B}_0, \tag{2.102}$$

- Threshold function for damage with loading/unloading conditions:

$$\begin{aligned}
\Phi^f &= -\frac{\partial g(d^e)}{\partial d^e} \langle \Psi_0^{e+} - \Psi_{\text{cr}}^e \rangle \zeta^e - \frac{\partial g(d^p)}{\partial d^p} \langle \Psi_0^p - \Psi_{\text{cr}}^p \rangle \zeta^p - G_c (\alpha^*, \tau_p^*) \left(\frac{d - l_f^2 \Delta d}{l_f} \right) \leq 0, \\
\dot{d} &\geq 0, \quad \Phi^f \dot{d} = 0 \quad \text{in } \mathcal{B}_0, \quad \nabla d \cdot \mathbf{N} = 0 \quad \text{on } \partial \mathcal{B}_0,
\end{aligned} \tag{2.103}$$

2.5.5 Equivalence and novelty

To close this section, we remark on the unified nature of the proposed model by reference to several recently developed CPFMs.

As suggested in Section 2.4, the plastic driving force and the degrading fracture toughness are the two major elements for realizing the ductile fracture of elastoplastic materials within the CPF framework. For instance, suppose we consider only the elastic and plastic driving forces while assuming constant fracture toughness. Then, this setup is equivalent to that of Miehe et al.⁸⁰⁾ by activating the damage thresholds, Ψ_{cr}^e and Ψ_{cr}^p , simultaneously and setting the damage coefficients at $\zeta^e = 1$ and $\zeta^p = 1$. Also, if $\Psi_{cr}^e = 0$ is assumed, and if any values are given for Ψ_{cr}^p , ζ^e and ζ^p , the same damage driving force as in Borden¹⁶⁴⁾ is realized by the proposed model. Similarly, our model is capable of realizing the assumptions on the damage driving force made in the other models^{87),146),167),91)}, as described in Section 2.4.3. The difference between these models and ours is the origin of the evolution laws of damage variables. The novelty of our proposed model is clear; that is, it is the first model to derive the damage evolution laws in Eq. (2.83) as a consequence of the variational formulation, whereas they were not properly considered in previous studies in spite of the introduction of the thresholds and coefficients.

On the other hand, if a degrading fracture toughness is utilized without introducing a plastic driving force, i.e., $\Psi_{cr}^p \rightarrow \infty$, the proposed model is equivalent to the models proposed by Dittmann et al.⁸⁴⁾, Yin & Kaliske⁸⁵⁾, Hu et al.¹⁵⁰⁾, as described in Section 2.4.4. Here, “equivalent” means that each model has the same degrading tendency for fracture toughness. That is, severe plastic deformation provokes damage, because the value of fracture toughness decreases as plastic strain accumulates. Also, it should be noted that the degrading fracture toughness introduced in the proposed model decreases not only by the accumulation of plastic strain but also by the increase in the negative hydrostatic pressure. Therefore, the degradation tendency can manifest the effect of stress triaxiality in addition to that of plastic deformation. This idea was originally proposed by Han et al.¹⁵²⁾ in their study designed to experimentally validate the failure tendency of advanced high strength steel (AHSS)¹⁵¹⁾.

In this context, the proposed model ¹⁵⁷⁾ can be regarded as a unification of several of the existing CPFMs for ductile fracture, as summarized in Table 2.2, where each model can be regarded as a specific case of the proposed model employing a set of parameters.

Table 2.2: Unified nature of the proposed model by reference to several recently developed CPFMs.

Working group	Ψ_{cr}^e	Ψ_{cr}^p	ζ^e	ζ^p	G_c
Alessi et al. ^{75),76)}	= 0	= 0	= 1	= 1	= const.
Kuhn et al. ⁸⁷⁾	= 0	= 0	= 1	= 1	= const.
Miehe et al. ⁸⁰⁾	$\neq 0$	$\neq 0$	= 1	= 1	= const.
Borden et al. ¹⁶⁴⁾	= 0	$\neq 0$	$\in [0, 1]$	$\in [0, 1]$	= const.
Dittmann et al. ⁸⁴⁾	= 0	= 0	= 1	= 1	\neq const.
Yin & Kaliske ⁸⁵⁾	= 0	= 0	= 1	= 1	\neq const.
Hu et al. ¹⁵⁰⁾	$\neq 0$	$\neq 0$	= 1	= 1	\neq const.
Han et al. ⁹¹⁾	$\neq 0$	$\neq 0$	= 1	= 1	\neq const.

Furthermore, another difference worthy of remark is the definition of yield function. The yield function in the proposed model is true to the theory of CDM ^{20),168),17)}, while being defined to coincide with the form of energies in previous studies. Consequently, the evolution laws for plastic deformation become equivalent to those in CDM for plasticity, and the evolutions of plastic strain and the plastic hardening variable are influenced by the corresponding damage variables, d^e and d^p .

Thus, the proposed model has the versatility to become equivalent to various models by turning the components relevant to damage modeling either on or off.

2.6 Numerical implementation of the proposed model

The return mapping algorithm for local plasticity and spatial discretization by Isogeometric analysis (IGA) ¹⁴⁰⁾ are presented in this section. For detailed forms of vectors and tensors, refer to Appendix A.3.

2.6.1 Return mapping algorithm for internal variables

Algorithm 1 Return mapping algorithm.

```

1: (% At time step  $t_{n+1}$ , the variables  $\mathbf{F}_{n+1}$ ,  $\mathbf{C}_n^{\text{p}-1}$  and  $r_{0,n}^{\text{p}}$  are known.)
2: Compute the following stress tensor for the trial state:  $\boldsymbol{\tau}_{0,\text{dev},n+1}^{\text{tr}} = \mu \text{dev}[\bar{\mathbf{b}}_{n+1}^{\text{e,tr}}]$  with  $\mathbf{b}_{n+1}^{\text{e,tr}} = \mathbf{F}_{n+1} \cdot \mathbf{C}_n^{\text{p}-1} \cdot \mathbf{F}_{n+1}^{\text{T}}$ 
3: Check the deformation state by the yield function:  $\Phi^{\text{p}}(\boldsymbol{\tau}_{0,\text{dev},n+1}^{\text{tr}}, r_{0,n}^{\text{p}}) = \|\boldsymbol{\tau}_{0,\text{dev},n+1}^{\text{tr}}\| - \sqrt{\frac{2}{3}}(y_0 + r_{0,n}^{\text{p}})$ 
4: if  $\Phi^{\text{p}} \leq 0$  then
5:   (% Elastic state)
6:    $(*)_{n+1} = (*)_{n+1}^{\text{tr}}$ 
7: else
8:   (% Plastic state)
9:   Solve  $\lambda_{n+1}^{\text{p}}$  and  $\mathbf{n}_{n+1}$  from two local governing equations,  $\|\boldsymbol{\tau}_{0,\text{dev},n+1}\| - \sqrt{\frac{2}{3}}(y_0 + r_{0,n+1}^{\text{p}}) = 0$  and  $\frac{\boldsymbol{\tau}_{0,\text{dev},n+1}}{\|\boldsymbol{\tau}_{0,\text{dev},n+1}\|} - \mathbf{n}_{n+1} = 0$ ,
10:   where  $\mathbf{b}_{n+1}^{\text{e}} = \exp\left(-2\frac{\lambda_{n+1}^{\text{p}}}{g(d^{\text{e}})}\Delta t_{n+1}\mathbf{n}_{n+1}\right) \cdot \mathbf{b}_{n+1}^{\text{e,tr}}$  and  $\bar{\alpha}_{n+1} = \bar{\alpha}_n + \sqrt{\frac{2}{3}}\frac{\lambda_{n+1}^{\text{p}}}{g(d^{\text{p}})}\Delta t_{n+1}$ 
11: end if

```

A pseudo-code for the local return mapping algorithm is shown in Algorithm 1. Here, the plastic multiplier λ^{p} and flow tensor \mathbf{n} are internal variables to be determined. Also, to ensure the incompressibility of the plastic deformation, exponential mapping is adopted.

The residuals of two local differential equations are expressed as

$$\mathbf{r}_k^{\lambda^{\text{p}}} = -\left(\|\boldsymbol{\tau}_{0,\text{dev},k}\| - \sqrt{\frac{2}{3}}(y_0 + r_{0,k}^{\text{p}})\right) \quad (2.104)$$

$$\mathbf{r}_k^{\mathbf{n}} = -\left(\frac{\boldsymbol{\tau}_{0,\text{dev},k}}{\|\boldsymbol{\tau}_{0,\text{dev},k}\|} - \mathbf{n}_k\right), \quad (2.105)$$

where the index k represents the iteration of the local Newton-Raphson scheme. By linearization, its tangent matrix yields

$$\mathbf{k} = \begin{bmatrix} \mathbf{k}_{\lambda^{\text{p}},\lambda^{\text{p}}} & \mathbf{k}_{\lambda^{\text{p}},\mathbf{n}} \\ \mathbf{k}_{\mathbf{n},\lambda^{\text{p}}} & \mathbf{k}_{\mathbf{n},\mathbf{n}} \end{bmatrix} \quad (2.106)$$

with diagonal components

$$\mathbf{k}_{\lambda^{\text{p}},\lambda^{\text{p}}} = \frac{\partial \|\boldsymbol{\tau}_{0,\text{dev},k}\|}{\partial \mathbf{b}^{\text{e}}} : \frac{\partial \exp\left(-2\frac{\lambda_k^{\text{p}}}{g(d^{\text{e}})}\Delta t_{n+1}\mathbf{n}_k\right) \cdot \mathbf{b}_{n+1}^{\text{e,tr}}}{\partial \lambda^{\text{p}}} - \sqrt{\frac{2}{3}}\frac{\partial r_{0,k}^{\text{p}}}{\partial \bar{\alpha}} \frac{\partial \left(\bar{\alpha}_n + \sqrt{\frac{2}{3}}\frac{\lambda_{n+1}^{\text{p}}}{g(d^{\text{p}})}\Delta t_{n+1}\right)}{\partial \lambda^{\text{p}}}, \quad (2.107)$$

$$\begin{aligned}
\mathbf{k}_{nn} &= \frac{1}{\|\boldsymbol{\tau}_{0,\text{dev},k}\|} \frac{\partial \boldsymbol{\tau}_{0,\text{dev},k}}{\partial \mathbf{n}} - \frac{\boldsymbol{\tau}_{0,\text{dev},k}}{\|\boldsymbol{\tau}_{0,\text{dev},k}\|^2} \otimes \frac{\partial \|\boldsymbol{\tau}_{0,\text{dev},k}\|}{\partial \mathbf{n}} - \underline{\mathbf{1}}_{\text{sym}} \\
&= \left(\frac{1}{\|\boldsymbol{\tau}_{0,\text{dev},k}\|} \frac{\partial \boldsymbol{\tau}_{0,\text{dev},k}}{\partial \mathbf{b}^e} - \frac{\boldsymbol{\tau}_{0,\text{dev},k}}{\|\boldsymbol{\tau}_{0,\text{dev},k}\|^2} \otimes \frac{\partial \|\boldsymbol{\tau}_{0,\text{dev},k}\|}{\partial \mathbf{b}^e} \right) : \frac{\partial \exp\left(-2 \frac{\lambda_k^p}{g(d^e)} \Delta t_{n+1} \mathbf{n}_k\right) \cdot \mathbf{b}_{n+1}^{\text{e,tr}}}{\partial \mathbf{n}} - \underline{\mathbf{1}}_{\text{sym}}
\end{aligned} \tag{2.108}$$

and off-diagonal components

$$\mathbf{k}_{\lambda^p \mathbf{n}} = \frac{\partial \|\boldsymbol{\tau}_{0,\text{dev},k}\|}{\partial \mathbf{b}^e} : \frac{\partial \exp\left(-2 \frac{\lambda_k^p}{g(d^e)} \Delta t_{n+1} \mathbf{n}_k\right) \cdot \mathbf{b}_{n+1}^{\text{e,tr}}}{\partial \mathbf{n}}, \tag{2.109}$$

$$\begin{aligned}
\mathbf{k}_{\mathbf{n} \lambda^p} &= \frac{1}{\|\boldsymbol{\tau}_{0,\text{dev},k}\|} \frac{\partial \boldsymbol{\tau}_{0,\text{dev},k}}{\partial \lambda^p} - \frac{\boldsymbol{\tau}_{0,\text{dev},k}}{\|\boldsymbol{\tau}_{0,\text{dev},k}\|^2} \frac{\partial \|\boldsymbol{\tau}_{0,\text{dev},k}\|}{\partial \lambda^p} \\
&= \left(\frac{1}{\|\boldsymbol{\tau}_{0,\text{dev},k}\|} \frac{\partial \boldsymbol{\tau}_{0,\text{dev},k}}{\partial \mathbf{b}^e} - \frac{\boldsymbol{\tau}_{0,\text{dev},k}}{\|\boldsymbol{\tau}_{0,\text{dev},k}\|^2} \otimes \frac{\partial \|\boldsymbol{\tau}_{0,\text{dev},k}\|}{\partial \mathbf{b}^e} \right) : \frac{\partial \exp\left(-2 \frac{\lambda_k^p}{g(d^e)} \Delta t_{n+1} \mathbf{n}_k\right)}{\partial \lambda^p} \cdot \mathbf{b}_{n+1}^{\text{e,tr}},
\end{aligned} \tag{2.110}$$

where

$$\frac{\partial \exp\left(-2 \frac{\lambda_k^p}{g(d^e)} \Delta t_{n+1} \mathbf{n}_k\right) \cdot \mathbf{b}_{n+1}^{\text{e,tr}}}{\partial \lambda^p} = \left\{ \text{D exp}\left(-2 \frac{\lambda_k^p}{g(d^e)} \Delta t_{n+1} \mathbf{n}_k\right) : \left(-2 \frac{1}{g(d^e)} \Delta t_{n+1} \mathbf{n}_k\right) \right\} \cdot \mathbf{b}_{n+1}^{\text{e,tr}} \tag{2.111}$$

$$\frac{\partial \exp\left(-2 \frac{\lambda_k^p}{g(d^e)} \Delta t_{n+1} \mathbf{n}\right) \cdot \mathbf{b}_{n+1}^{\text{e,tr}}}{\partial \mathbf{n}} = \underbrace{\left\{ \text{D exp}\left(-2 \frac{\lambda_k^p}{g(d^e)} \Delta t_{n+1} \mathbf{n}\right) : \left(-2 \frac{\lambda_k^p}{g(d^e)} \Delta t_{n+1} \underline{\mathbf{1}}_{\text{sym}}\right) \right\}}_{i a k l} * \underbrace{\mathbf{b}_{n+1}^{\text{e,tr}}}_{a j}. \tag{2.112}$$

Here, D exp denotes the derivative of the second order exponential tensor, and $\underline{\mathbf{1}}_{\text{sym}}$ is the fourth order symmetric identity tensor. Also, to show formulations explicitly in tensor notation, we define an operator $*$ that represents a contraction of the second basis of a fourth-order tensor $\underline{\mathbf{X}}$ and the first basis of a second-order tensor \mathbf{Y} , which corresponds to the index notation $X_{iajk} Y_{aj}$.

2.6.2 Spatial discretization

After some mathematical manipulation, the weak forms in the current configuration for the mechanical field, micromorphic plastic field, and crack phase-field yield

$$\int_{\mathcal{B}_t} \frac{\boldsymbol{\tau}}{J} : \nabla_{\mathbf{x}} \delta \mathbf{u} d\mathbf{v} - \int_{\mathcal{B}_t} \mathbf{b} \cdot \delta \mathbf{u} d\mathbf{v} - \int_{\partial \mathcal{B}_t^N} \mathbf{t} \cdot \delta \mathbf{u} da = 0, \quad (2.113)$$

$$\int_{\mathcal{B}_t} \frac{1}{J} \left\{ (\alpha - \bar{\alpha}) \delta \alpha + \frac{y_0 l_p^2}{p_p} \nabla \alpha \cdot \nabla \delta \alpha \right\} d\mathbf{v} = 0, \quad (2.114)$$

and

$$\int_{\mathcal{B}_t} \frac{1}{J} \left\{ -\frac{\partial g(d^e)}{\partial d^e} \langle \Psi_0^{e+} - \Psi_{cr}^e \rangle \zeta^e \delta d - \frac{\partial g(d^p)}{\partial d^p} \langle \Psi_0^p - \Psi_{cr}^p \rangle \zeta^p \delta d - \frac{G_c}{l_f} (d \delta d + l_f^2 \nabla d \cdot \nabla \delta d) \right\} d\mathbf{v} = 0. \quad (2.115)$$

Here, \mathbf{b} and \mathbf{t} are the body and traction forces in the current configuration defined as

$$\mathbf{b} = \frac{\mathbf{B}}{J} \quad \text{and} \quad \mathbf{t} = \frac{\mathbf{T}}{J \sqrt{\mathbf{N} \cdot \mathbf{C}^{-1} \cdot \mathbf{N}}}. \quad (2.116)$$

The state variables (\mathbf{u} , α and d) and their variations ($\delta \mathbf{u}$, $\delta \alpha$ and δd) are approximated in a general manner by using second-order NURBS basis functions \mathfrak{R}^I as

$$\begin{aligned} \mathbf{u} &\approx \mathbf{u}^h = \sum_{I=1}^{n_{\text{node}}} \mathfrak{R}^I \mathbf{u}^I, & \delta \mathbf{u} &\approx \delta \mathbf{u}^h = \sum_{I=1}^{n_{\text{node}}} \mathfrak{R}^I \delta \mathbf{u}^I, \\ \alpha &\approx \alpha^h = \sum_{I=1}^{n_{\text{node}}} \mathfrak{R}^I \alpha^I, & \delta \alpha &\approx \delta \alpha^h = \sum_{I=1}^{n_{\text{node}}} \mathfrak{R}^I \delta \alpha^I, \\ d &\approx d^h = \sum_{I=1}^{n_{\text{node}}} \mathfrak{R}^I d^I, & \delta d &\approx \delta d^h = \sum_{I=1}^{n_{\text{node}}} \mathfrak{R}^I \delta d^I, \end{aligned} \quad (2.117)$$

Additionally, the element-level residual vectors corresponding to the weak forms Eq. (2.113), Eq. (2.114) and Eq. (2.115) are given as, respectively,

$$\mathcal{R}_{\mathbf{u}_i}^I = - \int_{\mathcal{B}_t} \frac{\tau_{ia}^h}{J} \frac{\partial \mathfrak{R}^I}{\partial x_a} d\mathbf{v}, \quad (2.118)$$

$$\mathcal{R}_{\alpha}^I = - \int_{\mathcal{B}_t} \frac{1}{J} \left\{ (\alpha^h - \bar{\alpha}_{n+1}^h) \mathfrak{R}^I + \frac{y_0 l_p^2}{p_p} \frac{\partial \alpha^h}{\partial x_a} \frac{\partial \mathfrak{R}^I}{\partial x_a} \right\} d\mathbf{v}, \quad (2.119)$$

and

$$\mathcal{R}_d^I = - \int_{\mathcal{B}_t} \frac{1}{J} \left\{ - \frac{\partial g(d^{eh})}{\partial d^e} \mathcal{H}_{n+1}^{eh} \zeta^e \mathcal{R}^I - \frac{\partial g(d^{ph})}{\partial d^p} \mathcal{H}_{n+1}^{ph} \zeta^p \mathcal{R}^I - \frac{G_{c,n+1}^h}{l_f} \left(d^h \mathcal{R}^I + l_f^2 \frac{\partial d^h}{\partial X_a} \frac{\partial \mathcal{R}^I}{\partial X_a} \right) \right\} dv. \quad (2.120)$$

Here, we have introduced the history variables \mathcal{H}^e and \mathcal{H}^p to ensure the irreversibility of damage evolution, which was initially proposed by Miehe et al.⁴⁰⁾ and is defined in this study as follows:

$$\begin{aligned} \mathcal{H}_{n+1}^{eh} &= \begin{cases} \langle \Psi_{0,n+1}^{e+h} - \Psi_{cr}^e \rangle & \text{if } \langle \Psi_{0,n+1}^{e+h} - \Psi_{cr}^e \rangle > \mathcal{H}_n^e \\ \mathcal{H}_n^{eh} & \text{otherwise} \end{cases} \\ \mathcal{H}_{n+1}^{ph} &= \begin{cases} \langle \Psi_{0,n+1}^{ph} - \Psi_{cr}^p \rangle & \text{if } \langle \Psi_{0,n+1}^{ph} - \Psi_{cr}^p \rangle > \mathcal{H}_n^p \\ \mathcal{H}_n^{ph} & \text{otherwise} \end{cases}. \end{aligned} \quad (2.121)$$

Furthermore, the two damage variables, d_{n+1}^{eh} and d_{n+1}^{ph} , at current time step are, respectively, updated by

$$\begin{aligned} d_{n+1}^{eh} &= \sum_{l=1}^{n_{node}} \mathcal{R}^I \underbrace{\left\{ (d_{n+1}^I - d_n^I) \zeta^e \chi_{n+1}^e + d_n^{eI} \right\}}_{d_{n+1}^{eI}} \quad \text{and} \quad d_{n+1}^{ph} = \sum_{l=1}^{n_{node}} \mathcal{R}^I \underbrace{\left\{ (d_{n+1}^I - d_n^I) \zeta^p \chi_{n+1}^p + d_n^{pI} \right\}}_{d_{n+1}^{pI}} \\ \text{with } \chi^e &= \begin{cases} 1 & \text{if } \Psi_{0,n+1}^{e+h} - \Psi_{cr}^e > 0 \\ 0 & \text{otherwise} \end{cases} \quad \text{and} \quad \chi^p = \begin{cases} 1 & \text{if } \Psi_{0,n+1}^{ph} - \Psi_{cr}^p > 0 \\ 0 & \text{otherwise} \end{cases}. \end{aligned} \quad (2.122)$$

The tangent matrices are obtained by differentiating the residual vectors with respect to the state variables. In this study, we introduce the staggered scheme⁷⁷⁾ for stable damage computation. That is, instead of solving three state variables simultaneously, we solve the mechanical/micromorphic fields and crack phase-field alternately. Then, the original tangent matrices \mathcal{K} yields two blocks, \mathcal{K}_{ep} and \mathcal{K}_f , as follows:

$$\mathcal{K} = \begin{bmatrix} \mathcal{K}_{uu} & \mathcal{K}_{u\alpha} & \mathcal{K}_{ud} \\ \mathcal{K}_{\alpha u} & \mathcal{K}_{\alpha\alpha} & \mathcal{K}_{\alpha d} \\ \mathcal{K}_{du} & \mathcal{K}_{d\alpha} & \mathcal{K}_{dd} \end{bmatrix} \Rightarrow \mathcal{K}_{ep} = \begin{bmatrix} \mathcal{K}_{uu} & \mathcal{K}_{u\alpha} \\ \mathcal{K}_{\alpha u} & \mathcal{K}_{\alpha\alpha} \end{bmatrix} \quad \text{and} \quad \mathcal{K}_f = \begin{bmatrix} \mathcal{K}_{dd} \end{bmatrix}, \quad (2.123)$$

where

$$\mathcal{K}_{u_i u_j}^{IJ} = \int_{\mathcal{B}_t} \left\{ \frac{\partial \mathfrak{R}^I}{\partial x_a} \underline{C}_{iajb}^h \frac{\partial \mathfrak{R}^J}{\partial x_b} \right\} dv \quad \text{with} \quad \underline{C}_{iajb}^h = \frac{1}{J} \left(\frac{\partial \tau_{ia}^h}{\partial F_{jc}} F_{bc} - \tau_{ib}^h \delta_{ja} \right), \quad (2.124)$$

$$\mathcal{K}_{\alpha\alpha}^{IJ} = \int_{\mathcal{B}_t} \frac{1}{J} \left\{ \left(1 - \frac{\partial \bar{\alpha}_{n+1}^h}{\partial \alpha} \right) \mathfrak{R}^I \mathfrak{R}^J + \frac{y_0 l_p^2}{p_p} \frac{\partial \mathfrak{R}^I}{\partial X_a} \frac{\partial \mathfrak{R}^J}{\partial X_a} \right\} dv, \quad (2.125)$$

$$\mathcal{K}_{u_i \alpha}^{IJ} = \int_{\mathcal{B}_t} \frac{1}{J} \left\{ \frac{\partial \tau_{ia}^{*h}}{\partial \alpha} \frac{\partial \mathfrak{R}^I}{\partial x_a} \mathfrak{R}^J \right\} dv, \quad (2.126)$$

$$\mathcal{K}_{\alpha u_j}^{IJ} = \int_{\mathcal{B}_t} \frac{1}{J} \left\{ -\mathfrak{R}^I \frac{\partial \bar{\alpha}_{n+1}^h}{\partial F_{ja}} \frac{\partial \mathfrak{R}^J}{\partial X_a} \right\} dv, \quad (2.127)$$

and

$$\mathcal{K}_{dd}^{IJ} = \int_{\mathcal{B}_t} \frac{1}{J} \left\{ -\frac{\partial^2 g(d^{eh})}{\partial d^{e2}} \mathcal{H}_{n+1}^{eh} \zeta^{e2} \mathfrak{R}^I \mathfrak{R}^J - \frac{\partial^2 g(d^{ph})}{\partial d^{p2}} \mathcal{H}_{n+1}^{ph} \zeta^{p2} \mathfrak{R}^I \mathfrak{R}^J - \frac{G_{c,n+1}^h}{l_f} \left(\mathfrak{R}^I \mathfrak{R}^J + l_f^2 \frac{\partial \mathfrak{R}^I}{\partial X_a} \frac{\partial \mathfrak{R}^J}{\partial X_a} \right) \right\} dv. \quad (2.128)$$

In order to obtain converged solutions, the staggered iterative process ⁷⁷⁾ should be conducted, whose specific algorithm is omitted here but is explained in Chapter 4 along with the proposed diffusive-discrete crack transition scheme.

3 Numerical simulations by CPFIGA

Several numerical examples are presented to demonstrate the ability and performance of the proposed model. The simulations are conducted using our in-house isogeometric analysis (IGA) ¹⁴⁰⁾ program, which is referred to as “CPFIGA”. For the degrading fracture toughness, the following two forms are proposed:

$$\begin{aligned}
 \text{Cosinusoidal form: } G_c(\alpha^*, \tau_p^*) &:= (G_{c0} - G_{c\infty}) \cos^{p_1} \left(\frac{\beta_{G1} \alpha^*}{2} \right) \cos^{p_2} \left(\frac{\beta_{G2} \tau_p^*}{2} \right) + G_{c\infty} \\
 \text{Exponential form: } G_c(\alpha^*, \tau_p^*) &:= (G_{c0} - G_{c\infty}) \exp(-\beta_{G1} \alpha^*) \exp(-\beta_{G2} \tau_p^*) + G_{c\infty} \quad (3.1) \\
 \text{with } \alpha^* &= \langle \alpha - \alpha_{cr} \rangle, \quad \tau_p^* = \underbrace{\left\langle \frac{1}{3} \text{tr} [\boldsymbol{\tau}_0] - \tau_{cr} \right\rangle}_{\tau_p}.
 \end{aligned}$$

Here, G_{c0} and $G_{c\infty}$ are the initial and critical values. The degradation effects are determined by both the plastic hardening variable α and the negative hydrostatic pressure τ_p , for which saturation parameters, β_{G1} and β_{G2} , and thresholds, α_{cr} and τ_{cr} , are appropriately given. Also, p_1 and p_2 are the parameters to determine the slope of cosine functions. Note that the cosinusoidal form is used in the second and third numerical examples, while the exponential one is used in the last example.

3.1 Exmample 3-1: Tensile failure of a square element

The first example shows the characteristic features of the proposed model, and its performance is compared with that of the previous models in the literature. Uni-directional uniform deformation is imposed on a two-dimensional square element with a side length of $h_e = 1$ [mm]. For simplicity, the isotropic linear hardening law $\hat{H}(\bar{\alpha}) = h\bar{\alpha}$ is adopted, and

the material parameters for elastoplasticity and damage are listed in Table 3.1.

Table 3.1: Material parameters for the square element.

Parameter		Value	Unit
Young's modulus	E	200000	[MPa]
Poisson's ratio	ν	0.3	[-]
Initial yield stress	y_0	1000	[MPa]
Linear hardening parameter	h	1000	[MPa]
Plastic length scale parameter	l_p	5	[mm]
Penalty parameter	p_p	10000	[-]
Crack length scale parameter	l_f	5	[mm]
Elastic damage threshold	Ψ_{cr}^e	0	[MPa]

3.1.1 Parameter study for plastic damage threshold Ψ_{cr}^p

First, we present the evolution tendencies relevant to two damage variables, d^e and d^p , by changing the plastic damage threshold Ψ_{cr}^p . Fig. 3.1 shows the stress–total strain curves as well as the evolutions of damage and hardening variables with respect to the total strain. Here, two different values of constant fracture toughness, $G_c = 100$ and $G_c = 500$, are used, while $\zeta^e = 1$ and $\zeta^p = 1$ are fixed.

As can be seen from Fig. 3.1(a) and Fig. 3.1(b), the stress drop mainly depends on the threshold value Ψ_{cr}^p . Specifically, the larger the threshold value Ψ_{cr}^p is, the larger deformation the material sustains against external loading before exhibiting a rapid stress drop. Also, while all the cases with $G_c = 500$ hardly show a decrease in material stiffness before the rapid stress drop, the cases with $G_c = 100$ exhibit some decrease from the early stage of plastic deformation. This is because the amount of elastic strain energy Ψ_0^{e+} is sufficiently large compared to the smaller value of fracture toughness $G_c = 100$ and thus able to promote damage evolution. In fact, for the case with $\Psi_{cr}^p = 150$ & $G_c = 100$, the elastic damage variable has already reached $d^e \approx 0.5$ when the plastic damage variable starts to evolve, as shown in Fig. 3.1(c).

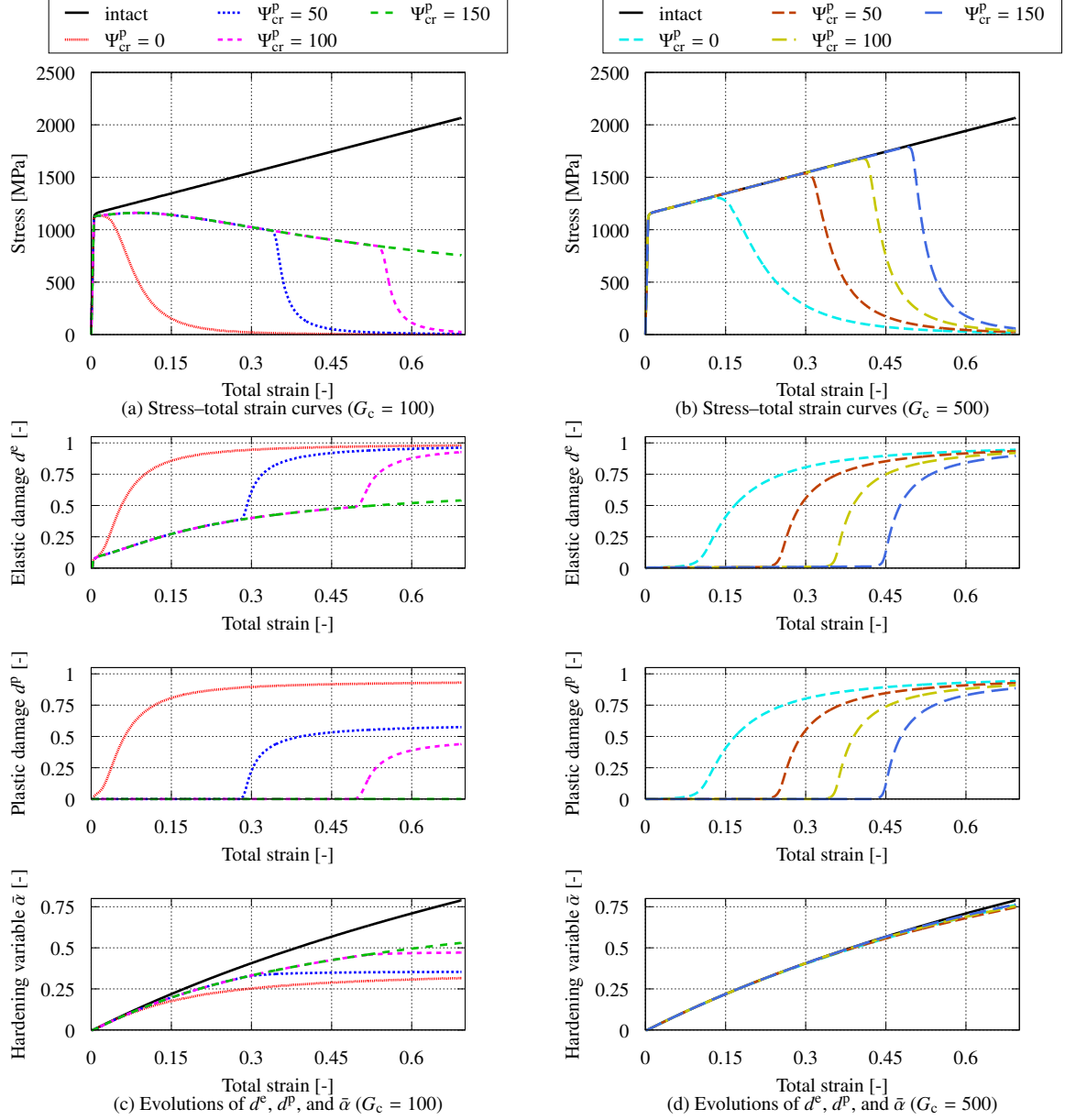


Fig. 3.1: Stress, damage variables, and hardening variable–total strain curves for the single square element: Comparisons of the value of threshold Ψ_{cr}^p .

In contrast, for all the cases with $G_c = 500$, the amount of elastic strain energy Ψ_0^{e+} is relatively small compared to the value of fracture toughness. As a result, damage evolutions are hardly seen before the plastic damage driving force is activated. Then, the plastic driving force becomes dominant for damage evolutions, and due to the relation $\lambda^f \zeta^e \chi^e = \lambda^f \zeta^p \chi^p$,

both the elastic and plastic damage variables have almost the same value, as shown in Fig. 3.1(d). Strictly speaking, however, $d^e = d^p$ is not realized because d^e also evolves in a purely elastic state.

In addition, as can be seen from the last graphs in Fig. 3.1(c) and Fig. 3.1(d), the evolution rate of hardening variable $\bar{\alpha}$ is smaller less than the intact case. This is because the two degradation functions, $g(d^e)$ and $g(d^p)$, are active in the evolution laws of the rate of plastic deformation d^p and the hardening variable $\bar{\alpha}$ in Eq. (2.83)_{1,2}. While each case with $G_c = 500$ exhibits almost the same evolution tendency, the value of hardening variable $\bar{\alpha}$ becomes smaller with smaller plastic threshold Ψ_{cr}^p for the cases employing $G_c = 100$.

3.1.2 Parameter study for plastic damage coefficient ζ^p

Next, we explore the evolution tendencies of d^e and d^p by changing the plastic damage coefficient ζ^p . Fig. 3.2 shows the effect of the coefficient on the stress–total strain curves and the evolutions of the elastic and plastic damage variables and hardening variable with respect to the total strain. Again, two different values of the constant fracture toughness, $G_c = 100$ and $G_c = 500$, are used, while $\zeta^e = 1$ and $\Psi_{cr}^p = 50$ are employed for all the cases.

It can be seen from Fig. 3.2(a) and Fig. 3.2(b) that, as ζ^p is reduced from one, the curves after the stress drops become gentle. Particularly for some cases with relatively small values of the plastic damage coefficient ζ^p , the curves become downwardly concave. This is because smaller values of ζ^p are associated with smaller amounts of the plastic driving force and have been used for damage computation.

In the meantime, as can be seen from Fig. 3.2(c) and Fig. 3.2(d), the evolution tendencies of d^e and d^p are different from those in the previous investigations in Section 3.1.1. Specifically, only the cases with $\zeta^p = 1.0$ exhibit the same tendency of damage evolution as those of Fig. 3.1(c) and Fig. 3.1(d). For all the other cases, the evolution of d^p is slower than that of d^e because the increasing rates for the elastic and plastic damage variables are not the same: that is, $\lambda^f \zeta^e \chi^e \neq \lambda^f \zeta^p \chi^p$ reflecting the condition $\zeta^e = 1 > \zeta^p$. For instance, for the case “ $\zeta^p = 0.50$ ” corresponding to the blue dashed line in Fig. 3.2(c), when d^p reaches about 0.25

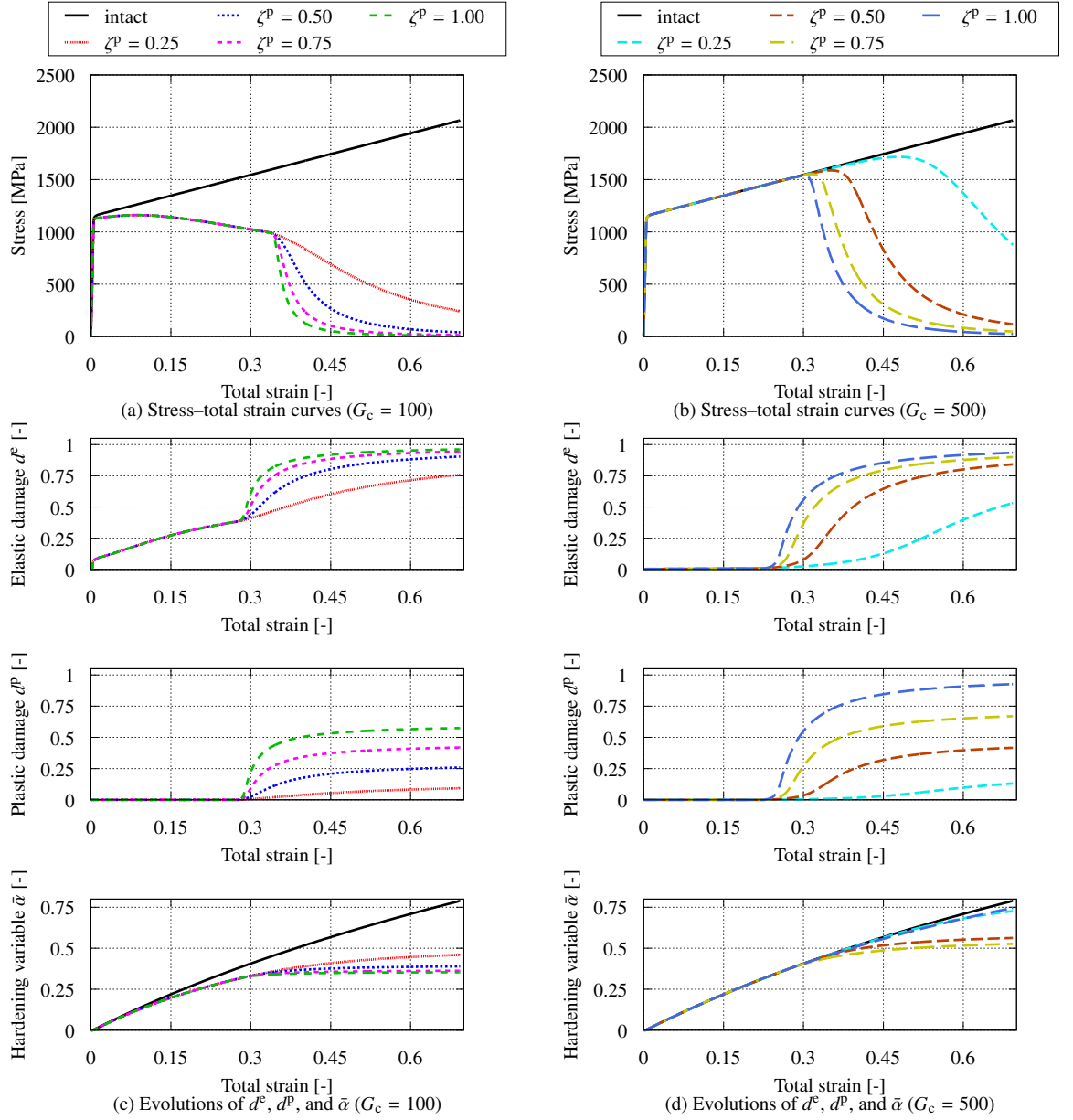


Fig. 3.2: Stress, damage variables, and hardening variable–total strain curves for the single square element: Comparisons of the value of coefficient ζ^p .

at a total strain 0.6, d^e has already reached about 0.85. It should be noted that d^p cannot reach one with the coefficient $\zeta^p < 1$. Still, this setup does not contradict the concept of the damage model, since $d^e \in [0, 1]$ is used to represent the actual material deterioration, as considered in Eq. (2.57) via the degradation function $g(d^e)$. On the other hand, in the concept of the crack

phase-field model, $d = 1$ represents the crack surfaces. In this context, it is reasonable to accept $d = d^e$ when considering actual phenomena even though d and d^e are independently determined in the present formulation. Otherwise, an inadequate stress transfer or unrealistic elastoplastic constitutive response would occur in the region where $d = 1$ but $d^e \neq 1$.

In the end, as can be seen from the last graphs in Fig. 3.2(c) and Fig. 3.2(d), for all the cases, the evolution rates of hardening variable $\bar{\alpha}$ are smaller than that of the intact case indicated by the black line. These results are similar to those in the previous parameter study shown in Section 3.1.1. However, while the value of hardening variable $\bar{\alpha}$ becomes smaller with larger plastic coefficient ζ^p for the cases with $G_c = 100$, a simple relation is not found for the cases with $G_c = 500$. This is because, for each case with different ζ^p , the evolution laws for the rate of plastic deformation d^p and hardening variable $\bar{\alpha}$ have nonlinear properties with respect to the degradation functions, $g(d^e)$ and $g(d^p)$, and the relationship between d^p and $\bar{\alpha}$ is also nonlinear as can be seen in Eq. (2.84).

3.1.3 Comparison of evolution laws

We compare the responses determined by the evolution laws employed in the proposed model and those employed in the previous studies^{(80),(83),(91)}. For the previous studies, the following relationships holds:

$$\left\{ \begin{array}{l} d^p = \lambda^p \frac{\tau_{0,\text{dev}}}{\|\tau_{0,\text{dev}}\|} \\ \dot{\bar{\alpha}} = \sqrt{\frac{2}{3}} \lambda^p \\ d^e = d^p = \dot{d} = \lambda^f \end{array} \right. \quad \text{with} \quad \left\{ \begin{array}{l} \lambda^p \geq 0, \quad \Phi^p \leq 0 \quad \text{and} \quad \lambda^p \Phi^p = 0 \\ \lambda^f \geq 0, \quad \Phi^f \leq 0 \quad \text{and} \quad \lambda^f \Phi^f = 0 \end{array} \right. . \quad (3.2)$$

Fig. 3.3 shows the stress–total strain, damage, and hardening variables–total strain curves, in which the prefix character “o” indicates the results obtained by using Eq. (3.2), while the curves with the prefix character “n” are obtained by the use of the evolution laws of the proposed model. Again, we consider two different values of constant fracture toughness, $G_c = 100$ and $G_c = 500$, and $\zeta^e = 1$ and $\zeta^p = 1$, for all the cases.

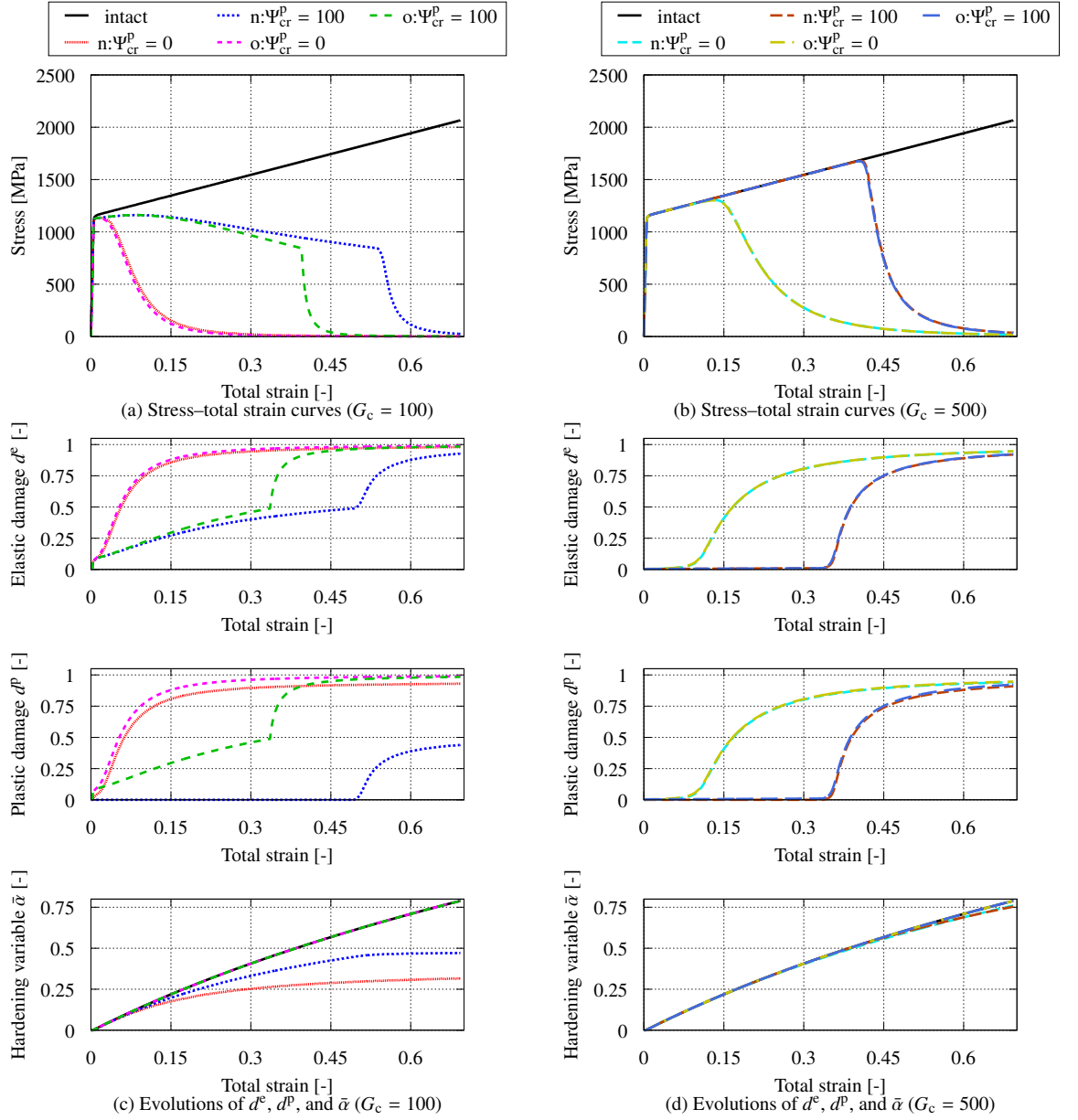


Fig. 3.3: Stress, damage variables, and hardening variable–total strain curves for the single square element: Comparisons of the evolution laws.

Fig. 3.3(a) shows the apparently different responses between the two sets of evolution laws. That is, the green dashed line indicated by “o: $\Psi_{cr}^p = 100$ ” exhibits a more rapid softening behavior than the blue dashed line indicated by “n: $\Psi_{cr}^p = 100$ ”. The difference is due to the different evolution laws for plasticity. Specifically, the damage evolution does not affect

the evolution of plastic strain or, equivalently, the plastic hardening variable in the evolution laws employed in the previous studies represented by Eq. (3.2). This is evidently shown in the last figure in Fig. 3.3(c). That is, the evolutions of the hardening variable for cases, “o: $\Psi_{cr}^p = 0$ ” and “o: $\Psi_{cr}^p = 100$ ”, are exactly the same as that without damage computation. Meanwhile, from the same figure, the other two cases “n: $\Psi_{cr}^p = 0$ ” and “n: $\Psi_{cr}^p = 100$ ” show more gentle evolutions of hardening variable. As explained in Section 3.1.1 and Section 3.1.2, these result from the damage variable-dependent evolution laws in Eq. (2.83)_{1,2}. Phenomenologically, the evolution laws of the proposed model appear to be physically reasonable since the cracked region does not have additional plastic deformation. On the contrary, in some existing models employing Eq. (3.2), the evolution of plastic deformation affects damage evolution, but the opposite does not hold. In short, even though $d \approx 1$, as shown in Fig. 3.3, a cracked region still exhibits plastic deformation, which is not physically reasonable.

On the other hand, as can be seen from Fig. 3.3(b) and Fig. 3.3(d), both sets of evolution laws lead to almost the same damage evolution regardless of the values of plastic damage threshold Ψ_{cr}^p . As described in Section 3.1.1, for the cases employing $G_c = 500$, the amount of elastic driving force is too small to contribute to the damage evolution. Therefore, we may conclude that when a fracture in the material under consideration exhibits severe dependency on plasticity or, equivalently when the damage evolution prior to the activation of the plastic driving force is small, the proposed model performs equivalently to the previous studies (80,83,91).

3.2 Exmample 3-2: Tensile failure of symmetrically notched specimen

The second example is devoted to demonstrating the ability of the proposed method to represent crack initiation and propagation in a two-dimensional structure. For that purpose, the symmetrically notched tensile specimen illustrated in Fig. 3.4 is taken as a target struc-

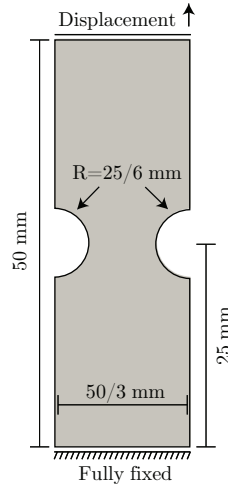


Fig. 3.4: Geometry and boundary conditions for the symmetrically notched specimen.

Table 3.2: Material parameters for the symmetrically notched specimen.

Parameter		Value	Unit
Young's modulus	E	200000	[MPa]
Poisson's ratio	ν	0.3	[-]
Strength coefficient	y_a	1169	[MPa]
Pre-strain parameter	α_b	0.0033	[-]
Hardening parameter	β_c	0.1	[-]
Plastic length scale parameter	l_p	0.2	[mm]
Penalty parameter	p_p	1000	[MPa]
Initial fracture toughness	G_{c0}	500	[N/mm]
Critical fracture toughness	$G_{c\infty}$	5	[N/mm]
Crack length scale parameter	l_f	0.2	[mm]

ture. A fine mesh having an element size of $h_e \approx 0.06$ is used for the potentially damaged region. In this particular example, the Swift hardening function $y_0 + \hat{H}(\bar{\alpha}) = y_a (\bar{\alpha} + \alpha_b)^{\beta_c}$ is adopted for the hardening behavior. The material properties and other parameters for damage computations are provided in Table 3.2. We consider five analysis cases listed in Table 3.3 with different sets of material parameters for the driving force and the degrading fracture toughness with the intention of indicating the likelihood of different crack patterns.

The load-displacement curves for five cases are shown in Fig. 3.5. First, let us discuss the

Table 3.3: Five cases under consideration for the symmetrically notched specimen.

Parameter	Case	I	II	III	IV	V	Unit
Elastic damage coefficient	ζ^e	1.0	1.0	1.0	1.0	1.0	[-]
Elastic damage threshold	Ψ_{cr}^e	0	0	0	0	0	[MPa]
Plastic damage coefficient	ζ^p	1.0	1.0	1.0	0.5	0.5	[-]
Plastic damage threshold	Ψ_{cr}^p	0	0	0	0	100	[MPa]
Saturation parameter	β_{G1}	10	15	15	10	5	[-]
Degradation threshold	α_{cr}	0	0	0	0	0	[-]
Slope parameter	p_1	2	2	2	2	2	[-]
Saturation parameter	β_{G2}	0.002	0.002	0.0025	0.002	0.002	[1/MPa]
Degradation threshold	τ_{cr}	300	300	300	300	800	[MPa]
Slope parameter	p_2	2	2	2	2	2	[-]

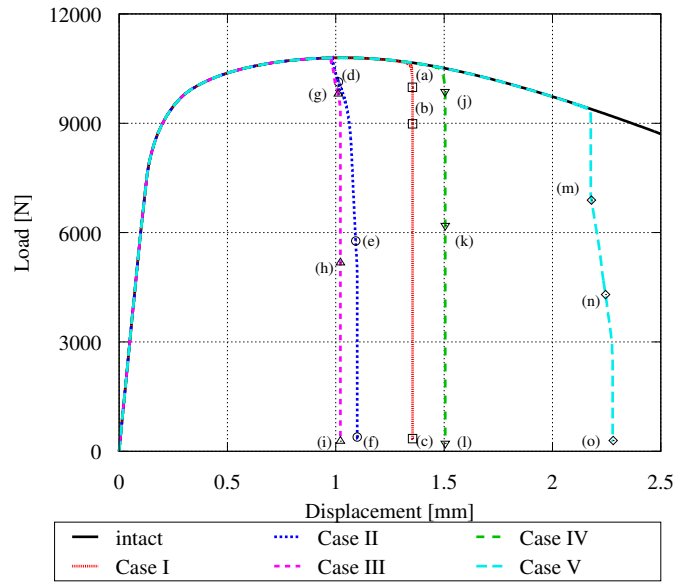


Fig. 3.5: Load-displacement curves for the symmetrically notched specimen.

results for the first three cases, for which the detailed evolutions of elastic & plastic damage variables and degrading fracture toughness are shown in Fig. 3.6, Fig. 3.7, and Fig. 3.8, respectively. For Case I, a slanted crack path is observed. Specifically, the crack initiates from the two notch surfaces, and these initial cracks propagate to form a single crack path. It is instructive that a similar crack propagation behavior is reported in Yin & Kaliske⁸⁵). Mean-

while, with a larger saturation parameter β_{G1} for $\bar{\alpha}$, a different crack path is found for Case II. That is, the crack initiates from the middle of two notch surfaces and propagates horizontally toward the center of the specimen. This is because the accumulation of plastic strain is first concentrated near the notch surfaces. Also, the material can sustain only a small amount of deformation before crack initiation due to the larger saturation parameter β_{G1} compared to Case I. In addition, as can be seen from Fig. 3.7(f), the leftward crack propagates in an oblique direction because the accumulation of plastic strain is distributed in that direction. This tendency is also reported in Ambati et al. ⁷⁷⁾, Miehe et al. ⁸⁰⁾, and Aldakheel et al. ⁸⁹⁾ with a smaller notch size or a different notch geometry. Here, the asymmetric crack patterns are due to numerical errors. Moreover, with a larger value for the saturation parameters β_{G2} and β_{G1} , the crack path for Case III tends to be straight, as shown in Fig. 3.8(i). This is due to the degrading effect of fracture toughness produced by the negative hydrostatic pressure. To be specific, the value of $\beta_{G2}\tau_p^*$ is larger near the center of the specimen than in other regions, as can be found by comparing the center of the specimen in Fig. 3.9(e) and (h).

On the other hand, Fig. 3.10 and Fig. 3.11 show the detailed evolutions of the elastic & plastic damage variables and degrading fracture toughness for Cases IV & V, respectively. For both of these two cases, the plastic damage driving force is decreased, and the degrading effect of fracture toughness is lowered. Specifically, a smaller plastic damage coefficient $\zeta^p = 0.5$ is given for Case IV compared to Case I. Also, in addition to ζ^p , a plastic damage threshold Ψ_{cr}^p , a smaller saturation parameter β_{G1} , and a larger degradation threshold τ_{cr} are given for Case V. As can be seen in Fig. 3.10 and Fig. 3.11, slanted crack paths are observed similar to Case I in Fig. 3.6, but the crack initiation mechanism is different. Indeed, the current two cases provide shear band-induced cracks; that is, the specimen first shows a necking behavior, then forms a shear band, and the crack eventually initiates from the center of the specimen, as explained in Han et al. ⁹¹⁾ with experimental investigations. For instance, as can be seen from Fig. 3.10 obtained for Case IV, a distinctive crack initiates at the center of the specimen and propagates at an angle to form a slanted crack path. It is worth mentioning that similar failure characteristics are also found in Ambati et al. ⁷⁷⁾ and Aldakheel et al.

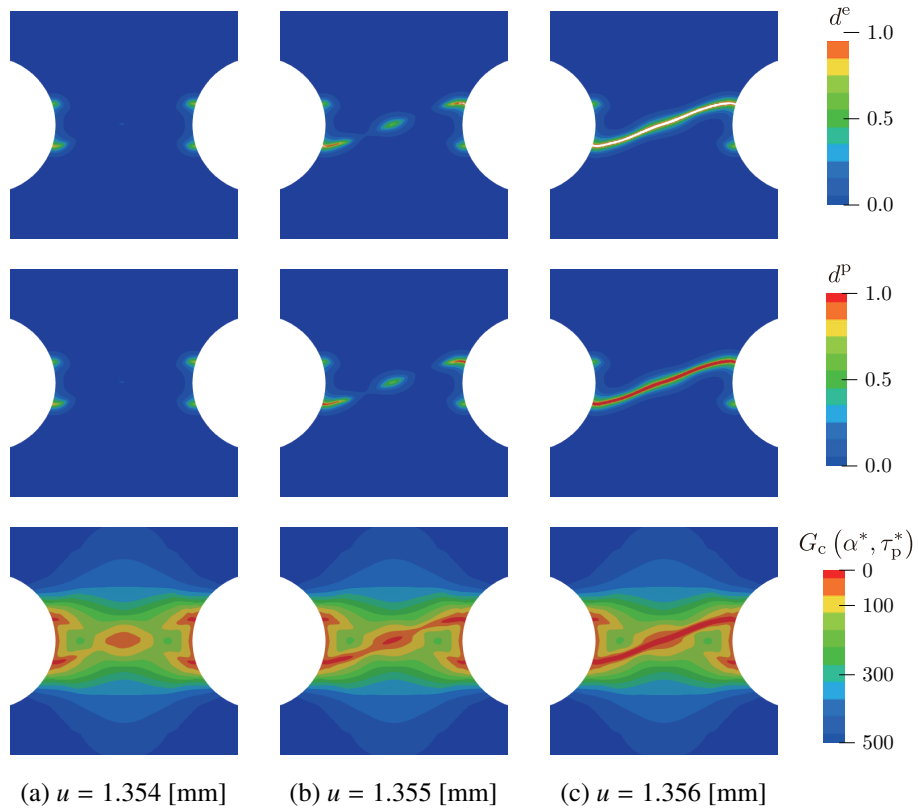


Fig. 3.6: Detailed evolution of elastic & plastic damage variables and degrading fracture toughness: Case I.

⁸⁹⁾. Meanwhile, this type of failure mechanism is also applied to Case V. However, since the plastic damage driving force or the degrading effect of fracture toughness is decreased, the crack propagates horizontally to some extent and then bends obliquely. Also, the crack propagation tends to be more stable than the previous four cases, which can be observed from the load-displacement curves in Fig. 3.11 as well as the values of displacement in Fig. 3.6, Fig. 3.7, Fig. 3.8, and Fig. 3.10. Although the crack path is not symmetrical due to the numerical errors, the proposed model is expected to reproduce a crack path similar to a cup-cone-like failure thanks to the novel degrading fracture toughness involving the effect of stress triaxiality. Therefore, it is safe to conclude that the proposed model is regarded as a unification of the existing CPFMs and can mimic various fracture behavior of elastoplastic materials by adjusting the parameters related to damage.

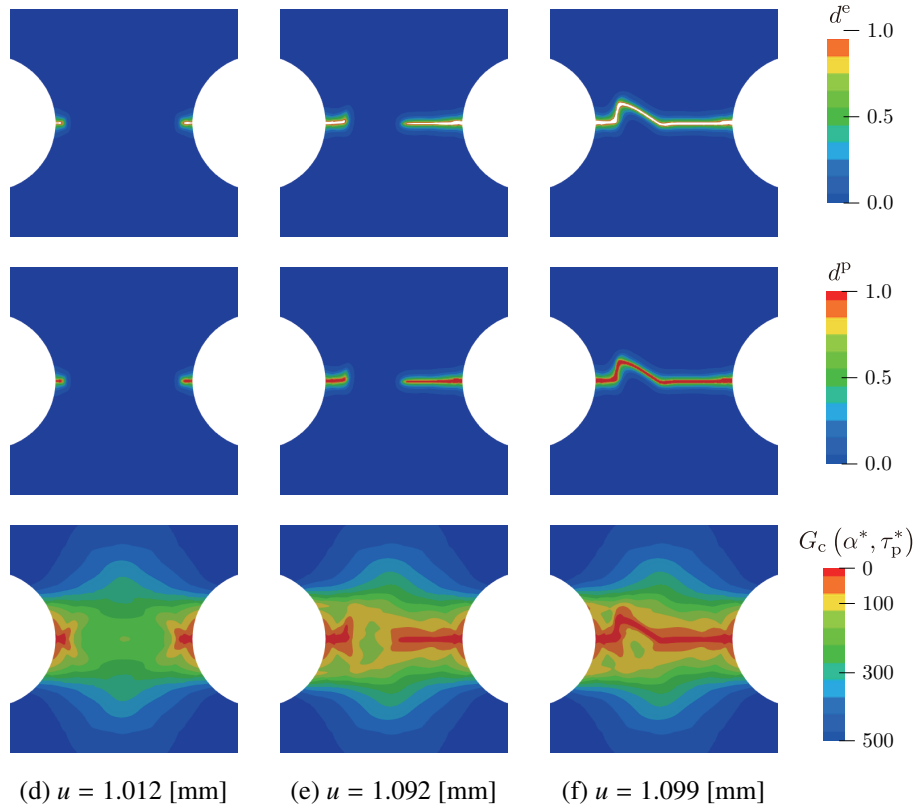


Fig. 3.7: Detailed evolution of elastic & plastic damage variables and degrading fracture toughness: Case II.

3.3 Exmample 3-3: Cup-cone failure of notched round bar

The third example aims to realize the “cup-cone” failure of a notched round bar (NRB) subjected to tensile loading. The geometry information with boundary conditions is illustrated in Fig. 3.12, and the experimental result is borrowed from Li et al. ¹⁶⁹⁾. We conduct numerical simulations for a 1/8 model to account for the symmetry of the NRB, and a fine mesh having an element size of $h_e \approx 0.07$ [mm] is used for the potentially damaged region. In this particular example, the Swift hardening function $y_0 + \hat{H}(\bar{\alpha}) = y_a (\bar{\alpha} + \alpha_b)^{\beta_c}$ is adopted for the hardening behavior. The material properties are provided in Table 3.4, in which those for elastoplastic deformation are also taken from Li et al. ¹⁶⁹⁾. To demonstrate the characteristic feature of the proposed model, we consider three analysis cases listed in Table 3.5 with different sets of material parameters for the damage driving forces and degrading fracture

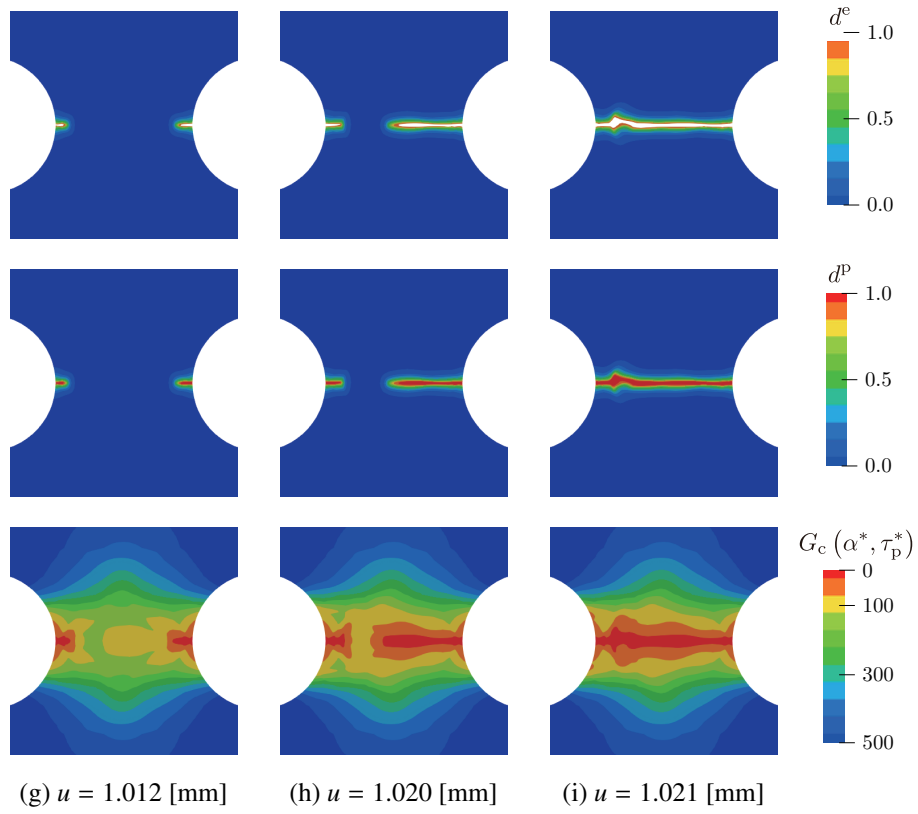


Fig. 3.8: Detailed evolution of elastic & plastic damage variables and degrading fracture toughness: Case III.

Table 3.4: Material parameters for the notched round bar.

Parameter		Value	Unit
Young's modulus	E	68900	[MPa]
Poisson's ratio	ν	0.33	[-]
Strength coefficient	y_a	561	[MPa]
Pre-strain parameter	α_b	0.015	[-]
Hardening parameter	β_c	0.11	[-]
Plastic length scale parameter	l_p	0.10	[mm]
Penalty parameter	p_p	1000	[MPa]
Initial fracture toughness	G_{c0}	20	[N/mm]
Critical fracture toughness	$G_{c\infty}$	0.50	[N/mm]
Crack length scale parameter	l_f	0.15	[mm]

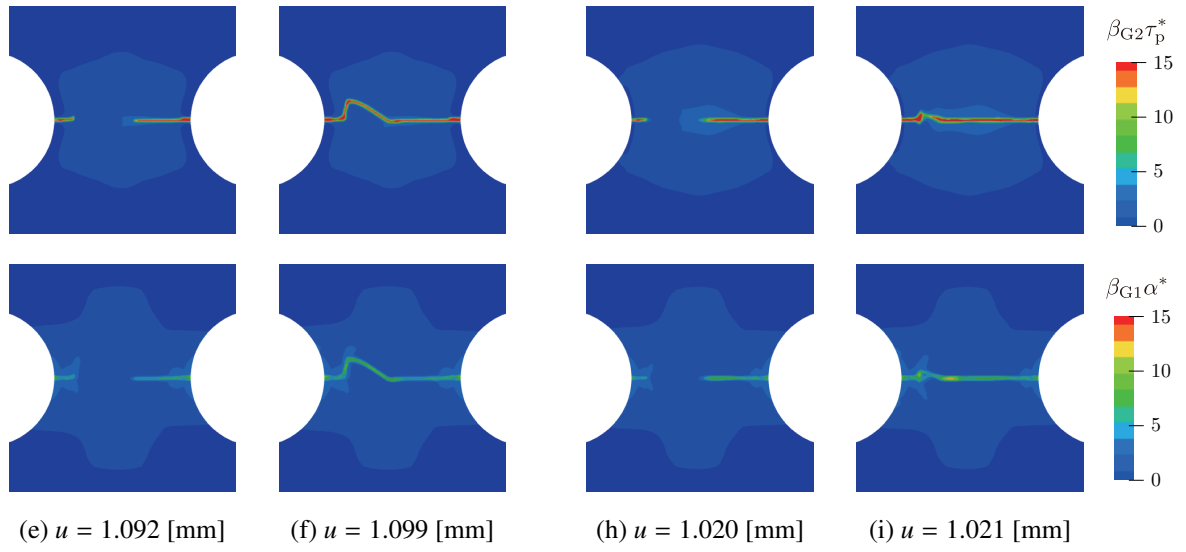


Fig. 3.9: Detailed evolution of parameters, $\beta_{G2}\tau_p^*$ and $\beta_{G1}\alpha^*$, in degrading fracture toughness: Case II and Case III.

Table 3.5: Three cases under consideration for the notched round bar.

Parameter	Case	I	II	III	Unit
Elastic damage coefficient	ζ^e	1.0	1.0	1.0	[-]
Elastic damage threshold	Ψ_{cr}^e	0	0	0	[MPa]
Plastic damage coefficient	ζ^p	1.0	0.75	0.50	[-]
Plastic damage threshold	Ψ_{cr}^p	0	6.5	10	[MPa]
Saturation parameter	β_{G1}	20	20	20	[-]
Degradation threshold	α_{cr}	0	0.005	0.005	[-]
Slope parameter	p_1	3	2	1	[-]
Saturation parameter	β_{G2}	0.02	0.02	0.02	[1/MPa]
Degradation threshold	τ_{cr}	450	450	450	[MPa]
Slope parameter	p_2	1	1	1	[-]

toughness.

Fig. 3.13 shows the load-displacement curves, where the experiment result (Exp.¹⁶⁹), a simulation result without damage (Intact), and three simulation results (Cases I~III) with damage are provided. Here, the value of displacement is taken at half the height of the

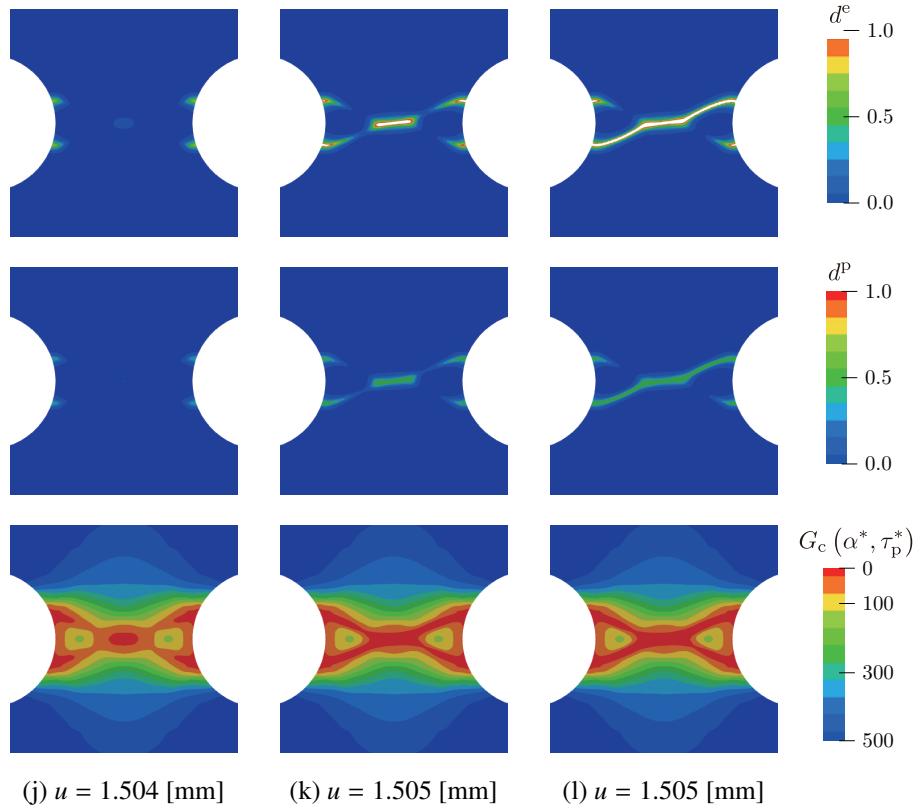


Fig. 3.10: Detailed evolution of elastic & plastic damage variables and degrading fracture toughness: Case IV.

1/8 model so that it is equivalent to the gauge displacement measured in the experiment. As shown in this figure, the curve of Case II is in agreement with experiment one, which shows a rapid drop of load as soon as the gauge displacement reaches $u \approx 0.57$ [mm]. Meanwhile, Case I & Case III exhibit hastened and delayed drops of load compared to Case I, respectively. This is because the plastic damage threshold & coefficient are not given (or set $\Psi_{cr}^p = 0$ & $\zeta^p = 1.0$) for Case I, and the threshold/coefficient is larger/smaller for Case III than Case II, as shown in Table 3.5. In short, the effect of plastic deformation contributing to damage evolution is reduced in the order of Case I, II, and III.

Fig. 3.14, Fig. 3.15, and Fig. 3.16 show the detailed evolutions of elastic & plastic damage variables, degrading fracture toughness along with two different cosine functions in Eq. (3.1). From the distribution of the elastic damage variable d^e , Case I & Case II show a typ-

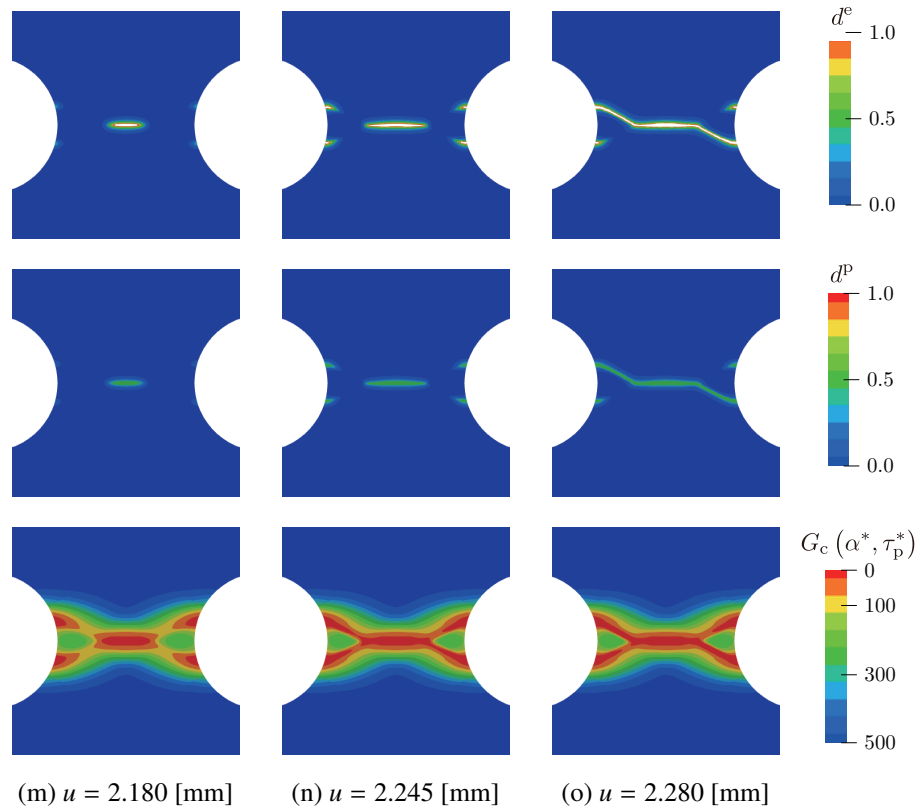


Fig. 3.11: Detailed evolution of elastic & plastic damage variables and degrading fracture toughness: Case V.

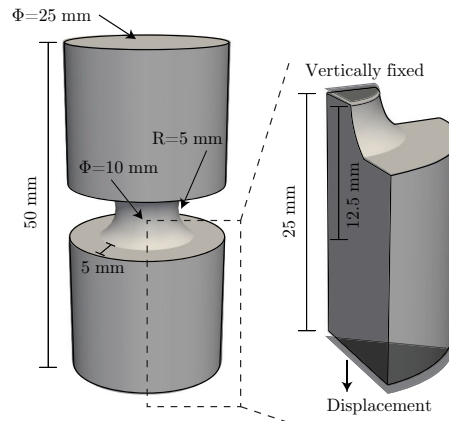


Fig. 3.12: Geometry and boundary conditions for the notched round bar.

ical failure mechanism in cup-cone failure, while Case III has an almost flat crack surface. Specifically for the first two cases, the crack initiates from the center of the NRB, which is

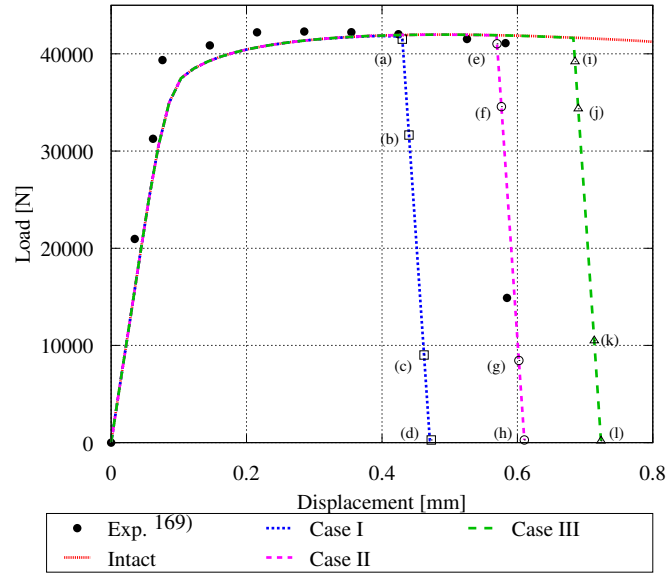


Fig. 3.13: Load-displacement curves for the notched round bar.

caused by both the plastic deformation and the negative hydrostatic pressure; see the distributions of two cosine functions $\cos^{p_1}(\beta_{G1}\alpha^*/2)$ & $\cos^{p_2}(\beta_{G2}\tau_p^*/2)$ in Fig. 3.14(a) and Fig. 3.15(e). Subsequently, as the crack propagates toward the surface of the NRB, the effect of the plastic deformation-induced damage becomes more prominent than that of the negative hydrostatic pressure-induced damage, as shown in Fig. 3.14(c) and Fig. 3.15(g). Thus, the crack eventually becomes inclined. Meanwhile, the slant cracked region becomes less distinctive in the order of Case I, II, and III. This is because some parameters in Table 3.5 are set to reduce the plastic damage driving force in this order. Therefore, we conclude that the proposed model can control the relative degree of contribution of damage driving forces caused by plastic deformation and the negative hydrostatic pressure.

In addition, for better visualization, the crack surface of cup-cone failure is shown in Fig. 3.17, where the region having $d^e \leq 0.99$ is removed, and the outline reveals the fractured geometry of the NRB. The crack surface is in agreement with the experimental one reported in Li et al. ¹⁶⁹⁾, and therefore, we may argue that the proposed model is able to reproduce the actual failures of elastoplastic materials.

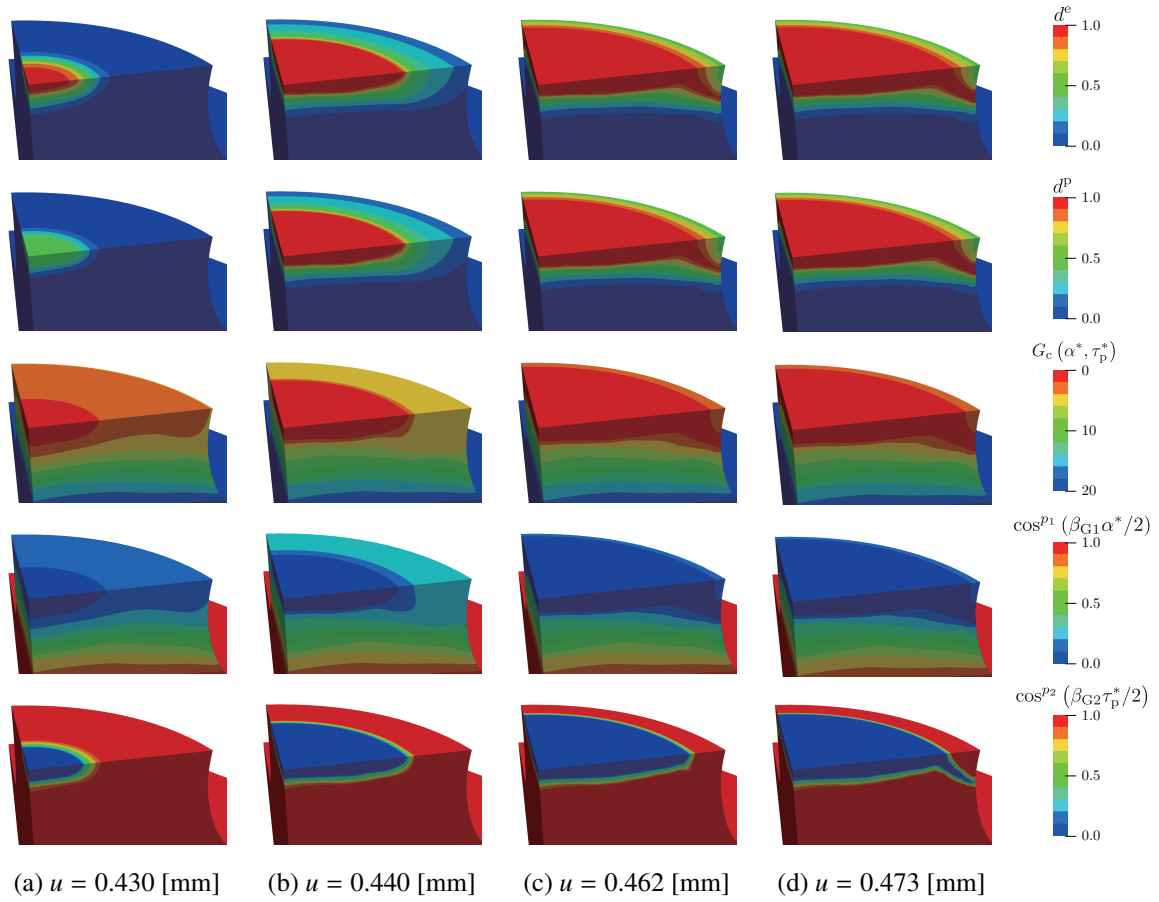


Fig. 3.14: Detailed evolutions of elastic & plastic damage variables, degrading fracture toughness, and two cosine functions: Case I.

3.4 Exmample 3-4: Tensile failure of notched specimens (AHSS sheet)

This section is devoted to demonstrating the ability of the proposed model to predict the breaking elongation, the transitional behavior from unstable to stable crack propagations, the load-displacement curves, and the crack initiation positions for single notched specimens subjected to tensile loading. The numerical results are compared with the experimental ones obtained by the corresponding tensile tests ¹⁵¹⁾ we have conducted for the purpose of verification.

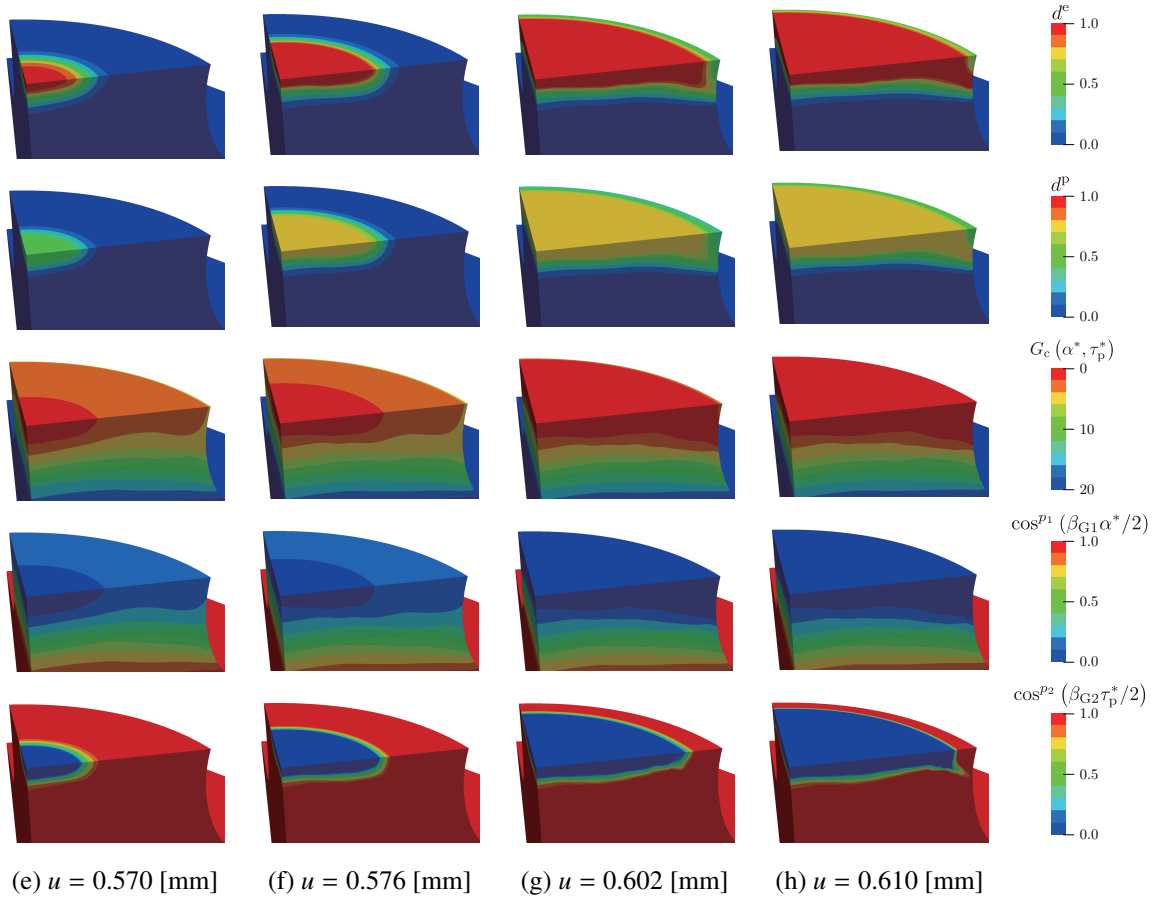


Fig. 3.15: Detailed evolutions of elastic & plastic damage variables, degrading fracture toughness, and two cosine functions: Case II.

3.4.1 Experimental setup and classification of crack growth behavior

A specimen is made of advanced high strength steel sheet (AHSS sheet) “JSC1180” or “JSC980”. Here, the number after “JSC” refers to its tensile strength in MPa units. The appearance of the experimental setup is shown in Fig. 3.18(a), in which the specimen is fixed to the tension testing machine (MTS-810) by two jigs. Photos are taken by a high-speed camera (NAC MEMRECAM AC-1) and a CCD camera (Ximea MQ042MG-CM), focusing on the region where the crack initiates and propagates. As illustrated in Fig. 3.18(b), two specimens with different notch geometries ($R = 5.0$ [mm] and $R = 0.5$ [mm]) are used, and the dark-gray region outside the parallel portion is sandwiched by two plate-like jigs.

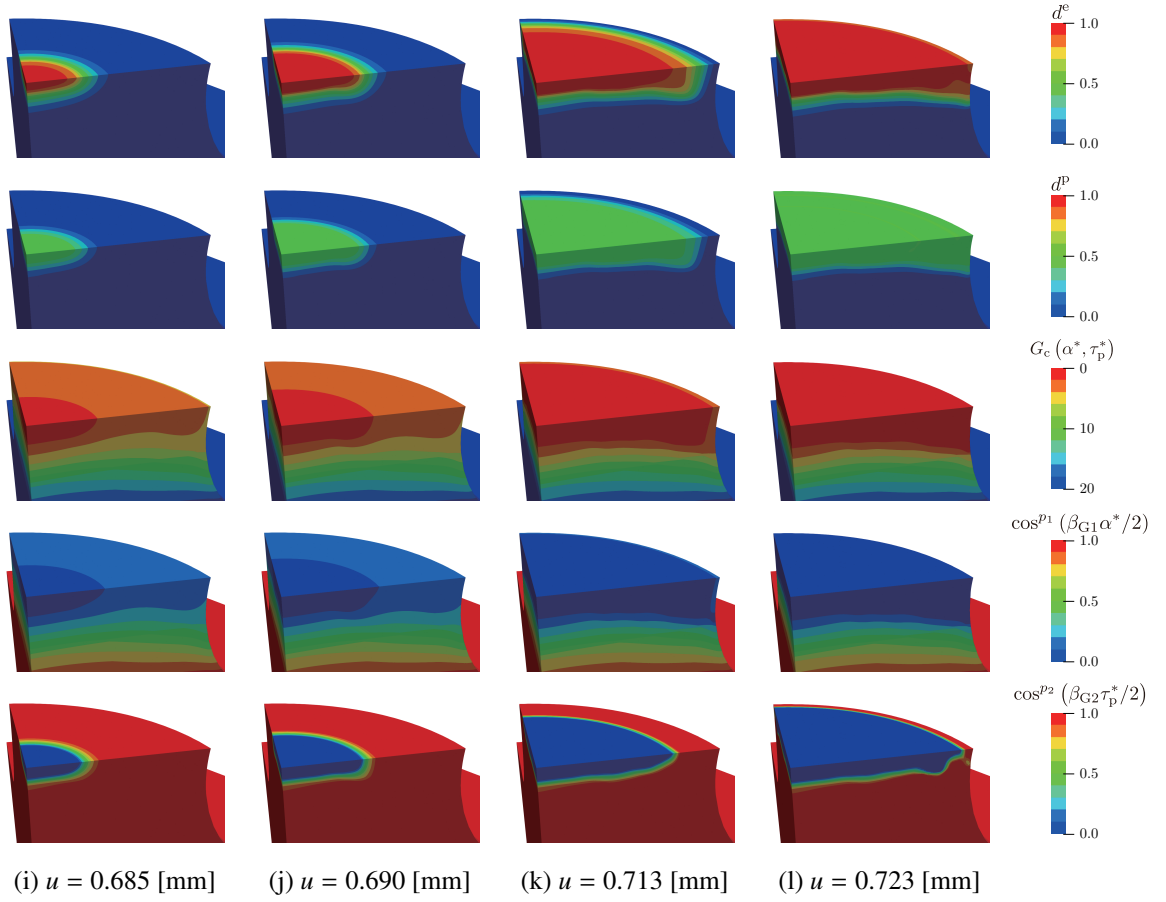


Fig. 3.16: Detailed evolutions of elastic & plastic damage variables, degrading fracture toughness, and two cosine functions: Case III.

During experiments, a rate of forced displacement of $1/6$ [mm/s] is applied to the entire surface of the topside jigs, while the downside jigs are immovably fixed; hereafter, this forced displacement is called “stroke displacement” and is denoted by u_s . On the other hand, the relative displacement between the two points shown in Fig. 3.18(b), which is measured by the CCD camera, is called “gauge displacement” and denoted by u_g .

In general, crack propagation behavior can be classified into two states: “stable” and “unstable”¹⁷⁰⁾. These can be used to classify the observed crack growth behavior in the experiments described above. When the crack growth does not continue without any external energy supply, it is called “stable crack propagation”, in which the crack resistance increases with crack propagation (R-curve). Since the speed of stable crack growth is relatively slow,

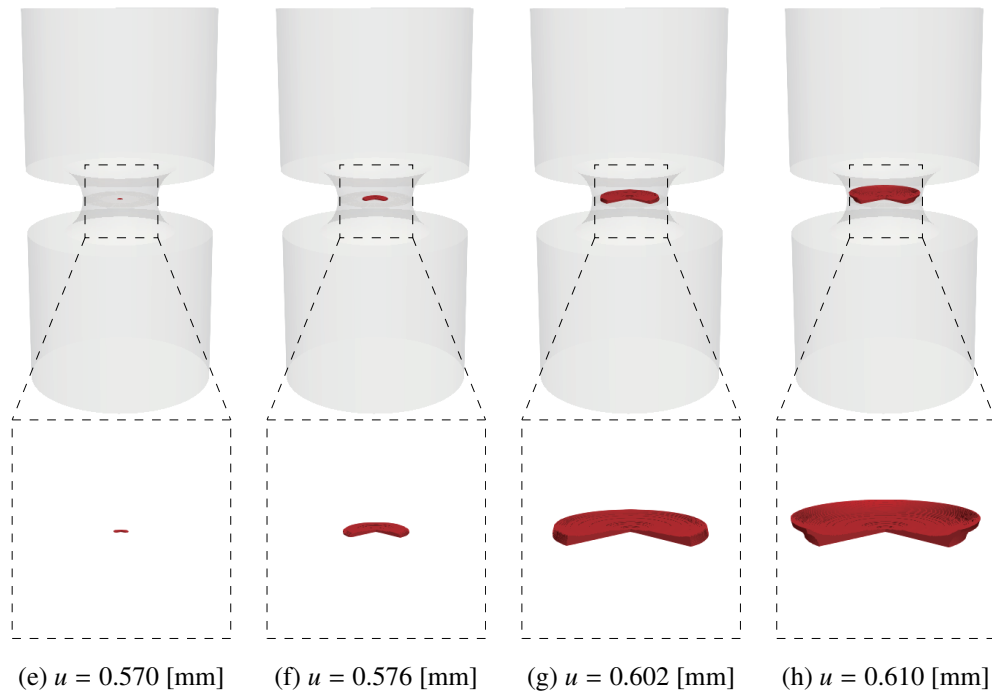


Fig. 3.17: Crack propagation of the NRB: Case II (The region having $d^c \leq 0.99$ is removed, and only the 3/4 crack surface is shown).

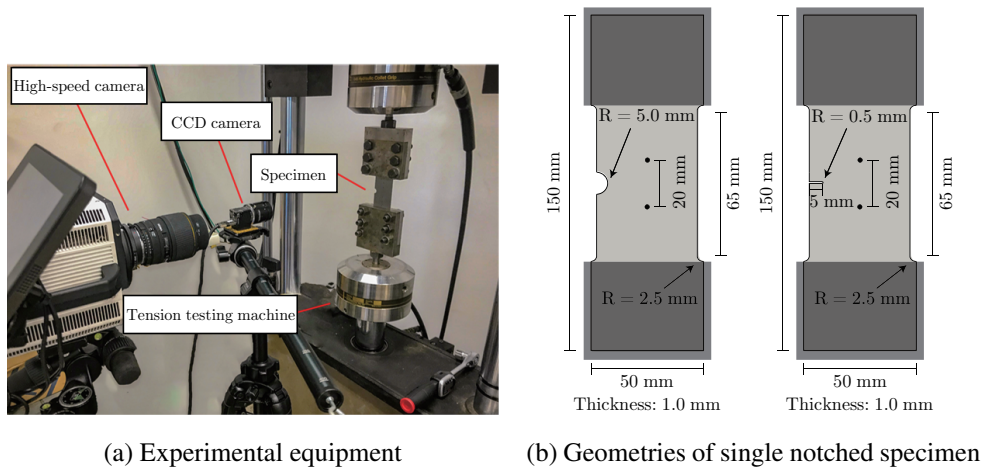


Fig. 3.18: Experimental setup for single notched specimen.

the kinetic energy component may be insignificant. On the other hand, when the crack grows without any external energy supply, it is called “unstable crack propagation”. The material acquires kinetic energy from the inertia of the material surrounding the rapidly separating

crack walls ¹⁷¹⁾. In such dynamic cases, the static equilibrium conditions of Griffith and Irwin-Orowan no longer apply. Subsequent theoretical works done by Mott ¹⁷²⁾, Yoffe ¹⁷³⁾, and Broberg ¹⁷⁴⁾ extended Griffith's concept by adding the kinetic energy term in the expression of the total energy balance and exploring the terminal velocity in linear elastodynamics. Also, see Reference ¹⁷⁵⁾.

From the above-described perspective, the crack propagation speed is a possible indicator for the purpose of classification. In our measurement, the shutter speed of the CCD camera is set at five fps, and one point for a load-displacement curve is plotted in every frame. In the following discussions, whether a crack growth is stable or unstable will be determined by the clearance between two adjacent points in the load-displacement curve, which corresponds to 0.2 seconds. That is, if the clearance is sufficiently large so that curve plotted by points looks discontinuous, then the crack growth is regarded as an "unstable" state. Otherwise, it represents a "stable" crack propagation.

3.4.2 Experimental result

First, we summarize the experimental results for JSC1180. Fig. 3.19 shows the load-displacement curves and snapshots of crack growths for the specimens with notch radii of $R = 5.0$ [mm] and $R = 0.5$ [mm], respectively. Here, the black and gray plots in Fig. 3.19(a) and (b) indicate the gauge and stroke displacements, respectively. As can be seen from these figures, a characteristic response is observed for each of the specimens. Specifically, the load suddenly drops after the peak. During this decrease in load, the gauge displacement increases significantly from $u_g \approx 0.37$ [mm] to $u_g \approx 1.31$ [mm] for the specimen with $R = 5.0$ [mm] and $u_g \approx 0.24$ [mm] to $u_g \approx 1.05$ [mm] for the specimen with $R = 0.5$ [mm], while the stroke displacements u_s hardly increase. These tendencies result from the crack initiation and subsequent rapid growth, as can be recognized from Fig. 3.19(c) and (d). Thus, the crack propagation can be categorized as an unstable crack growth. To be specific, within the time interval (about 0.2 seconds) starting from (C) to (D) for $R = 5.0$ [mm] specimen and (I) to (J) for $R = 0.5$ [mm] specimen, the crack initiates near the notch, propagates horizontally to

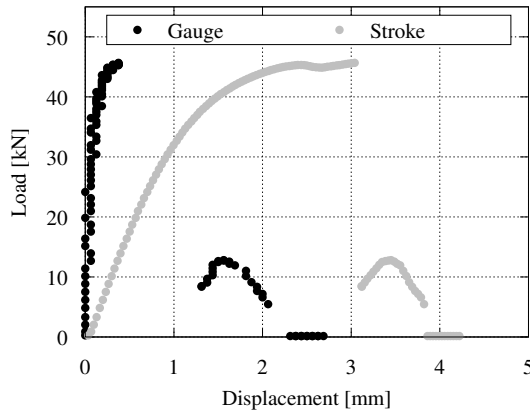
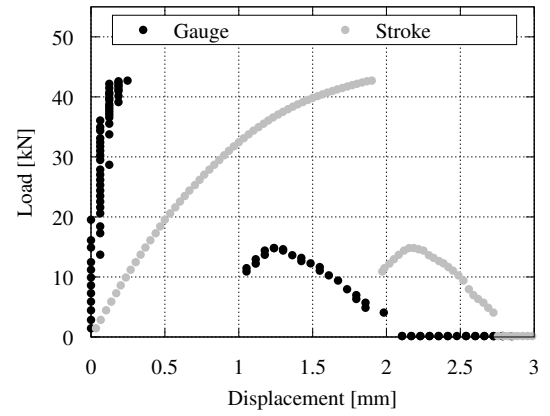
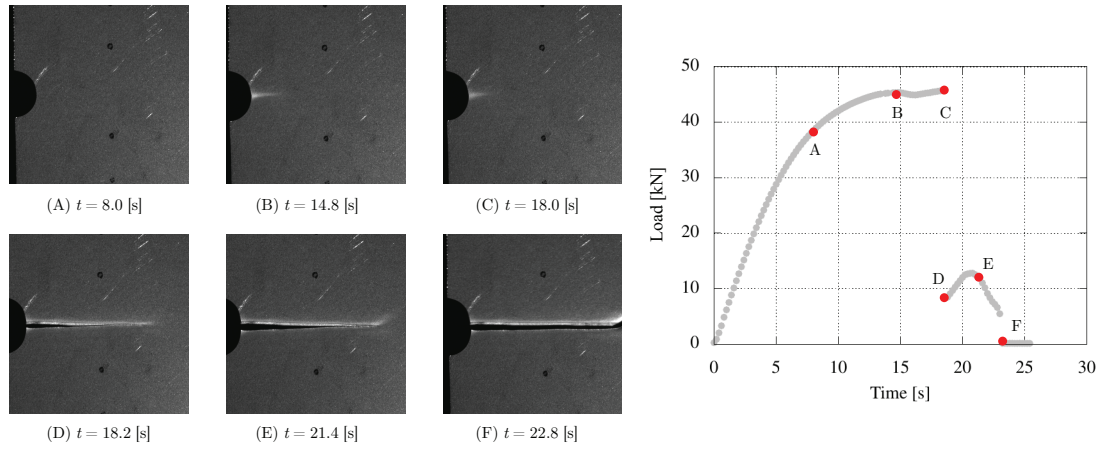
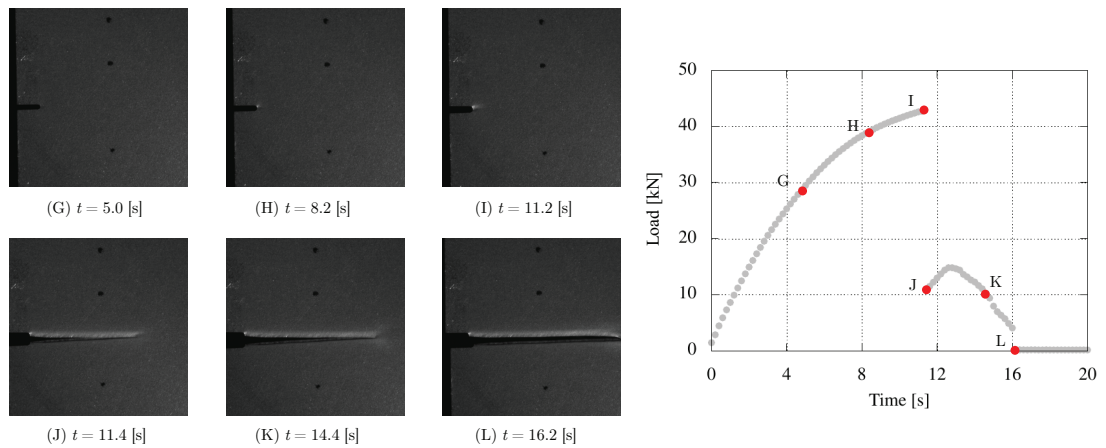
(a) Load-displacement curves for $R = 5.0$ [mm](b) Load-displacement curves for $R = 0.5$ [mm](c) Crack growth in time series for $R = 5.0$ [mm](d) Crack growth in time series for $R = 0.5$ [mm]

Fig. 3.19: Experimental results for JSC1180.

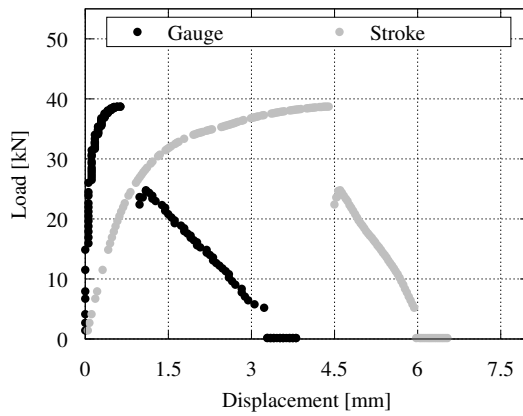
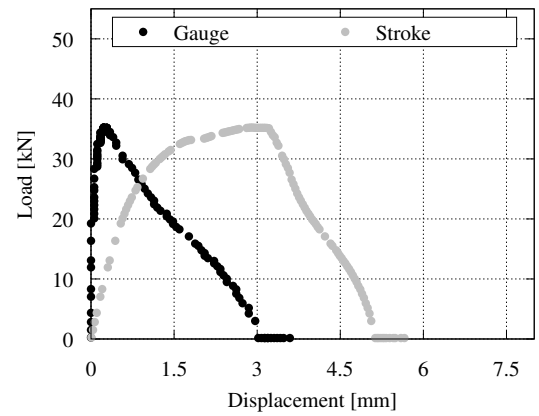
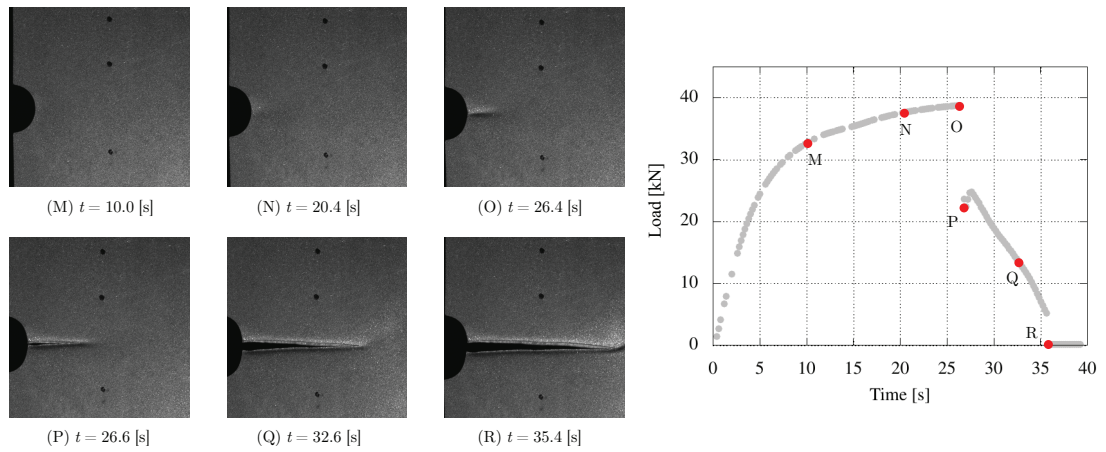
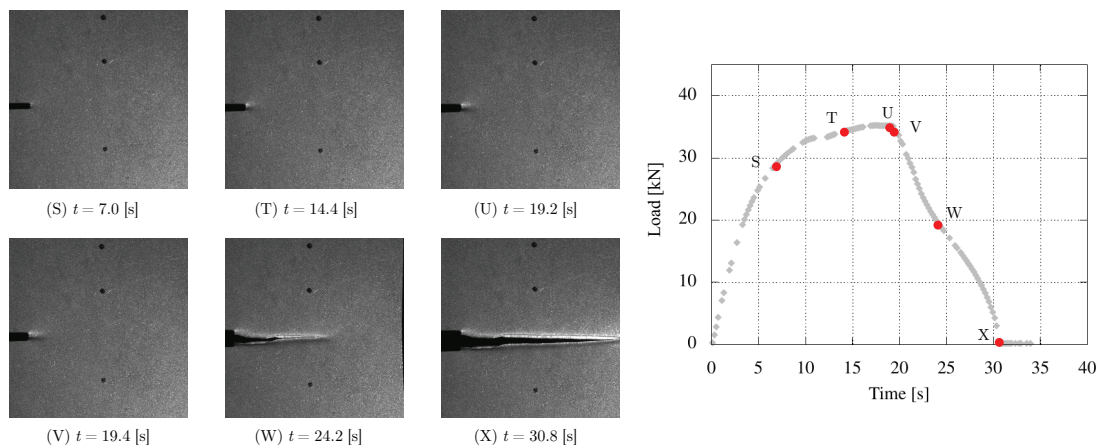
(a) Load-displacement curves for $R = 5.0$ [mm](b) Load-displacement curves for $R = 0.5$ [mm](c) Crack growth in time series for $R = 5.0$ [mm](d) Crack growth in time series for $R = 0.5$ [mm]

Fig. 3.20: Experimental results for JSC980.

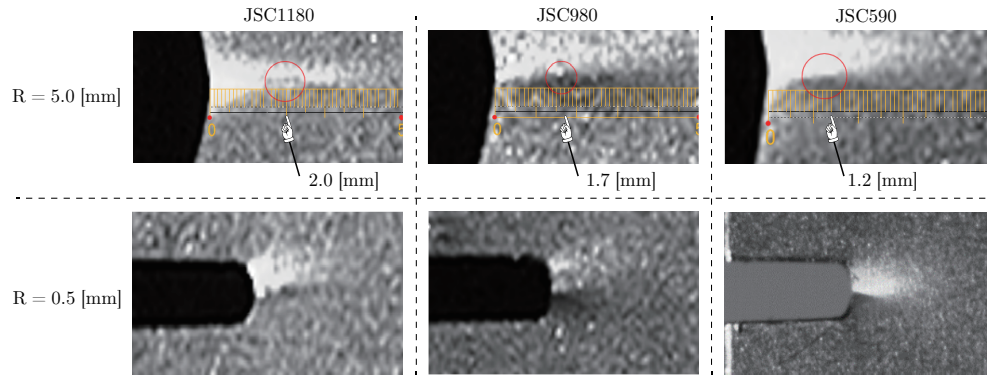


Fig. 3.21: Various crack initiation positions depending on different tensile strength and notch geometry.

the right and stops at about 3/4 of the width of specimen.

After the first unstable crack growth, a relatively stable crack growth is observed until each of the two specimens is finally broken. That is, the load versus stroke and gauge displacements show almost the same tendency right after the peak load. During the stable crack growth, the load attains “the second peak” for both cases. This is surely due to the rotation of jigs since it allows the specimen to bend along with the crack growth. In fact, Fig. 3.19(c) and (d) show that the specimen is moving horizontally to the left; see the transitions from (C) to (D) and (I) to (J). As the bending mode reduces the effect of tensile loading around the right portion, it is considered that an increase in tensile load is required for subsequent crack propagation.

Next, let us describe the experimental results for JSC980. As for the case with JSC1180, Fig. 3.20 shows the load-displacement curves and snapshots of crack growths for the specimens with two different notch radii. It should be noted here that, unlike JSC1180, JSC980 shows different tendencies depending on the notch radius. That is, for the larger notch radius ($R = 5.0$ [mm]), unstable crack growth is confirmed like the results for JSC1180, while the $R = 0.5$ [mm] specimen reveals a stable crack propagation throughout the experiment. Specifically, as can be seen from Fig. 3.20(a) and (b), a rapid drop in the load is observed for $R = 5.0$ [mm] but not for $R = 0.5$ [mm]. These tendencies are also evident in the photos in Fig. 3.20(c) and (d). To be more specific, in the case of $R = 5.0$ [mm], the crack initiates and

propagates horizontally to the right until it extends to about 1/3 of the width of the specimen within the 0.2 seconds; see the transition from (O) to (P). On the other hand, from (U) to (X), such a rapid crack growth does not appear, and only a gradual crack propagation is observed. It can be inferred from these results that the notch radius is also an influential factor in the crack growth behavior as well as the tensile strength.

Additionally, the crack initiation positions for the four test cases should be noted. The photographs in Fig. 3.21 show the enlarged views near the notches right after crack initiation. Here, we have added the results of two JSC590 specimens with the same set of notch radii, both of which were confirmed to exhibit stable crack growths. As can be seen from these photos, the position of crack initiation varies depending on both the tensile strength and notch radius. To be specific, in the case of the specimens with a larger notch radius, the crack initiates inside the specimen, and a higher tensile strength tends to be associated with the crack initiation occurring at a position away from the tip of the notch. This difference in crack initiation position is probably due to the difference in the relative magnitude of failure resistances against the plastic deformation and the negative hydrostatic pressure. Detailed discussions will be made later, along with numerical investigations. Meanwhile, the crack initiation position in the specimen with a notch radius of $R = 0.5$ [mm] hardly can be identified from the photos in Fig. 3.21 and therefore would be a suitable target for prediction by the proposed model.

3.4.3 Exemplification

To exemplify the performance of the proposed model, we first identify the material parameters in the employed elastoplastic constitutive law. For that purpose, tensile tests were conducted on an I-shaped flat specimen made of JSC1180 and JSC980 using the same testing machine. Fig. 3.22(a) shows the experimentally obtained relationships between the true stress and equivalent plastic strain (drawn with black and gray markers) that have been converted from the relationships between the load and gauge displacement. By conducting calibration, we determined the material parameters as provided in Table 3.6 and obtained

Table 3.6: Material parameters for single notched specimens.

Parameter		Value	Unit
JSC1180			
Young's modulus	E	196500	[MPa]
Poisson's ratio	ν	0.27	[-]
Strength coefficient	y_a	1828	[MPa]
Pre-strain parameter	α_b	0.00053	[-]
Hardening parameter	β_c	0.11	[-]
Initial fracture toughness	G_{c0}	2000	[N/mm]
Critical fracture toughness	$G_{c\infty}$	10	[N/mm]
Crack length scale parameter	l_f	0.6	[mm]
JSC980			
Young's modulus	E	196600	[MPa]
Poisson's ratio	ν	0.28	[-]
Strength coefficient	y_a	1572	[MPa]
Pre-strain parameter	α_b	0.00055	[-]
Hardening parameter	β_c	0.14	[-]
Initial fracture toughness	G_{c0}	2000	[N/mm]
Critical fracture toughness	$G_{c\infty}$	10	[N/mm]
Crack length scale parameter	l_f	0.6	[mm]
Pseudo-arm			
Young's modulus	E	210000	[MPa]
Poisson's ratio	ν	0.30	[-]

the fitted curves (the red and blue solid lines) in the same figure. Here, the Swift hardening function $r^p(\alpha) = y_a(\alpha_b + \alpha)^{\beta_c}$ is adopted for the hardening behavior of plastic deformation, and local plasticity is adopted in this example.

As can be seen from Fig. 3.19 or Fig. 3.20, the stroke displacement is much larger than the gauge displacement, which indicates the stiffness of the testing machine is evidently reflected. It should also be noted that the bending of specimens is accompanied by the rotation of jigs. Thus, both the stiffness and rotational effects should be taken into account

Table 3.7: Two cases under consideration for single notched specimens.

Parameter	Case	JSC980	JSC1180	Unit
Elastic damage coefficient	ζ^e	1.0	1.0	[-]
Elastic damage threshold	Ψ_{cr}^e	0	0	[MPa]
Plastic damage coefficient	ζ^p	0.0	0.0	[-]
Plastic damage threshold	Ψ_{cr}^p	$+\infty$	$+\infty$	[MPa]
Saturation parameter	β_{G1}	8.5	11	[-]
Degradation threshold	α_{cr}	0	0	[-]
Saturation parameter	β_{G2}	0.008	0.008	[1/MPa]
Degradation threshold	τ_{cr}	400	400	[MPa]

in our numerical simulations so that both the load versus the stroke and gauge displacements individually coincide with experimental results using the same set of material parameters. Otherwise, the relationship between the load and time would become unrealistic because the tensile loading (forced displacement) is in accord with time advance. However, modeling the actual jigs and other parts of the testing machine is not only unnecessarily cumbersome but also computationally expensive. Thus, to accommodate those effects, a “pseudo-arm” is attached to each of the ends of the numerical model of the specimen as shown in Fig. 3.22(b) along with the boundary conditions. This pseudo-arm is assumed to be a purely elastic material, and Young’s modulus and Poisson’s ratio are arbitrarily set at 210 GPa and 0.3. Then, its geometry is determined by trial and error so that the numerical results can reasonably be consistent with the experimental ones provided in Fig. 3.19(a) & (b) and Fig. 3.20(a) & (b) for all four cases. The fitted curves are shown in Fig. 3.22(c) for the purpose of comparison with the experimentally obtained curves. Note here that no damage computations have been conducted in this calibration process.

Next, the material parameters for damage computation are determined so that the simulated load versus the stroke and gauge displacements matches as closely as possible with those of Fig. 3.19(a) & (b) and Fig. 3.20(a) & (b). Here, the crack length scale parameter is fixed at $l_f = 0.6$ [mm], so that the element size in the potentially damaged region is set

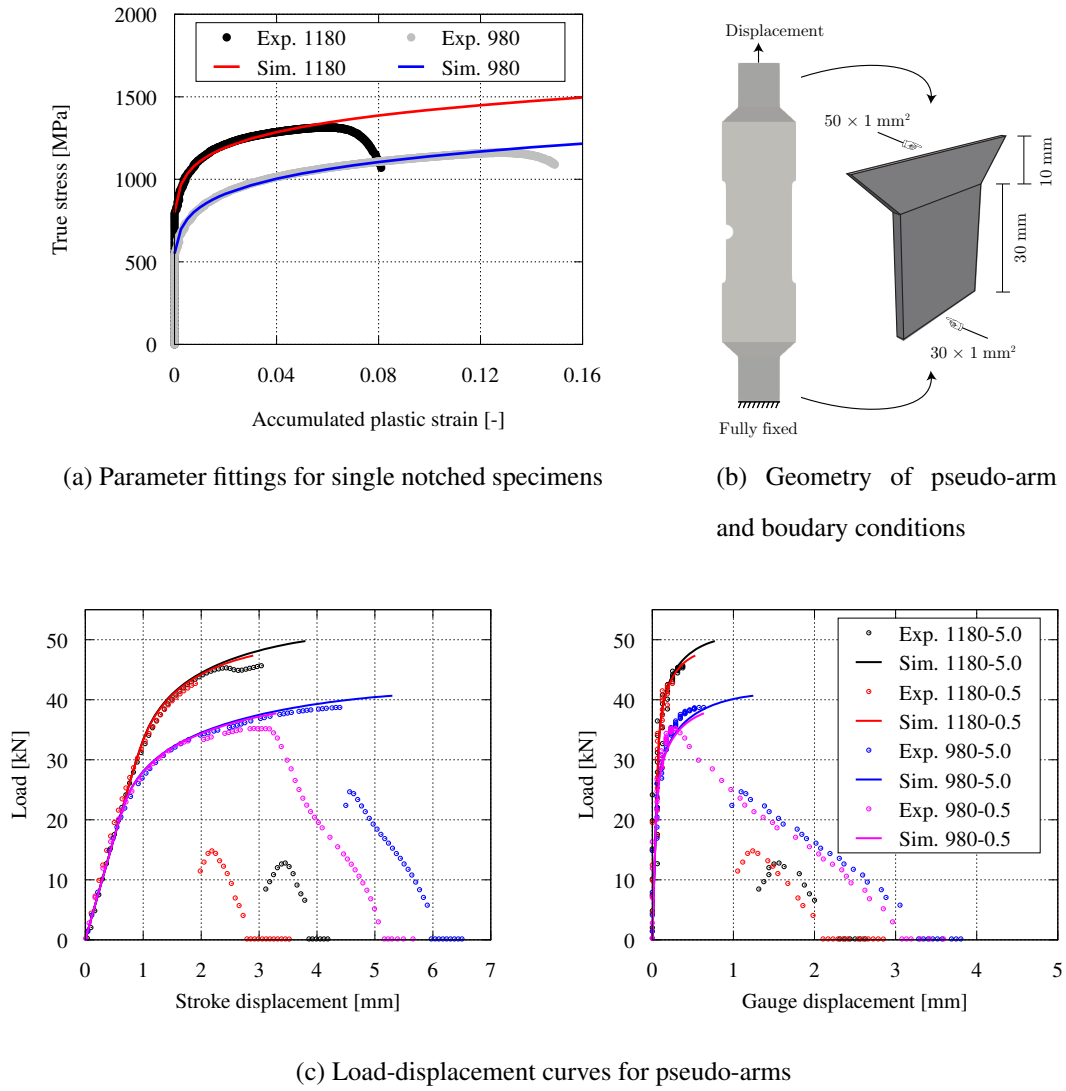


Fig. 3.22: Numerical setups for single notched specimens.

to be $h_e \approx 0.25 \sim 0.30$ [mm]. A trial-and-error procedure is again carried out to finally determine the parameters provided in Table 3.7. Note that the plastic damage driving force is not considered in this example, so only the local plasticity is employed.

The numerical results for JSC1180 shown in Fig. 3.23 indicate that the simulated failure responses conform to the experimental ones. As can be seen from Fig. 3.23(a) for the case of $R = 5.0$ [mm], the load exhibits a sudden drop from its peak to about 15 [kN]. During this decrease in load, the gauge displacement significantly increases from $u_g \approx 0.47$ to $u_g \approx 1.48$ [mm], whereas only a small increase in the stroke displacement u_s is obtained. Also, it

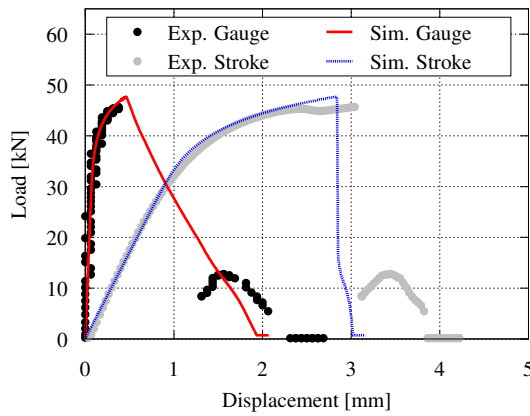
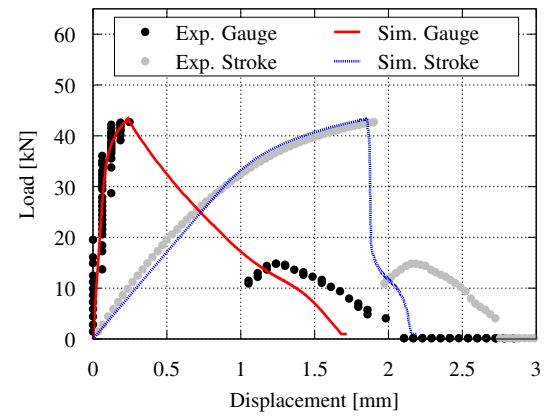
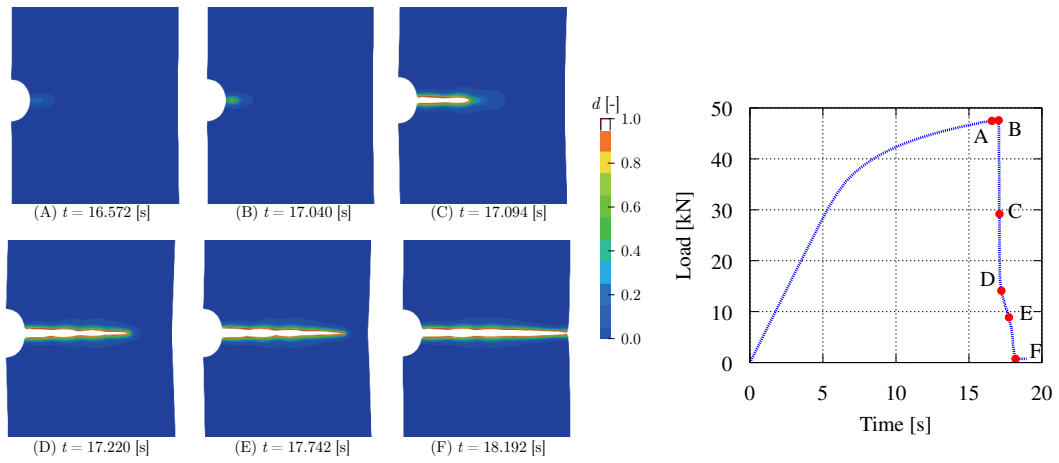
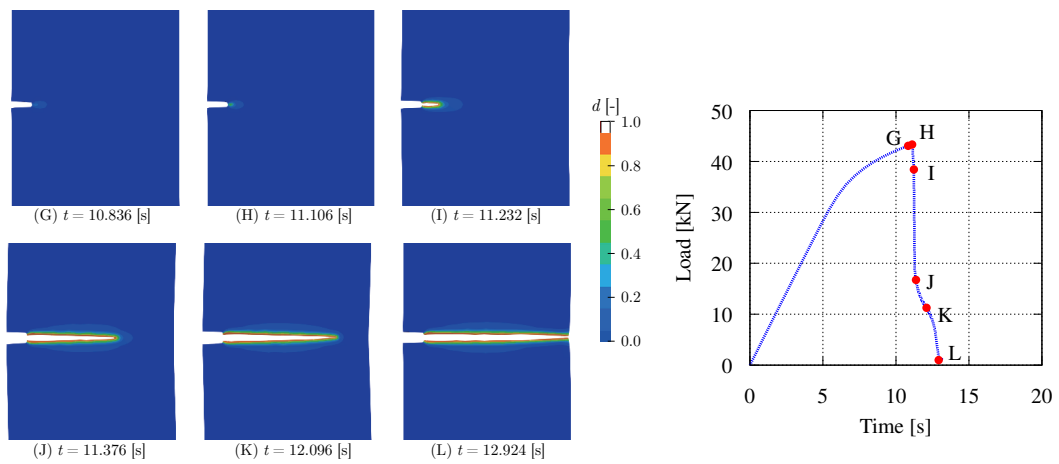
(a) Load-displacement curves for $R = 5.0$ [mm](b) Load-displacement curves for $R = 0.5$ [mm](c) Crack growth in time series for $R = 5.0$ [mm](d) Crack growth in time series for $R = 0.5$ [mm]

Fig. 3.23: Numerical results for JSC1180.

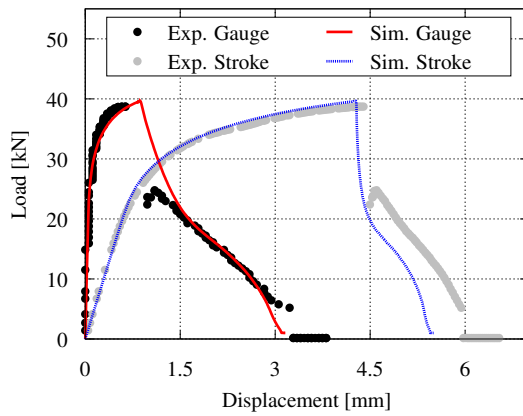
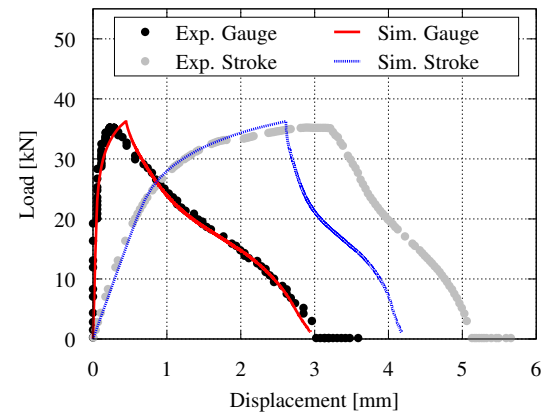
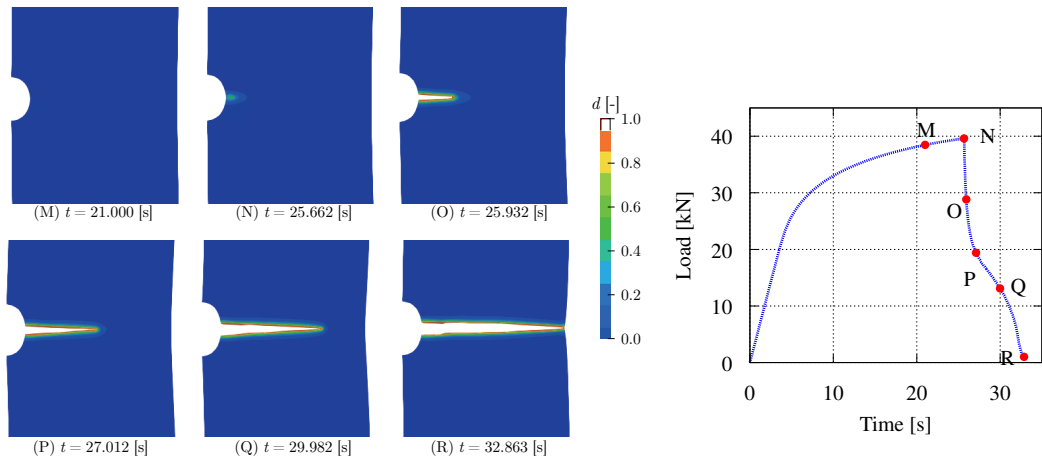
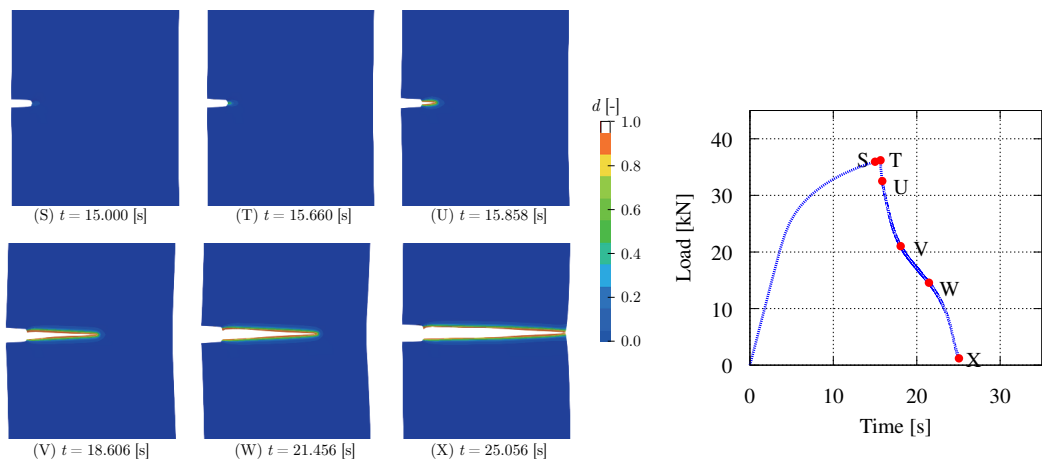
(a) Load-displacement curves for $R = 5.0$ [mm](b) Load-displacement curves for $R = 0.5$ [mm](c) Crack growth in time series for $R = 5.0$ [mm](d) Crack growth in time series for $R = 0.5$ [mm]

Fig. 3.24: Numerical results for JSC980.

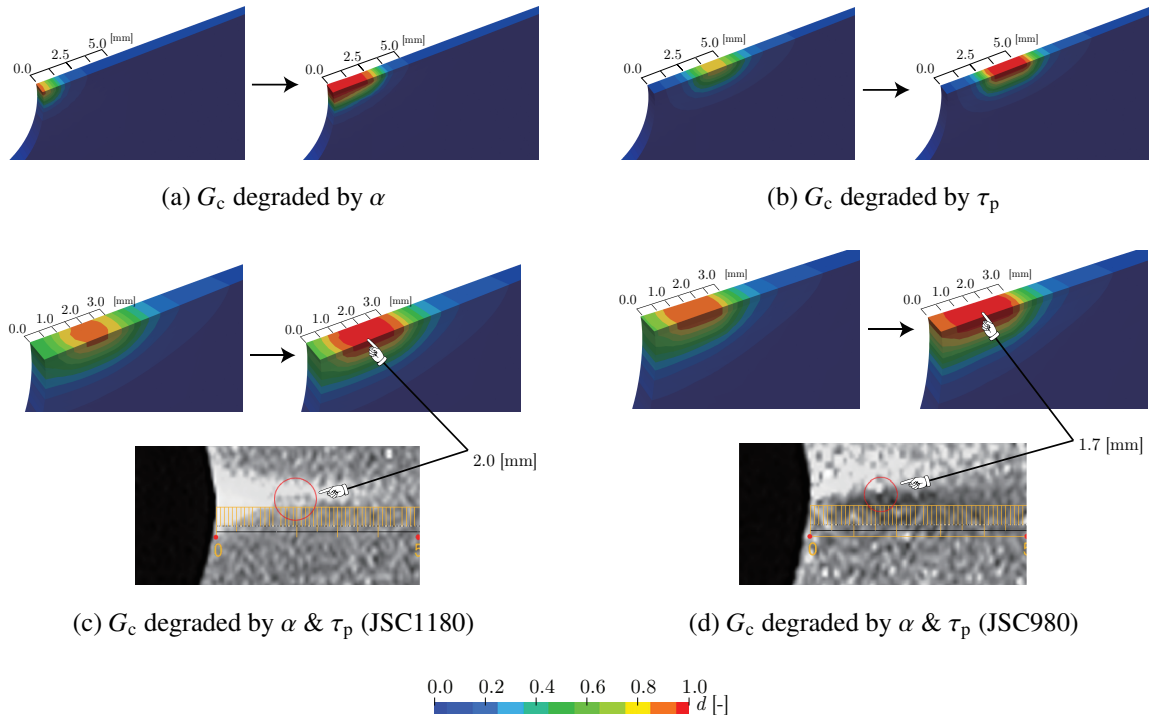


Fig. 3.25: Various crack initiation positions (left: before crack initiation, right: after crack initiation) depending on the degradation of degrading fracture toughness for $R = 5.0$ [mm].

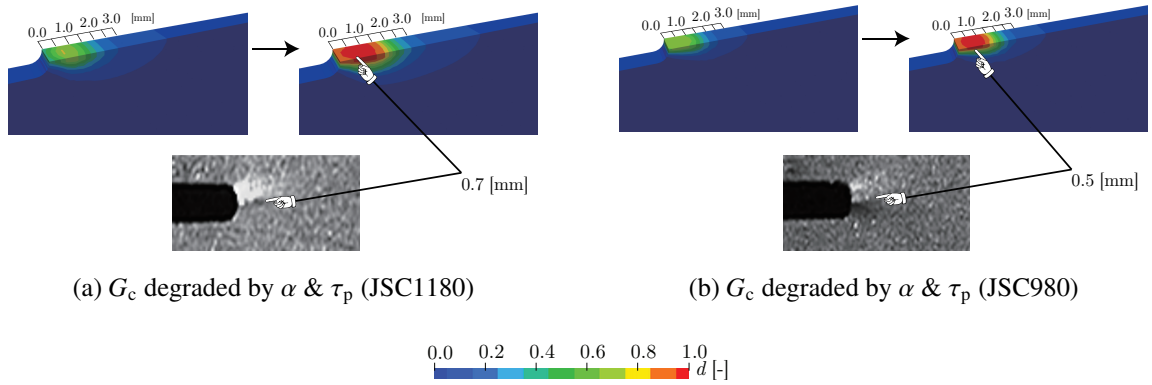


Fig. 3.26: Various crack initiation positions (left: before crack initiation, right: after crack initiation) depending on the degradation of degrading fracture toughness for $R = 0.5$ [mm].

can be seen from (B)~(D) in Fig. 3.23(c) that the crack rapidly grows right after the initiation. After this unstable crack growth, the fracture behavior becomes stable, and the crack grows

with tensile loading, as indicated from (D)~(F) in this figure. By using the same set of material parameters, almost the same tendency of the fracture behavior can be simulated for the case of $R = 0.5$ [mm] as can be seen from Fig. 3.23(d). Specifically, within the time interval (about 0.27 seconds) starting from (H) to (J), the crack initiates near the notch, propagates horizontally to the right, and stops when it reaches about 3/4 of the width of the specimen. After this point, the crack grows with tensile loading; see (J)~(L).

Meanwhile, Fig. 3.24 shows the simulation results for JSC980, which are also in close agreement with the experimental results. For the case of $R = 5.0$ [mm], unstable crack growth is again confirmed to be consistent with the experimental results. To be specific, the load significantly decreases from the peak to about 30 [kN], and the crack initiates near the edge of the notch and propagates to about 1/3 of the width of the specimen; see (N)~(O) in Fig. 3.24(c). After this period of unstable crack growth, the stable crack growth is simulated until the specimen finally breaks. In contrast, the result for the case of $R = 0.5$ [mm] indicates stable crack growth throughout the numerical simulation. It is confirmed from Fig. 3.24(d) that the crack inconsiderably propagates after its initiation; see (T) and (U) in particular. This is probably due to the fact that the specimen with $R = 0.5$ [mm] attains less negative hydrostatic pressure and exhibits more ductility than that of $R = 5.0$ [mm].

In the above discussion, we have demonstrated that the proposed model successfully reproduces the failure behavior of AHSS sheets. In what follows, its prediction ability for a crack initiation position is examined. As mentioned in relation to Fig. 3.21, the crack initiates inside the specimen but not on the notch surface in the case of $R = 5.0$ [mm]. This is probably due to the effect of negative hydrostatic pressure developed away from the notch surface, although the position of the maximum negative hydrostatic pressure and its magnitude seem to depend on the tensile strength as well as the notch size. Fig. 3.25(a) shows the enlarged views around the obtained crack initiation position for the JSC1180 specimen using the degrading fracture toughness that is degraded only by the accumulated plastic strain, which is conceptionally equivalent to the results of previous studies^{84),85)}. Note that the damage evolves in the order from the left view to the right view. As can be seen, the crack initiates

from the edge of the notch, which is thought to have experienced the most significant plastic deformation. Additionally, Fig. 3.25(b) shows the corresponding results with the degrading fracture toughness that is degraded only by the negative hydrostatic pressure. Since the damage contribution of plastic deformation is neglected in this case, the crack initiates at a position further away from the notch surface than the actual crack in the experiments. In this way, neither result is realistic nor consistent with the experimental results.

On the other hand, Fig. 3.25(c) and (d) show enlarged images of the vicinity of the crack initiation position for the specimen with a $R = 5.0$ [mm] notch taken from the numerical results, which correspond to the simulated fractures shown in Fig. 3.23(c) and 3.24(c), respectively. In the cases of JSC1180 and JSC980, crack initiation occurred at almost the same position as those of the experiments. It is thus concluded that to accurately predict crack initiation, at least the damage contribution from both plastic deformation and negative hydrostatic pressure should be properly taken into consideration. It should also be noted that since several previous models for ductile fracture ^{77),79),84),85)} focus only on the plastic deformation-induced damage evolution, they are unable to reproduce this kind of characteristic feature of crack initiation.

Additionally, Fig. 3.26 shows the enlarged views around the crack initiation positions for the specimen with $R = 0.5$ [mm], which correspond to the simulated fractures shown in Fig. 3.23(d) and 3.24(d). Again, for each figure, the damage evolves in order from the left view to the right view. As can be seen from these results, the crack initiates slightly inside the specimen for each of the cases. It should be remembered that we could not identify the crack initiation position from the experiments because the phenomenon occurred within a very short period of time, and the notch radius is small. Given that the crack initiation positions are well reproduced for JSC1180/980 with $R = 5.0$ [mm], those obtained here can be presumed to be correct.

Finally, let us summarize our experimental and numerical simulation results. In our experiments, the transitions from unstable to stable crack propagations are observed for AHSS sheets JSC1180/980. Also, we could observe crack initiation positions for JSC1180/980 with

$R = 5.0$ [mm] but not for JSC1180/980 with $R = 0.5$ [mm]. Meanwhile, in numerical simulations, we successfully simulated the failure tendency for JSC1180/980 with $R = 5.0$ [mm] after conducting calibration. Also, we simulated crack initiations from almost the same positions as in the experiments for them. Then, by conducting numerical simulations for JSC1180/980 with $R = 0.5$ [mm] using the same set of parameters, we found that the crack propagations, as well as the load-displacement curves, agreed with the experimental results. Therefore, we concluded that the simulated crack initiation positions for JSC1180/980 with $R = 0.5$ [mm] are also correct, even though they were not confirmed in our experiments.

4 Crack phase-field enhanced finite cover method: CPFFCM

The finite cover method (FCM) ^{108),109)} is a generalization of the FEM and is considered as an alias for the numerical manifold method (NMM) ¹⁰⁷⁾. In the first half of this chapter, the fundamentals of the FCM are explained, and the spatial and temporal discretizations of the governing equations derived in Section 2 are presented. Subsequently, in the second half, the numerical algorithm for realizing the diffusive-discrete crack topological transition, which we have named “Crack phase-field enhanced finite cover method (CPFFCM)”, is explained step by step along with graphical explanations.

It is worth mentioning that while the original theory of the FCM is different from that of the XFEM ^{105),106)}, which is also called the GFEM ^{103),104)}, the two methods have equivalent capabilities for capturing the strong discontinuity of a state variable.

4.1 Finite cover method

4.1.1 Mathematical and physical covers

In the FCM, we define two separate domains as shown in Fig. 4.1(a) & (b). One is the mathematical domain \mathcal{M} that is independent of physics, and the other is the physical domain \mathcal{B} that accommodates physical quantities. In what follows, we suppose that the physical domain is divided into two subdomains $\mathcal{B} = \mathcal{B}^{[1]} \cup \mathcal{B}^{[2]}$, as shown in Fig. 4.1(b), and that the mathematical domain \mathcal{M} is constructed as a union of a finite number of “mathematical

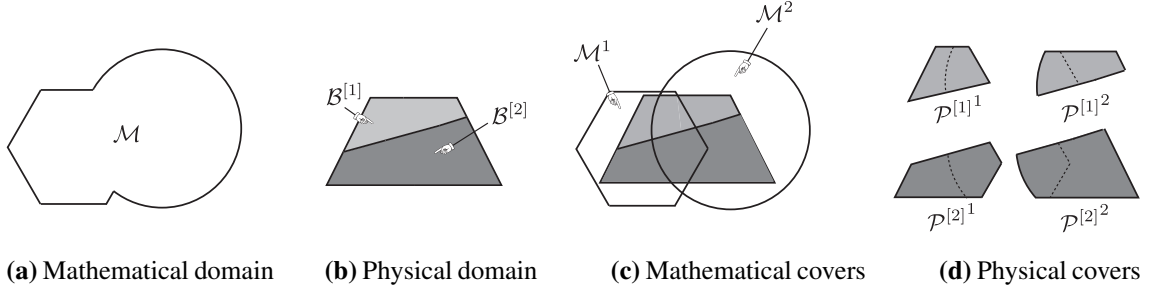


Fig. 4.1: Definitions of mathematical and physical covers.

covers” \mathcal{M}^I :

$$\mathcal{M} = \bigcup_{I=1}^{n_{\mathcal{M}}} \mathcal{M}^I, \quad (4.1)$$

where $n_{\mathcal{M}}$ is the total number of mathematical covers. Here, the mathematical covers can be either partially or totally overlapped, as illustrated in Fig. 4.1(c). Additionally, from the same figure, when describing a physical problem, the mathematical domain does not have to coincide with the physical domain, although it covers the whole physical domain. Then, the common region shared by a mathematical cover \mathcal{M}^I and a physical domain $\mathcal{B}^{[\alpha]}$ is called the “physical cover”, which is denoted by $\mathcal{P}^{[\alpha]I}$. For instance, as shown in Fig. 4.1(d), the two mathematical covers cover the two physical domains, so four physical covers are defined.

4.1.2 Finite cover approximation

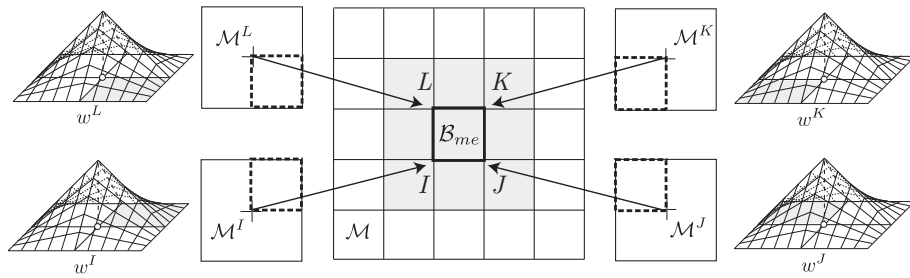


Fig. 4.2: Definition of a mathematical element and weight functions for PU approximation.

The finite cover approximation for a state variable is made over the physical domain using the partition of unity (PU) property. For each mathematical cover, the corresponding

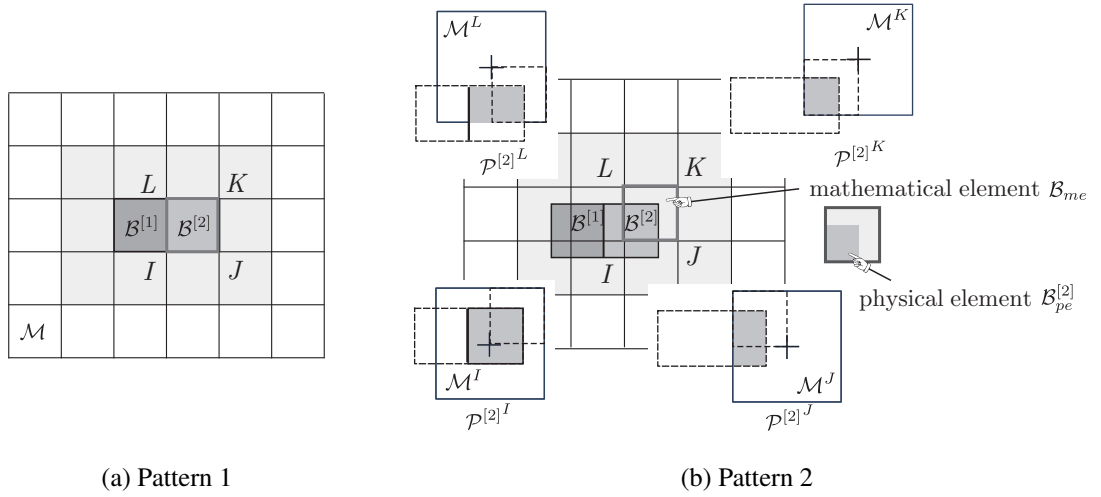


Fig. 4.3: Definition of physical elements.

weight function is defined as follows:

$$\begin{aligned} w^I(\mathbf{X}) &\geq 0 \quad \text{for } \mathbf{X} \in \mathcal{M}^I \\ w^I(\mathbf{X}) &= 0 \quad \text{for } \mathbf{X} \notin \mathcal{M}^I \end{aligned} \quad \text{with PU: } \sum_{I=1}^{n_M} w^I(\mathbf{X}) = 1 \quad \text{on } \mathcal{M} \quad (4.2)$$

Then, the common domain of mathematical covers is called the “mathematical element”, and the union of mathematical elements is called an FCM mesh. Fig. 4.2 illustrates the definition of mathematical element \mathcal{B}_{me} , which is expressed as

$$\mathcal{B}_{me} = \bigcap_{\beta=I,J,K,L} \mathcal{M}^\beta. \quad (4.3)$$

Furthermore, the physical domain is covered by the FCM mesh, and a “physical element” is defined as the common domain of the physical covers. Fig. 4.3 shows two patterns of physical elements for the physical domain $\mathcal{B} = \mathcal{B}^{[1]} \cup \mathcal{B}^{[2]}$. In Pattern 1, the FCM mesh coincides with the physical domain so that the mathematical elements and physical elements are identical, which is recognized as the discretization of the standard FEM. On the other hand, in Pattern 2, although the FCM mesh covers the whole physical domain, each mathematical element does not need to be compatible with the physical domain. For instance, the mathematical element \mathcal{B}_{me} partially covers the physical domain $\mathcal{B}^{[2]}$, and the common domain is defined as the physical element $\mathcal{B}_{pe}^{[2]}$. This is the feature of the FCM and character-

izes it as a generalized version of the FEM. Additionally, due to the definition of the physical element in the FCM, an arbitrary discontinuity can be represented.

4.2 Spatial discretization by FCM

The spatial discretization of the FCM is almost the same as that of the FEM. First, let us postulate the following governing equations, which consider damage evolution in a dynamic elastoplastic system within the finite strain framework:

- Equilibrium for mechanical field:

$$\begin{aligned}\nabla \cdot \mathbf{P} + \nabla \cdot (\underline{\mathbf{C}} : \dot{\mathbf{F}}) + \mathbf{B} &= \rho_0 \ddot{\mathbf{u}} \quad \text{in } \mathcal{B}_0, \\ \mathbf{P} \cdot \mathbf{N} + (\underline{\mathbf{C}} : \dot{\mathbf{F}}) \cdot \mathbf{N} &= \bar{\mathbf{T}} \quad \text{on } \partial \mathcal{B}_0^{\mathbf{N}}, \\ \mathbf{u} &= \bar{\mathbf{u}} \quad \text{on } \partial \mathcal{B}_0^{\mathbf{D}},\end{aligned}\tag{4.4}$$

- Equilibrium for micromorphic plastic field:

$$\begin{aligned}p_p(\alpha - \bar{\alpha}) - y_0 l_p^2 \Delta \alpha &= 0 \quad \text{in } \mathcal{B}_0, \\ \nabla \alpha \cdot \mathbf{N} &= 0 \quad \text{on } \partial \mathcal{B}_0,\end{aligned}\tag{4.5}$$

- Threshold function for plasticity with loading/unloading conditions:

$$\Phi^p = \|\tau_{0,\text{dev}}\| - \sqrt{\frac{2}{3}}(y_0 + r_0^p) \leq 0, \quad \dot{\alpha} \geq 0, \quad \Phi^p \dot{\alpha} = 0 \quad \text{in } \mathcal{B}_0,\tag{4.6}$$

- Threshold function for damage with loading/unloading conditions:

$$\begin{aligned}\Phi^f &= -\frac{\partial g(d^e)}{\partial d^e} \langle \Psi_0^{e+} - \Psi_{\text{cr}}^e \rangle \zeta^e - \frac{\partial g(d^p)}{\partial d^p} \langle \Psi_0^p - \Psi_{\text{cr}}^p \rangle \zeta^p - G_c(\alpha^*, \tau_p^*) \left(\frac{d - l_f^2 \Delta d}{l_f} \right) \leq 0, \\ \dot{d} &\geq 0, \quad \Phi^f \dot{d} = 0 \quad \text{in } \mathcal{B}_0, \\ \nabla d \cdot \mathbf{N} &= 0 \quad \text{on } \partial \mathcal{B}_0.\end{aligned}\tag{4.7}$$

Here, one may notice that the above equations combine two models independently explained in Section 2.3 and Section 2.5. Multiplying the governing equations Eq. (4.4), Eq. (4.5), and Eq. (4.7) by the corresponding variations $\{\delta \mathbf{u}, \delta \alpha, \delta d\}$, the weak forms of the mechanical,

micromorphic plastic, and damage fields are derived as follows:

$$\begin{aligned} & \int_{\mathcal{B}_0} \mathbf{P} : \frac{\partial \delta \mathbf{u}}{\partial \mathbf{X}} dV + \int_{\mathcal{B}_0} \rho_0 \ddot{\mathbf{u}} \cdot \delta \mathbf{u} dV + \int_{\mathcal{B}_0} (\underline{\mathbf{C}} : \dot{\mathbf{F}}) : \frac{\partial \delta \mathbf{u}}{\partial \mathbf{X}} dV \\ & - \int_{\mathcal{B}_0} \mathbf{B} \cdot \delta \mathbf{u} dV - \int_{\partial \mathcal{B}_0^N} \bar{\mathbf{T}} \cdot \delta \mathbf{u} dA = 0 \end{aligned} \quad (4.8)$$

$$\int_{\mathcal{B}_0} \left\{ (\alpha - \bar{\alpha}) \delta \alpha + \frac{y_0 l_p^2}{p_p} \nabla \alpha \cdot \nabla \delta \alpha \right\} dV = 0, \quad (4.9)$$

and

$$\int_{\mathcal{B}_0} \left\{ -\frac{\partial g(d^e)}{\partial d^e} \langle \Psi_0^{e+} - \Psi_{cr}^e \rangle \zeta^e \delta d - \frac{\partial g(d^p)}{\partial d^p} \langle \Psi_0^p - \Psi_{cr}^p \rangle \zeta^p \delta d - \frac{G_c}{l_f} (d \delta d + l_f^2 \nabla d \cdot \nabla \delta d) \right\} dV \leq 0. \quad (4.10)$$

Here, the displacement vector, hardening and damage variables, as well as their variations, are approximated at the physical element level in a general manner by using the shape function \mathcal{N}^I as follows:

$$\begin{aligned} \mathbf{u} &\approx \mathbf{u}^h = \sum_{I=1}^{n_{pe}} \mathcal{N}^I \mathbf{u}^I, \quad \alpha \approx \alpha^h = \sum_{I=1}^{n_{pe}} \mathcal{N}^I \alpha^I, \quad d \approx d^h = \sum_{I=1}^{n_{pe}} \mathcal{N}^I d^I \\ \delta \mathbf{u} &\approx \delta \mathbf{u}^h = \sum_{I=1}^{n_{pe}} \mathcal{N}^I \delta \mathbf{u}^I, \quad \delta \alpha \approx \delta \alpha^h = \sum_{I=1}^{n_{pe}} \mathcal{N}^I \delta \alpha^I, \quad \delta d \approx \delta d^h = \sum_{I=1}^{n_{pe}} \mathcal{N}^I \delta d^I, \end{aligned} \quad (4.11)$$

where \mathcal{N}^I is the shape function at the global level and is identical to the weight function w^I , and n_{pe} is the number of physical covers constructing a physical element.

Substituting Eq. (4.11) into the weak forms Eqs. (4.8), (4.9), (4.10), we derive the following node-level (physical cover-level) residuals:

$$\begin{aligned} \mathcal{R}_{u_i, n+1}^I &= - \left\{ \int_{\mathcal{B}_0} \left(P_{ia, n+1}^h \frac{\partial \mathcal{N}^I}{\partial X_a} + \rho_0 \ddot{u}_{i, n+1}^h \mathcal{N}^I + \underline{C}_{iacd, n+1}^h \dot{F}_{cd, n+1}^h \frac{\partial \mathcal{N}^I}{\partial X_a} - \rho_0 g_i^h \mathcal{N}^I \right) dV \right. \\ &\quad \left. - \int_{\partial \mathcal{B}_0^N} \bar{T}_{i, n+1}^h \mathcal{N}^I dA \right\}, \end{aligned} \quad (4.12)$$

$$\mathcal{R}_{\alpha, n+1}^I = - \int_{\mathcal{B}_0} \left\{ (\alpha_{n+1}^h - \bar{\alpha}_{n+1}^h) \mathcal{N}^I + \frac{y_0 l_p^2}{p_p} \frac{\partial \alpha_{n+1}^h}{\partial X_a} \frac{\partial \mathcal{N}^I}{\partial X_a} \right\} dV, \quad (4.13)$$

and

$$\begin{aligned} \mathcal{R}_{d,n+1}^I = & - \int_{\mathcal{B}_0} \left\{ -\frac{\partial g(d_{n+1}^{eh})}{\partial d^e} \mathcal{H}_{n+1}^{eh} \zeta^e \mathcal{N}^I - \frac{\partial g(d_{n+1}^{ph})}{\partial d^p} \mathcal{H}_{n+1}^{ph} \zeta^p \mathcal{N}^I \right. \\ & \left. - \frac{G_{c,n+1}^h}{l_f} \left(d_{n+1}^h \mathcal{N}^I + l_f^2 \frac{\partial d_{n+1}^h}{\partial X_a} \frac{\partial \mathcal{N}^I}{\partial X_a} \right) \right\} dV, \end{aligned} \quad (4.14)$$

where a subscript $n + 1$ on a quantity indicates that it is evaluated at time t_{n+1} . Here, to ensure the irreversibility of the damage evolution, two history variables in Eq. (2.121) have been introduced.

The tangent matrices in the corresponding linearized equations are obtained by differentiating the residuals with respect to the state variables $\{u, \alpha, d\}$ as follows:

$$\mathcal{K}_{n+1} = \begin{bmatrix} \mathcal{K}_{uu,n+1} & \mathcal{K}_{u\alpha,n+1} & \mathcal{K}_{ud,n+1} \\ \mathcal{K}_{\alpha u,n+1} & \mathcal{K}_{\alpha\alpha,n+1} & \mathcal{K}_{\alpha d,n+1} \\ \mathcal{K}_{du,n+1} & \mathcal{K}_{d\alpha,n+1} & \mathcal{K}_{dd,n+1} \end{bmatrix} \quad (4.15)$$

where the components of each block matrix are given as

$$\begin{aligned} \mathcal{K}_{u_i u_j, n+1}^{IJ} = & \int_{\mathcal{B}_0} \left(\frac{\partial \mathcal{N}^I}{\partial X_a} \frac{\partial P_{ia,n+1}^h}{\partial F_{jb}} \frac{\partial \mathcal{N}^J}{\partial X_b} + \rho_0 \frac{\partial \ddot{u}_{i,n+1}^h}{\partial X_j} \mathcal{N}^I \mathcal{N}^J \right. \\ & \left. + \frac{\partial \mathcal{N}^I}{\partial X_a} \left(\frac{\partial C_{iacd,n+1}^h}{\partial F_{jb}} \dot{F}_{cd,n+1}^h + C_{iacd,n+1}^h \frac{\partial \dot{F}_{cd,n+1}^h}{\partial F_{jb}} \right) \frac{\partial \mathcal{N}^J}{\partial X_b} \right) dV, \end{aligned} \quad (4.16)$$

$$\mathcal{K}_{u_i \alpha, n+1}^{IJ} = \int_{\mathcal{B}_0} \left\{ \frac{\partial \mathcal{N}^I}{\partial X_a} \frac{\partial P_{ia,n+1}^h}{\partial \alpha} \mathcal{N}^J \right\} dV, \quad (4.17)$$

$$\mathcal{K}_{u_i d, n+1}^{IJ} = \int_{\mathcal{B}_0} \left\{ \frac{\partial \mathcal{N}^I}{\partial X_a} \frac{\partial P_{ia,n+1}^h}{\partial d^e} \zeta^e \mathcal{N}^J \right\} dV, \quad (4.18)$$

$$\mathcal{K}_{\alpha u_j, n+1}^{IJ} = \int_{\mathcal{B}_0} \left\{ -\frac{\partial \bar{\alpha}_{n+1}^h}{\partial F_{jb}} \mathcal{N}^I \frac{\partial \mathcal{N}^J}{\partial X_b} \right\} dV, \quad (4.19)$$

$$\mathcal{K}_{\alpha\alpha, n+1}^{IJ} = \int_{\mathcal{B}_0} \left\{ \left(1 - \frac{\partial \bar{\alpha}_{n+1}^h}{\partial \alpha} \right) \mathcal{N}^I \mathcal{N}^J + \frac{y_0 l_p^2}{p_p} \frac{\partial \mathcal{N}^I}{\partial X_a} \frac{\partial \mathcal{N}^J}{\partial X_a} \right\} dV, \quad (4.20)$$

$$\mathcal{K}_{ad,n+1}^{IJ} = \int_{\mathcal{B}_0} \left\{ -\frac{\partial \bar{\alpha}_{n+1}^h}{\partial d} \mathcal{N}^I \mathcal{N}^J \right\} dV, \quad (4.21)$$

$$\mathcal{K}_{du_j,n+1}^{IJ} = \int_{\mathcal{B}_0} \left\{ -\frac{\partial g(d_{n+1}^{eh})}{\partial d^e} \frac{\partial \mathcal{H}_{n+1}^{eh}}{\partial F_{jb}} \zeta^e \mathcal{N}^I \frac{\partial \mathcal{N}^J}{\partial X_b} - \frac{\partial G_{c,n+1}^h}{\partial F_{jb}} \frac{\partial \mathcal{N}^J}{\partial X_b} \frac{1}{l_f} \left(d_{n+1}^h \mathcal{N}^I + l_f^2 \frac{\partial d_{n+1}^h}{\partial X_a} \frac{\partial \mathcal{N}^I}{\partial X_a} \right) \right\} dV. \quad (4.22)$$

$$\mathcal{K}_{d\alpha,n+1}^{IJ} = \int_{\mathcal{B}_0} \left\{ -\frac{\partial g(d_{n+1}^{ph})}{\partial d^p} \frac{\partial \mathcal{H}_{n+1}^{ph}}{\partial \alpha} \zeta^p \mathcal{N}^I \mathcal{N}^J - \frac{\partial G_{c,n+1}^h}{\partial \alpha} \mathcal{N}^J \frac{1}{l_f} \left(d_{n+1}^h \mathcal{N}^I + l_f^2 \frac{\partial d_{n+1}^h}{\partial X_a} \frac{\partial \mathcal{N}^I}{\partial X_a} \right) \right\} dV, \quad (4.23)$$

$$\begin{aligned} \mathcal{K}_{dd,n+1}^{IJ} = \int_{\mathcal{B}_0} & \left\{ -\frac{\partial^2 g(d_{n+1}^{eh})}{\partial d^{e2}} \mathcal{H}_{n+1}^{eh} \zeta^{e2} \mathcal{N}^I \mathcal{N}^J \right. \\ & \left. - \frac{\partial^2 g(d_{n+1}^{ph})}{\partial d^{p2}} \mathcal{H}_{n+1}^{ph} \zeta^{p2} \mathcal{N}^I \mathcal{N}^J - \frac{G_{c,n+1}^h}{l_f} \left(\mathcal{N}^I \mathcal{N}^J + l_f^2 \frac{\partial \mathcal{N}^I}{\partial X_a} \frac{\partial \mathcal{N}^J}{\partial X_a} \right) \right\} dV, \end{aligned} \quad (4.24)$$

4.3 Temporal discretization by Newton method

By adopting the Newmark method ¹⁷⁶⁾, the acceleration and velocity vectors, $\ddot{\mathbf{u}}_{n+1}$ and $\dot{\mathbf{u}}_{n+1}$, at time t_{n+1} can be written as

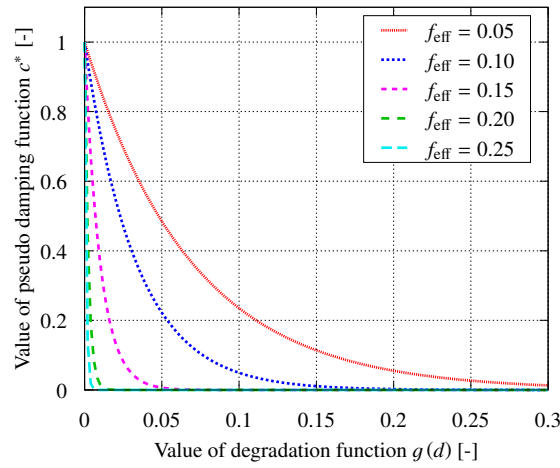
$$\begin{aligned} \ddot{\mathbf{u}}_{n+1} &= \frac{1}{\beta \Delta t_{n+1}^2} (\mathbf{u}_{n+1} - \mathbf{u}_n - \dot{\mathbf{u}}_n \Delta t_{n+1}) - \frac{1-2\beta}{2\beta} \ddot{\mathbf{u}}_n, \\ \dot{\mathbf{u}}_{n+1} &= \dot{\mathbf{u}}_n + \Delta t_{n+1} \{ (1-\gamma) \ddot{\mathbf{u}}_n + \gamma \ddot{\mathbf{u}}_{n+1} \}, \end{aligned} \quad (4.25)$$

where β and γ are parameters that determine the ratio of the contributions of the quantities at consecutive times, t_n and t_{n+1} .

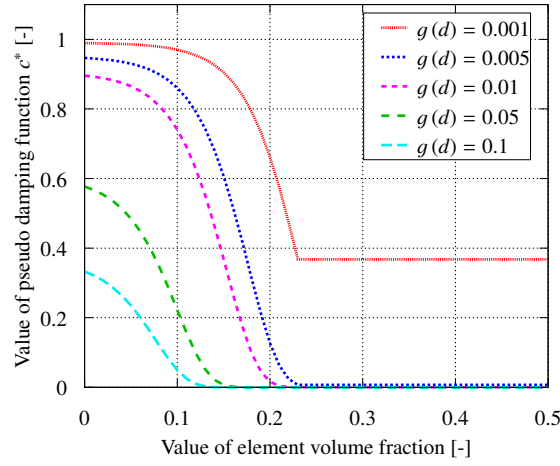
On the other hand, the standard numerical damping tensor consists of two terms as follows:

$$\underline{\mathbf{C}}_{n+1} = c_m \underline{\mathbf{M}}_{n+1} + c_k \underline{\mathbf{K}}_{n+1}, \quad (4.26)$$

where $\underline{\mathbf{M}}_{n+1}$ and $\underline{\mathbf{K}}_{n+1}$ represent the mass and stiffness matrices in this general description and c_m and c_k , respectively, are their coefficients. However, in this study, the introduction of



(a) With respect to fixed values of the volume fraction of physical domain



(b) With respect to fixed values of the degradation function

Fig. 4.4: Drawings of the pseudo damping function.

this matrix is not intended to have the usual damping effect in dynamic problems. Instead, the damping effect is limited only to damaged physical elements whose mathematical elements are only partially occupied by the physical domain. Specifically, the following numerical damping matrix is proposed:

$$\underline{C}_{n+1} = c_{n+1}^* (\bar{d}_n, f_{\text{eff}}) \underline{K}^*. \quad (4.27)$$

Here, c_{n+1}^* is the damping function to be evaluated element by element and is defined as

$$c_{n+1}^* = \exp\left(-\zeta(f_{\text{eff}})g(\bar{d}_n)\right),$$

$$\text{with } \zeta = \min[\zeta_{\min} + \exp(\zeta_{\text{cof}}f_{\text{eff}}), \zeta_{\max}], \quad \bar{d}_n = \frac{\sum_{l=1}^{n_{pe}} d_n^l}{n_{pe}}, \quad f_{\text{eff}} = \min\left[\frac{V_{\text{phy}}^{1/s}}{\bar{h}_e}, 1.0\right], \quad (4.28)$$

where \bar{d}_n is the damage variable averaged over a mathematical element and f_{eff} is the volume fraction of the physical domain within a mathematical element. Here, V_{phy} and \bar{h}_e denote the volume occupied by the physical domain within a mathematical element and the representative size of the mathematical element, respectively. Additionally, the coefficient ζ is computed using three constants, ζ_{\min} , ζ_{\max} , ζ_{cof} , and f_{eff} . Since both the averaged damage variable \bar{d}_n and the volume fraction f_{eff} are independent of the physical quantities at the current time step t_{n+1} , $\partial_d c_{n+1}^* = 0$ and $\partial_u c_{n+1}^* = 0$ hold. It should also be noted that the proposed damping function is defined to have a decreasing property such that $\partial_{g(\bar{d}_n)} c_{n+1}^* \leq 0$ and $\partial_{f_{\text{eff}}} c_{n+1}^* \leq 0$; for a better understanding, see Fig. 4.4, which is drawn using the parameters $\zeta_{\min} = 10$, $\zeta_{\max} = 1000$, and $\zeta_{\text{cof}} = 30$. This figure shows that the damping becomes effective only when the volume fraction of the physical domain is small and the mathematical element is severely damaged. Additionally, \underline{K}^* denotes the pseudo stiffness matrix, whose tensor components are set to be constant, so that $\partial \underline{C}_{iacd,n+1}^h / \partial F_{jb} = 0$ holds in Eq. (4.16). At a local level, this matrix is defined as

$$\underline{K}_{iajb}^* = \lambda_{\text{pse}} \delta_{ia} \delta_{jb} + \mu_{\text{pse}} (\delta_{ij} \delta_{ab} + \delta_{ib} \delta_{aj}), \quad (4.29)$$

where λ_{pse} and μ_{pse} are pseudo material constants.

Substituting Eq. (4.25) and Eqs. (4.27)–(4.29) into Eqs. (4.12) and (4.16), we obtain the time-discretized residual vector and tangent matrix for the mechanical field as follows:

$$\begin{aligned} \mathcal{R}_{u_i,n+1}^I = & - \left\{ \int_{\mathcal{B}_0} \left\{ P_{ia,n+1}^h \frac{\partial \mathcal{N}^I}{\partial X_a} + \rho_0 (\ddot{u}_{i,n+1}^h - g_i^h) \mathcal{N}^I \right. \right. \\ & + c_{n+1}^* \underline{K}_{iacd}^h \left(\frac{\partial \ddot{u}_{c,n}^h}{\partial X_d} + \Delta t_{n+1} \left((1 - \gamma) \frac{\partial \ddot{u}_{c,n}^h}{\partial X_d} + \gamma \frac{\partial \ddot{u}_{c,n+1}^h}{\partial X_d} \right) \right) \frac{\partial \mathcal{N}^I}{\partial X_a} \Big\} dV \\ & \left. - \int_{\partial \mathcal{B}_0^N} \bar{T}_{i,n+1}^h \mathcal{N}^I dA \right\} \end{aligned} \quad (4.30)$$

and

$$\mathcal{K}_{u_i u_j, n+1}^{IJ} = \int_{\mathcal{B}_0} \left(\frac{\partial \mathcal{N}^I}{\partial X_a} \frac{\partial P_{ia, n+1}^h}{\partial F_{jb}} \frac{\partial \mathcal{N}^J}{\partial X_b} + \frac{1}{\beta \Delta t_{n+1}^2} \rho_0 \delta_{ij} \mathcal{N}^I \mathcal{N}^J + \frac{\gamma}{\beta \Delta t_{n+1}} c_{n+1}^* \frac{\partial \mathcal{N}^I}{\partial X_a} \underline{K}_{iajb}^{*h} \frac{\partial \mathcal{N}^J}{\partial X_b} \right) dV. \quad (4.31)$$

4.4 Numerical algorithm

Algorithm 2 FC-based staggered iterative algorithm.

- 1: (% At time step t_n , $\mathbf{u}_{n,k=0} = \mathbf{u}_{n-1}$, $\alpha_{n,k=0} = \alpha_{n-1}$, $\bar{\alpha}_{n,k=0} = \bar{\alpha}_{n-1}$, and $d_{n,k=0} = d_{n-1}$ are known.)
 - 2: Update the old velocity and acceleration for the Newmark method: $\dot{\mathbf{u}}_{n-1} = \dot{\mathbf{u}}_{n,k=0}$ and $\ddot{\mathbf{u}}_{n-1} = \ddot{\mathbf{u}}_{n,k=0}$
 - 3: **while** $\text{norm}[\mathbf{res}_{\text{stag},k}] > \text{TOL}_{\text{st}}$ **do**
 - 4: $k = k + 1$ (% FC-based staggered iteration)
 - 5: NR loop: Compute the damage $d_{n,k}$ with the fixed displacement $\mathbf{u}_{n,k-1}$ and the global and local hardening variables $\alpha_{n,k-1}$ & $\bar{\alpha}_{n,k-1}$
 - 6: NR loop: Compute the displacement $\mathbf{u}_{n,k}$ and the global and local hardening variables $\alpha_{n,k}$ & $\bar{\alpha}_{n,k}$ with the fixed damage $d_{n,k}$
 - 7: Update the configuration for computing the deformation gradient: $\mathbf{X}_{n,k+1} = \mathbf{x}_{n,k}$
 - 8: Compute the staggered iterative residual via Eq. (4.32)
 - 9: **if** $\text{norm}[\mathbf{res}_{\text{stag},k}] > \text{TOL}_{\text{st}}$ **then**
 - 10: Check whether a transition from diffusive to discrete cracks is needed; See Section 4.5 and Reference ¹⁷⁷⁾
 - 11: **end if**
 - 12: **end while**
-

Algorithm 2 presents an overview of the enhanced staggered iterative algorithm to realize the transition from diffusive to discrete cracks. This algorithm was originally developed for quasi-static crack propagation problems by Han et al. ¹⁷⁷⁾ but can be applied to dynamic and elastoplastic problems without much modification. Note that the algorithm takes advantage of both the CPFEM and the strong discontinuity of the FCM, allowing a discrete crack path to propagate and even curve within a short time interval within the finite strain framework.

According to the algorithm, in each FC-based staggered iteration k , the damage field and the mechanical and plastic fields are alternately computed. When both fields are determined, the configuration for computing the deformation gradient is updated. Subsequently, the norm of the error $\mathbf{res}_{\text{stag},k}$, which has a dimensionality equal to the total number of nodes, is computed as

$$\text{norm}[\mathbf{res}_{\text{stag},k}] \quad \text{with} \quad \mathbf{res}_{\text{stag},k}^I = \frac{\mathcal{E}_k^I + \mathcal{K}_k^I - \mathcal{E}_{k-1}^I - \mathcal{K}_{k-1}^I}{\mathcal{E}_k^I + \mathcal{K}_k^I}, \quad (4.32)$$

where \bullet^I denotes the value of \bullet at node I . If the value of this norm is smaller than a prescribed threshold $\text{TOL}_{\text{st.}}$, the two fields are considered to have converged in the current loading step, and a new displacement/force increment is imposed for the next loading step. Otherwise, the necessity of updating explicit crack tips is checked before proceeding to the next FC-based staggered iteration $k + 1$.

It is noted that the configuration for computing the deformation gradient $\mathbf{F}_{n,k}$ is updated at the end of every FC-based staggered iteration. That is, the deformation gradient at the time step t_n is modified at the k -th FC-based staggered iteration using the updated deformation gradient during the staggered iterative procedure such that

$$\begin{aligned}
 \mathbf{F}_{n,k} &= \Delta \mathbf{F}_{n,k} \cdot \mathbf{F}_{n,k-1} \\
 &= \Delta \mathbf{F}_{n,k} \cdot \Delta \mathbf{F}_{n,k-1} \cdot \mathbf{F}_{n,k-2} \\
 &= \underbrace{\Delta \mathbf{F}_{n,k} \cdot \Delta \mathbf{F}_{n,k-1} \cdot \dots \cdot \Delta \mathbf{F}_{n,k=2} \cdot \Delta \mathbf{F}_{n,k=1}}_{=\Delta \mathbf{F}_n} \cdot \mathbf{F}_{n-1} \\
 \text{with } \Delta \mathbf{F}_{n,k} &= \frac{\partial (\Delta \mathbf{u}_{n,k} + \mathbf{X}_{n,k-1})}{\partial \mathbf{X}_{n,k-1}} = \frac{\partial \Delta \mathbf{u}_{n,k}}{\partial \mathbf{X}_{n,k-1}} + \mathbf{1}.
 \end{aligned} \tag{4.33}$$

Although a detailed discussion is not provided here, this incremental modification of the deformation gradient is effective for maintaining computational stability when the damage evolves dramatically or when a large deformation is experienced within a single loading step. On the other hand, the velocity and acceleration from the previous time step, $\dot{\mathbf{u}}_{n-1}$ and $\ddot{\mathbf{u}}_{n-1}$, are updated only at the beginning of the time step t_n .

4.5 Transition scheme from diffusive to discrete crack topologies

This section presents a transition scheme from diffusive to discrete crack topologies by enjoying the benefits of both the crack phase-field and a strong discontinuity approach. The proposed scheme can reproduce the geometry of a discrete crack path that is propagated and even curved in a short time interval within the finite strain framework.

4.5.1 Explicit crack tip determination technique

Algorithm 3 presents the overview of the moving circle algorithm ¹⁷⁷⁾ that exploits the feature of non-local damage and determines new explicit crack tips while updating discrete cracks. Note that while the detailed procedures to determine the center of the circle are different, the moving circle algorithm is conceptually the same as the medial-axis-based algorithm proposed by Tamayo-Mas & Rodríguez-Ferran ¹³⁹⁾.

In **Step 1**, the old explicit crack tip coordinates $\mathbf{X}_{\text{tip,o}}$ and the direction vector $\mathbf{V}_{\text{dir,o}}$ for each crack tip element *inel* are input. At the same time, the possibility of the appearance of an additional crack tip is checked. Additionally, the old direction vector is sometimes modified by the distribution of the spatial gradient of the damage variable. In **Step 2**, the average values, \bar{d}_{inel} and \bar{d}_{jnel} , of the damage variables for *inel* and the adjacent elements *jnel*, respectively, are computed. If the value for one element among them is larger than the critical value d_{cr1} , then element *inel* needs to be divided by the explicit opposite crack surfaces. In **Step 3**, the representative point of a boundary element *knel*, $\mathbf{X}_{\text{ab,knel}}$, is computed as follows:

$$\mathbf{X}_{\text{ab,knel}} = \frac{\|\mathbf{X}_b - \mathbf{X}_{\text{tip,o}}\|\mathbf{X}_a + \|\mathbf{X}_a - \mathbf{X}_{\text{tip,o}}\|\mathbf{X}_b}{\|\mathbf{X}_a - \mathbf{X}_{\text{tip,o}}\| + \|\mathbf{X}_b - \mathbf{X}_{\text{tip,o}}\|}$$

$$\text{with } \mathbf{X}_a = C_1\mathbf{X}_i + (1 - C_1)\mathbf{X}_j, \mathbf{X}_b = C_2\mathbf{X}_k + (1 - C_2)\mathbf{X}_l \quad (4.34)$$

$$d_{\text{cr2}} = C_1d_i + (1 - C_1)d_j, d_{\text{cr2}} = C_2d_k + (1 - C_2)d_l.$$

In **Step 4**, a tentative set of center coordinates of a circle, $\bar{\mathbf{X}}_{\text{ct,snel,tnel,unel}}$, is computed using an arbitrary set of three points, $\mathbf{X}_{\text{ab,snel}}$, $\mathbf{X}_{\text{ab,tnel}}$, and $\mathbf{X}_{\text{ab,unel}}$. When m such tentative center points have been computed, the new center coordinates are determined as

$$\mathbf{X}_{\text{ct}} = \frac{\sum_{i=1}^m [W_{\text{snel,tnel,unel}}]_i [\bar{\mathbf{X}}_{\text{ct,snel,tnel,unel}}]_i}{\sum_{i=1}^m [W_{\text{snel,tnel,unel}}]_i}, \quad (4.35)$$

where $W_{\text{snel,tnel,unel}}$ is the total distances of three points, which work as a weight. Finally, the intersection point between the new direction vector $\mathbf{V}_{\text{dir,n}} = \mathbf{X}_{\text{ct}} - \mathbf{X}_{\text{tip,o}}$ and *inel* becomes the new explicit crack tip $\mathbf{X}_{\text{tip,n}}$.

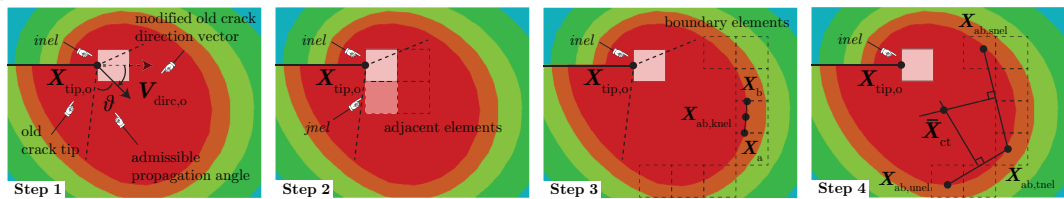
After Algorithm 3 has finished, the state variables and the local physical quantities are mapped from the old to the new nodes and Gaussian points, respectively. Then, the equi-

Algorithm 3 Moving circle algorithm.

```

1: Step 1: Input the explicit crack tip coordinate  $\mathbf{X}_{\text{tip},o}$  and direction vector  $\mathbf{V}_{\text{dir},o}$  for element inel.
2: if Explicit crack tip does not exist, or an additional tip is needed then
3:   Compute the average value of the damage variable  $\bar{d}_{inel}$  for one element inel.
4:   if  $\bar{d}_{inel} \geq d_{cr1}$  then
5:     for jnel within a radius of  $C_3 l_f$  from inel do (%  $C_3 = 2$ : constant)
6:       if  $\bar{d}_{jnel} > \bar{d}_{inel}$  then
7:         inel = jnel (% the explicit crack candidate element is changed)
8:         if There is an explicitly cracked element knel within a radius of  $C_3 l_f$  from inel then
9:           A new explicit crack tip is unnecessary, and this algorithm is terminated.
10:        end if
11:      end if
12:    end for
13:  end if
14: end if
15: Modify the direction vector  $\mathbf{V}_{\text{dir},o}$  by the spatial gradient of damage variable,  $\nabla d$ .
16: Step 2: Compute the average values of the damage variable  $\bar{d}_{inel}$  &  $\bar{d}_{jnel}$  for inel & the adjacent elements jnel.
17: if  $\max[\bar{d}_{inel}, \bar{d}_{jnel}] \geq d_{cr1}$  then (% the explicit crack tip is updated)
18:   while knel  $\leq$  mmel do (% mmel: circle boundary elements,  $\bar{d}_{mmel} \approx d_{cr2}$ )
19:     if  $d_i \leq d_{cr2} \leq d_j$  and  $d_k \leq d_{cr2} \leq d_l$  then
20:       Step 3: Compute the coordinate  $\mathbf{X}_{ab,knel}$  by Eq. (4.34).
21:     end if
22:   end while
23:   while snel  $\leq$  mmel do
24:     while tnel  $\leq$  mmel do
25:       while unel  $\leq$  mmel do (% Three elements should be different from each other.)
26:         Step 4: Compute the tentative center coordinate of circle  $\bar{\mathbf{X}}_{ct}$  with  $\mathbf{X}_{ab,snel}$ ,  $\mathbf{X}_{ab,tnel}$ ,  $\mathbf{X}_{ab,unel}$ .
27:       end while
28:     end while
29:   end while
30:   Compute the new center coordinate  $\mathbf{X}_{ct}$  by Eq. (4.35) and update  $\mathbf{X}_{\text{tip},n}$  &  $\mathbf{V}_{\text{dir},n}$ .
31: end if

```

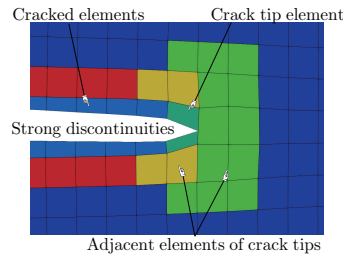


librium conditions of the mechanical and damage fields are no longer fulfilled since the positions of the Gaussian points are changed. Thus, an additional NR loop is conducted to update the geometries around the new crack tips before proceeding to the next FC-based staggered iteration $k + 1$. As a result, the “closed” crack surfaces are opened. However, the opening of a crack tip usually exhibits a large deformation, which is sufficiently large for the size of the cracked element. Given the degraded stiffness of the cracked elements, the global NR computations might not converge. Therefore, we propose a stabilization technique in the following subsection to overcome this concern.

4.5.2 Crack opening stabilization technique

Algorithm 4 Stabilization algorithm for crack opening processes.

- 1: Determine an initial relaxation parameter $C_{\text{relax}} \geq 1$
- 2: **while** $\text{norm}[\text{res}_{u\alpha,s}] > \text{TOL}_{u\alpha}$ **do** (% NR loop for crack openings: $\mathcal{R}_u \in \text{res}_{u\alpha}$ and $\mathcal{R}_\alpha \in \text{res}_{u\alpha}$)
- 3: $s = s + 1$ (% NR iterations)
- 4: Assembling loop for the residual vectors $\mathcal{R}_{u,s}$ and $\mathcal{R}_{\alpha,s}$ and the tangent stiffness matrices $\mathcal{K}_{uu,s}$, $\mathcal{K}_{u\alpha,s}$, $\mathcal{K}_{\alpha u,s}$, and $\mathcal{K}_{\alpha\alpha,s}$.
- 5: **while** $\text{inel} \leq \text{tnel}$ **do** (% tnel : the number of total elements)
- 6: **if** inel is a cracked element except for a crack tip element **then**
- 7: Obtain pseudo-stiffness by $g(d^e) = \max[g(d^e), g_{\min}]$
- 8: **end if**
- 9: **if** inel is a crack tip element or an adjacent element around the crack tips **then**
- 10: Obtain pseudo-stiffness by $g(d^e) = \max[g(d^e), g_{\min}/s]$
- 11: **end if**
- 12: **end while**
- 13: Compute the increments of the displacement vector and global hardening variable, $\delta \mathbf{u}_s$ and $\delta \alpha_s$
- 14: Update the total increments of the displacement vector and global hardening variable, $\Delta \mathbf{u}_{n+1,s}$ and $\Delta \alpha_{n+1,s}$ by Eq. (4.37)
- 15: Update the current displacement vector $\mathbf{u}_{n+1,s}$ by $\mathbf{u}_{n+1,s} = \mathbf{u}_n + \Delta \mathbf{u}_{n+1,s}$
- 16: Update the global hardening variable $\alpha_{n+1,s}$ by $\alpha_{n+1,s} = \alpha_n + \Delta \alpha_{n+1,s}$
- 17: $C_{\text{relax}} = \max[C_{\text{relax}} - 1, 1]$
- 18: **end while**



To maintain numerical stability during the opening process of an explicit crack tip under

quasi-static condition, we introduce a stabilization technique inspired by Mediavilla et al. (1993, 1998). As explained in Algorithm 4, this technique consists of two parts: providing pseudo-stiffness to severely damaged elements and controlling the correctors of the increments of the displacement vector and the global hardening variable within a single NR loop.

In general, in each iteration of an NR loop, the residual vectors $\mathcal{R}_{u,s}$ & $\mathcal{R}_{\alpha,s}$ and tangent stiffness matrices $\mathcal{K}_{uu,s}$, $\mathcal{K}_{u\alpha,s}$, $\mathcal{K}_{\alpha u,s}$, and $\mathcal{K}_{\alpha\alpha,s}$ are obtained in the finite element assembly process. Then, the correctors of the increments of the displacement vector and the global hardening variable, $\delta \mathbf{u}_s$ and $\delta \alpha_s$, are obtained by solving the linearized equation constructed by Eq. (4.12), Eq. (4.13), Eq. (4.16), Eq. (4.17), Eq. (4.19), Eq. (4.20). For the tangent stiffness matrix assembled from the element stiffness matrices of severely damaged elements, the condition number tends to be so large that the NR computation has difficulty in converging. Additionally, an excessively large displacement corrector may cause the collapse of finite elements. To suppress the first factor of instability, pseudo-stiffness is given to severely damaged elements by providing the lowest admissible value g_{\min} for the elastic degradation function $g(d^e)$. Specifically, the following modifications are made to the degradation function:

- For cracked elements except for a crack tip element:

$$g(d^e) = \max [g(d^e), g_{\min}] \quad , \quad (4.36)$$

- For a crack tip element or an adjacent element around a crack tip:

$$g(d^e) = \max [g(d^e), g_{\min}/s]$$

where s denotes the NR iteration number.

Furthermore, to maintain the convergence property of the global NR computations, the reduction in the second factor of instability is made by modifying the correctors of the displacement vector and the global hardening variable, respectively, such that

$$\begin{aligned} \Delta \mathbf{u}_{n+1,s} &= \Delta \mathbf{u}_{n+1,s-1} + \delta \mathbf{u}_s & \Rightarrow & \Delta \mathbf{u}_{n+1,s} = \Delta \mathbf{u}_{n+1,s-1} + \frac{\delta \mathbf{u}_s}{C_{\text{relax}}} \\ \Delta \alpha_{n+1,s} &= \Delta \alpha_{n+1,s-1} + \delta \alpha_s & \Rightarrow & \Delta \alpha_{n+1,s} = \Delta \alpha_{n+1,s-1} + \frac{\delta \alpha_s}{C_{\text{relax}}} \end{aligned} \quad (4.37)$$

where $C_{\text{relax}} \geq 1$ is introduced as a relaxation parameter. Here, the value of C_{relax} is gradually reduced to one at every iteration so that the modified correctors gradually approach the actual ones.

It should be noted that the NR computation for a finite strain problem involving damage tends to diverge with a high probability without this kind of relaxation. As mentioned above, this is not only because the tangent stiffness matrix has a bad condition number but also because the displacement correctors associated with the damaged elements become excessively large. This relaxation is an artificial modification of the NR method and leads to a slow convergence rate but has the advantage that convergent solutions are robustly obtained; this tendency is demonstrated in Section 5.1. It should be noted that the techniques presented here may be needless within the small strain framework assuming linear elastic responses.

Remark 6 *Lowest admissible value g_{\min} :* As explained in Section 4.3, the lowest admissible value g_{\min} is given to severely damaged elements, but its reasonable value is difficult to establish. In light of actual failures, since the regions around discrete crack surfaces are still sound or only have slight deterioration, a full or nearly full recovery of the degradation function, i.e., $g_{\min} \rightarrow 1$, seems to be reasonable. Nevertheless, such an artificial recovery would result in an imbalance in the stress state around the crack tip, which may also affect the geometry of the crack path. In this study, to reproduce the same crack path obtained by the CPFEM along with the standard FEM, we only give a small value $g_{\min} = 0.05 \sim 0.10$ to avoid significantly changing the stress state. Note that the treatment of the stiffness recovery during the transition process from diffuse to discrete cracks is an open topic and is left as a future research item.

Table 4.1: Similarities and differences between previous studies and this study.

Working group	Strain	2D/3D	Method	Crack tip	Targeting problem
	When and How crack paths or tips are updated				
Giovanardi et al. ¹²⁹⁾	Small	2D	XFEM	Implicit	Brittle fracture
	The regions outside of crack tips are updated at the end of each time step.				
Geelen et al. ¹³⁰⁾	Small	2D	XFEM	Explicit*	Brittle fracture
	Crack tips are updated by a switching criterion at the end of each time step.				
Muixí et al. ¹³¹⁾	Small	2D/3D	XFEM	Implicit	Brittle fracture
	The regions outside of crack tips are updated at the end of each time step.				
Sun et al. ¹³²⁾	Small	2D/3D	FEMM	Explicit*	Brittle fracture
	Crack tips are updated by a switching criterion ¹³⁰⁾ at the end of each time step.				
Hussein et al. ¹³³⁾	Small	2D	VEM	Explicit*	Brittle fracture
	Crack tips are updated by length minimization problems at the end of each time step.				
Yang et al. ¹³⁴⁾	Small	2D	NMM	Explicit*	Brittle fracture
	Crack tips are updated by finding the farthest damaged nodes at the end of each time step.				
This study	Finite	2D/3D	FCM	Explicit	Brittle, dynamic, and ductile fractures
	Crack tips are updated by the moving circle algorithm at the end of each staggered iteration.				

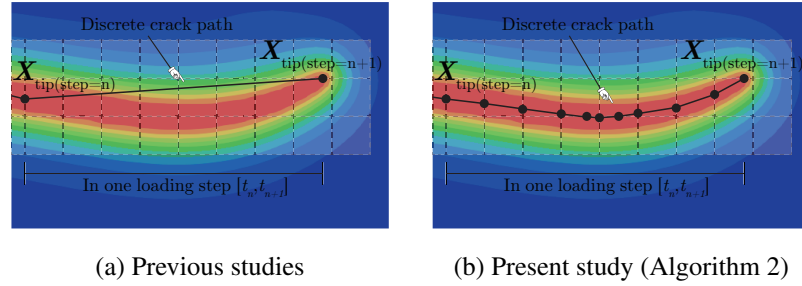


Fig. 4.5: Example of updating discrete crack surfaces: comparison between previous studies and this study.

4.6 Similarities and differences between previous studies and this study

To close this chapter, let us explore the similarities and differences between the previous studies and this study, as summarized in Table 4.1. First, they have the same motivation and concept. That is, the crack initiation and propagation steps are predicted by an energy minimization problem within the CPF framework, while the predicted diffusive crack is rep-

resented explicitly by introducing a strong discontinuity by a meshfree method. Specifically, the proposed scheme is similar to those of some previous studies ^{130),132),133),134)} in that both the crack tips and paths are expressed explicitly. In contrast, this study differs from several previous studies ^{129),131)}, in which the crack tips were treated implicitly. In the former four studies, the explicit path of a propagated crack was generated only at the end of each loading step by connecting the old and new crack tips with a straight line. This approach may cause inconvenience when the crack propagates dramatically at once or while bending within a single loading step. As illustrated in Fig. 4.5(a), if the crack propagated during one loading step is curved, the discrete crack path is not consistent with the diffusive path.

On the other hand, we have proposed a different scheme to realize the transition from diffuse to discrete crack topologies. That is, the explicit crack tips are updated at each FC-based staggered iteration in the FC-based staggered iterative algorithm with the help of the technique presented in Section 4.2 and FCM technology. Due to this approach, the proposed scheme successfully realizes the discrete crack path by tracing the diffusive path, as illustrated in Fig. 4.5(b), which demonstrates that the present scheme is superior to other existing techniques. In addition, while all the previous studies shown in Table 1.1 were made within the small strain framework, this study adheres to finite strain theory because configuration changes are often critical to predicting the failure processes of structures. Also, while they were only applied to the quasi-static brittle fracture problems, the proposed framework can simulate the brittle and ductile fractures under both the quasi-static and dynamic conditions. To accomplish crack opening and propagation in a stable manner, we have introduced the stabilization techniques presented in Section 4.3 and Section 4.5.2 for both the quasi-static and dynamic conditions, by which the new explicit crack tip is gradually and stably opened.

5 Numerical simulations by CPFFCM

In this chapter, several numerical examples are presented to demonstrate the ability and performance of the developed method (CPFFCM). In particular, a series of failure events from the damage initiation to the post-failure phase, occurring in brittle and ductile materials under quasi-static and dynamic conditions, are simulated.

5.1 Quasi-static brittle fracture

Table 5.1: Material parameters for numerical simulations in Section 5.1.1 ~ Section 5.1.4.

Parameter		Value	Unit
Young's modulus	E	200000	[MPa]
Poisson's ratio	ν	0.3	[-]
Fracture toughness	G_c	2.7	[N/mm]
Crack length scale parameter	l_f	0.008	[mm]

This section is devoted to demonstrating the ability of the scheme proposed in the previous chapter by solving four representative numerical examples describing the quasi-static brittle fracture. For the sake of comparison, we conduct simulations using both the present scheme with the FCM and the standard FEM with the conventional CPF model. Throughout this section, the former is referred to as “CPFFCM”, and the latter is denoted as “CPFFEM”. Furthermore, the same set of material parameters listed in Table 5.1 is used for the numerical examples in Section 5.1.1 ~ Section 5.1.4. Additionally, we redefine degradation functions for CPFFEM as $g(d) = \max[g(d), k]$ with a small value $k = 0.0001$ to maintain the conver-

gence of the NR computations.

5.1.1 Example 5-1-1: Tensile failure of single-edge notched specimen

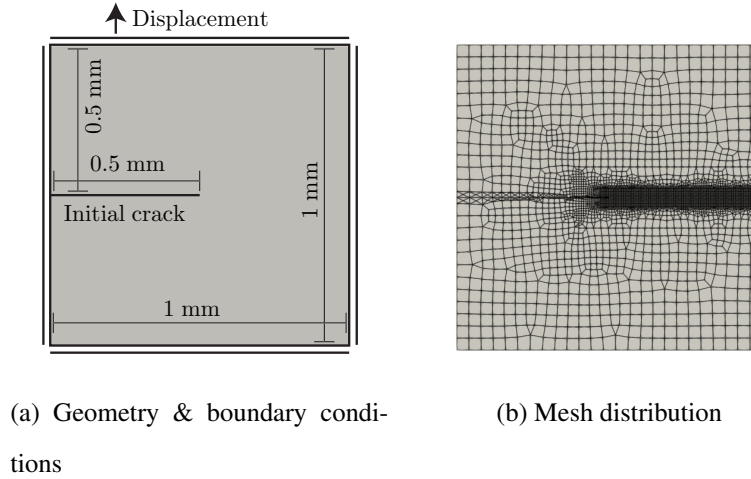


Fig. 5.1: Geometry with boundary conditions and mesh distribution for Example 5-1-1.

The first example considers the tensile failure of a single-edge notched specimen, illustrated in Fig. 5.1(a), along with the boundary conditions. In this example, the basic performance of the proposed scheme is examined, and the necessity of the crack opening stabilization technique is also discussed. An initial crack is located at the center of the left edge and has a length of 0.5 [mm]. The right and left edges are fixed horizontally, while the bottom edge is fixed vertically. Vertical displacement is gradually applied to the top edge until a crack path separates the specimen. A displacement increment of $\Delta u = 1 \cdot 10^{-5}$ [mm] is applied at each loading step starting just before the crack forms. Additionally, the element size h_e is set at $2h_e < l_f$ for the potentially damaged region, as shown in Fig. 5.1(b). In addition, we use $d_{cr1} = 0.98$, $d_{cr2} = 0.50$, $C_{relax} = 10$, and $g_{min} = 0.05$ for Algorithm 3 and Algorithm 4.

In this tension test, we conduct simulations by employing the quadratic and cubic degradation functions, so the number of analysis cases is four. Fig. 5.2 shows the load-displacement curves for the four cases, in which the left and right figures show the overview and enlarged view around the load peaks, respectively. Here, Cases Q1 & Q2 employ the quadratic func-

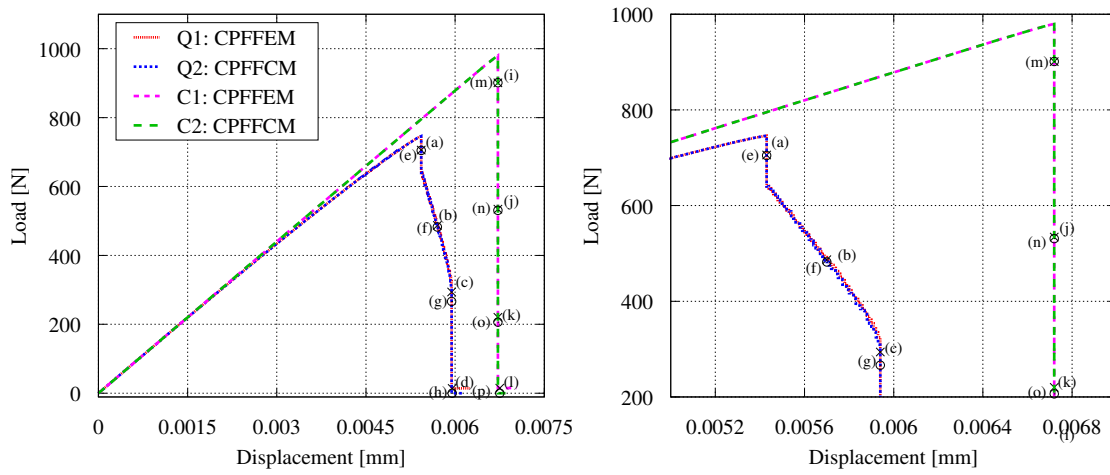


Fig. 5.2: Load-displacement curves obtained for Example 5-1-1.

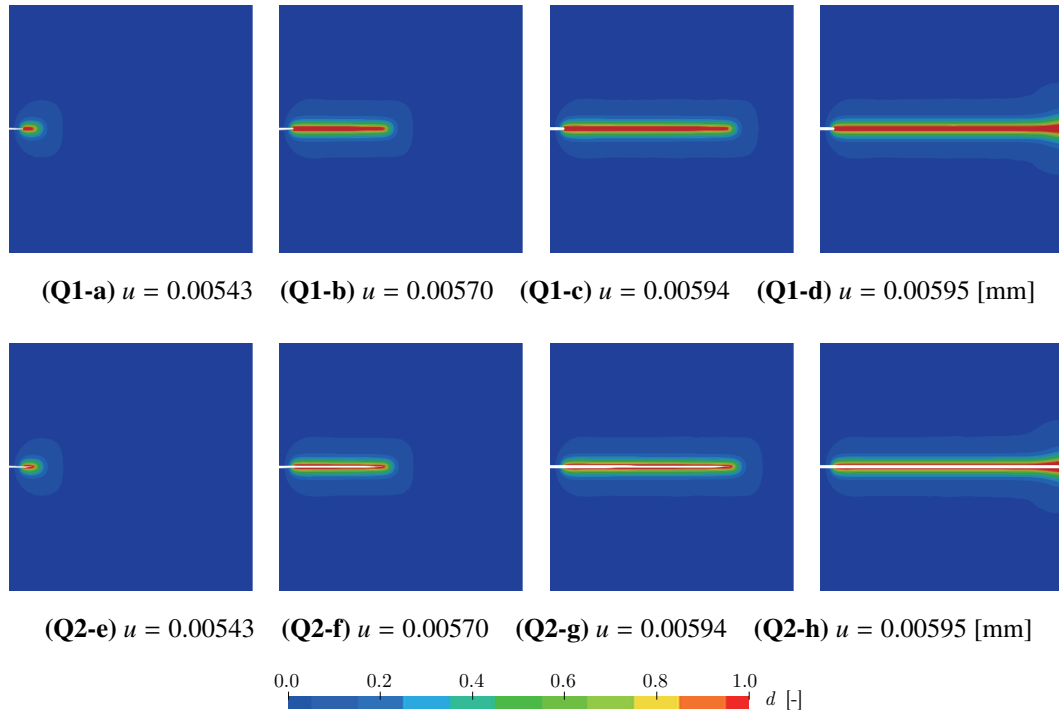


Fig. 5.3: Snapshots of the crack evolutions obtained for Example 5-1-1 (Cases Q1 and Q2).

tion, while Cases C1 & C2 employ the cubic function. Additionally, Cases Q1 & C1 are computed by CPFFEM, while Cases Q2 & C2 are computed by CPFFCM. As seen from this figure, Case Q2 exhibits a slightly faster load drop than Case Q1; see the red and blue dashed lines in the enlarged view. In fact, the crack propagation process of Case Q2 is also

slightly faster than that of Case Q1, as shown in Fig. 5.3. Although only a slight difference is observed here, the difference becomes clear in the following numerical examples. This tendency is thought to be due to the strong discontinuity representation ability of CPFFCM; that is, stress transfer does not occur between the crack surfaces in the CPFFCM case. Additionally, due to the explicit representation of crack surfaces, the load becomes exactly zero when the specimen is separated, whereas the load of Case Q1 still has a small value due to the parameter $k = 0.0001$ set to maintain the numerical stability, as shown in Fig. 5.2. Note that similar tendencies and considerations are reported in Geelen et al.¹³⁰.

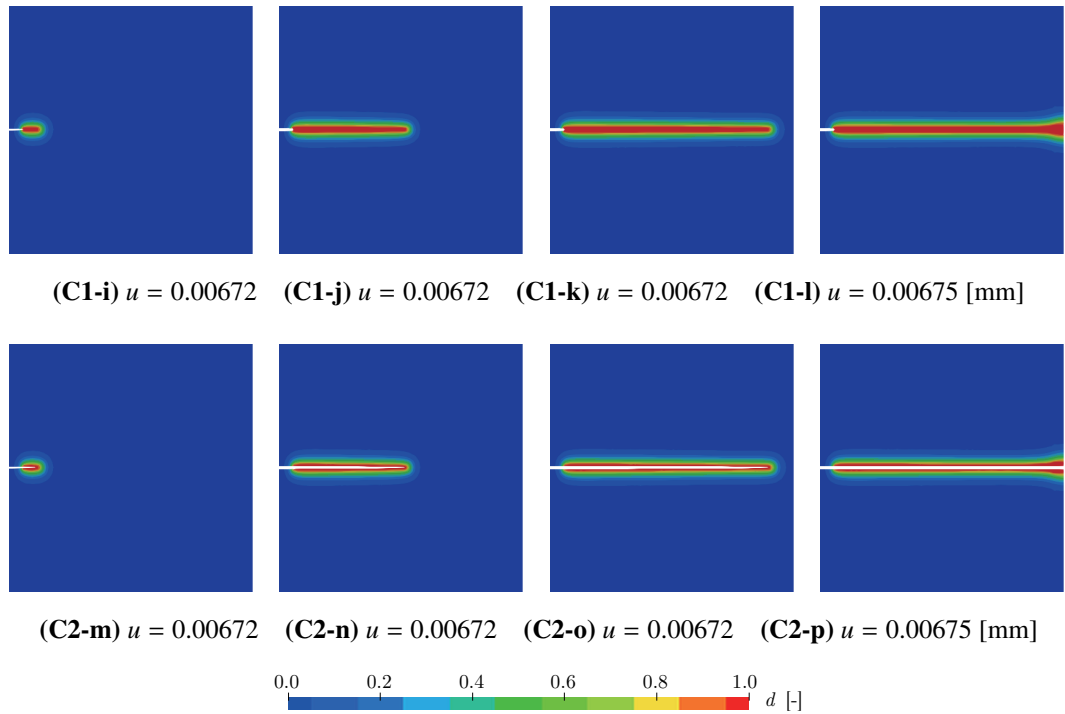


Fig. 5.4: Snapshots of the crack evolutions obtained for Example 5-1-1 (Cases C1 and C2).

On the other hand, the load-displacement curves of Cases C1 & C2 exhibit almost the same response. That is, they have higher load peaks and reveal more brittle-like failures than Cases Q1 & Q2. This is due to the property of the cubic degradation function. Specifically, since the cubic degradation function slightly exhibits a softening behavior up to the peak stress, Cases C1 & C2 have almost linear load increases. Once they reach the stress peak, both cases show load reductions in the almost vertical direction until the loads become nearly

zero. In fact, crack initiation and propagation followed by specimen separation occur in one loading step with approximately 250 FC-based staggered iterations. The first three stages in Fig. 5.4 show the crack propagations that occur during the FC-staggered iterative procedure in one loading step, so the value of displacement does not increase. Additionally, since the explicit crack tip is updated in each FC-based staggered iteration if needed, the length of its path gradually increases even in one loading step. If some of the previous studies presented in Table 1.1 solved this problem, they could update the discrete crack path only at the end of each loading step. This is somewhat unreasonable when a curved crack appears in a short time interval, which will be seen in the following numerical examples.

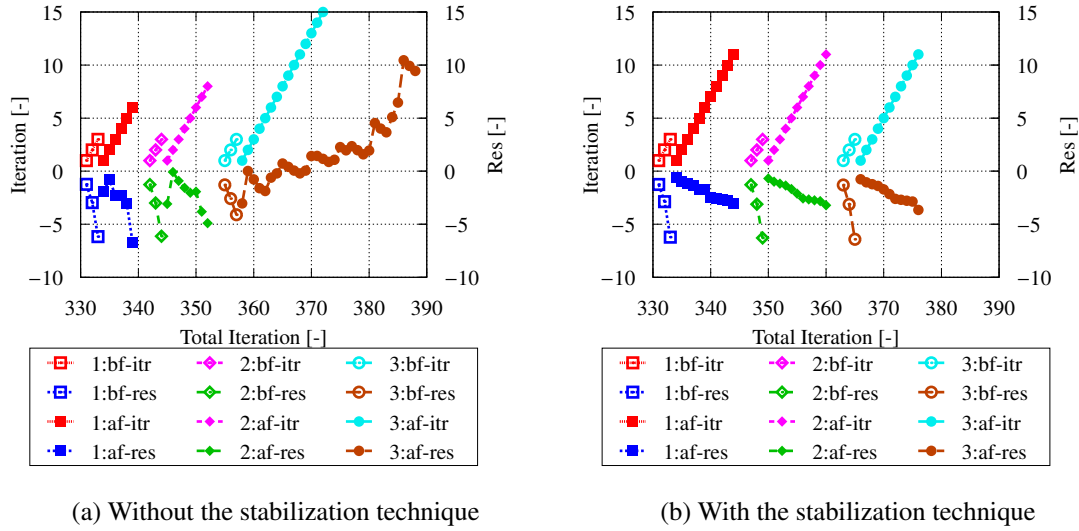


Fig. 5.5: Relationships between the number of iterations and residuals obtained for Example 5-1-1 (without/with the stabilization technique in Algorithm 4).

In addition, let us use the result of Case C2 to discuss the accomplished numerical stability of CPFFCM in solving finite deformation problems. Fig. 5.5 shows the relationships between the numbers of iterations and the residuals at the range in which the first three elements are divided after crack initiation, where the left and right figures, (a) & (b), show the curves obtained without & with the stabilization technique, respectively. Note here that the logarithmic residuals of the displacement field are shown, and the relationships for the

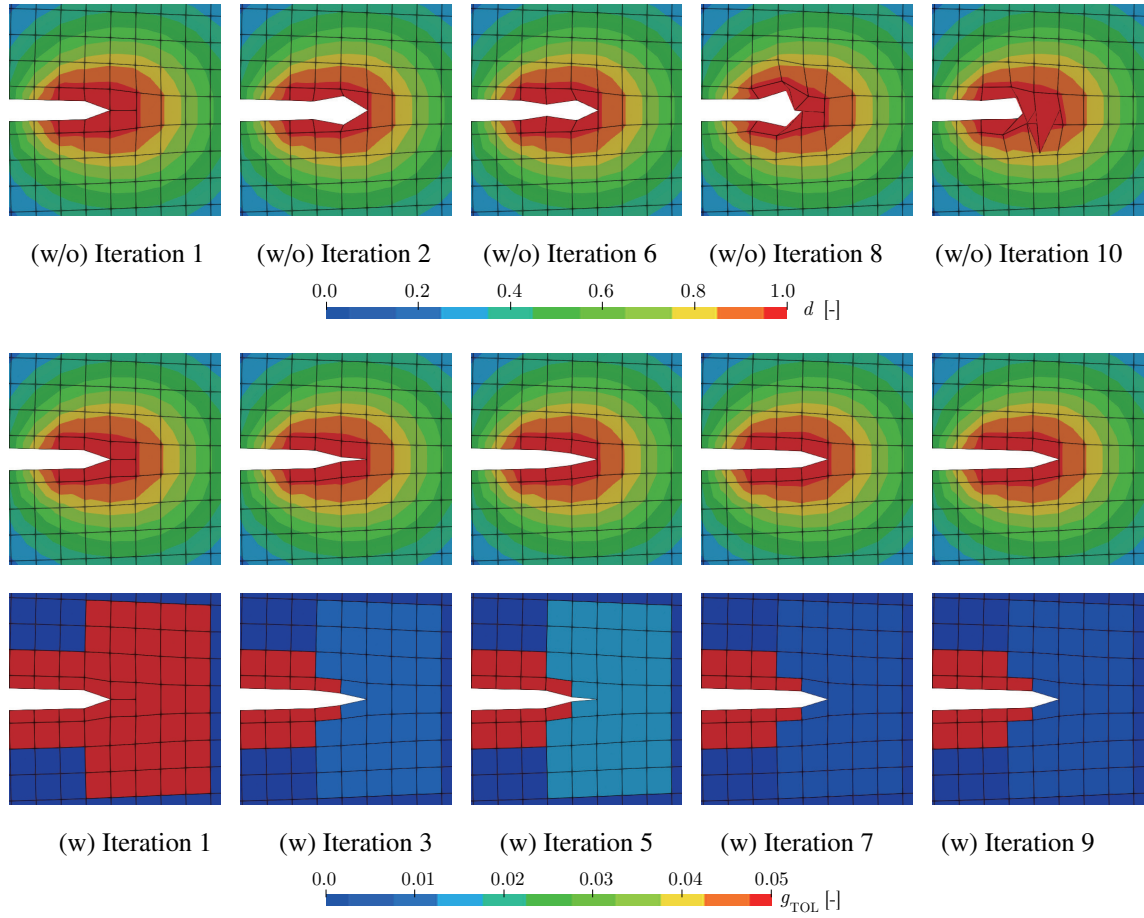


Fig. 5.6: Snapshots of the crack openings obtained for Example 5-1-1 (without/with the stabilization technique) (Algorithm 4).

crack phase-field are not presented. Here, the labels “digit”, “bf/af” and “itr/res” of “digit-bf/af-itr/res” in Fig. 5.5 indicate the number of divided elements, the situation before/after the explicit crack tip update by the FCM, and the iteration/residual curve, respectively. For instance, “2-af-res” indicates the residual curve of the NR loop immediately after the second crack is explicitly expressed by the FCM.

As shown in Fig. 5.5(a), which presents the results obtained without the stabilization technique, the NR computation process diverges when the third divided element opens. In contrast, although each “af” case in Fig. 5.5(b) does not exhibit a fast convergence behavior, the logarithmic residual gradually decreases. Additionally, Fig. 5.6 shows the processes of crack opening for the NR loop “3-af”, where the labels “w/o” and “w” denote the cases with-

out and with the stabilization technique, respectively. As seen from the top five snapshots that show the results obtained without the stabilization technique, the improper evaluation of the displacement around the crack tip results in computational failure. In contrast, as seen from the middle/bottom five figures showing the distributions of the CPF variable and the lowest admissible value for pseudo-stiffness, the crack is gradually opened, iteration by iteration, due to the stabilization algorithm. Thus, the proposed scheme successfully realizes stable crack opening within the finite strain framework involving severely damaged elements.

Remark 7 *Breakdown of computation time:* The added cost of CPFFCM to CPFFEM is relevant to lines 7-11 in Algorithm 2. As explained above, the crack penetrates the specimen in one loading step for Cases C1 & C2. Then, the computation times by the two methods are 673 seconds for CPFFEM and 1459 seconds for CPFFCM, respectively. More specifically, for CPFFCM, the breakdown is as follows: 76 seconds (5.2%) for the moving circle algorithm, 32 seconds (2.2%) for the reconstruction of input files defining an updated geometry with its boundary conditions, 571 seconds (39.1%) for the stabilization, 680 seconds (46.6%) for the remaining standard CPF computations, and 100 seconds (6.8%) for the switching of CPF and FCM programs. Depending on the setup, the computation time of CPFFCM takes about twice as long as that of CPFFEM.

5.1.2 Example 5-1-2: Shear failure of single-edge notched specimen

The second example considers a shear failure of the same specimen presented in the previous example but with different boundary conditions, as shown in Fig. 5.7(a). Here, the performance of the moving circle algorithm (Algorithm 3) is investigated along with its illustration. A horizontal displacement is applied to the top edge, while the right and left edges are fixed vertically, and the bottom edge is fully fixed. Then, a displacement increment of $\Delta u = 2 \cdot 10^{-6}$ [mm] is applied at each loading step starting just before crack initiation occurs. The element size is set at $2h_e < l_f$ for the potentially damaged region, as shown in Fig. 5.7(b). Additionally, we use $d_{cr1} = 0.98$, $d_{cr2} = 0.60$, $C_{relax} = 10$, and $g_{min} = 0.05$ for the algorithms in Algorithm 3 and Algorithm 4.

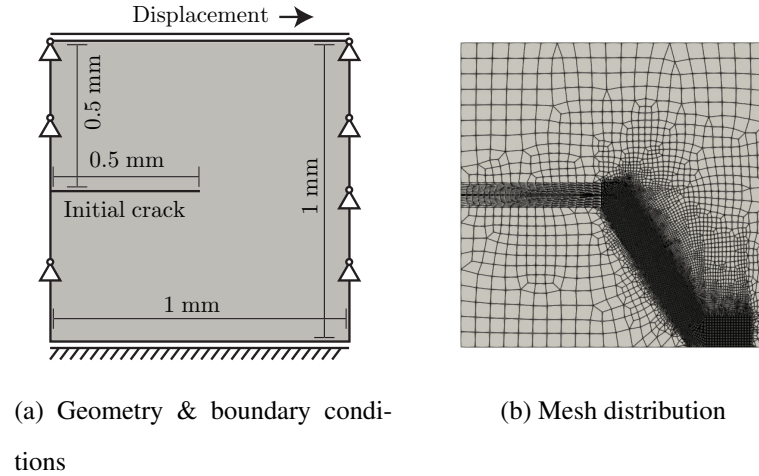


Fig. 5.7: Geometry with boundary conditions and mesh distribution for Example 5-1-2.

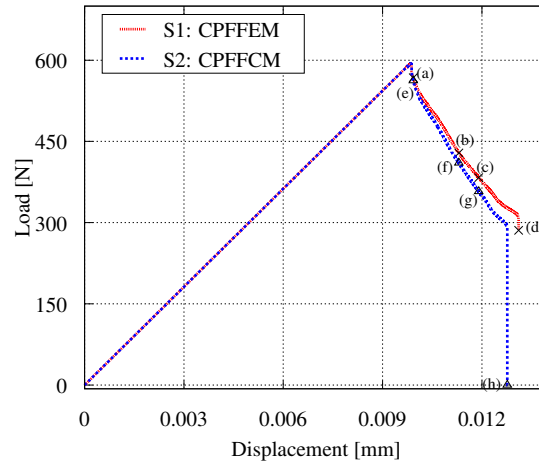


Fig. 5.8: Load-displacement curves obtained for Example 5-1-2.

Simulations are conducted with CPFFEM (Case S1) and CPFFCM (Case S2) separately. The obtained load-displacement curves are shown in Fig. 5.8. The curve of Case S2 exhibits a faster load drop than that of Case S1. As explained in the previous example, this is due to the strong discontinuity representation as explained before. Fig. 5.9 shows snapshots of the crack evolution processes for the two cases. Additionally, for further visual understanding, Fig. 5.10 provides the overlay of Case S1 on S2, where the dotted lines indicate diffusive cracks with $d \approx 0.95$. As seen from these figures, the crack path of Case S2 is in agreement with that of Case S1. Nevertheless, it is confirmed that CPFFCM certainly shows faster crack

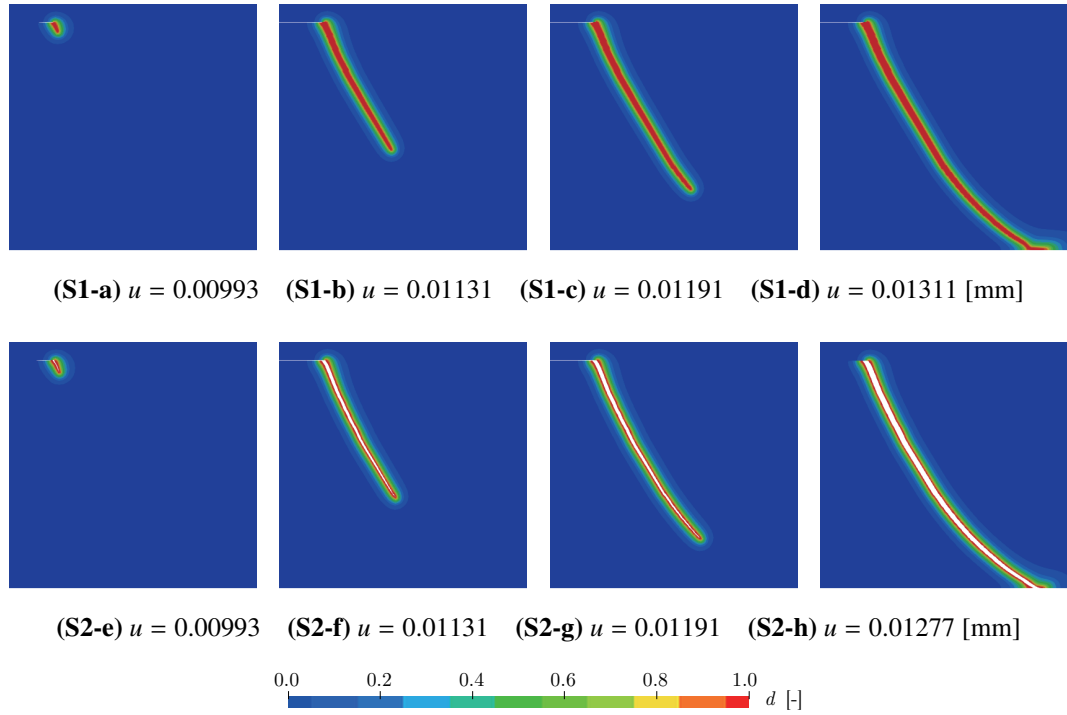


Fig. 5.9: Snapshots of the crack evolutions obtained for Example 5-1-2.

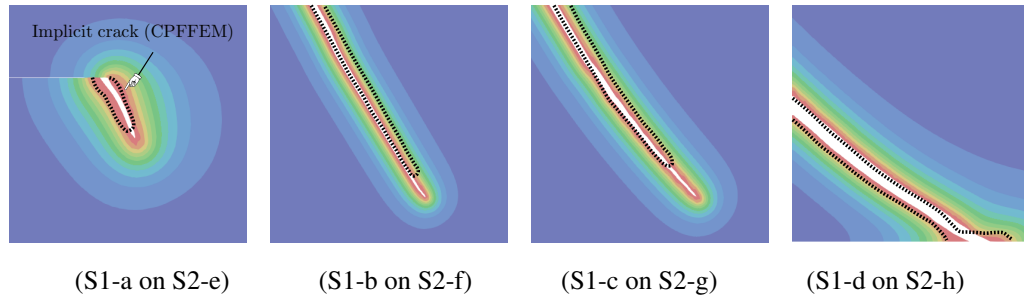


Fig. 5.10: Overlay of a diffuse crack obtained by CPFFEM on a discrete crack provided by CPFFCM for Example 5-1-2 (the dotted lines indicate $d \approx 0.95$).

propagation than CPFFEM.

Furthermore, for the sake of illustration, Fig. 5.11 provides snapshots of the procedure in the moving circle algorithm. When the diffuse crack propagates enough to update a new explicit crack tip (Fig. 5.11(a)&(b)), the center of the moving circle (Fig. 5.11(c)) is determined by Algorithm 3. Then, if the direction vector originating from the coordinates of the old crack tip toward the center of the circle penetrates the damaged elements, the explicit

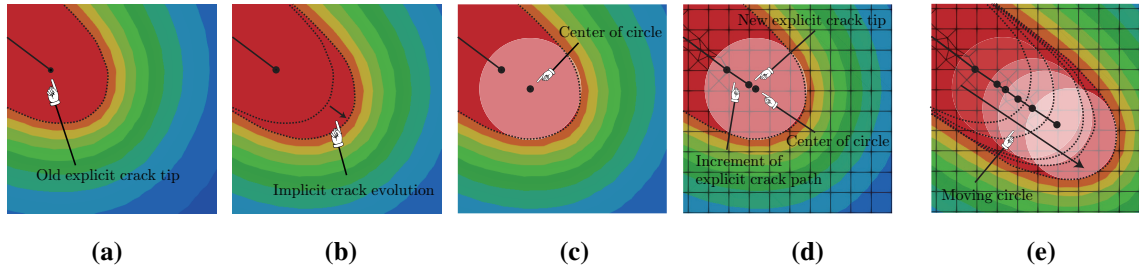


Fig. 5.11: Illustration of the moving circle algorithm (the dotted lines indicate $d \approx 0.60$).

crack tip is updated (Fig. 5.11(d)). As the circle moves in this manner, the trajectory of the center draws the discrete crack path (Fig. 5.11(e)). Thanks to the moving circle algorithm, a smooth crack path is explicitly reproduced. This ability may be helpful for solving the contact problem of divided elements, although it is not yet our current agenda.

5.1.3 Example 5-1-3: Tensile failure of double-edge notched asymmetric specimen

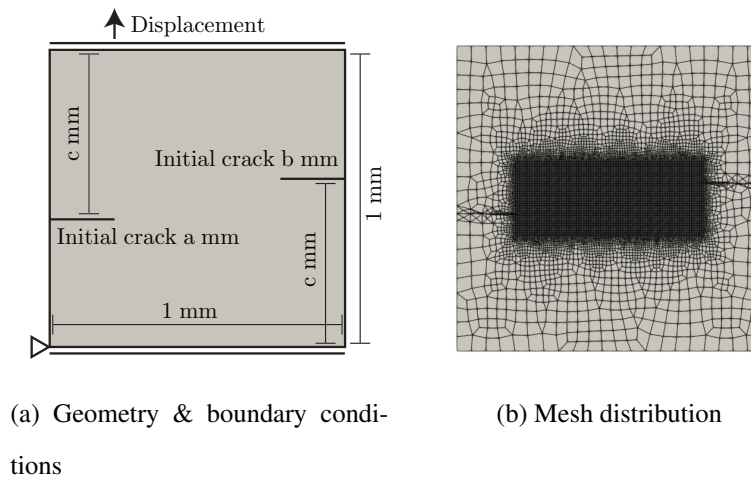


Fig. 5.12: Geometry with boundary conditions and mesh distribution for Example 5-1-3.

The third example targets the tensile failure of a double-edge notched asymmetric specimen, as illustrated in Fig. 5.12(a), along with the boundary conditions. The main objective of this example is to compare CPFFEM and CPFFCM in terms of numerical stability. In particular, we show that CPFFCM enables us to conduct simulations until the specimens are

completely separated, whereas CPFFEM cannot. Additionally, the ability of Algorithm 3 to reproduce the smooth paths of discrete cracks is demonstrated as in the previous example. The initial cracks are placed asymmetrically at the left and right edges. We prepare three geometries with different initial crack lengths and different distances from the top and bottom edges: Cases D1 & D2 with $(a, b, c) = (0.20, 0.20, 0.55)$, Cases D3 & D4 with $(a, b, c) = (0.30, 0.20, 0.55)$, and Cases D5 & D6 with $(a, b, c) = (0.20, 0.20, 0.585)$. Here, CPFFEM is used for Cases D1, D3, and D5, while CPFFCM is used for D2, D4, and D6. For each geometry, a vertical displacement is given to the top edge, and the bottom edge is fixed in the vertical direction. A displacement increment of $\Delta u = 1 \cdot 10^{-5}$ [mm] is applied for each loading step starting just before crack initiation occurs. Furthermore, the element size h_e is set at $2h_e < l_f$ for the potentially damaged region, as shown in Fig. 5.12(b). In addition, $d_{cr1} = 0.98$, $d_{cr2} = 0.50$, and $C_3 = 5$ are given for Algorithm 3, and $C_{relax} = 10$ & $g_{min} = 0.05$ are used in Algorithm 4.

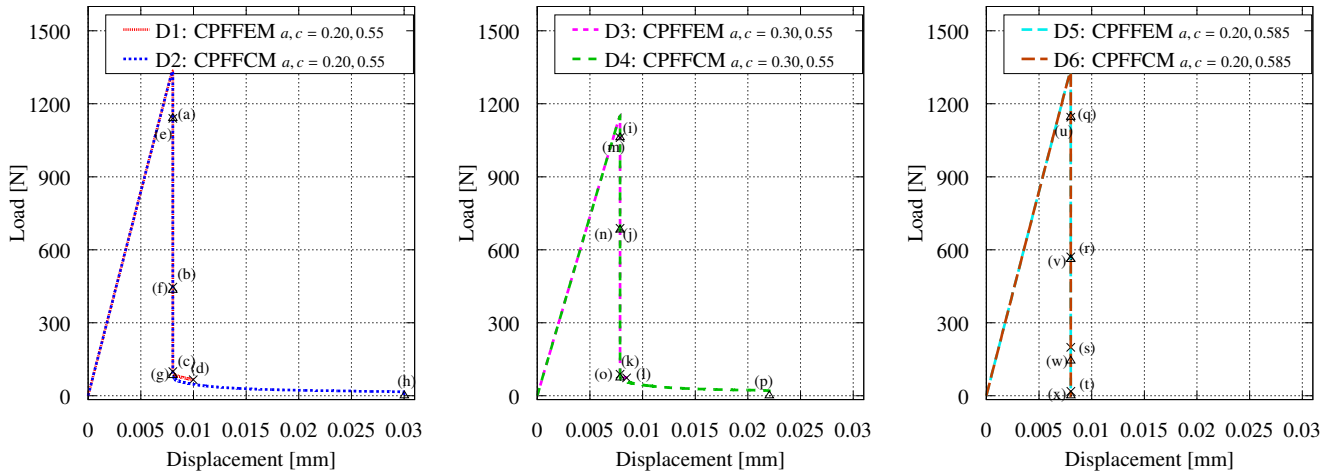


Fig. 5.13: Load-displacement curves obtained for Example 5-1-3.

Fig. 5.13 shows the load-displacement curves obtained for the six cases, and snapshots of the crack evolution processes are shown in Fig. 5.14 ~ Fig. 5.16. Here, the first three figures of each case are obtained in one loading step, and the last figure corresponds to the moment either just before the NR computation diverges when using CPFFEM or just after the specimen is separated by a discrete crack when using CPFFCM. Curved crack paths are

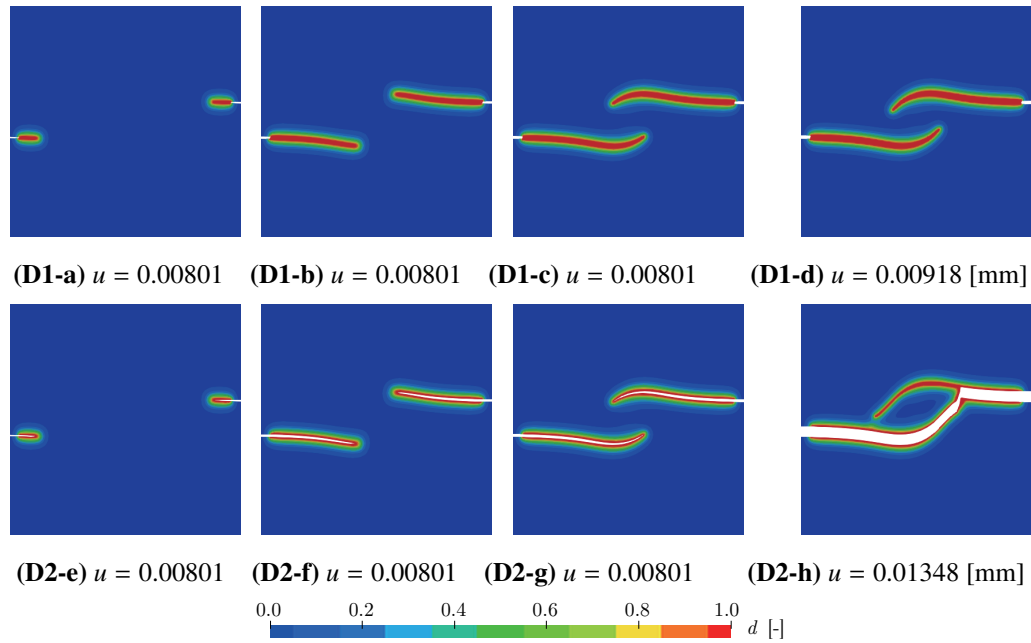


Fig. 5.14: Snapshots of the crack evolutions obtained for Example 5-1-3: Case D1 and Case D2.

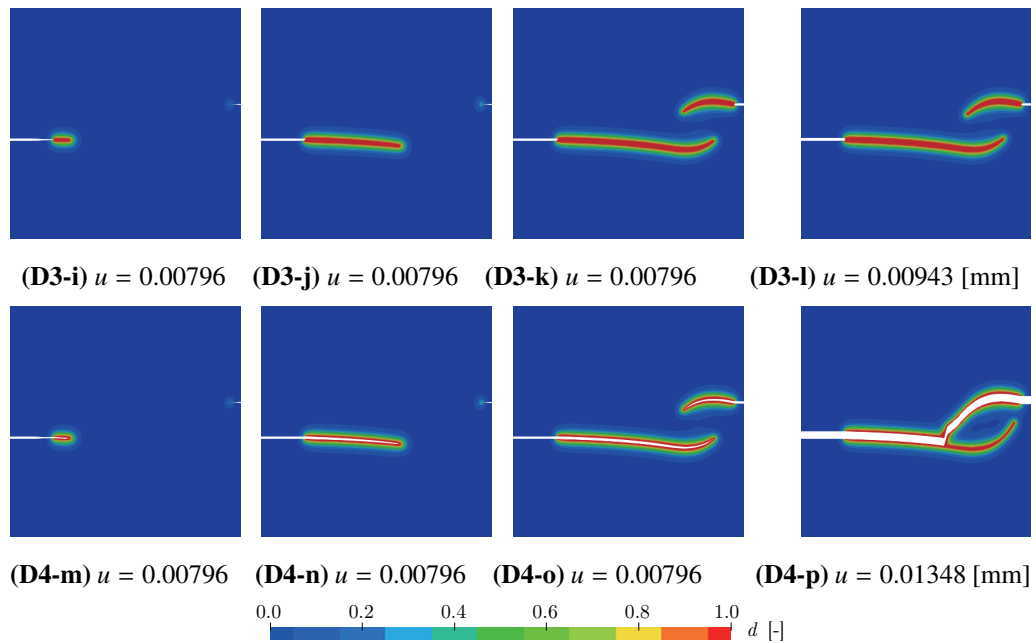


Fig. 5.15: Snapshots of the crack evolutions obtained for Example 5-1-3: Case D3 and Case D4.

observed in the first three snapshots for the three geometries, in which the results produced

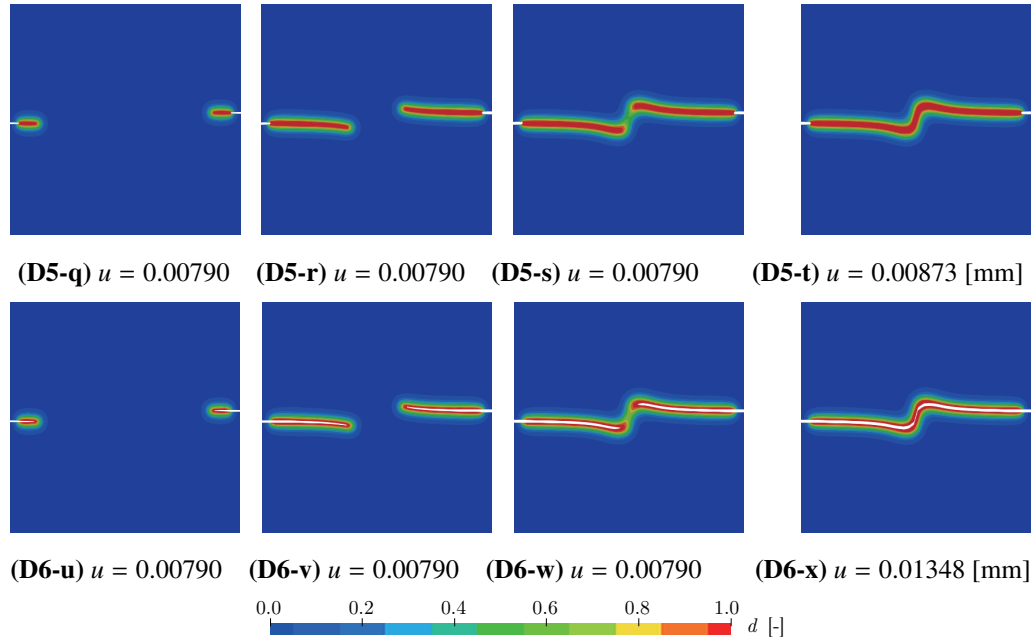


Fig. 5.16: Snapshots of the crack evolutions obtained for Example 5-1-3: Case D5 and Case D6.

by the CPFFCM are in good agreement with those by the CPFFEM. As explained in Section 4.4, in previous studies, the explicit crack tips were updated at the end of each loading step by connecting the old and new crack tips with a straight line. In that case, the curved crack path is difficult to trace. In contrast, the proposed scheme overcomes this inconvenience and realizes smooth paths for discrete cracks because the explicit crack tips are updated in each FC-based staggered iteration.

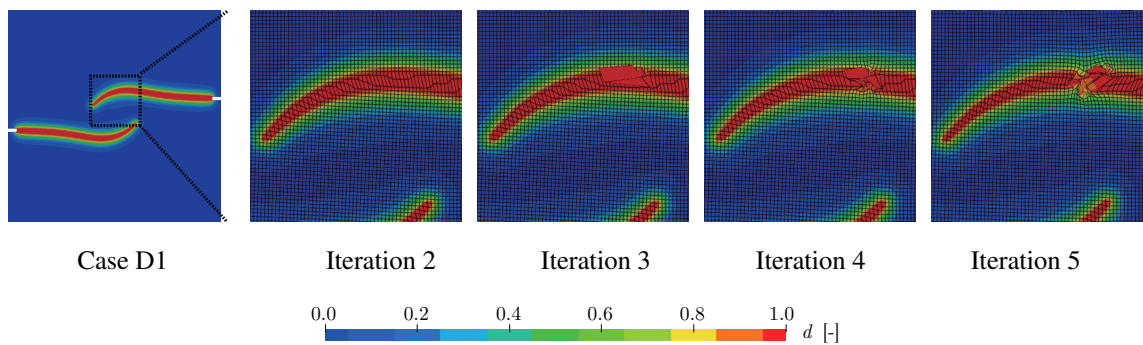


Fig. 5.17: Illustration of the collapsed element group when the global NR computation diverges in CPFFEM: Case D1 in Example 5-1-3.

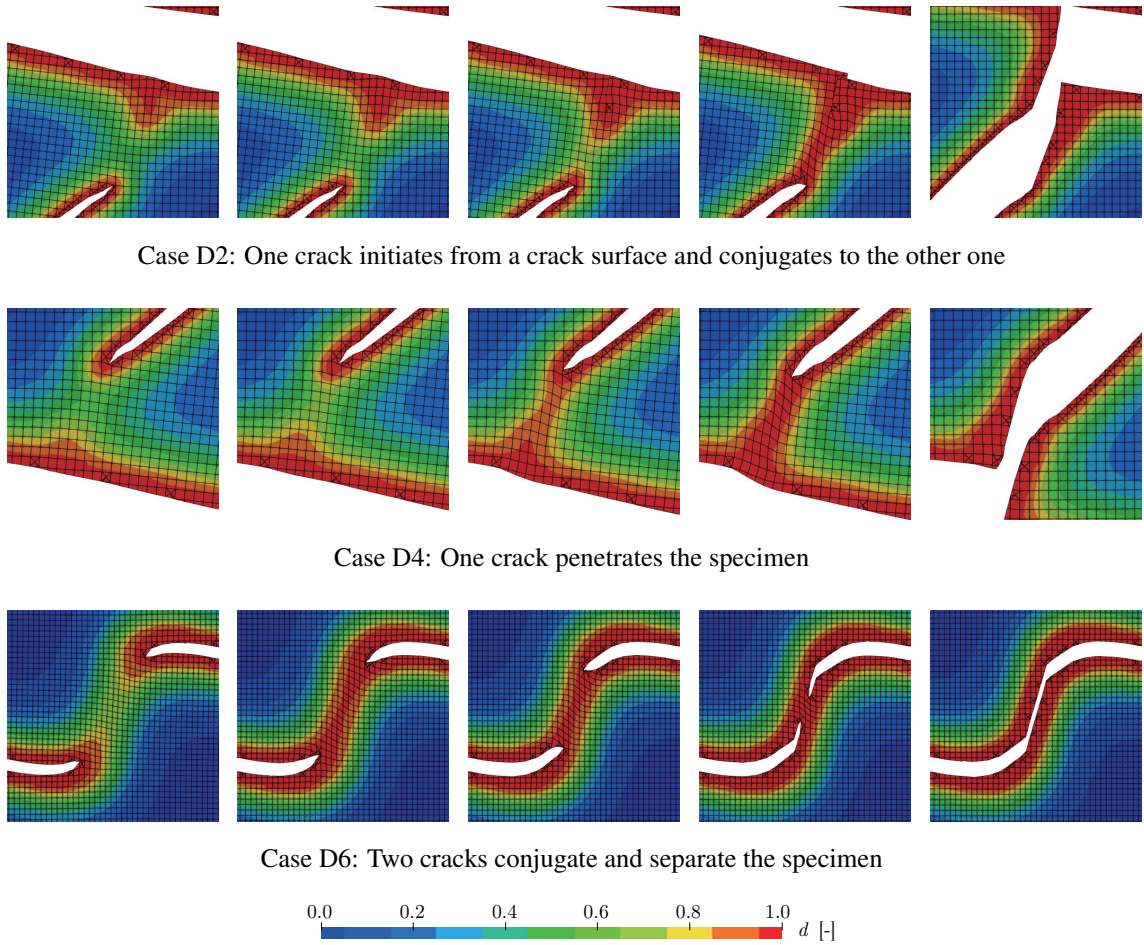


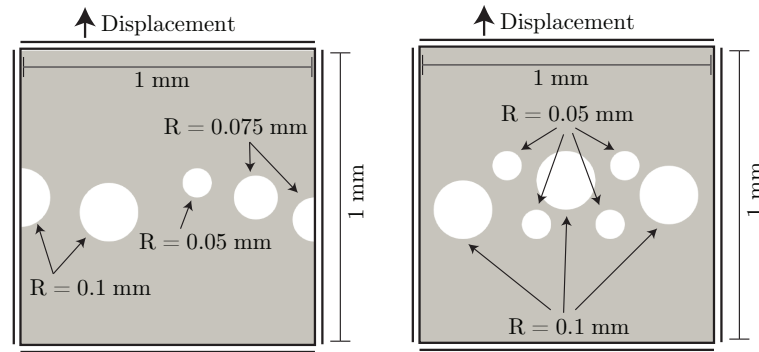
Fig. 5.18: Illustrations of different scenarios involving two crack connections with three geometries in Example 5-1-3.

On the other hand, as seen from the results of Cases D1~D4 in Fig. 5.13, the total displacements of CPFFEM are much smaller than those of CPFFCM. This is because the NR computations diverge when using CPFFEM due to the oscillatory correctors or the collapse of damaged elements. Fig. 5.17 illustrates an example of a collapsed element group obtained using CPFFEM at the loading step immediately after (D1-d) in Fig. 5.14. Conversely, the computations performed using CPFFCM continue until the specimens are separated by discrete cracks. Indeed, thanks to the explicit representations of crack surfaces in CPFFCM, different scenarios for two crack connections with the three geometries are successfully obtained, as shown in Fig. 5.18. Specifically, for Case D2, when the lower crack tip approaches the upper crack surface, a new crack tip appears from the middle part of the upper crack

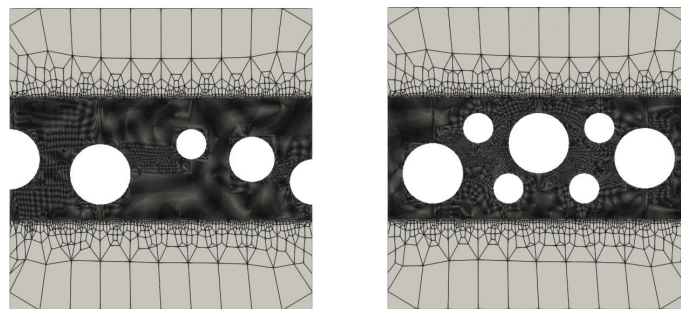
surface and connects with the lower crack tip. Accordingly, the specimen is separated by a single crack path, and the upper crack is closed at the end, as shown in Fig. 5.14(D2-h). Although an area where the physical domains overlap with each other is observed, this can be avoided if we consider the contact condition between them, which will be another future research topic. On the other hand, Case D4 is the case in which the upper crack penetrates the specimen without the appearance of a crack tip on the middle part of the lower crack surface, and the lower crack is closed at the end; see Fig. 5.15(D4-p) and the middle panel of Fig. 5.18. In addition, as seen from Fig. 5.16(D6) and the bottom panel of Fig. 5.18 for Case D6, the upper and lower cracks form a single crack path without ever crossing each other. Given that these separation scenarios cannot be computed with CPFFEM, we can safely conclude that CPFFCM endowed with the proposed scheme is more stable in terms of simulating crack propagations than the conventional methods.

5.1.4 Example 5-1-4: Tensile failure of multiholed specimen

The last example considers the tensile failures of complex geometries without initial cracks. Two geometries are considered, as shown in Fig. 5.19(a), along with the boundary conditions: Case H1 “5-hole” and Case H2 “7-hole”. The 5-hole specimen has two half and three whole circular holes, whose center coordinates are set at $(x, y) = (0, 0.5)$, $(0.35, 0.45)$, $(0.6, 0.55)$, $(0.75, 0.5)$, $(1, 0.425)$ from left to right. On the other hand, the 7-hole specimen has three large and four small circular holes, whose center coordinates are set at $(x, y) = (0.15, 0.4)$, $(0.5, 0.55)$, $(0.85, 0.5)$ for the larger holes and $(x, y) = (0.3, 0.55)$, $(0.4, 0.35)$, $(0.65, 0.35)$, $(0.7, 0.6)$ for the smaller holes from left to right. In the simulations, a vertical displacement is applied on the top edge, the right and left edges are fixed in the horizontal direction, and the bottom edge is fixed in the vertical direction. Then, a displacement increment of $\Delta u = 2 \cdot 10^{-6}$ [mm] is applied for each loading step starting just before crack initiation occurs. The element size h_e is set at $2h_e < l_f$ for the potentially damaged region, as shown in Fig. 5.19(b). Additionally, $d_{cr1} = 0.98$, $d_{cr2} = 0.50$, $C_3 = 5$, $C_{relax} = 10$, and $g_{min} = 0.10$ are used for Algorithm 3 and Algorithm 4.



(a) Geometry & boundary conditions (Left: 5-hole specimen, Right: 7-hole specimen)



(b) Mesh distribution (Left: 5-hole specimen, Right: 7-hole specimen)

Fig. 5.19: Geometry with boundary conditions and mesh distributions for Example 5-1-4.

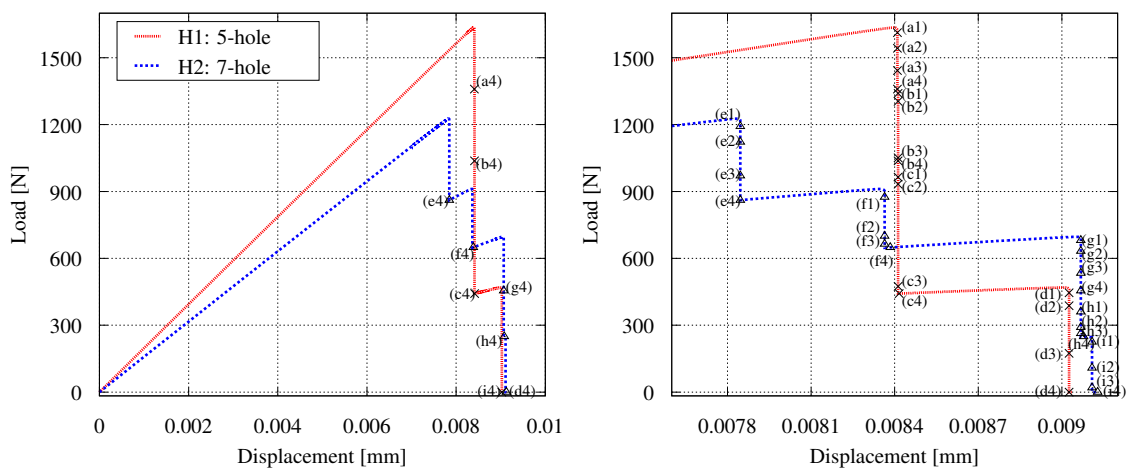


Fig. 5.20: Load-displacement curves obtained for Example 5-1-4.

The simulated load-displacement curves for the two geometries are shown in Fig. 5.20,

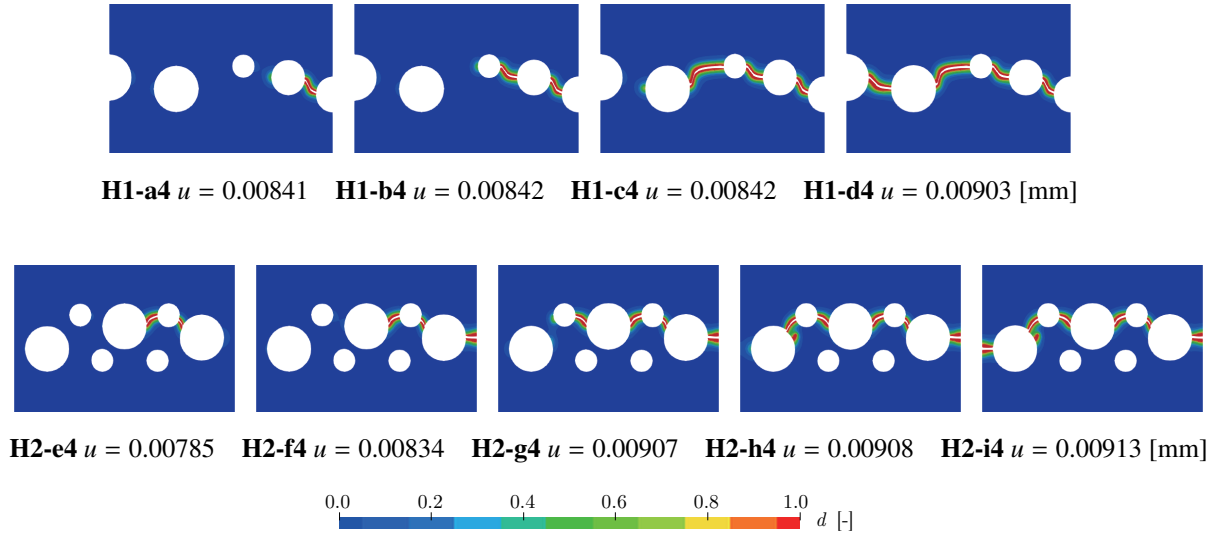


Fig. 5.21: Snapshots of the crack evolutions obtained for Example 5-1-4.

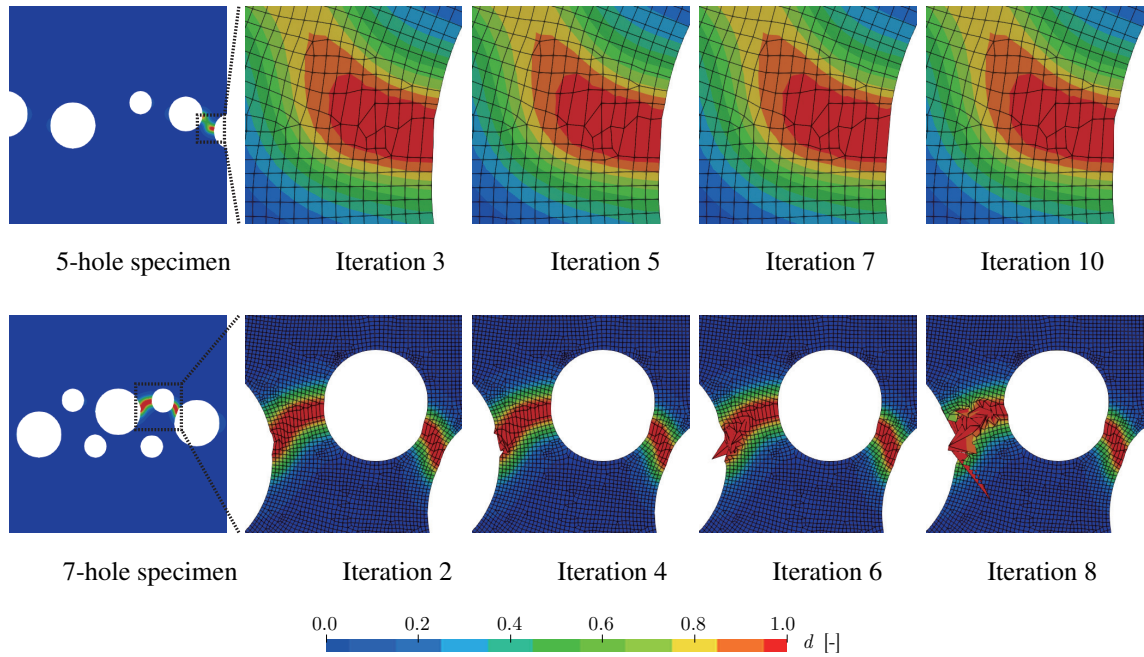


Fig. 5.22: Illustration of severely damaged elements involving oscillatory displacements and collapsed element groups when the global NR computation diverges in CPFFEM: 5-hole & 7-hole specimens in Example 5-1-4.

in which the left and right figures show the overview and enlarged view around the load peaks, respectively. As seen in this figure, the results of Case H1 and Case H2 have two and four load peaks, respectively. Additionally, for each case, an increase in the displacement

between the adjacent peaks is observed. Fig. 5.21 provides a better understanding of these multiple load peaks. For Case H1, the crack initiates and propagates until it reaches the third hole from right to left. Subsequently, additional displacement loading is required to promote further crack evolution; see (H1-c4) & (H1-d4) in Fig. 5.20 as well. For Case H2, additional displacement loading is necessary if the crack initiates from the larger hole; see (H2-e4) & (H2-f4) or (H2-f4) & (H2-g4). It should be noted here that these results are difficult to compute with CPFFEM because the severely damaged elements diminish the numerical stability, as demonstrated in the previous numerical examples. For example, Fig. 5.22 shows the unstable results obtained for both geometries using CPFFEM, in which the severely damaged elements involve oscillatory displacements and collapse for the 5-hole and 7-hole specimens, respectively. It is therefore confirmed that CPFFCM is more stable than CPFFEM for simulating crack propagation problems.

Furthermore, the mechanisms of crack initiation and propagation are further investigated. Fig. 5.23 and Fig. 5.24 show the detailed crack evolutions for two selected regions between the adjacent holes for each of the 5-hole and 7-hole specimens, respectively. As seen in these figures, these crack propagations possess two main mechanisms. One is that a crack initiates from one hole and penetrates toward the other. The other is that two cracks initiate from adjacent holes and propagate to form a single crack path. However, the mechanism shown in the panel consisting of (h1)~(h4) in Fig. 5.24 seems to be an exception. In this case, although multiple cracks initiate from adjacent holes, one of them penetrates toward the other hole, and the other crack stops increasing and is closed at the end. Based on these numerical results, we confirm that the proposed scheme can reproduce the crack initiation and propagation scenarios computed by the energy minimization problem of the crack phase-field within the finite strain framework.

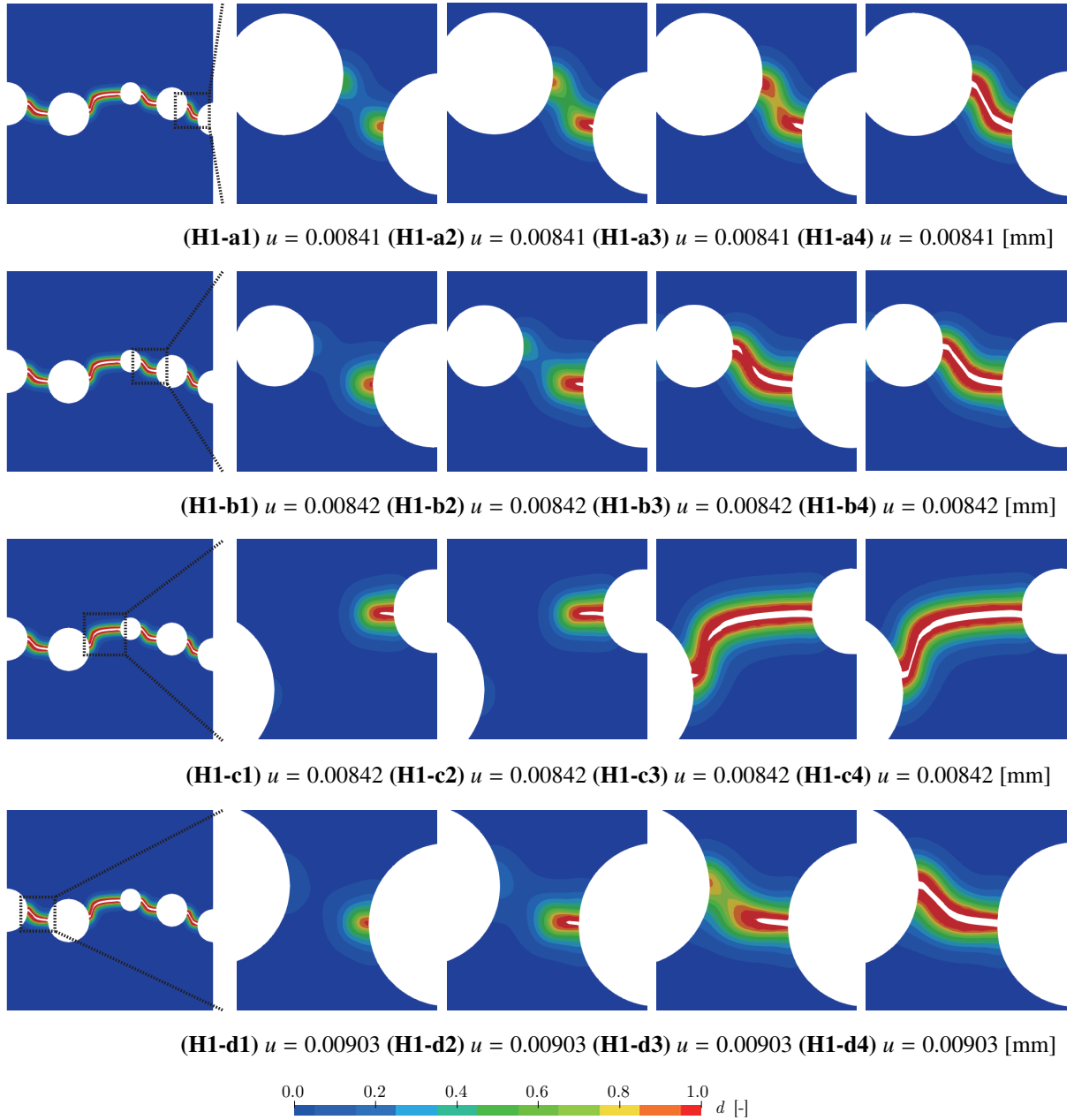


Fig. 5.23: Snapshots of the crack evolutions obtained for Example 5-1-4 (Case H1).

5.2 Dynamic brittle fracture

This section is devoted to demonstrating the capabilities of the proposed method in simulating dynamic fractures involving arbitrary crack initiation, propagation, bifurcation, division of the original object into multiple portions, and subsequent independent motions of the divided portions. Four representative numerical examples are presented and discussed

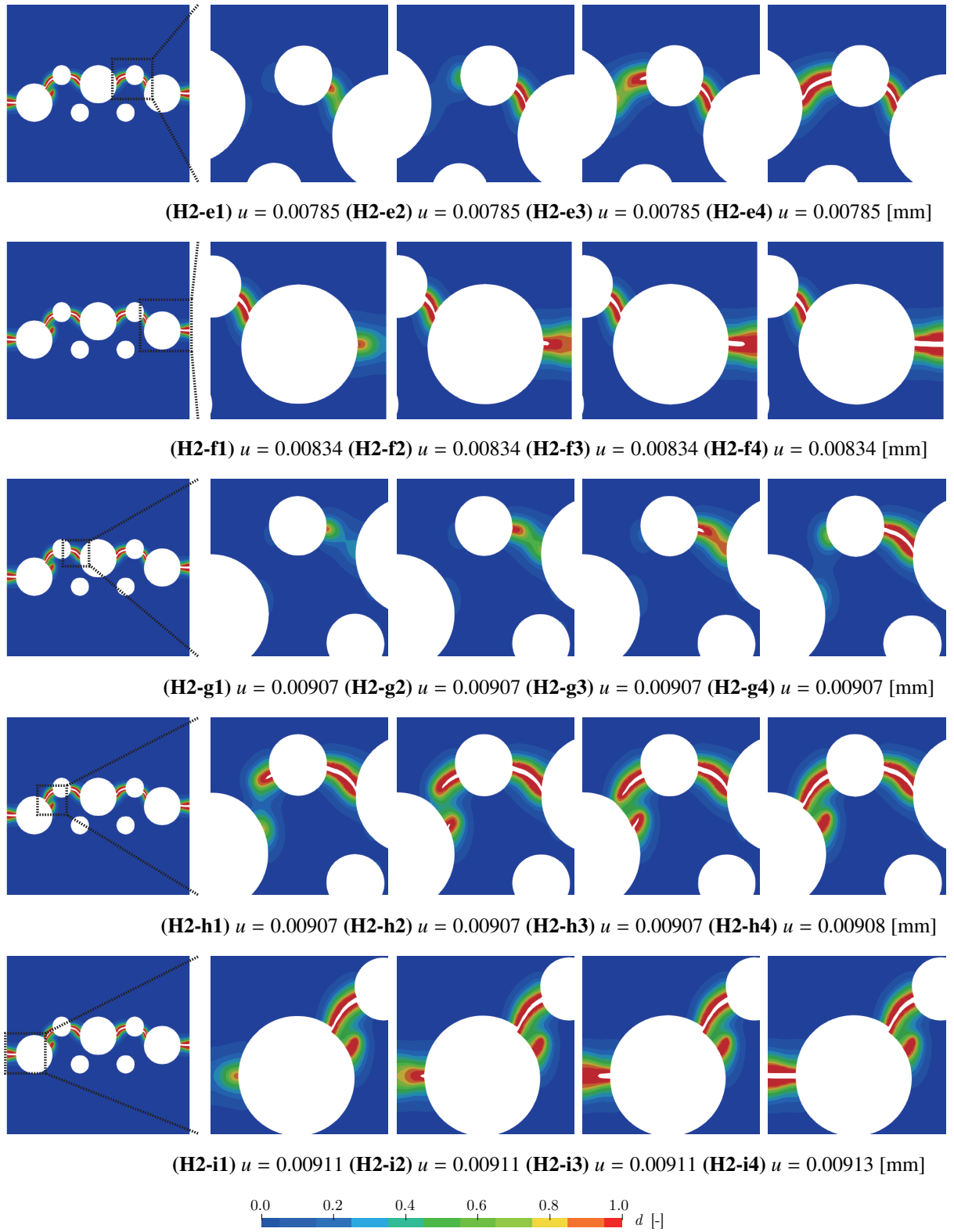


Fig. 5.24: Snapshots of the crack evolutions obtained for Example 5-1-4 (Case H2).

regarding the conservation and variation of energy components and the motions of divided portions by cracks. Note that several well-known benchmark tests, such as the dynamic crack branching test ^{179),180)} and the Kalthoff-Winkler test ¹⁸¹⁾, are not demonstrated in this study since they can be performed within the standard framework of incorporating a CPFM into the FEM. Instead, we focus on fractures involving large deformation and rotation.

As a common setup for the following examples, the components of the displacement vector \mathbf{u} , u_1 and u_2 , correspond to the x and y axes, respectively. Additionally, the numerical simulations are conducted under the plane strain condition, and $\beta = 0.25$ and $\gamma = 0.50$ are used in the Newmark method. Values $\zeta_{\min} = 10$, $\zeta_{\max} = 1000$, and $\zeta_{\text{cof}} = 30$ are used for numerical damping. The energy components in Eq. (2.7) and Eq. (2.15) are computed as follows:

$$\text{Elastic strain energy (Ela.): } \mathcal{E}_{n+1}^e = \int_{\mathcal{B}_0} \Psi^e(\mathbf{F}_{n+1}, d_{n+1}) dV, \quad (5.1)$$

$$\text{Crack generation energy (Fra.): } \mathcal{E}_{n+1}^f = \int_{\mathcal{B}_0} \Psi^f(d_{n+1}, \nabla d_{n+1}) dV, \quad (5.2)$$

$$\text{Kinetic energy (Kin.): } \mathcal{K}_{n+1} = \int_{\mathcal{B}_0} \frac{1}{2} \rho_0 \|\dot{\mathbf{u}}_{n+1}\|^2 dV, \quad (5.3)$$

Dissipation energy of numerical damping (Dis.):

$$\mathcal{D}_{n+1} = \mathcal{D}_n + \int_{\mathcal{B}_0} \frac{1}{2} (\underline{\mathbf{C}}_n : \dot{\mathbf{F}}_n + \underline{\mathbf{C}}_{n+1} : \dot{\mathbf{F}}_{n+1}) : \frac{\partial \Delta \mathbf{u}_{n+1}}{\partial \mathbf{X}} dV, \quad (5.4)$$

$$\text{External energy of body force (Bod.): } \mathcal{P}_{n+1}^b = \mathcal{P}_n^b + \int_{\mathcal{B}_0} \frac{1}{2} \rho_0 \mathbf{g} \cdot \Delta \mathbf{u}_{n+1} dV, \quad (5.5)$$

and

$$\begin{aligned} \text{External energy of traction force (Tra.): } \mathcal{P}_{n+1}^t &= \mathcal{P}_n^t + \int_{\partial \mathcal{B}_0} \frac{1}{2} (\mathbf{T}_n + \mathbf{T}_{n+1}) \cdot \Delta \mathbf{u}_{n+1} dA \\ &= \mathcal{E}_{n+1}^e + \mathcal{E}_{n+1}^f + \mathcal{K}_{n+1} + \mathcal{D}_{n+1} - \mathcal{P}_{n+1}^b \end{aligned} \quad (5.6)$$

Additionally, to better support the reader's understanding, movies of the following simulations are available in our repository ¹⁸²⁾.

5.2.1 Example 5-2-1: Vibration test of cantilever beam

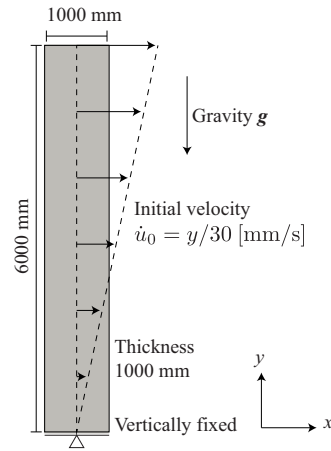


Fig. 5.25: Geometry with boundary conditions for Example 5-2-1.

Table 5.2: Material parameters for Example 5-2-1.

Parameter		Value	Unit
Young's modulus	E	1.25×10^{-4}	[MPa]
Poisson's ratio	ν	0.48	[-]
Density	ρ_0	1.0×10^{-9}	[kg/mm ³]
Gravity	\mathbf{g}	$(0, -0.981, 0)$	[mm/s ²]
Pseudo-Lamé's constant	λ_{pse}	7.78	[MPa]
Pseudo-Lamé's constant	μ_{pse}	0.338	[MPa]

Table 5.3: Numerical simulation cases for Example 5-2-1.

Case	Gravity	Damping	Separation
cb1	—	—	—
cb2	✓	✓	—
cb3	—	—	✓
cb4	✓	✓	✓

The first example concerns a vibration test of a cantilever beam. The main objective of this example is to demonstrate that if the damage is not considered, the energy is conserved

regardless of the introduction of the body force and numerical damping effects and the discontinuity represented by the FCM. Therefore, the computation of the crack phase-field is not considered here. The geometry of the beam is schematically illustrated in Fig. 5.25 along with the boundary conditions, and the numerical setup is borrowed from Bonet et al.¹⁸³⁾. Specifically, the element size is $h_e = 250$ [mm], and the bottom edge of the beam is fully fixed. The initial velocity is horizontal and gradually increases in proportion to the height. The material parameters are provided in Table 5.2. To discuss the effects of the body force, numerical damping, and breaking of the beam, we consider the four simulation cases listed in Table 5.3. It should be noted that the damping coefficient in Eq. (4.28) is set to $c^* = 1$ in this example to demonstrate the ordinary damping effect but will be consistent with the definition in Eq. (4.28) in the next three examples. Additionally, the time increment is set to $\Delta t = 0.125$ [s], and the gravitational force is assumed to be only 0.01% of the Earth's gravity for visualization purposes to allow the free fall motions of the divided portions of the beam over a reasonable range of the time to be captured in a single figure.

Fig. 5.26 shows the transitions of the energy components given in Eqs. (5.1)-(5.6). Here, the crack generation energy is excluded since the damage is not considered in this numerical example. As seen from the black dashed line in each graph, the energy conservation relations are satisfied in all the cases. Specifically, the result for Case cb1, in which the effects of the body force, damping, or beam breakage are not considered, exhibits the same trends as the results in Reference¹⁸³⁾. That is, the kinetic strain energy first reached its maximum value, followed by the elastic strain energy, as shown in Fig. 5.27. Accordingly, these two energy components have opposite phases over time; see also the movies posted in our repository¹⁸²⁾. This is a simple verification but is the premise upon which the validity of the subsequent calculations will be discussed.

The results for Case cb2 show similar trends to Case cb1 in terms of the transition of the energy components. However, the amplitudes of the elastic and kinetic energies are reduced by the damping effect, as shown in Fig. 5.26(b). Additionally, the dissipation energy increases with an increasing number of cycles, and the external energy exerted by the body

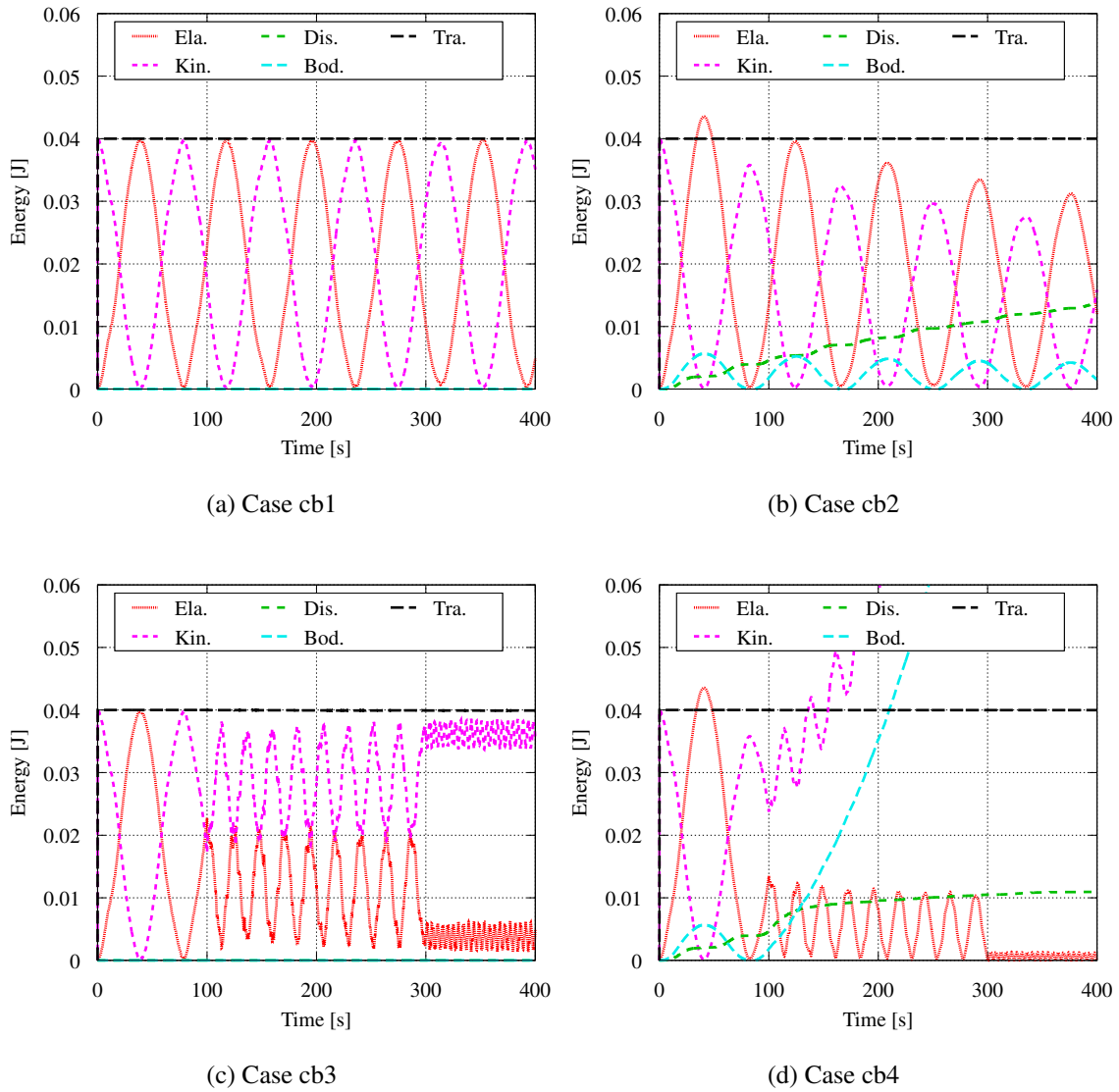


Fig. 5.26: Transition trends of energy components for Example 5-2-1. Ela: elastic strain energy; Kin: kinetic energy; Dis: dissipation energy; Bod: external energy of body force; Tra: external energy of traction force ($Tra = Ela + Kin + Dis - Bod$).

force shows increasing and decreasing behavior, as observed in Fig. 5.28. It should be noted that the initial amplitude of the elastic component in Case cb2 is larger than that in Case cb1 due to the effect of body force.

Meanwhile, as seen from Figs. 5.26(c) & (d), the results for the latter two cases, Case cb3, and Case cb4, exhibit different trends of motion due to the breaking of the beam. In

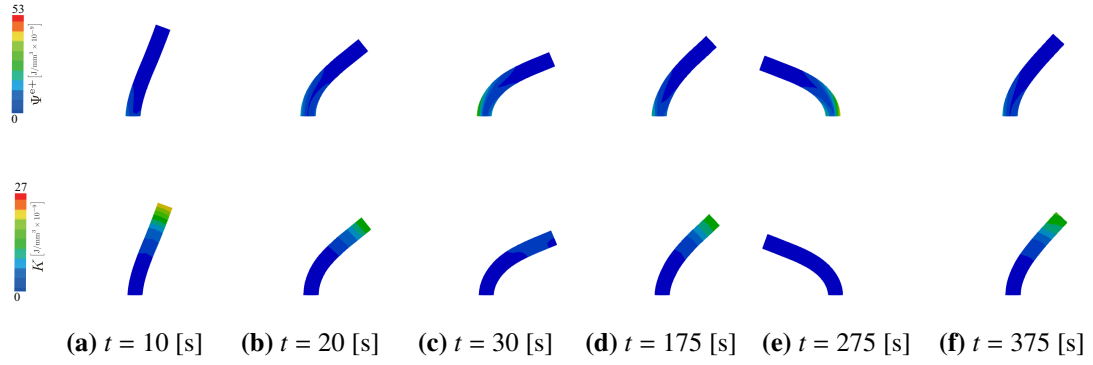


Fig. 5.27: Energy states for Example 5-2-1: Case cb1. Elastic strain energy density in tension Ψ^{e+} and kinetic energy density K in order from the top.

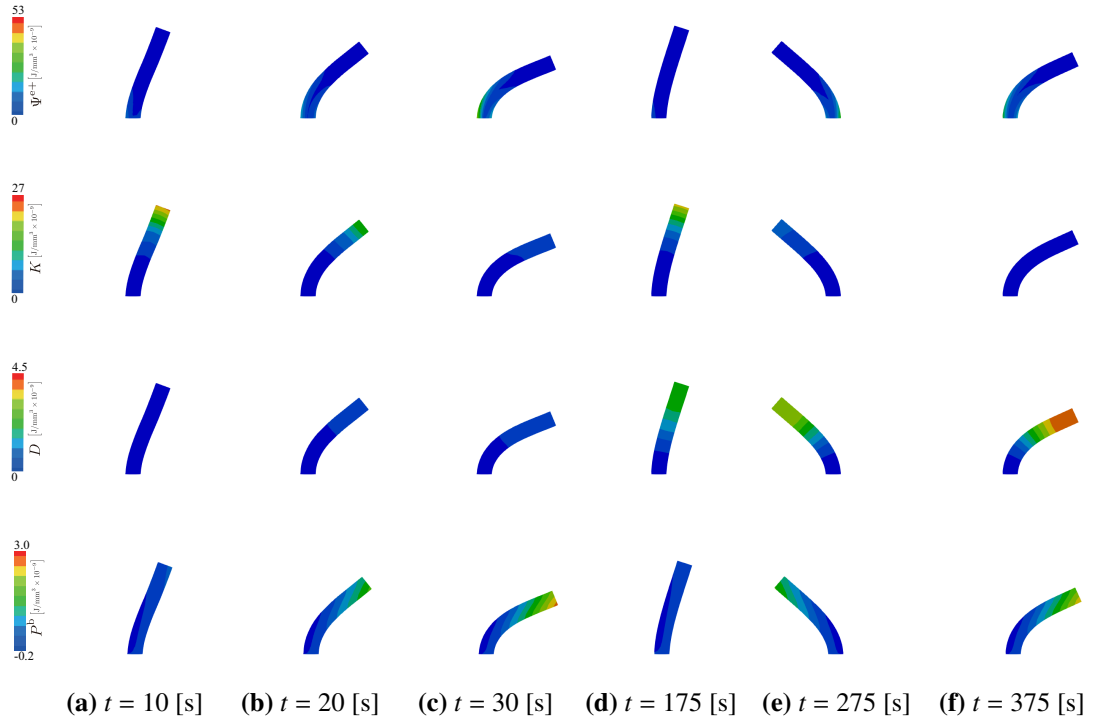


Fig. 5.28: Energy states for Example 5-2-1: Case cb2. Elastic strain energy density in tension Ψ^{e+} , kinetic energy density K , dissipation energy density D , and external energy density of body force P^b in order from the top.

these cases, we intentionally break the original beam horizontally into two, three, and four portions at the positions $y = 3125$, 4625 , and 1125 [mm] at times $t = 100$, 200 , and 300 [s], respectively. The frequencies of the curves of the elastic strain and kinetic energies increase

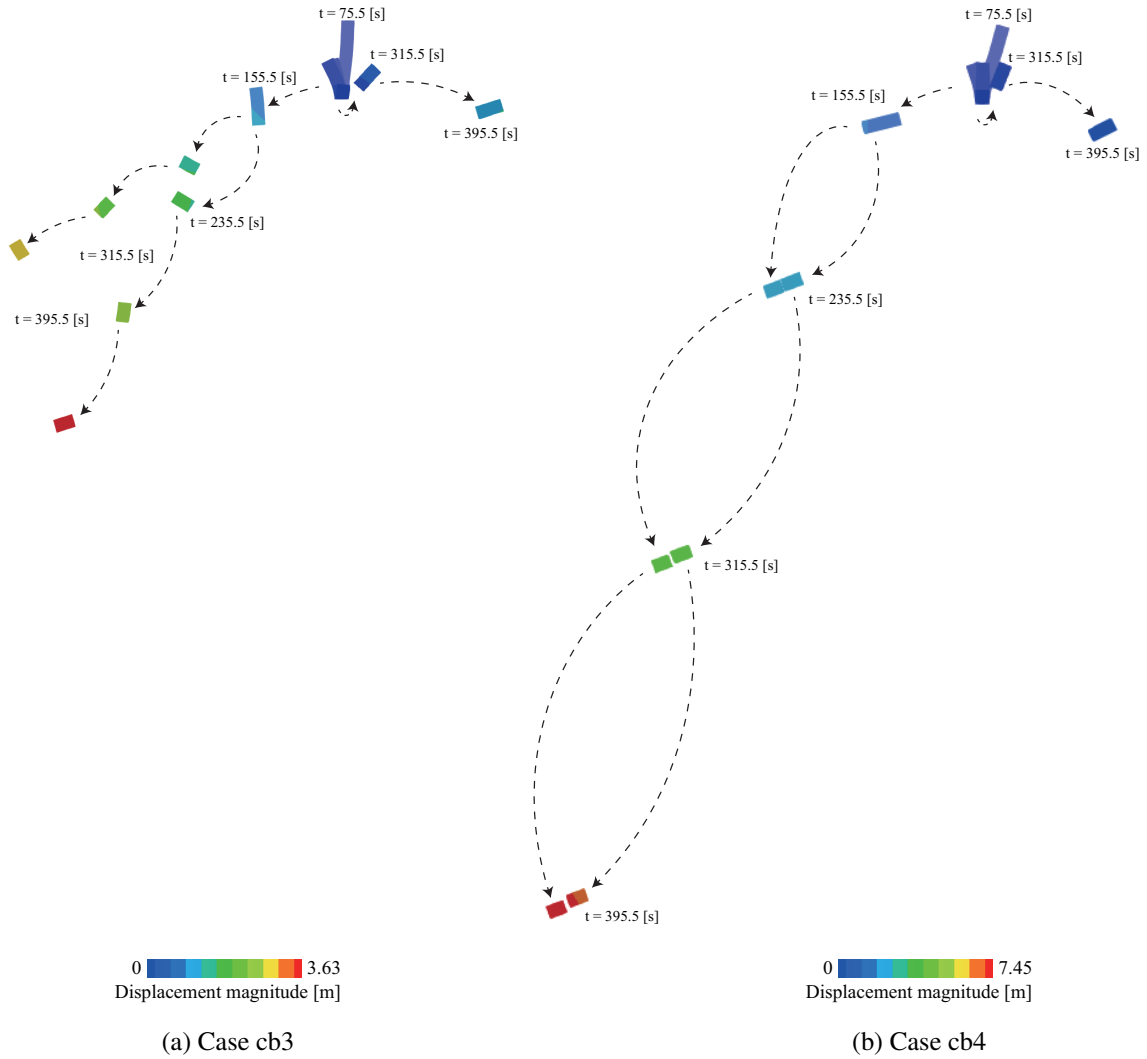


Fig. 5.29: Trajectories of motion for Example 5-2-1: Case cb3 and Case cb4.

whenever the lengths of the divided portions become shorter. In Case cb4, the amplitudes of the elastic and kinetic components are also reduced by the damping effect, but the free fall of the divided portions shows the largest energy component in the latter part of the simulation; see the magenta and light blue dashed lines in Fig. 5.26(d). To better support the reader's understanding, the trajectories of motion in Case cb3 and Case cb4 are illustrated in Fig. 5.29, and corresponding movies are provided in our repository¹⁸². As shown in the figure, the portions divided from the original beam exhibit individual motions, including rotations. Additionally, the divided portions in Case cb4 are in free fall because of the introduction of the body force; see the distances every 80 seconds between the adjacent divided bodies cor-

responding to the intervals, $t = 155.5\text{-}235.5$, $235.5\text{-}315.5$ and $315.5\text{-}395.5$ [s], as indicated in the right panel of Fig. 5.29.

5.2.2 Example 5-2-2: Rotation test of hollow square plate

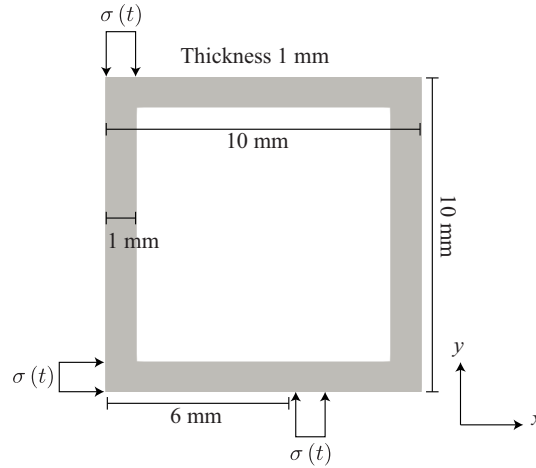


Fig. 5.30: Geometry with boundary conditions for Example 5-2-2.

Table 5.4: Material parameters for Example 5-2-2.

Parameter		Value	Unit
Young's modulus (Quasi-rigid)	E	1.5×10^9	[MPa]
Young's modulus (Elasticity)	E	1.5×10^4	[MPa]
Poisson's ratio	ν	0.3	[-]
Density	ρ_0	1.0×10^3	[kg/mm ³]
Fracture toughness	G_c	200	[N/mm]
Crack length scale parameter	l_f	2.0	[mm]
Pseudo-Lamé's constant	λ_{pse}	0.577	[MPa]
Pseudo-Lamé's constant	μ_{pse}	0.385	[MPa]

The second example concerns a rotation test of a hollow square plate. Fig. 5.30 illustrates the geometry of the plate along with the boundary conditions. As indicated in this figure, the following sinusoidal pressure is applied to the three subregions of the plate's external surface

Table 5.5: Numerical simulation cases for Example 5-2-2.

Case	Damage	Damping	Separation
hs1 (quasi-rigid)	–	–	–
hs2 (elasticity)	✓	–	✓
hs3 (elasticity)	✓	✓	✓

during the first 5 seconds, and no external loading is applied after $t > 0.5$ [s]:

$$\sigma(t) = \sigma_0 f(t) \quad \text{with} \quad \sigma_0 = 250 \text{ [MPa]}, \quad f(t) = \begin{cases} \sin\left(\frac{\pi}{0.5}t\right) & \text{if } 0 \leq t \leq 0.5 \text{ [s]} \\ 0 & \text{otherwise} \end{cases}. \quad (5.7)$$

In this example, we consider the effects of damage, for which a quadratic form of the degradation function is employed. The material parameters are provided in Table 5.4, and three simulation cases, including quasi-rigid and elastic setups, are considered, as listed in Table 5.5. Additionally, the effects of numerical damping are discussed, whereas the body force is neglected here. The time increment is set to $\Delta t = 0.001$ [s], and the element size is $h_e = 1$ [mm]. It should be mentioned that this example is inspired by the work of Hesch & Weinberg⁴⁵⁾, in which numerical simulations were conducted for flying rigid/elastic L-shaped specimens with/without damage computation within the finite strain framework. For Algorithm 3, $d_{\text{crl}} = 0.98$ and $C_{\text{relax}} = 10$ are used.

Fig. 5.31 and Fig. 5.32 show the transitions of the energy components and the trajectories of motion, respectively, for the three cases. For Case hs1, in which a quasi-rigid body is assumed, almost all the work done by external loading is transformed into kinetic energy, as shown in Fig. 5.31(a). Additionally, from Fig. 5.32(a), a horizontal motion involving large rotation is confirmed; see the motion of the dark blue-colored element and the corresponding movie¹⁸²⁾.

Meanwhile, Case hs2 and Case hs3 assume elastic bodies with damage evolution. As seen from Figs. 5.32(b) & (c), one severely damaged element is divided at time $t \approx 1.26$ [s] in each case. Accordingly, the crack opens, and the two crack surfaces move independently;

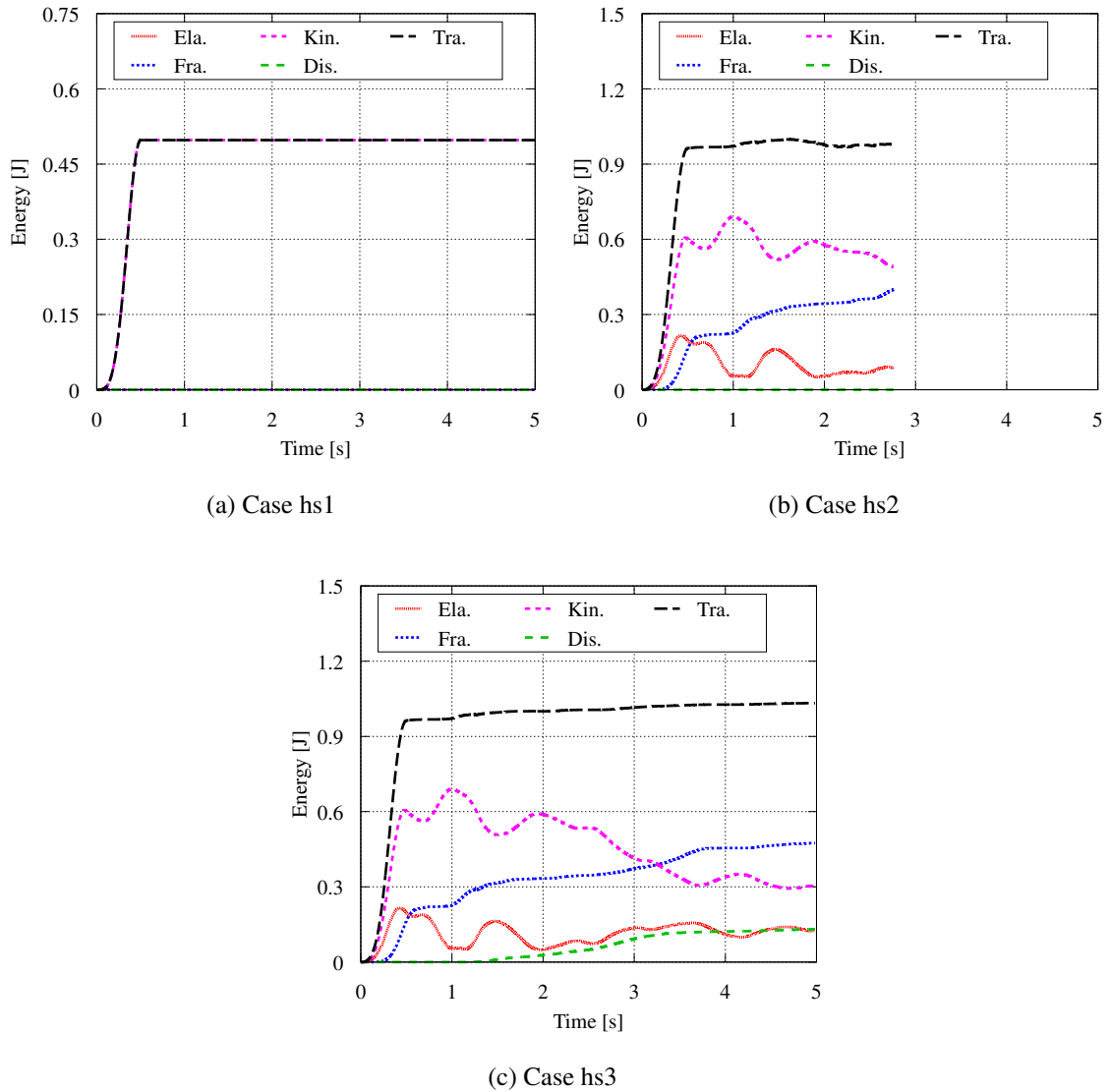
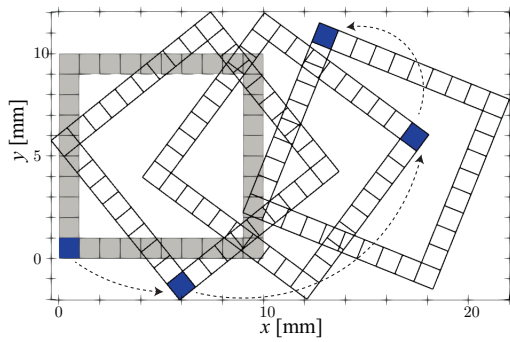
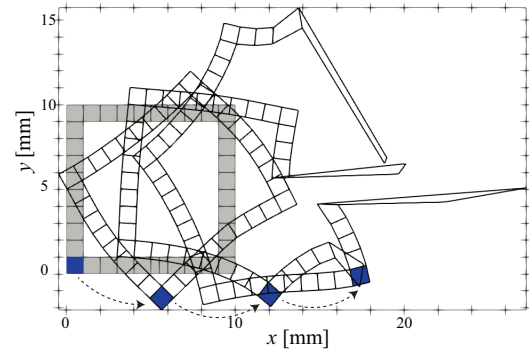


Fig. 5.31: Transition trends of all energy components for Example 5-2-2. Ela: elastic strain energy; Fra: crack generation energy; Kin: kinetic energy; Dis: dissipation energy; Tra: external energy of initial traction force ($Tra = Ela + Fra + Kin + Dis$).

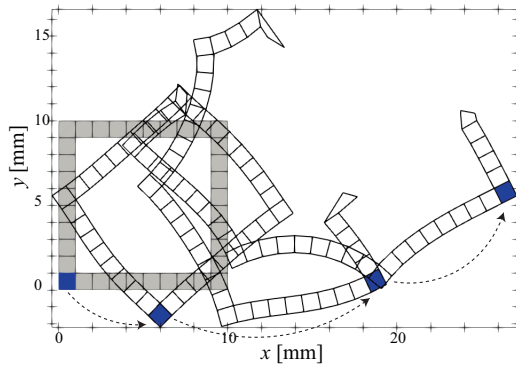
see Figs. 5.32(b) & (c). This demonstrates an advantage of the proposed method over some conventional approaches, such as that of Hesch & Weinberg⁴⁵⁾. As seen from their reference results shown in Fig. 5.32(d), a tendency of damage evolution similar to that in this example is confirmed; the element is severely damaged while the object is moving horizontally and rotating. However, since the breaking of the damaged element is not considered, the object



(a) Case hs1



(b) Case hs2



(c) Case hs3

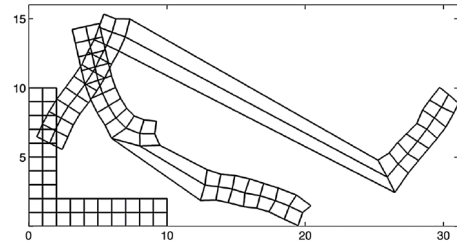
(d) Reference result ⁴⁵⁾

Fig. 5.32: Trajectories of motion for Example 5-2-2.

is not divided into two portions, and the independent motions of the divided portions cannot be captured. As a result, the computation will fail due to the collapse of the finite elements.

However, as seen from the black dashed lines in Fig. 5.31(c) & (d), energy conservation is not satisfied for Case hs2 and Case hs3. Based on the results for Example 5-2-1 and Case hs1 of the present example, the failure of energy conservation is a unique issue when damage is computed. There seem to be one minor and two major reasons for this failure. The minor reason is a numerical error due to the rearrangement of the finite covers for crack division. In fact, this error also arises in the first and subsequent numerical examples, but they are too small to be observed. Since this is a unique problem of the FCM as well as several other

meshfree methods, no deeper discussion is presented here; detailed observations are merely presented in Appendix A.3.

Meanwhile, one of the major reasons for the failure of energy conservation is the distortion of severely damaged elements. In fact, as shown in Fig. 5.32(b), the severely damaged elements in Case hs2 exhibit extremely large deformations, which eventually result in inadequate variations in the energy components and failure of the Newton-Raphson (NR) computation; see also the black dashed line in Fig. 5.31(b). In contrast, with the introduction of numerical damping, these extremely large deformations are somewhat mitigated, and the computation can proceed to the end; see Fig. 5.31(c) and Fig. 5.32(c). Nevertheless, the black dashed line in Fig. 5.31(c), which is indirectly computed from the relation in Eq. (5.6)₂, still exhibits an increasing tendency. In particular, there is still a trend of unreasonable energy increase even before the element is severely damaged; see the black dashed lines within the time range $t \in [0.5, 1.2]$ [s] in Fig. 5.31(b) and Fig. 5.31(c).

The other major reason is the ability of finite covers (or linear shape functions) to approximate the damage profiles, which must be responsible for the inappropriate energy increase observed above. In particular, in fracture simulations, the elastic strain energy usually exhibits second- or third-order nonlinearity in terms of the damage variable and second-order nonlinearity in the displacement. Hence, the approximation of the damage driving force may cause overestimation (or underestimation) compared to the actual one, which will eventually lead to an inappropriate energy increase (or decrease). Although this issue is not further discussed here, appropriate measures should be adopted against these discrepancies in energy conservation. For instance, an energy-momentum consistent integrator⁴⁵⁾ or a higher-order approximation function such as NURBS may be helpful for preserving energy conservation; however, incorporating such a tool into a diffusive-discrete crack transition scheme is challenging from a program implementation perspective. Hence, further insight into this issue is left for future work.

5.2.3 Example 5-2-3: Three-point bending test of notched beam (John-Shah test)

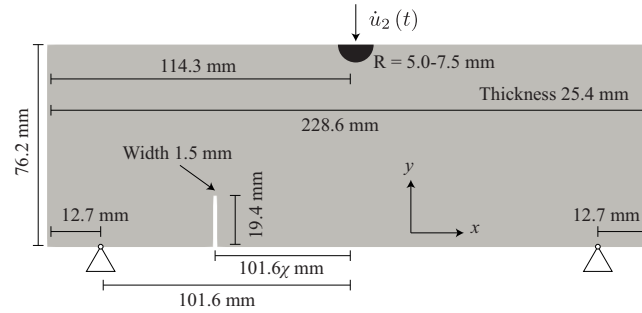


Fig. 5.33: Geometry with boundary conditions for Example 5-2-3.

Table 5.6: Material parameters for Example 5-2-3.

Parameter		Value	Unit
Young's modulus	E	3.14×10^4	[MPa]
Poisson's ratio	ν	0.2	[-]
Density	ρ_0	2.4×10^{-6}	[kg/mm ³]
Fracture toughness	G_c	0.0165	[N/mm]
Crack length scale parameter	l_f	1.5	[mm]
Pseudo-Lamé's constant	λ_{pse}	1.04×10^{-3}	[MPa]
Pseudo-Lamé's constant	μ_{pse}	6.94×10^{-4}	[MPa]

The third example is dedicated to a three-point bending test of a notched beam, which is referred to as the John-Shah test ¹⁸⁴⁾. In experiments, tests were conducted on several concrete beams with single notches at different locations, and some characteristic fracture patterns were observed. The specimen geometry is illustrated in Fig. 5.33 along with the boundary conditions. Here, $\chi \in [0, 1]$ is a ratio that controls the position of the notch. Two points on the bottom edge are fixed vertically, while point loading is applied by forced dis-

Table 5.7: Numerical simulation cases, crack initiation time, point, and propagation angle for Example 5-2-3.

Setup		Result		
Case	χ	Crack initiation time [$s \times 10^{-6}$]	Crack initiation point	Crack propagation angle [deg.]
js1	0	648	center (notch)	0
js2	0.5	826	notch	23.4
js3	0.810	1436 \rightarrow 1446	notch \rightarrow center	35.9 \rightarrow 0.5
js4	0.815	1436	notch and center	37.5 and 0.1
js5	0.825	1476 \rightarrow 1492	center \rightarrow notch	0.4 \rightarrow 38.5
js6	0.875	1428	center	0

placement (velocity) at the center of the top edge in accordance with the following condition:

$$\dot{u}(t) = \begin{cases} \dot{u}_2 \frac{t}{t_1} & \text{if } 0 \leq t \leq t_1 \text{ [s]} \\ \dot{u}_2 & \text{otherwise} \end{cases} \quad \text{with } t_1 = 1.96 \times 10^{-4} \text{ [s]}, \quad \dot{u}_2 = 65 \text{ [mm/s]}. \quad (5.8)$$

The material parameters are provided in Table 5.6. Here, the body force of the beam is neglected. The element size within the potentially damaged region is set to $h_e \approx 0.5$ [mm], and the time increment is set to $\Delta t = 1 \times 10^{-6}$ [s] and remains fixed throughout the simulation. It should be noted that since the damage evolution tendency of the employed damage model, i.e., the volumetric-deviatoric split AT2 model, is not in perfect agreement with that in actual concrete materials, the black-colored region shown in Fig. 5.33 is assumed to be intact. Additionally, the fracture toughness value is determined from the peak stress-strain correspondence of the employed cubic degradation function; see Borden et al. ¹⁸⁵⁾. Thus, the objective of this numerical example is to qualitatively reproduce the dynamic fracture patterns that were observed in the actual experiments (John-Shah test ¹⁸⁴⁾). For comparison purposes, six simulation cases with different notch positions are considered, as summarized in the left two columns of Table 5.7. For Algorithm 3, $d_{cr1} = 0.98$, $d_{cr2} = 0.50$ and $C_{relax} = 10$ are used.

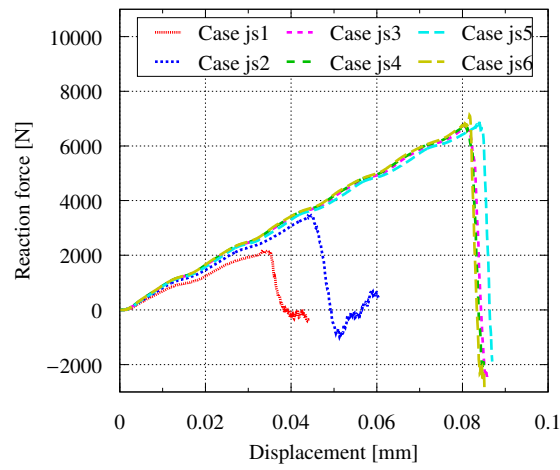


Fig. 5.34: Reaction force-displacement curves for Example 5-2-3.

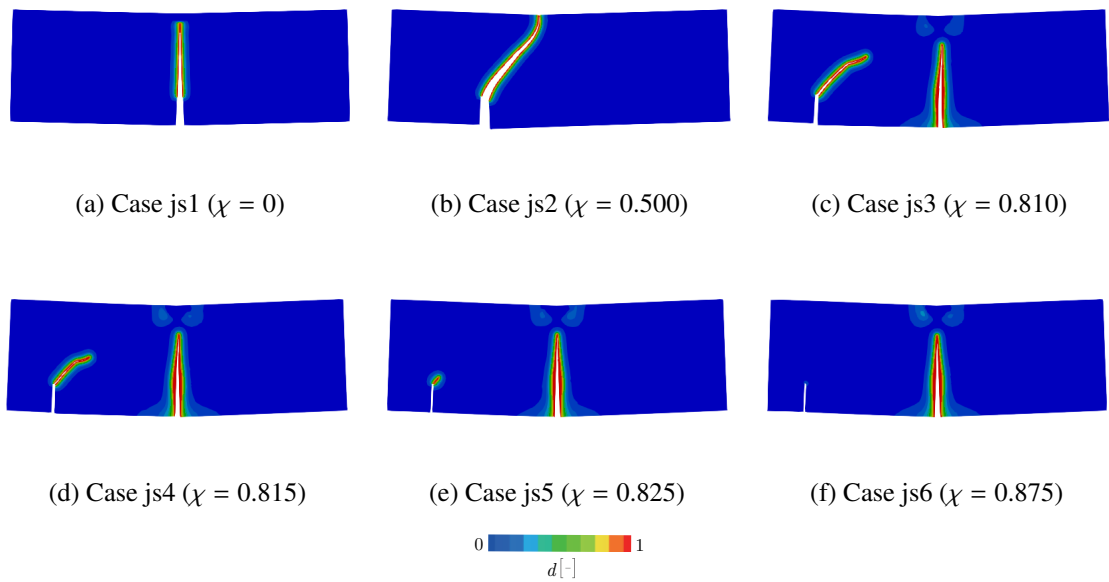


Fig. 5.35: Comparison of crack paths for Example 5-2-3. Deformation magnitude: 50 times.

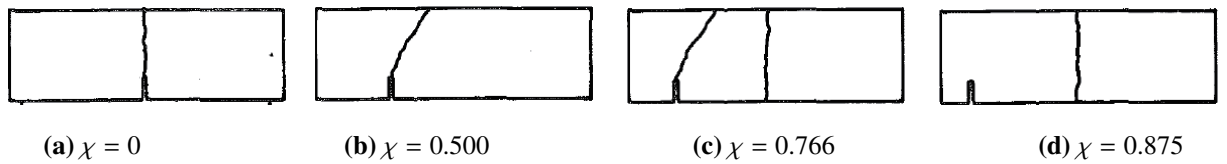


Fig. 5.36: Experiment results¹⁸⁴⁾ for Example 5-2-3.

Fig. 5.34 and Fig. 5.35 show the reaction force-displacement curves and final crack patterns, respectively, for the six cases. Additionally, the crack initiation times, initiation points, and propagation angles are summarized in the right three columns of Table 5.7. Here, the reaction force is the sum of the forces at the two support points, while the displacement is the vertical component taken at the center of the top edge. As shown in Fig. 5.34, the peak value of the reaction force increases as the position of the notch moves away from the center. Additionally, as shown in Fig. 5.35, the crack initiation positions and propagation angles for Case js1, Case js2, and Case js6 are in good agreement with the experimental results¹⁸⁴⁾ shown in Fig. 5.36, i.e., the crack initiates from the notch for Case js1 and Case js2 but does not for Case js6. Indeed, it is known that there is a critical ratio χ_{cr} at which the crack initiation point changes from the notch to the center. According to experimental observations¹⁸⁴⁾, this ratio has been identified to be $\chi_{cr} \approx 0.766$. However, the ratio obtained from the employed damage model reads $\chi_{cr} \approx 0.815$, as shown in Figs. 5.35(c), (d), & (e). The discrepancy between the experimental results and our simulation results is probably due to the capabilities of the employed damage model. To bring the simulation results closer to the experimental ones, the damage driving force should be modified to match the response of actual concrete, and another failure mechanism, such as cohesive force, may be needed; for example, refer to several other damage models^{46),55),34),186)}. These modifications are left to future work, but it can nevertheless be concluded that the developed scheme can reproduce several typical dynamic fracture patterns qualitatively observed in the experiments.

5.2.4 Example 5-2-4: Impact failure of L-shaped plate

The last example concerns the impact test of an L-shaped plate and aims to demonstrate a series of dynamic fracture events that involve arbitrary crack initiation, propagation, bifurcation, division of the original object into multiple portions, and independent motions of the divided portions. The geometry and boundary conditions are illustrated in Fig. 5.37. As schematically visualized in this figure, the top edge is fully fixed, while the following

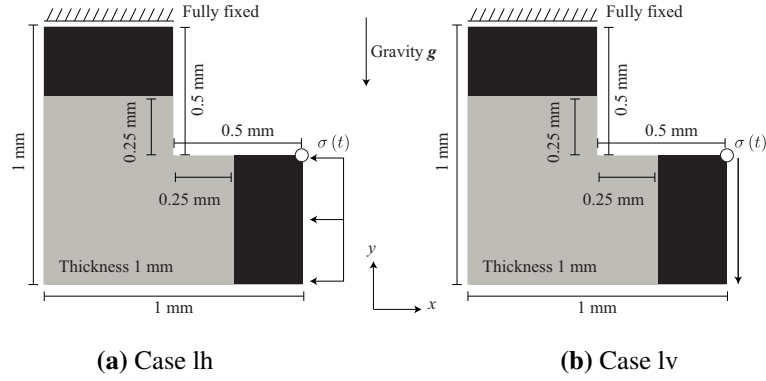


Fig. 5.37: Geometry with boundary conditions for Example 5-2-4.

Table 5.8: Material parameters for Example 5-2-4.

Parameter		Value	Unit
Young's modulus	E	1.5×10^4	[MPa]
Poisson's ratio	ν	0.3	[-]
Density	ρ_0	1.0×10^3	[kg/mm ³]
Gravity	\mathbf{g}	$(0, -9.81, 0)$	[mm/s ²]
Fracture toughness	G_c	1.0	[N/mm]
Crack length scale parameter	l_f	0.015	[mm]
Pseudo-Lamé's constant	λ_{pse}	0.577	[MPa]
Pseudo-Lamé's constant	μ_{pse}	0.385	[MPa]

sinusoidal pressure is horizontally or vertically applied to the right edge:

$$\sigma(t) = \sigma_0 f(t) \quad \text{with} \quad \sigma_0 = 15 \text{ [MPa]}, \quad f(t) = \begin{cases} \sin\left(\frac{\pi}{0.005}t\right) & \text{if } 0 \leq t \leq 0.005 \text{ [s]} \\ 0 & \text{otherwise} \end{cases}. \quad (5.9)$$

Here, the black-colored regions are assumed to be intact in the simulations. For convenience, the two cases of horizontal and vertical pressure are called “Case lh” and “Case lv”, respectively. The material parameters are provided in Table 5.8, where the gravitational force is assumed to be 0.1% of Earth's gravity for visualization purposes. The cubic degradation function is employed to represent the deterioration of the material. Additionally, the element size within the potentially damaged region is set to $h_e \approx 0.005$ [mm], and the time incre-

ment is set to $\Delta t = 4 \times 10^{-5}$ [s] throughout the simulations. For Algorithm 3, $d_{cr1} = 0.98$, $d_{cr2} = 0.50$ and $C_{relax} = 10$ are used.

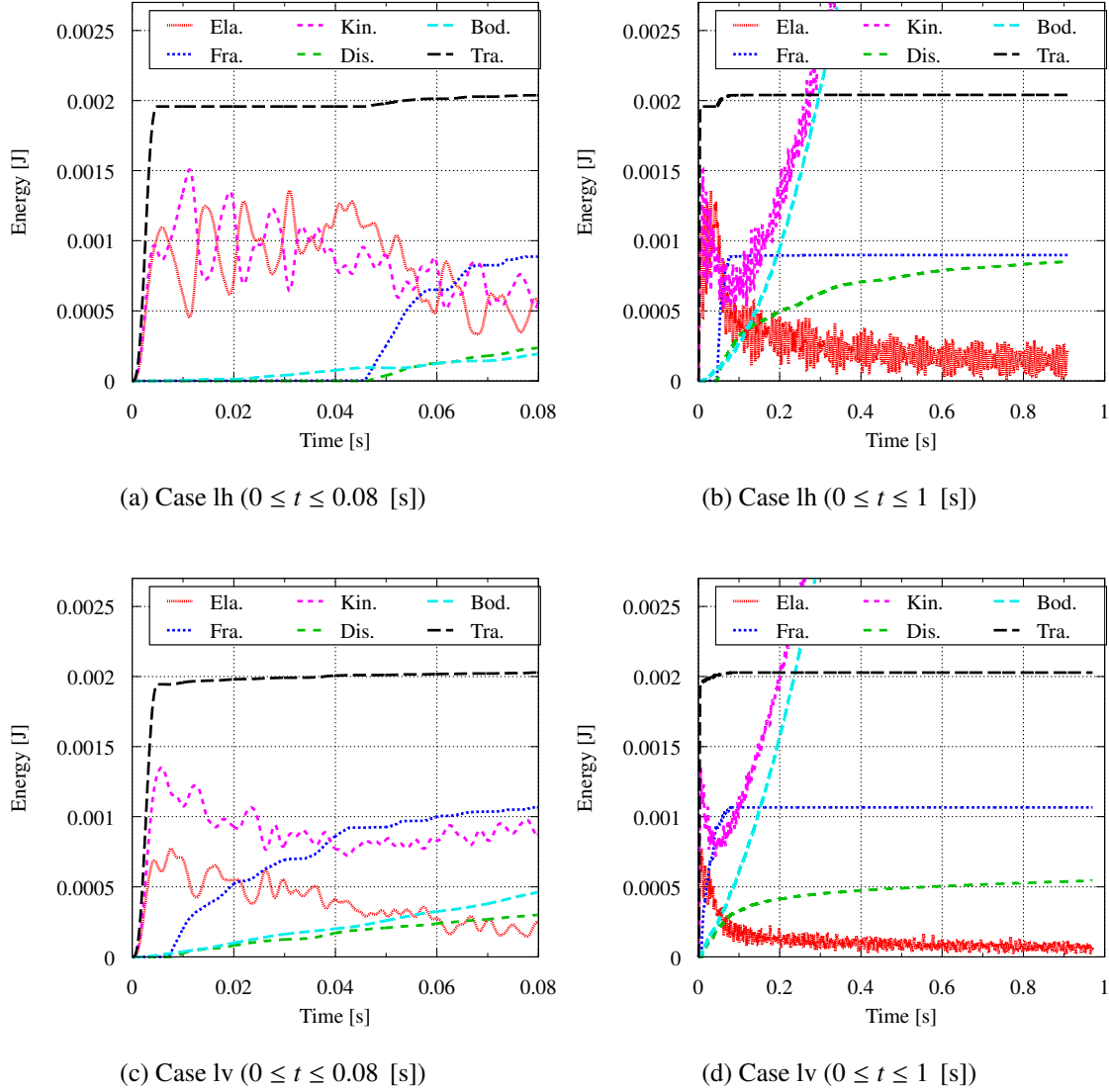


Fig. 5.38: Transition trends of all energy components for Example 5-2-4. Ela: elastic strain energy; Fra: crack generation energy; Kin: kinetic energy; Dis: dissipation energy; Bod: external energy of body force; Tra: external energy of traction force (Tra=Ela+Fra+Kin+Dis-Ext).

The transitional trends of the energy components and snapshots of the crack propagation processes are shown in Fig. 5.38 and Fig. 5.39, respectively. As shown in Fig. 5.39, the

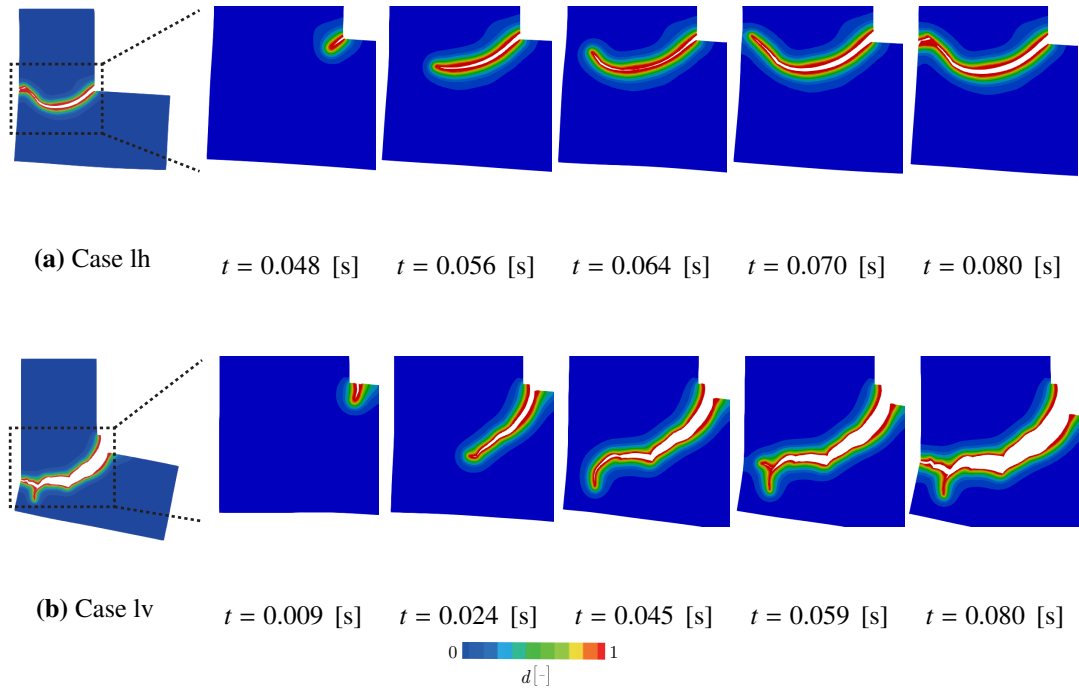


Fig. 5.39: Snapshots of crack propagations for Example 5-2-4.

crack initiation times, positions, and propagation directions vary with the applied pressure: Case lh exhibits a single horizontal crack without bifurcation, whereas Case lv exhibits an oblique crack direction with bifurcation. Additionally, the crack propagation speeds vary, and the crack surfaces are alternately opened and closed by the transfer of stress waves; see also the corresponding movies ¹⁸²⁾. Moreover, when the external energy of the traction force is indirectly computed from the relation in Eq. (5.6)₂, inappropriate increases are confirmed; see the black dashed lines in Fig. 5.38(a) and Fig. 5.38(c). As explained in Section 4.2, these tendencies are probably due to the limited approximation ability of the employed linear finite covers. In contrast, energy conservation is satisfied before crack initiation and after the division of the plates by the propagating cracks; see the black dashed lines in Fig. 5.38(b) and Fig. 5.38(d).

On the other hand, the motions in Cases lh and lv after division are shown in Fig. 5.40 and Fig. 5.41, respectively. Here, the displacement values are taken from the white point at the top of the right edge, as indicated in Fig. 5.37. Fig. 5.40 shows that while the motions in the

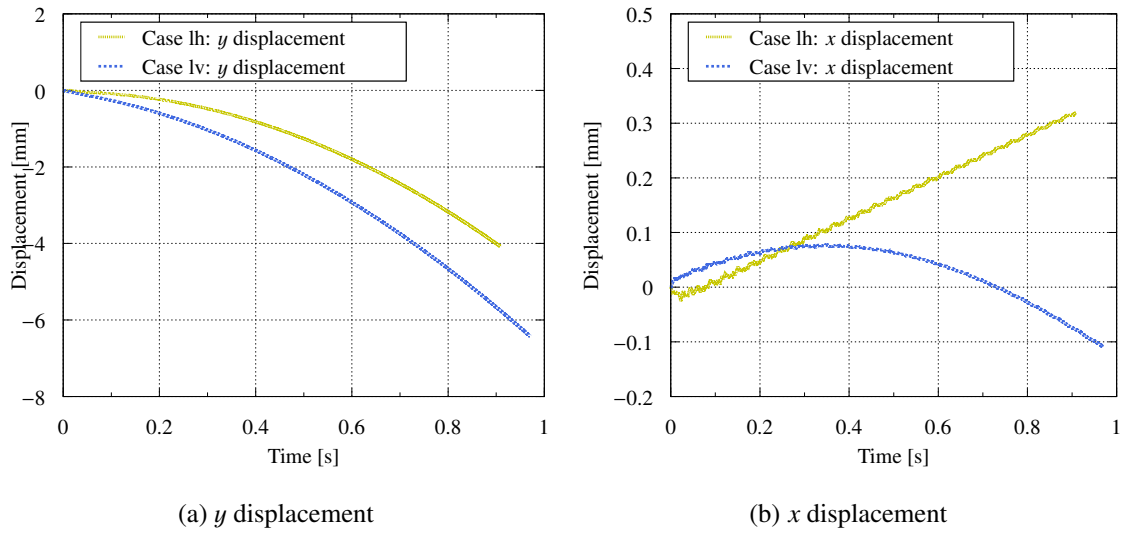


Fig. 5.40: Displacement-time curves for Example 5-2-4.

y direction are consistent with free fall, those in the x direction exhibit different tendencies in the two cases. Specifically, translation with an almost constant velocity and small oscillations is observed in Case lh, while rotation seems to be dominant in Case lv. Fig. 5.41(b) shows that the divided portion is indeed in free fall while rotating. It should be noted that the fall speed in Case lv is faster than that in Case lh because of the initial loading direction; see also the corresponding movies ¹⁸²⁾.

Based on the presented simulation results, we confirm that a series of dynamic fracture events from arbitrary crack initiation to independent motions of the divided portions of the broken object is successfully simulated with the proposed approach. Since several trends of motion involving large rotations cannot be adequately captured by a simulation assuming the small strain framework, the proposed method can be regarded as a promising and reasonable candidate for dynamic fracture simulations with large translations and rotations.

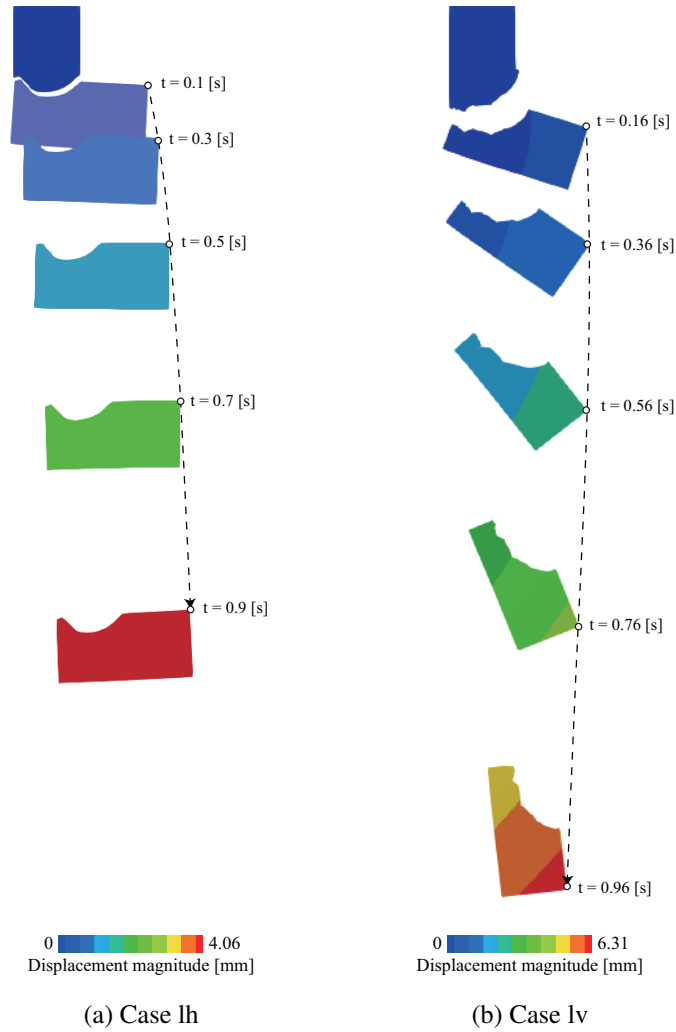


Fig. 5.41: Trajectory of motion for Example 5-2-4.

5.3 Ductile fracture

This section is devoted to demonstrating the ability of the proposed scheme with three representative numerical examples describing ductile fracture. In particular, in the last numerical example, another cup-cone failure simulation is conducted to reproduce the discrete cup-cone crack surfaces. The proposed model, whose formulation is derived in Section 2.5, is used for damage computations, and different crack evolution trends are demonstrated by changing the values regarding damage driving force and degrading fracture toughness. Note that the cosinusoidal form in Eq. (3.1) is employed in this section.

5.3.1 Example 5-3-1: Tensile failure of I-shaped specimen

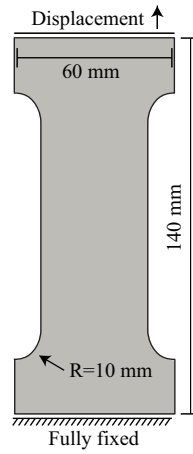


Fig. 5.42: Geometry with boundary conditions for Example 5-3-1.

Table 5.9: Material parameters for Example 5-3-1.

Parameter		Value	Unit
Young's modulus	E	190000	[MPa]
Poisson's ratio	ν	0.29	[-]
Initial yield stress	y_0	343	[MPa]
Linear hardening parameter	h	300	[MPa]
Critical yield stress	y_∞	680	[MPa]
Saturation parameter	β_y	16.93	[-]
Plastic length scale parameter	l_p	1.5	[mm]
Penalty parameter	p_p	1000	[MPa]
Fracture toughness	G_c	25	[N/mm]
Crack length scale parameter	l_f	1.5	[mm]

The first example is devoted to demonstrating the performance of CPFFCM for ductile fracture. For this purpose, an I-shaped specimen subject to tensile loading is considered, whose geometry and boundary conditions are illustrated in Fig. 5.42. The material parameters and five simulation cases are presented in Table 5.9 and Table 5.10, respectively. Here, the degrading fracture toughness is assumed to be constant, and only the plastic damage

Table 5.10: Numerical simulation cases for Example 5-3-1.

Parameter	Case	i1	i2	i3	i4	i5	Unit
Elastic damage coefficient	ζ^e	1.0	1.0	1.0	1.0	1.0	[-]
Elastic damage threshold	Ψ_{cr}^e	0	0	0	0	0	[MPa]
Plastic damage coefficient	ζ^p	1.0	1.0	1.0	1.0	1.0	[-]
Plastic damage threshold	Ψ_{cr}^p	0	5	15	30	45	[MPa]

threshold Ψ_{cr}^p changes for the five cases. Note that the numerical setup in this example is equivalent to some CPFMs^{87),80),83)}, in which only the plastic damage driving force, in addition to the elastic contribution, is employed to compute damage evolution. The cubic degradation function is used to represent the deterioration of material stiffness, and the Voce hardening function $\hat{H}(\bar{\alpha}) = h\alpha + (y_\infty - y_0)(1 - \exp(\beta_y \alpha))$ is adopted for the hardening behavior. Additionally, a fine mesh having an element size of $h_e \approx 0.50$ [mm] is used for the potentially damaged region. For Algorithm 3 and Algorithm 4, $d_{cr1} = 0.98$, $d_{cr2} = 0.50$, $C_{relax} = 10$, and $g_{min} = 0.05$ are used.

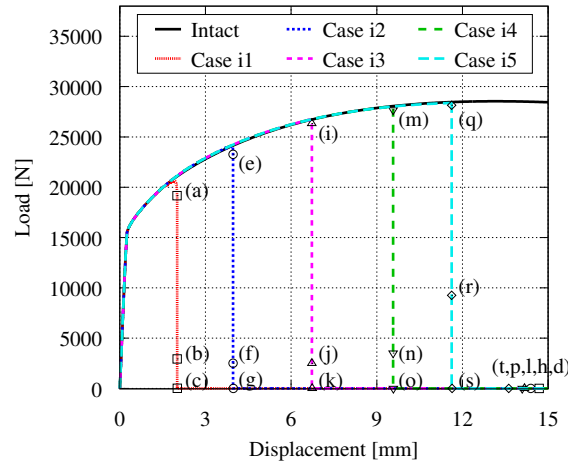


Fig. 5.43: Load-displacement curves for Example 5-3-1.

The load-displacement curves for the five cases are shown in Fig. 5.43. Here, the forced displacement is applied until the value of 15 [mm] even after the specimen is separated by a crack. As seen in the figure, the distinctive drop of the load, i.e., the severe damage evolution,

is delayed by providing a larger value of the plastic damage threshold Ψ_{cr}^p . This trend affects the crack initiation position as well as its propagation mechanism; see Figs. 5.44, 5.45, 5.47, 5.48, and 5.49 that show the deformation of the specimen and the detailed evolution of elastic damage variable d^e . Here, the labels in these figures correspond to those in Fig. 5.43.

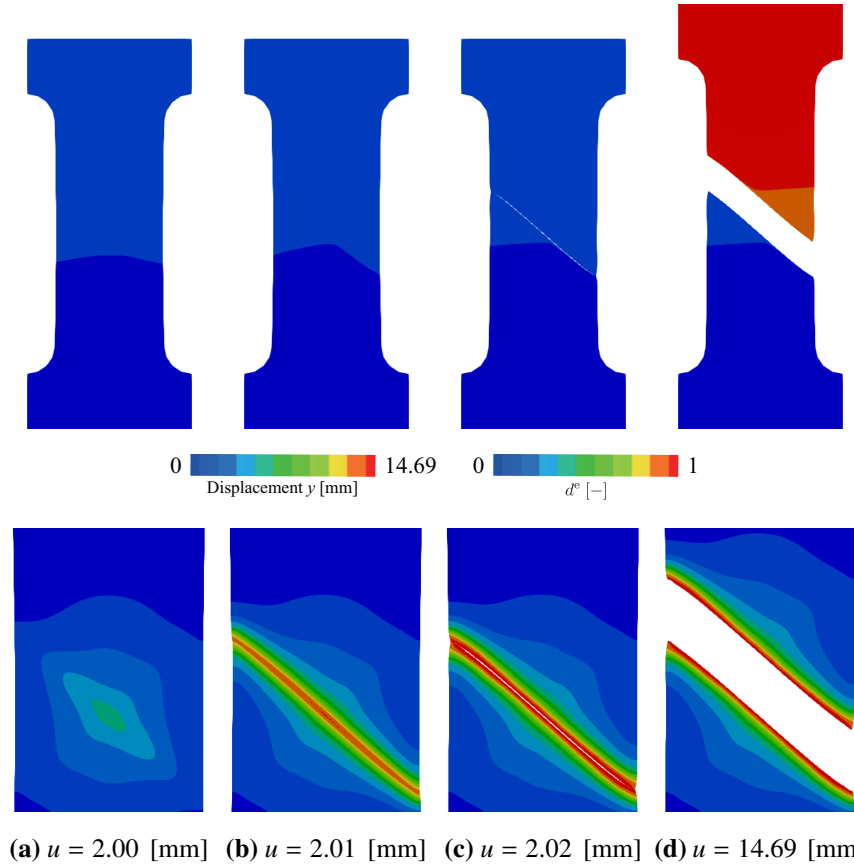


Fig. 5.44: Snapshots of deformation and detailed evolution of elastic damage variable d^e for Example 5-3-1: Case i1. The top row shows the vertical displacement, and the bottom row shows the elastic damage variable.

For Case i1 and Case i2, the crack propagation occurs at the center and the upper side of the specimen prior to and in the middle of the localization of the plastic deformation, as shown in Fig. 5.44 and Fig. 5.45. To be specific, the damage evolution mechanism for Case i1 is as follows:

1. The specimen experiences almost uniform plastic deformation.

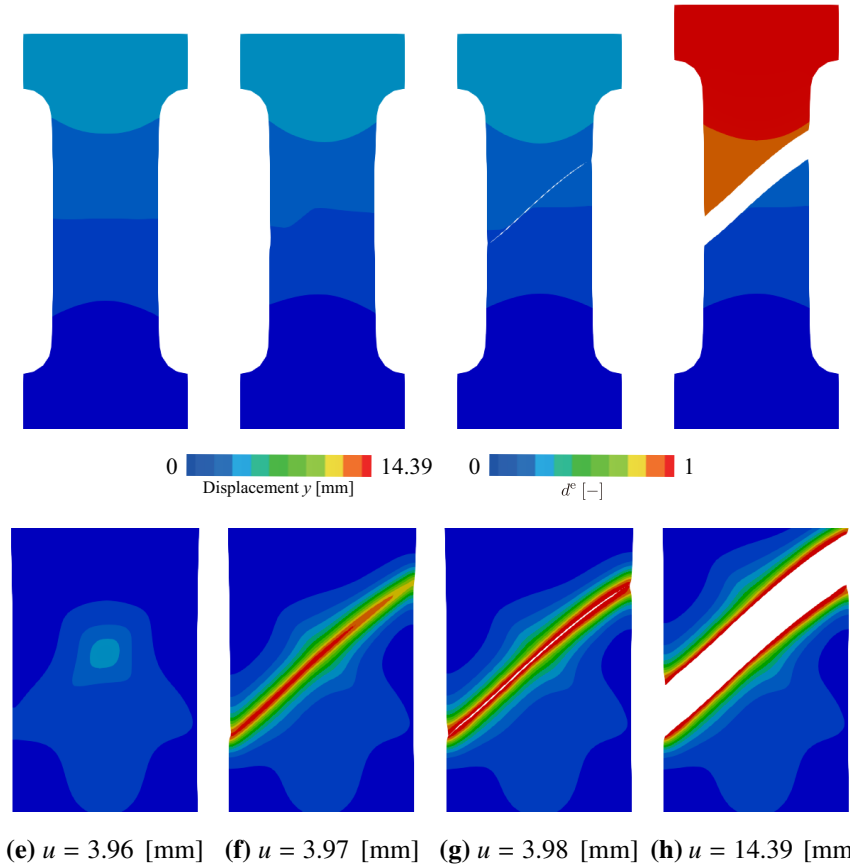


Fig. 5.45: Snapshots of deformation and detailed evolution of elastic damage variable d^e for Example 5-3-1: Case i2. The top row shows the vertical displacement, and the bottom row shows the elastic damage variable.

2. The damage occurs at the center of the specimen prior to necking.
3. The damage causes the localization of the plastic deformation.
4. The oblique crack path is made by plastic deformation.

On the other hand, that for Case i2 is as follows:

1. The accumulation of the plastic strain changes its evolution tendency from uniform to localizing.
2. The damage occurs in the meantime of the transition of the evolution tendency.
3. The crack initiates the upper side of the specimen prior to the localization.

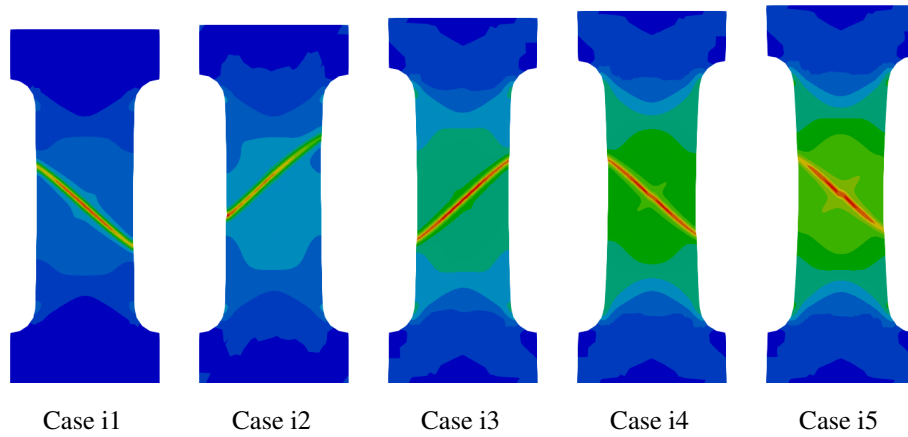


Fig. 5.46: Snapshots of the localization of global hardening variable α immediately before crack initiation for Example 5-3-1. The maximum value in each snapshot is shown in red and the minimum value in blue.

4. The accumulation of the plastic deformation concentrates at the location of the strain localization, and the oblique crack path is eventually made.

To facilitate these discussions, Fig. 5.46 would be helpful, which shows the localization of global hardening variable α immediately before crack initiation for five cases. As can be seen from the figure, typical necking behavior and subsequently appearing shear band are not confirmed for Case i1 and Case i2.

Meanwhile, by providing a larger value of the plastic damage threshold Ψ_{cr}^p , the shear band due to the localization of the plastic deformation appears, specifically for Case i4 and Case i5, as shown in Fig. 5.46. Accordingly, the severe damage evolution occurs at the center of the specimen; see Fig. 5.47, 5.48, and 5.49. It is worth mentioning that the diffusive damage region becomes more narrow as the plastic damage threshold Ψ_{cr}^p becomes larger. This is because the distinctive damage evolution is delayed, and therefore the damage occurs only at the location of larger plastic deformation. Additionally, for all the cases, the forced displacement is given to the separated upper segment until the value $u = 15$ [mm], and the large displacement differences are confirmed, which are difficult to be realized by the conventional FEM; see the last snapshots in Figs. 5.44, 5.45, 5.47, 5.48, and 5.49. It is worth

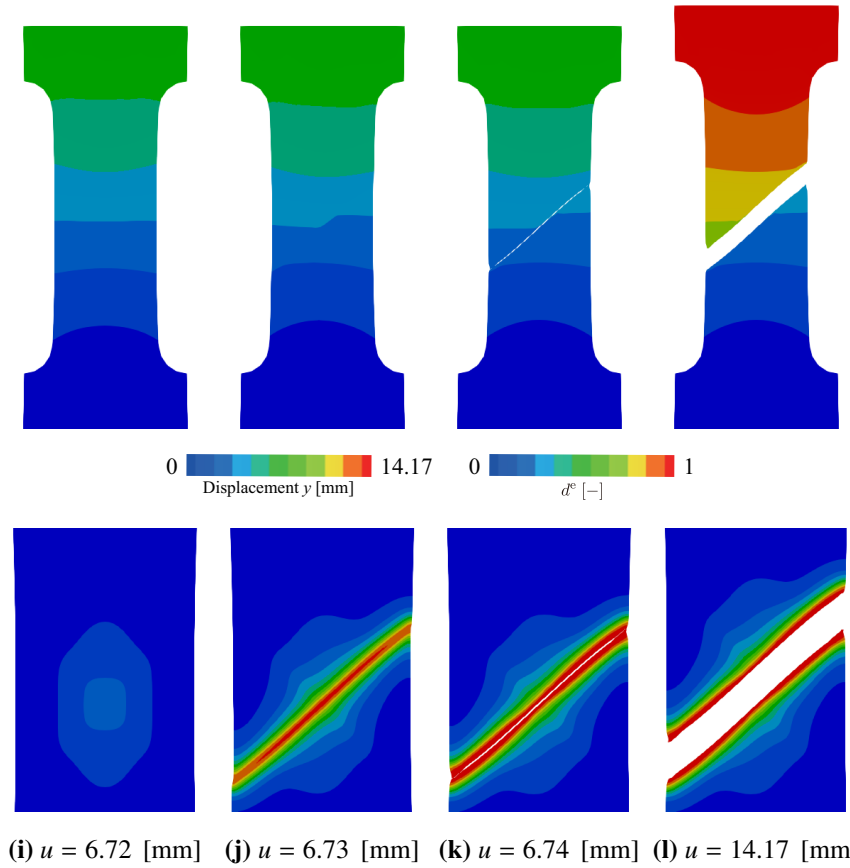


Fig. 5.47: Snapshots of deformation and detailed evolution of elastic damage variable d^e for Example 5-3-1: Case i3. The top row shows the vertical displacement, and the bottom row shows the elastic damage variable.

mentioning that elastic unloading occurs on the divided segments, but due to the irreversibility of the plastic deformation, residual deformation is visible, unlike elastic systems. In this context, we may argue that the developed CPFFCM successfully transfers the diffusive crack computed by CPFEM for the ductile fracture to the discrete representation.

5.3.2 Example 5-3-2: Tensile failure of asymmetrically notched specimen

The second example targets the tensile failure for an asymmetrically notched specimen. The objective of this example is to demonstrate the realization of ductile fracture having discrete crack surfaces by CPFFCM and to reproduce different crack patterns by changing

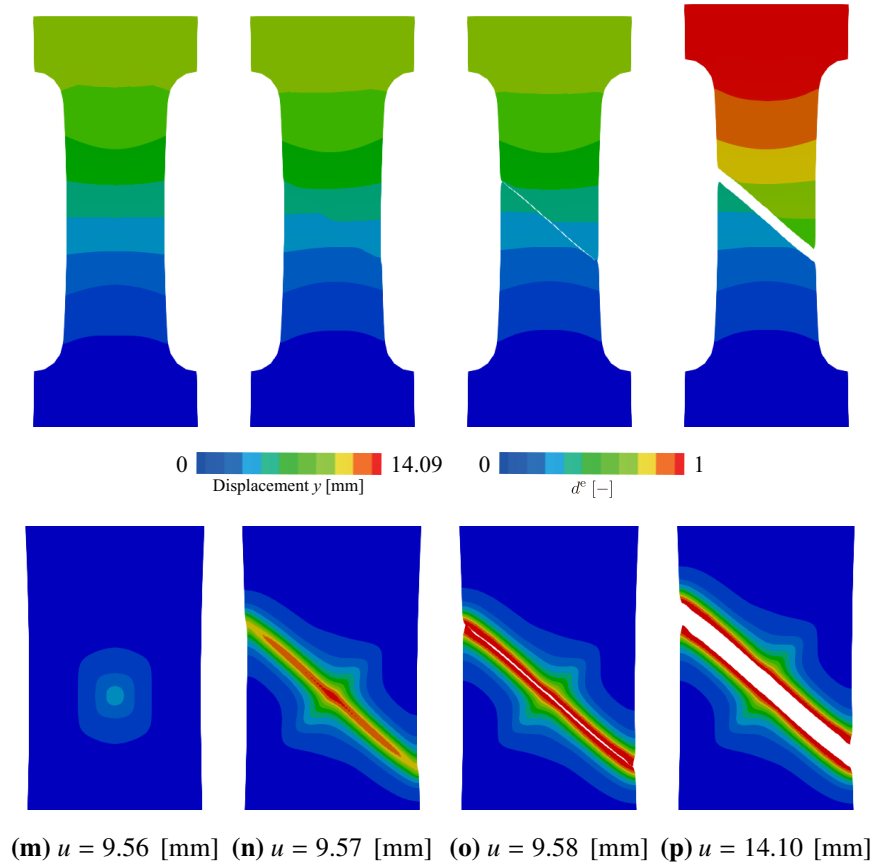


Fig. 5.48: Snapshots of deformation and detailed evolution of elastic damage variable d^e for Example 5-3-1: Case i4. The top row shows the vertical displacement, and the bottom row shows the elastic damage variable.

the parameter β_{G2} in the degrading fracture toughness, i.e., demonstrating the negative hydrostatic pressure-induced damage evolution in addition to the plasticity-induced one. The geometry of the specimen is schematized in Fig. 5.50 along with the boundary conditions: the bottom edge of the beam is fully fixed, while a vertical displacement is imposed on the top edge. Also, the material parameters and four simulation cases are provided in Table 5.11 and Table 5.12, respectively. In this particular example, the cubic degradation function is used to represent the deterioration of the material stiffness, the Voce hardening function $\hat{H}(\bar{\alpha}) = h\alpha + (y_\infty - y_0)(1 - \exp(\beta_y\alpha))$ is adopted for the hardening behavior. In addition, a fine mesh having an element size of $h_e \approx 0.20$ [mm] is used for the potentially damaged region. For Algorithm 3 and Algorithm 4, $d_{cr1} = 0.98$, $d_{cr2} = 0.50$, $C_{relax} = 10$, and $g_{min} = 0.05$

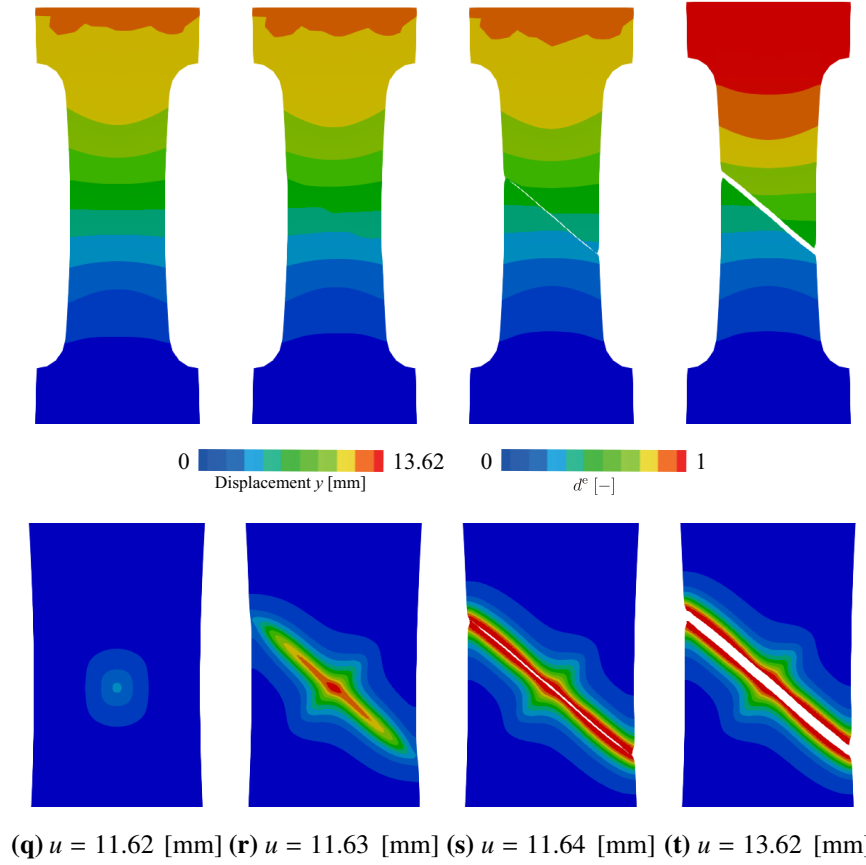


Fig. 5.49: Snapshots of deformation and detailed evolution of elastic damage variable d^e for Example 5-3-1: Case i5. The top row shows the vertical displacement, and the bottom row shows the elastic damage variable.

are used.

The load-displacement curves for four cases are shown in Fig. 5.51. Also, the detailed evolutions of elastic damage variable d^e and two degradation terms, $\cos^{p_1}(\beta_{G1}\alpha^*/2)$ & $\cos^{p_2}(\beta_{G2}\tau_p^*/2)$, for the degrading fracture toughness Eq. (3.1) are shown in Fig. 5.52~Fig. 5.55, respectively. As be seen from Fig. 5.51, for each case, a rapid load decrease is confirmed after a gradual one, which implies that the crack propagates from stably to unstably. In fact, for instance, Fig. 5.52 shows that the crack propagates stably in the displacement range $u \in [0, 2.18]$ [mm], but the specimen is suddenly separated by the crack afterward. Note that similar crack propagation behavior is also observed in the other three cases; see Fig. 5.53~Fig. 5.55.

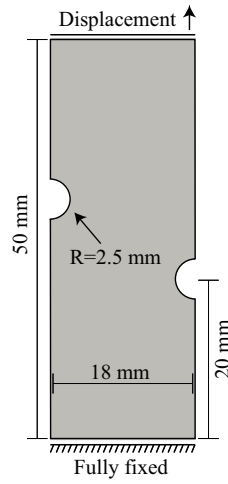


Fig. 5.50: Geometry with boundary conditions for Example 5-3-2.

Table 5.11: Material parameters for Example 5-3-2.

Parameter		Value	Unit
Young's modulus	E	220000	[MPa]
Poisson's ratio	ν	0.3	[-]
Initial yield stress	y_0	810	[MPa]
Linear hardening parameter	h	1500	[MPa]
Critical yield stress	y_∞	1000	[MPa]
Saturation parameter	β_y	100	[-]
Plastic length scale parameter	l_p	1.0	[mm]
Penalty parameter	p_p	2000	[MPa]
Initial fracture toughness	G_{c0}	500	[N/mm]
Critical fracture toughness	$G_{c\infty}$	50	[N/mm]
Crack length scale parameter	l_f	0.6	[mm]

Next, let us discuss the relationship between the crack path and the given parameters for damage computation. As listed in Table 5.12, the saturation parameter β_{G2} is set zero for Case h1 but nonzero for the other three cases, i.e., the negative hydrostatic pressure-induced damage evolution is neglected in Case h1 but considered in Cases h2, h3, and h4. Accordingly, Case h1 has a typical crack path to the one obtained from an elastoplastic damage model only

Table 5.12: Numerical simulation cases for Example 5-3-2.

Parameter	Case	h1	h2	h3	h4	Unit
Elastic damage coefficient	ζ^e	1.0	1.0	1.0	1.0	[-]
Elastic damage threshold	Ψ_{cr}^e	0	0	0	0	[MPa]
Plastic damage coefficient	ζ^p	1.0	1.0	1.0	1.0	[-]
Plastic damage threshold	Ψ_{cr}^p	0	0	0	0	[MPa]
Saturation parameter	β_{G1}	10	10	10	10	[-]
Degradation threshold	α_{cr}	0.05	0.05	0.05	0.05	[-]
Slope parameter	p_1	2	2	2	2	[-]
Saturation parameter	β_{G2}	0	0.002	0.003	0.004	[1/MPa]
Degradation threshold	τ_{cr}	800	800	800	800	[MPa]
Slope parameter	p_2	2	2	2	2	[-]

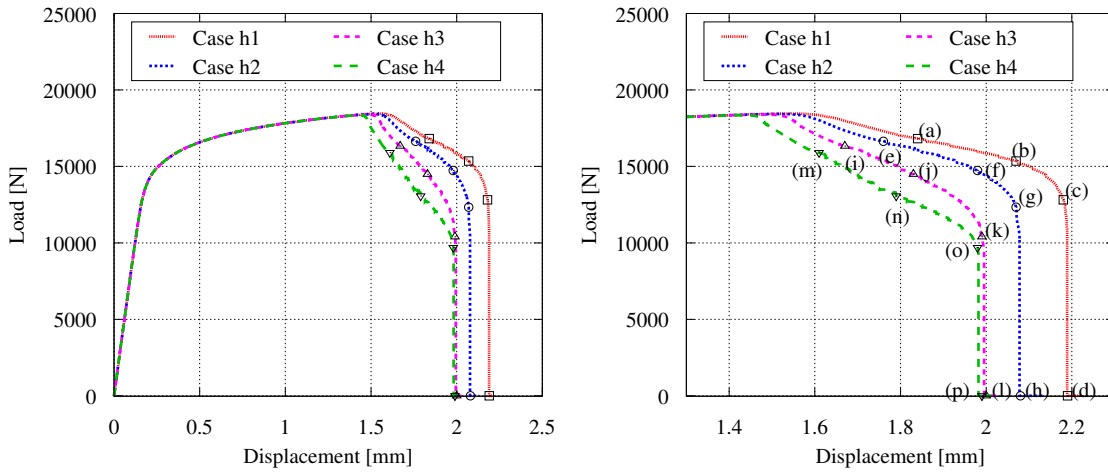


Fig. 5.51: Load-displacement curves for Example 5-3-2.

considering the plastic deformation into damage computation; the remaining three cases exhibit different trends. That is, by increasing the parameter β_{G2} , the crack initiation and initial propagation from notches tend to be horizontal. In particular, the initially propagated crack of Case h4 somewhat resembles the one computed by a CPFEM for brittle fracture; see Fig. 5.55(o) and Fig. 5.57. Also, as shown in the second and third rows in Fig. 5.53~Fig. 5.55, the crack paths initially follow the degrading tendencies of the function $\cos^{p_2}(\beta_{G2}\tau_p^*/2)$ that

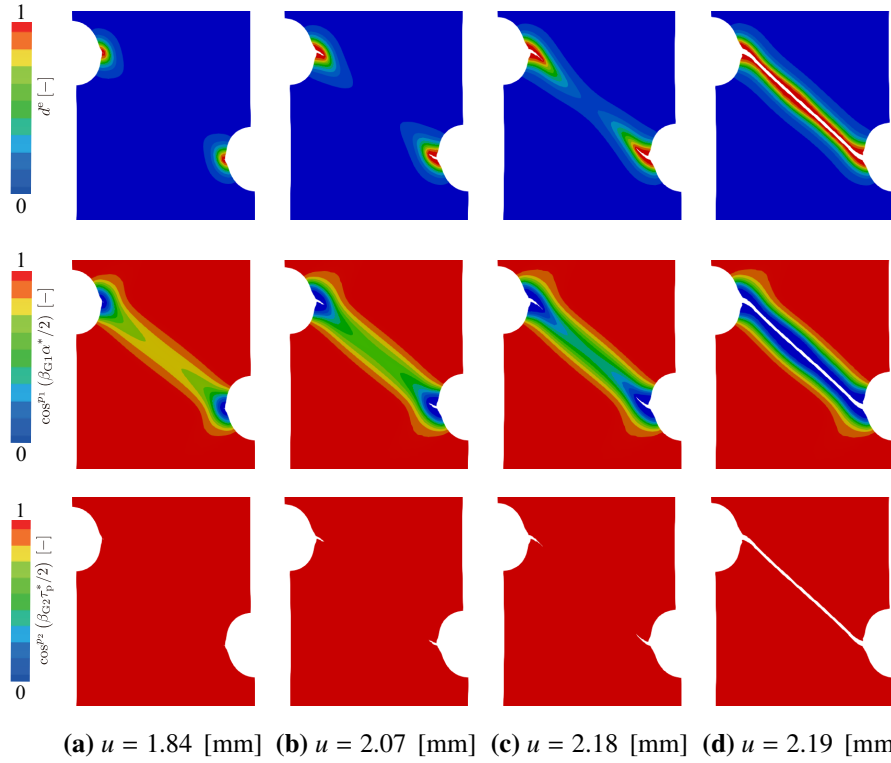


Fig. 5.52: Detailed evolution of elastic damage variable d^e and two degradation functions, $\cos^{p_1}(\beta_{G1}\alpha^*/2)$ & $\cos^{p_2}(\beta_{G2}\tau_p^*/2)$, for degrading fracture toughness in Eq. (3.1): Case h1.

are determined by the negative hydrostatic stress. Additionally, Fig. 5.56 illustrates the crack paths of four cases in the initial configuration, which is helpful for understanding the damage driving trend by the negative hydrostatic stress. Hence, enjoying the feature of the diffusive-discrete crack transition scheme, the discrete crack is successfully simulated, which allows comparisons between several cases considering different parameters for damage. As a side note, by introducing the discrete crack, the load becomes exactly zero in Fig. 5.51, and the upper divided segment can move up, as demonstrated in the previous example.

5.3.3 Example 5-3-3: Cup-cone failure of smooth/notched round bars

The last example is devoted to reproducing the cup-cone failure for smooth/notched round bars (SRB and NRB). The objective of this example is to show the capability of the CPFFCM in simulating ductile fracture for three-dimensional problems. The geometries of

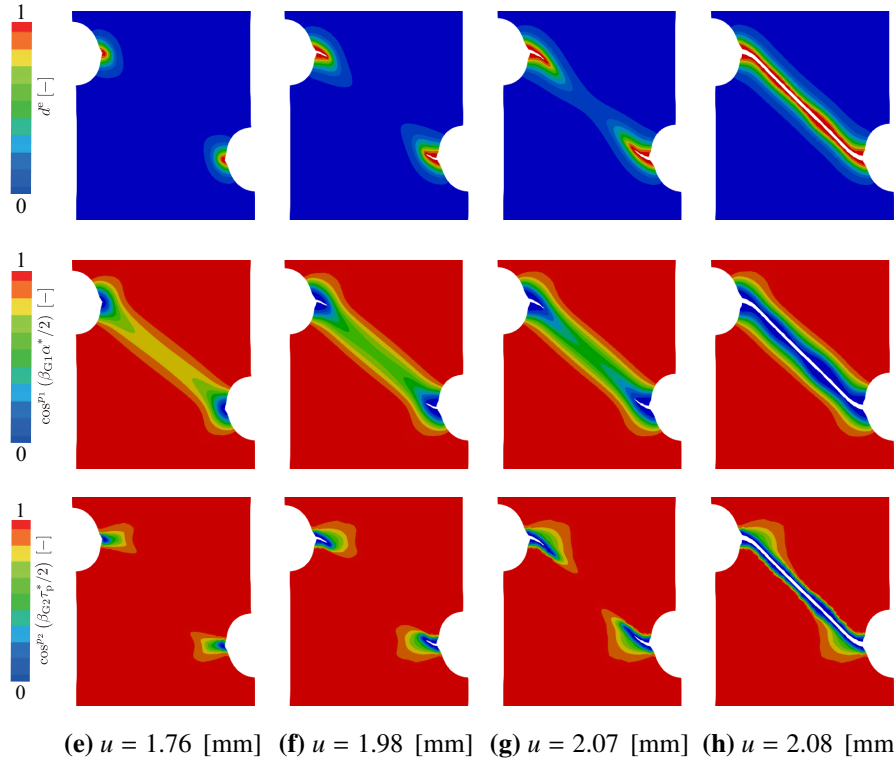


Fig. 5.53: Detailed evolution of elastic damage variable d^e and two degradation functions, $\cos^{p_1}(\beta_{G1}\alpha^*/2)$ & $\cos^{p_2}(\beta_{G2}\tau_p^*/2)$, for degrading fracture toughness in Eq. (3.1): Case h2.

the SRB and NRB are illustrated in Fig. 5.58 along with the boundary conditions: the bottom surface of each round bar is fully fixed, and a vertical displacement is imposed on the top surface. Also, the material parameters are listed in Table 5.13, in which the parameters related to the elastoplastic response have been borrowed from References ^{187),188)}. Meanwhile, the parameters concerning damage evolution are determined by trial-and-error calibration to meet the failure trend of SRB in the experiments ^{187),188)}. In this particular example, the cubic degradation function is used to represent the deterioration of the material stiffness, and the Voce hardening function $\hat{H}(\bar{\alpha}) = h\alpha + (y_\infty - y_0)(1 - \exp(\beta_y\alpha))$ is adopted for the hardening behavior. Here, the spatial gradient term for plastic hardening is neglected in this example. In addition, a mesh having an element size of $h_e \approx 0.05$ [mm] is used for the potentially damaged region. For Algorithm 3 and Algorithm 4, $d_{cr1} = 0.95$, $d_{cr2} = 0.50$, $C_{relax} = 8$, and $g_{min} = 0.05$ are used.

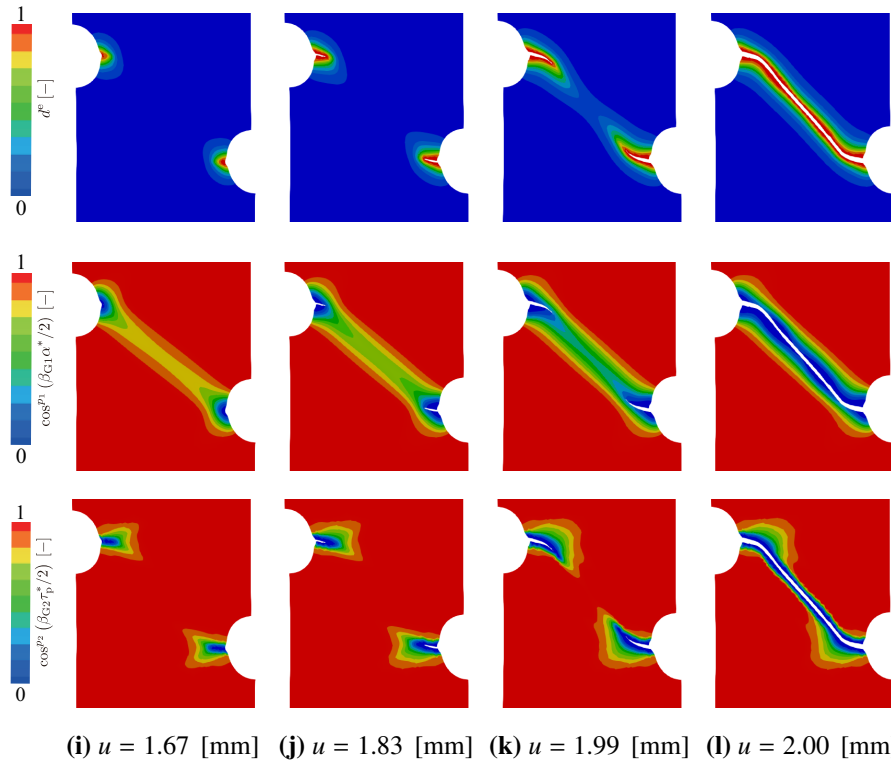


Fig. 5.54: Detailed evolution of elastic damage variable d^e and two degradation functions, $\cos^{p_1}(\beta_{G1}\alpha^*/2)$ & $\cos^{p_2}(\beta_{G2}\tau_p^*/2)$, for degrading fracture toughness in Eq. (3.1): Case h3.

The load-gauge displacement curves for the SRB and NRB are shown in Fig. 5.59 along with the experiment datum. As can be seen from the figure, the typical failure trend of elastoplastic materials is realized, i.e.,

1. The specimen first experiences uniform plastic deformation to some extent after the yielding.
2. The localization of the plastic deformation occurs, and the plastic strain concentrates on the center of the specimen.
3. An initial crack appears at the location that has experienced a large plastic strain localization.

In fact, the first and second rows in Fig. 5.60 shows the detailed evolutions of discrete crack surfaces and elastic damage variable d^e , in which the crack initiates at the center of the in-

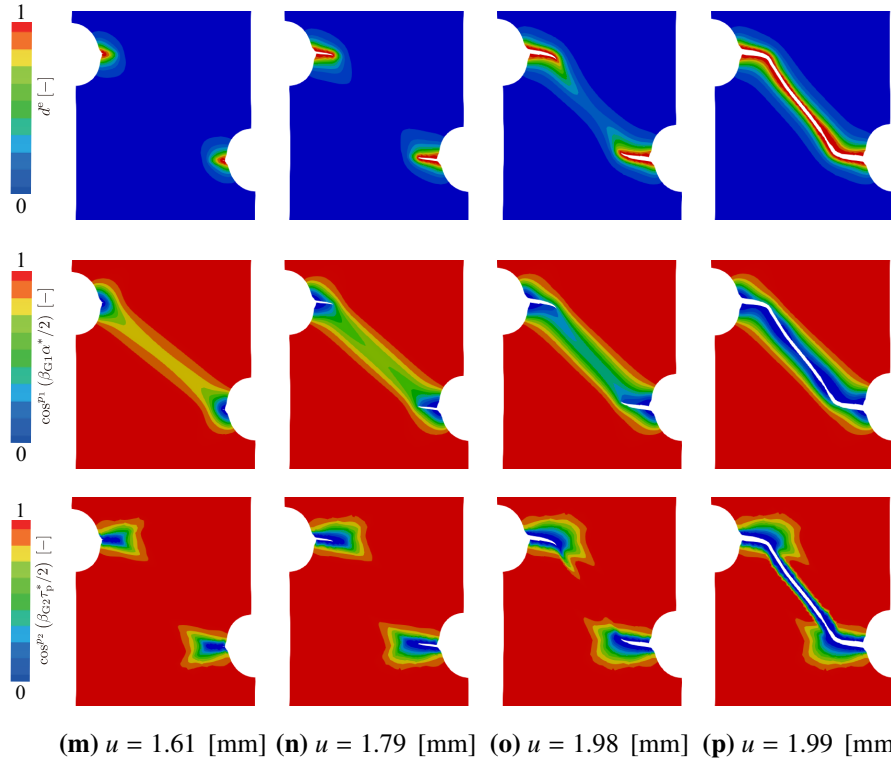


Fig. 5.55: Detailed evolution of elastic damage variable d^e and two degradation functions, $\cos^{p_1}(\beta_{G1}\alpha^*/2)$ & $\cos^{p_2}(\beta_{G2}\tau_p^*/2)$, for degrading fracture toughness in Eq. (3.1): Case h4.

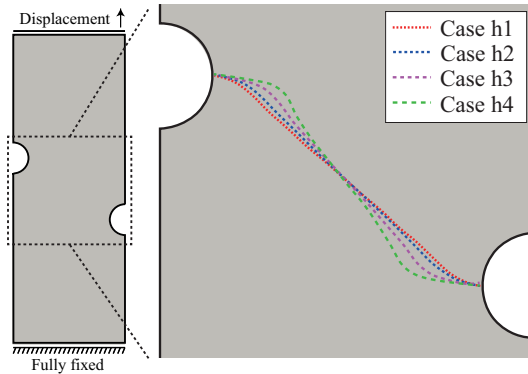


Fig. 5.56: Crack path in initial configuration for Example 5-3-2.

terior of the round bar. Subsequently, the crack propagates horizontally toward the surface of the round bar and eventually becomes inclined to form a shear lip. Here, the labels in Fig. 5.60 correspond to those in Fig. 5.59. More specifically, since both degradation terms, $\cos^{p_1}(\beta_{G1}\alpha^*/2)$ & $\cos^{p_2}(\beta_{G2}\tau_p^*/2)$, have small values at the center of the interior of the round

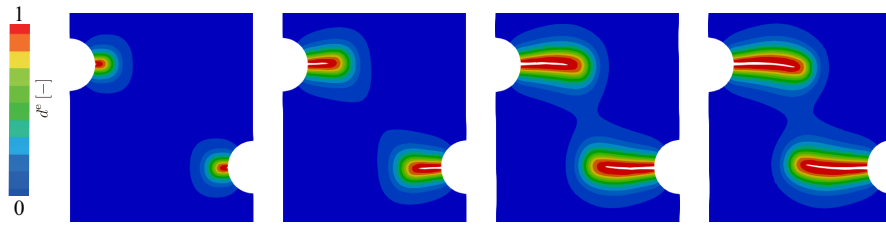


Fig. 5.57: Detailed evolution of elastic damage variable d^e : Brittle fracture.

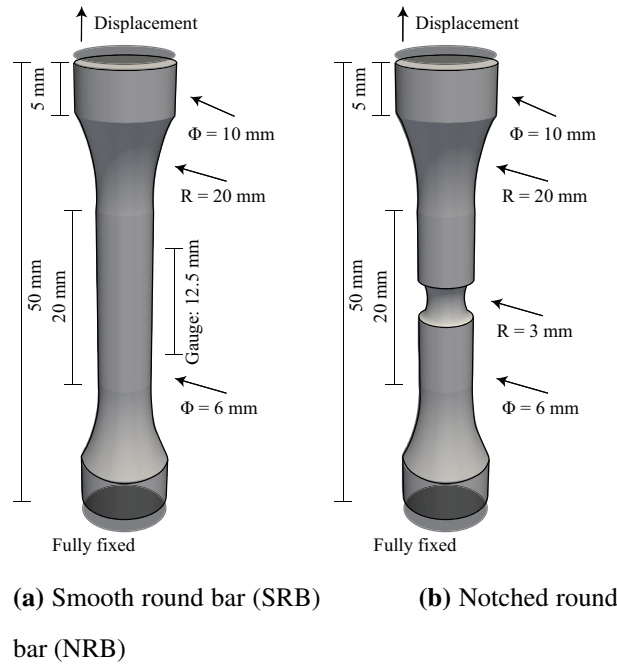


Fig. 5.58: Geometry with boundary conditions for Example 5-3-3.

bar, as shown in the third and fourth rows in Fig. 5.60(a), the crack initiation can be understood as plasticity/negative hydrostatic pressure-induced phenomenon. On the contrary, in the region where the crack becomes inclined, only the degradation term $\cos^{p_1} (\beta_{G1} \alpha^*/2)$ has a small value, which infers that the shear lip is made only by plastic deformation; see the third and fourth rows in Fig. 5.60(c).

On the other hand, while the parameters concerning damage evolution are fitted to meet the failure trend of SRB in the experiments^{187),188)}, the load-gauge displacement relation of NRB is in good agreement with the experimental one; see the lower black-colored plots and blue-colored line in Fig. 5.59. Additionally, as shown in Fig. 5.61, a series of scenarios of

Table 5.13: Material parameters for Example 5-3-3.

Parameter		Value	Unit
Young's modulus	E	68900	[MPa]
Poisson's ratio	ν	0.33	[-]
Initial yield stress	y_0	209.6	[MPa]
Linear hardening parameter	h	0	[MPa]
Critical yield stress	y_∞	272.2	[MPa]
Saturation parameter	β_y	38.81	[-]
Initial fracture toughness	G_{c0}	2.0	[N/mm]
Critical fracture toughness	$G_{c\infty}$	0.2	[N/mm]
Crack length scale parameter	l_f	0.1	[mm]
Elastic damage coefficient	ζ^e	1.0	[-]
Elastic damage threshold	Ψ_{cr}^e	0	[MPa]
Plastic damage coefficient	ζ^p	1.0	[-]
Plastic damage threshold	Ψ_{cr}^p	10	[MPa]
Saturation parameter	β_{G1}	10	[-]
Degradation threshold	α_{cr}	0.025	[-]
Slope parameter	p_1	1	[-]
Saturation parameter	β_{G2}	0.005	[1/MPa]
Degradation threshold	τ_{cr}	180	[MPa]
Slope parameter	p_2	1	[-]

cup-cone failure similar to those of SRB are successfully realized, i.e., the crack initiates from the center of the interior of the round bar, propagates horizontally toward the surface, and eventually becomes inclined to form a shear lip. It is worth mentioning that the determination of parameters in damage models can follow the above-mentioned manner. That is, once parameters concerning damage evolution of a material are fitted, with which the simulated result is in agreement with the experimental one, they should be adopted to another case, such as another geometry of the specimen, another loading speed, and so on. Then, if the fitted parameters still work well for another case, as demonstrated by the SRB and NRB in this example, they may have “objectivity”. If not, they may be “case-dependent”, so we

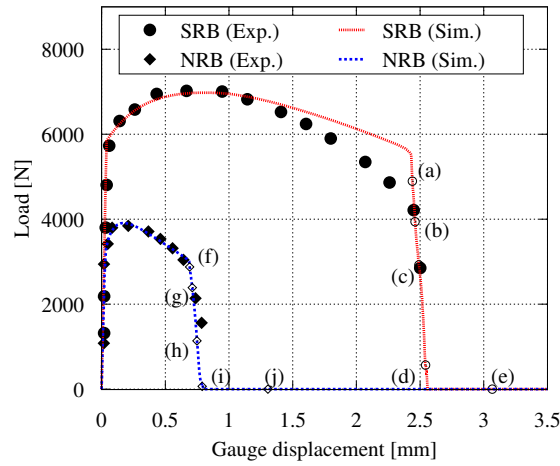


Fig. 5.59: Load-gauge displacement curves for Example 5-3-3.

should sometimes re-fit parameters.

In addition, Fig. 5.62 compares the discrete crack surfaces obtained from experiments^{187),188)} and our numerical simulations. As can be seen in the figure, a large shear lip is computed for the SRB, and a small one is computed for the NRB in our numerical simulations. Note that this trend is well consistent with experimental observations. Also, since the discrete crack surfaces are realized by CPFFCM, the observation of simulated crack surfaces becomes easier than conventional FEMs. In this context, we conclude that the developed approach, CPFFCM, is a reasonable method to reproduce and predict ductile fracture.

Remark 8 While three dimensional problems are successfully solved here, a few issues in terms of the algorithmic treatments are still unresolved. For instance, a proper crack path detection direction should be considered. In the two dimensional situation, we can just define an angle θ shown in Algorithm 3 but should consider the depth direction in three dimensional situation. Also, the discrete crack surfaces in one mathematical element should be modified to be nonlinear geometries. If the discrete crack surfaces in one mathematical element are plane surfaces, i.e., linear geometries, they may immediately determine the geometries of discrete crack surfaces in adjacent mathematical elements. Accordingly, discrete crack topologies may not be consistent with diffuse crack ones.

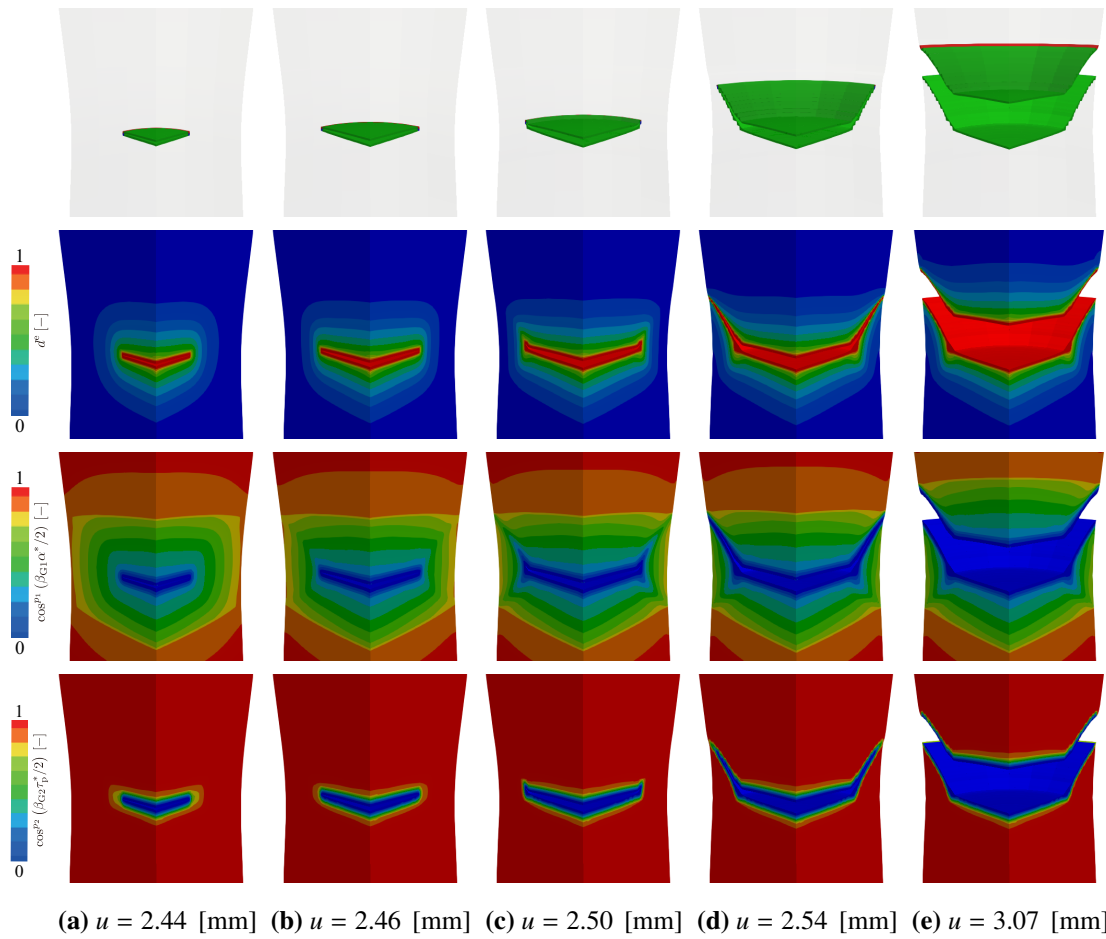


Fig. 5.60: Detailed evolution of discrete crack surfaces, elastic damage variable d^e and two degradation functions, $\cos^{p_1}(\beta_{G1}\alpha^*/2)$ & $\cos^{p_2}(\beta_{G2}\tau_p^*/2)$, for degrading fracture toughness in Eq. (3.1): SRB. (Only 1/4 of the round bar is shown.)

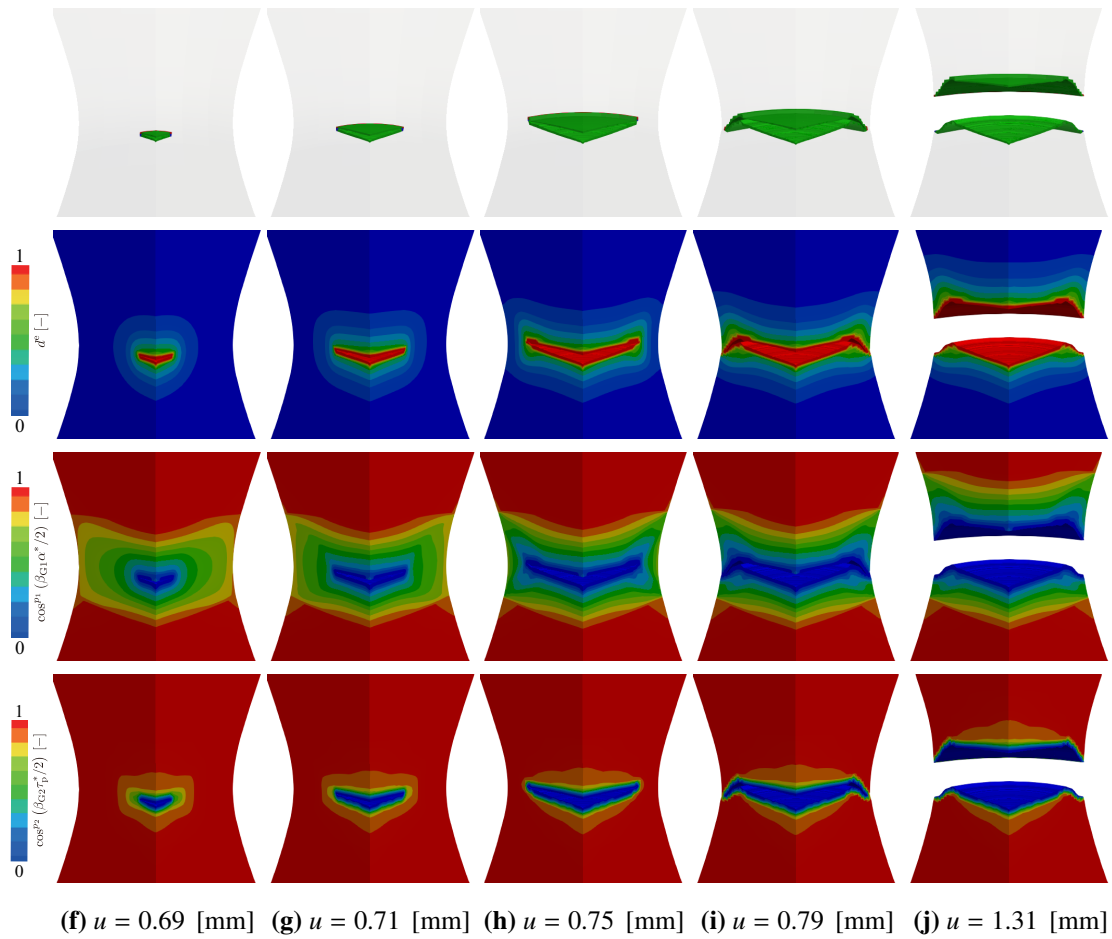


Fig. 5.61: Detailed evolution of discrete crack surfaces, elastic damage variable d^e and two degradation functions, $\cos^{p_1}(\beta_{G1}\alpha^*/2)$ & $\cos^{p_2}(\beta_{G2}\tau_p^*/2)$, for degrading fracture toughness in Eq. (3.1): NRB. (Only 1/4 of the round bar is shown.)

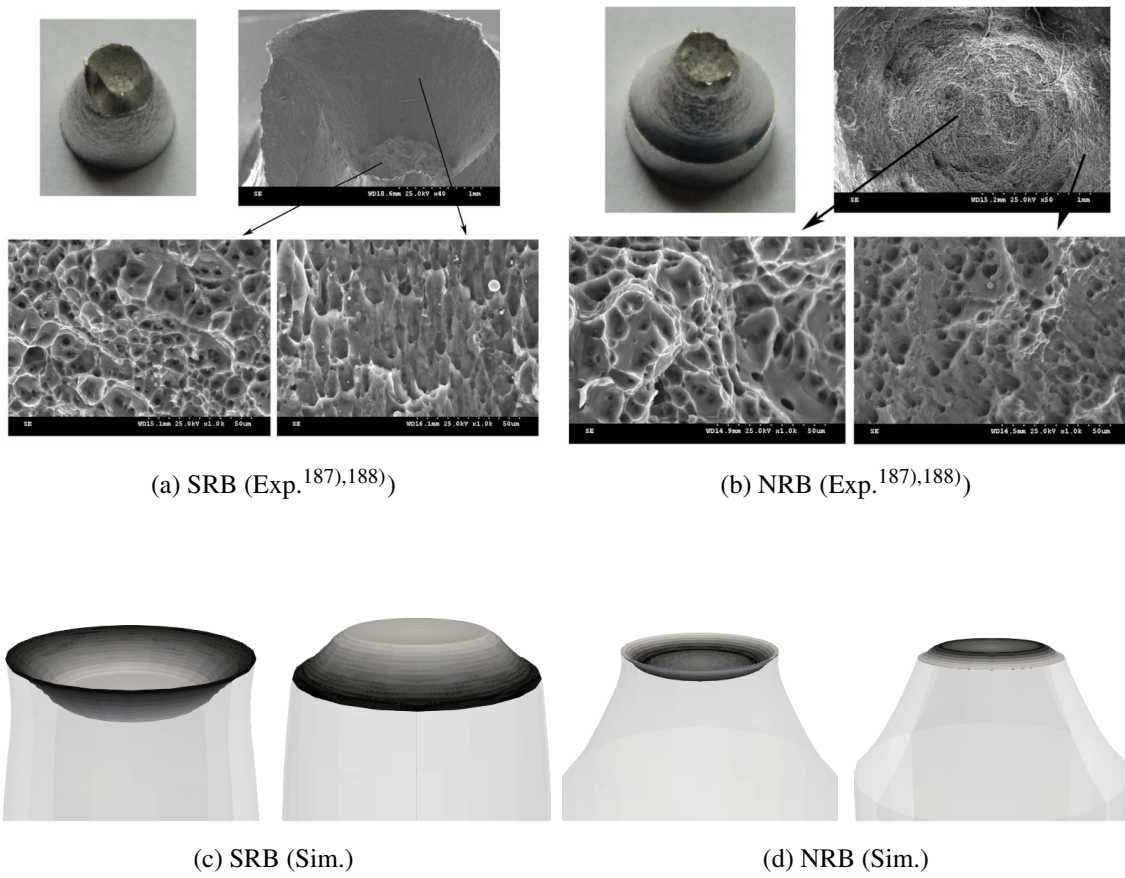


Fig. 5.62: Crack surfaces of the cup-cone failure.

6 Conclusion

This study aimed to pave the road toward the comprehensive evaluation and prediction of the multistage and multiscale failure events of a structure. To realize the purpose, a novel crack phase-field model was proposed, and a diffusive-discrete crack transition scheme was developed.

6.1 Regarding the enhancement of crack phase-field modeling

The crack phase-field model (CPFM) is known for its ability to predict the initiation of an arbitrary crack, propagation, and bifurcation while remaining compatible with classical fracture mechanics. After revisiting the fundamentals of CPFMs for brittle and dynamic fractures and reviewing the distinctive features of the plastic driving force, as well as the degrading fracture toughness and yield functions introduced in the existing models to realize ductile fracture, we have established a new model for ductile fracture.

Based on the reviewed features of existing models, a variational formulation was carried out to derive relevant evolution laws separately for plasticity and damage as stationary conditions of the supremum problem of the dissipative potential. As a result, the proposed model involved two damage variables associated with the elastic and plastic driving forces for damage evolution. For parameter studies and experimental verifications, numerical simulations have been conducted within the IGA framework. After several parameter studies were made to confirm the basic performance of the proposed model, we targeted a symmet-

rically notched specimen subjected to tensile loading to demonstrate the ability to represent the typical fracture behavior of elastoplastic materials. Based on the results of the numerical studies, both the proposed and earlier models were investigated to elucidate their similarities and differences. Also, by conducting numerical simulations with a three-dimensional setup, it is well demonstrated that the proposed model successfully reproduced the cup-cone fracture of a notched round bar, whose fracture behavior was in agreement with the experiment result reported in the literature. In addition, the fracture behavior of advanced high strength steel sheets (AHSS sheets) was simulated by the proposed model. From experimental observations, AHSS sheets exhibited unstable to stable crack propagation trends in addition to characteristic crack initiation positions. By introducing the negative hydrostatic pressure-induced degradation effect into the degrading fracture toughness, these characteristic fracture trends of AHSS sheets were successfully reproduced. Therefore, the proposed model can be regarded as a promising candidate for simulating several typical fracture events for elastoplastic materials.

6.2 Regarding the enhancement of numerical simulation method

To realize divisions of segments from an original object for the comprehensive investigation of fracture events from crack initiation to collapse, a transition scheme from diffusive to discrete crack topologies was proposed, which had been developed through the combined use of crack phase-field theory and a strong discontinuity representation. In the scheme, the crack initiation and propagation processes are determined from an energy minimization problem within the framework of CPF modeling, and the predicted crack path is explicitly represented by the finite cover method (FCM). Specifically, the proposed scheme reproduces the geometry of a discrete crack path by updating its crack tip during a staggered iteration procedure involving a transition from a diffusive crack topology to a discrete crack topology, which is realized by the proposed technique to determine explicit crack tips. Additionally,

by introducing stabilization techniques to crack opening processes, the collapse of severely damaged elements can be avoided, and the crack tips are opened gradually and stably under both quasi-static and dynamic conditions within the finite strain framework. Due to these features, the proposed scheme enables us to trace the paths of dramatically propagated and curved discrete cracks without any difficulty.

Four numerical examples, including well-known benchmark problems for brittle fracture, were presented to demonstrate the performance and capability of the proposed scheme. From these simulations, we have shown the superiority of the proposed method “CPFFCM” over the conventional method “CPFFEM” in terms of computational stability. Also, four other numerical examples for dynamic fracture were presented, in which a series of fracture events involving crack initiation at an arbitrary location, crack propagation and bifurcation in arbitrary directions, arbitrary divisions of an original object into multiple portions, and independent motions of these portions in the post division phase were successfully simulated. In addition, the other three numerical examples were conducted to demonstrate the CPFFCM to ductile fracture. Similar to the results of brittle and dynamic fractures, crack initiation and propagation trends were successfully reproduced along with the explicit representation of crack surfaces.

6.3 Future works

Some issues to be considered in the future are as follows:

- *Additional investigations of the proposed model.*

In this study, we have not deepened the discussions about the physical interpretations of the two damage variables and the evolution laws for plasticity and damage. This remains untouched and must be addressed along with further experimental investigations in future work. In particular, if a reasonable manner to determine the parameters concerning damage evolution is found, the proposed model can be a strong candidate to reveal unresolved fracture behavior in elastoplastic materials.

- *Improvements in three dimensional problems.*

As discussed before, the definition of the crack surface patch in three dimensional problems should be reconsidered. Specifically, if the crack surface patch is linear, it encounters difficulty in properly representing geometries, and the diffusive-discrete crack transition cannot be correctly performed. To address the issue, the bend of a crack surface patch within an element can be considered.

- *Incorporations of other damage models.*

While the proposed scheme is developed for CPFMs, the applications to other non-local damage models are relatively easy. On the other hand, the applications to local damage models may require modifications of the crack path detection scheme since the distribution of damage variables is not such well located as seen in non-local damage models. In addition, if a model without having the damage variable is targeted, other graphic information should be installed into the developed scheme.

- *Extensions to multifield/multistage problems.*

The separation of materials enables further consideration of various situations after fracture, such as frictional contact between opposite crack surfaces, the inflow/outflow of gases and fluids, and the secondary fracture of segmented bodies. For such cases, more degrees of freedom may be required, and computation time would be a bottleneck. Thus, efficient spatial discretizations, computational algorithms, and sophisticated parallelization techniques are needed.

- *Combinations with other research fields.*

The proposed diffusive-discrete crack transition scheme was developed to fracture problems but can be employed in other research fields. This is because the proposed scheme is essentially a technique to realize discontinuity in the state field based on some criteria. For instance, the combination with topology optimization may be interesting: the interfaces determined by design variables can be represented explicitly so that the issue of resolution may be alleviated.

Since the author's voyage continues, these extensions are left to future work.

Appendix A Supplements for CPFM

A.1 Original motivation to introduce two damage variables

d^e and d^p

Suppose that we have a CPFM for ductile fracture having elastic and plastic damage driving forces without thresholds. Then, its dissipation rate, yield function (threshold function), dissipation potential rate, and evolution law of d yield, respectively,

$$\begin{aligned}\mathcal{D}^f &= \tau^f \dot{d} - r^f \dot{d} \quad \text{with} \quad \tau^f = -g'(d) (\Psi_0^{e+} + \Psi_0^p), \quad r^f = \delta_d \Psi^f = \frac{G_c}{l_f} (d - l_f^2 \Delta d) \\ \Phi^f &:= \tau^f - r^f \leq 0 \\ \Upsilon &= \sup_{\tau^f, r^f} [\tau^f \dot{d} - r^f \dot{d} - \lambda^f \Phi^f] \quad \Rightarrow \quad \dot{d} = \lambda^f \frac{\partial \Phi^f}{\partial (\tau^f - r^f)},\end{aligned}\tag{A.1}$$

where the dissipation due to plastic deformation is omitted since it does not contribute to the discussion here. In this case, we have only one crack phase-field variable d , since the components, τ^f and r^f , are commonly used in \mathcal{D}^f and Φ^f ; see, for example, Kuhn et al. ⁸⁷⁾ that belongs to this case. As discussed in Alessi et al. ⁹²⁾, this kind of model is not rich enough to capture a variety of anticipated ductile fractures.

Then, if thresholds Ψ_{cr}^e & Ψ_{cr}^p and coefficients β_e & β_p are introduced, as considered by Borden et al. ⁸³⁾, we deal with the following format:

$$\begin{aligned}\mathcal{D}^f &= \tau^f \dot{d} - r^f \dot{d} \quad \text{with} \quad \tau^f = -g'(d) (\Psi_0^{e+} + \Psi_0^p), \quad r^f = \delta_d \Psi^f = \frac{G_c}{l_f} (d - l_f^2 \Delta d) \\ \Phi^f &:= \tau^{f*} - r^f \quad \text{with} \quad \tau^{f*} = -g'(d) (\beta_e \Psi_0^{e+} + \beta_p < \Psi_0^p - \Psi_{cr}^p >) \\ \Upsilon &= \sup_{\tau^f, r^f} [\tau^f \dot{d} - r^f \dot{d} - \lambda^f \Phi^f] \quad \Rightarrow \quad \dot{d} = \lambda^f \frac{\partial \Phi^f}{\partial (\tau^f - r^f)} = \lambda^f \frac{\partial (\tau^{f*} - r^f)}{\partial (\tau^f - r^f)}.\end{aligned}\tag{A.2}$$

Because of the existence of these post-introduced parameters, it is impossible to derive variationally consistent evolution law for this case. This is the “dilemma” explained in Section 1.2.1.

From the above discussion, it can be seen that the variationally consistent evolution law cannot be derived because both the thermodynamic force τ^f and the dissipative resistance force r^f are conjugate to the same crack phase-field variable d . We thus define separate variables for them following the relation between the rates of plastic strain d^p and hardening variable $\tilde{\alpha}$ in plasticity theory. To be specific, we define two damage variables d^e and d^p conjugate to elastic and plastic driving forces in addition to the original crack phase-field variable d conjugate to the dissipative resistance force r^f . Then, their variationally consistent evolution laws can be derived as

$$\begin{aligned}
 \mathcal{D}^f &= \tau^{fe} \dot{d}^e + \tau^{fp} \dot{d}^p - r^f \dot{d} \\
 \Phi^f &:= \tau^{fe*} + \tau^{fp*} - r^f \quad \text{with} \quad \tau^{fe*} = -\frac{\partial g(d^e)}{\partial d^e} \langle \Psi_0^{e+} - \Psi_{cr}^e \rangle \zeta^e, \quad \tau^{fp*} = -\frac{\partial g(d^p)}{\partial d^p} \langle \Psi_0^p - \Psi_{cr}^p \rangle \zeta^p \\
 \Upsilon &= \sup_{\tau^{fe}, \tau^{fp}, r^f} \left[\tau^{fe} \dot{d}^e + \tau^{fp} \dot{d}^p - r^f \dot{d} - \lambda^f \Phi^f \right] \\
 \Rightarrow \quad \dot{d}^e &= \lambda^f \frac{\partial \Phi^f}{\partial \tau^{fe}} = \lambda^f \zeta^e \underbrace{\chi^e}_{\text{Eq. (2.80)}}, \quad \dot{d}^p = \lambda^f \frac{\partial \Phi^f}{\partial \tau^{fp}} = \lambda^f \zeta^p \underbrace{\chi^p}_{\text{Eq. (2.80)}}, \quad \dot{d} = -\lambda^f \frac{\partial \Phi^f}{\partial r^f} = \lambda^f.
 \end{aligned} \tag{A.3}$$

A.2 Confirmation of $\mathcal{K}_{22} > 0$

Assuming a homogenous deformation ($\Delta d = \nabla^2 d = 0$) and taking into account $\Phi^f = 0$ in Eq. (2.79), an equation

$$-\frac{\partial g(d^e)}{\partial d^e} (\Psi_0^{e+} - \Psi_{cr}^e) \zeta^e - \frac{\partial g(d^p)}{\partial d^p} (\Psi_0^p - \Psi_{cr}^p) \zeta^p - \frac{G_c}{l_f} d = 0. \tag{A.4}$$

is obtained. Given that the cubic form is used, the damage variable d_{cr}^e at the moment when the plastic driving force is activated, namely, the situation $\Psi_0^p = \Psi_{\text{cr}}^p$, yields

$$\begin{aligned}
 & -\frac{\partial g(d_{\text{cr}}^e)}{\partial d^e} (\Psi_0^{e+, \text{cr}} - \Psi_{\text{cr}}^e) \zeta^e - \frac{G_c}{l_f} d_{\text{cr}}^e = 0 \\
 \Rightarrow \quad d_{\text{cr}}^e &= \frac{4s - 6 + \mathcal{W} - \sqrt{4s^2 + 8(\mathcal{W} - 3)s + (\mathcal{W} - 6)^2}}{6s - 12} \\
 \text{with } \mathcal{W} &= \frac{G_c}{l_f} \frac{1}{(\Psi_0^{e+, \text{cr}} - \Psi_{\text{cr}}^e) \zeta^e},
 \end{aligned} \tag{A.5}$$

where $\Psi_0^{e+, \text{cr}}$ is the amount at the moment when the plastic driving force is activated. It should be noted that we assume the relation $d = d^e > d^p$ since d^e is computed even before the material exhibits plastic deformation. Then, the plastic damage variable $d^p = d^e - d_{\text{cr}}^e$ when both two driving forces are active yields

$$\begin{aligned}
 & -\frac{\partial g(d^e)}{\partial d^e} (\Psi_0^{e+} - \Psi_{\text{cr}}^e) \zeta^e - \frac{\partial g(d^p)}{\partial d^p} (\Psi_0^p - \Psi_{\text{cr}}^p) \zeta^p - \frac{G_c}{l_f} d^e = 0 \\
 \Rightarrow \quad d^p &= \frac{-\mathcal{T} - \sqrt{\mathcal{T}^2 - 4\mathcal{S}\mathcal{U}}}{2\mathcal{S}} \\
 \text{with } \left\{ \begin{array}{l} \mathcal{S} = (3s - 6) \{ (\Psi_0^{e+} - \Psi_{\text{cr}}^e) \zeta^e + (\Psi_0^p - \Psi_{\text{cr}}^p) \zeta^p \} \\ \mathcal{T} = (6 - 4s) \{ (\Psi_0^{e+} - \Psi_{\text{cr}}^e) \zeta^e + (\Psi_0^p - \Psi_{\text{cr}}^p) \zeta^p \} \\ \quad + (6s - 12) (\Psi_0^{e+} - \Psi_{\text{cr}}^e) \zeta^e d_{\text{cr}}^e - \frac{G_c}{l_f} \\ \mathcal{U} = (3s - 6) (\Psi_0^{e+} - \Psi_{\text{cr}}^e) \zeta^e d_{\text{cr}}^e{}^2 + \left\{ (6 - 4s) (\Psi_0^{e+} - \Psi_{\text{cr}}^e) \zeta^e - \frac{G_c}{l_f} \right\} d_{\text{cr}}^e \\ \quad + s \{ (\Psi_0^{e+} - \Psi_{\text{cr}}^e) \zeta^e + (\Psi_0^p - \Psi_{\text{cr}}^p) \zeta^p \} \end{array} \right. .
 \end{aligned} \tag{A.6}$$

Sustituting Eq. (A.5) and Eq. (A.6) into Eq. (2.95), the component \mathcal{K}_{22} is rewritten as

$$\begin{aligned}
 \mathcal{K}_{22} &= \frac{\partial^2 g(d^e)}{\partial d^{e2}} (\Psi_0^{e+} - \Psi_{\text{cr}}^e) \zeta^{e2} + \frac{\partial^2 g(d^p)}{\partial d^{p2}} (\Psi_0^p - \Psi_{\text{cr}}^p) \zeta^{p2} + \frac{G_c}{l_f} - \underbrace{\frac{d^2}{dX^2} \frac{\partial G_c l_f \Delta d}{\partial \Delta d}}_{=0} \\
 &= \{(12 - 6s) d^p + 4s - 6\} \{ (\Psi_0^{e+} - \Psi_{\text{cr}}^e) \zeta^{e2} + (\Psi_0^p - \Psi_{\text{cr}}^p) \zeta^{p2} \} \\
 &\quad + (12 - 6s) d_{\text{cr}}^e (\Psi_0^{e+} - \Psi_{\text{cr}}^e) \zeta^{e2} + \frac{G_c}{l_f}.
 \end{aligned} \tag{A.7}$$

Now, we may provide $\zeta^e = 1$ and $\zeta^p = 1$ without losing generality and provide $s = 0$ for

the boundary condition ($s > 0$). Then, the modified \mathcal{K}_{22}^* is

$$\begin{aligned}
 \mathcal{K}_{22}^* &= (12d^{\text{e}*} - 6) \underbrace{(\Psi_0^{\text{e}+} - \Psi_{\text{cr}}^{\text{e}})}_{\mathcal{X}} + (12d^{\text{p}*} - 6) \underbrace{(\Psi_0^{\text{p}} - \Psi_{\text{cr}}^{\text{p}})}_{\mathcal{Y}} + \frac{G_{\text{c}}}{l_{\text{f}}} \\
 &= (12d^{\text{p}*} - 6)(\mathcal{X} + \mathcal{Y}) + 12d_{\text{cr}}^{\text{e}*} \mathcal{X} + \frac{G_{\text{c}}}{l_{\text{f}}}, \\
 d_{\text{cr}}^{\text{e}*} &= 1 - \frac{1}{6} \frac{G_{\text{c}}}{l_{\text{f}}} \frac{1}{\underbrace{(\Psi_0^{\text{e}+, \text{cr}} - \Psi_{\text{cr}}^{\text{e}})}_{\mathcal{X}^*}} \quad \text{and} \quad d^{\text{p}*} = \frac{-\mathcal{T}^* - \sqrt{\mathcal{T}^{*2} - 4\mathcal{S}^*\mathcal{U}^*}}{2\mathcal{S}^*}
 \end{aligned} \tag{A.8}$$

$$\text{with} \quad \begin{cases} \mathcal{S}^* = -6(\mathcal{X} + \mathcal{Y}) \\ \mathcal{T}^* = (6 - 12d_{\text{cr}}^{\text{e}*})\mathcal{X} + 6\mathcal{Y} - \frac{G_{\text{c}}}{l_{\text{f}}} \\ \mathcal{U}^* = 6(d_{\text{cr}}^{\text{e}*} - d_{\text{cr}}^{\text{e}*2})\mathcal{X} - \frac{G_{\text{c}}}{l_{\text{f}}}d_{\text{cr}}^{\text{e}*} \end{cases}$$

In order to figure out the shape of the surface Eq. (A.8), let us derive the following derivative:

$$\begin{aligned}
 \frac{\partial \mathcal{K}_{22}^*}{\partial \mathcal{X}} &= 12d^{\text{p}*} + 12d_{\text{cr}}^{\text{e}} - 6 + 12(\mathcal{X} + \mathcal{Y}) \frac{\partial d^{\text{p}*}}{\partial \mathcal{X}} \\
 &= \frac{\mathcal{T}^*}{(\mathcal{X} + \mathcal{Y})} + \frac{\sqrt{\mathcal{T}^{*2} - 4\mathcal{S}^*\mathcal{U}^*}}{(\mathcal{X} + \mathcal{Y})} + 12d_{\text{cr}}^{\text{e}} - 6 \\
 &\quad + \frac{\frac{G_{\text{c}}}{l_{\text{f}}} - 12d_{\text{cr}}^{\text{e}}\mathcal{Y}}{(\mathcal{X} + \mathcal{Y})} \\
 &\quad + \frac{\left(72d_{\text{cr}}^{\text{e}2}\mathcal{Y} + 6\frac{G_{\text{c}}}{l_{\text{f}}}\right)\mathcal{X} - 72d_{\text{cr}}^{\text{e}2}\mathcal{Y}^2 + (24d_{\text{cr}}^{\text{e}} + 6)\frac{G_{\text{c}}}{l_{\text{f}}}\mathcal{Y} - \left(\frac{G_{\text{c}}}{l_{\text{f}}}\right)^2}{(\mathcal{X} + \mathcal{Y})\sqrt{\mathcal{T}^{*2} - 4\mathcal{S}^*\mathcal{U}^*}}
 \end{aligned} \tag{A.9}$$

$$\text{with} \quad \frac{\partial d^{\text{p}*}}{\partial \mathcal{X}} = \frac{\frac{G_{\text{c}}}{l_{\text{f}}} - 12d_{\text{cr}}^{\text{e}}\mathcal{Y}}{12(\mathcal{X} + \mathcal{Y})^2} + \frac{\left(72d_{\text{cr}}^{\text{e}2}\mathcal{Y} + 6\frac{G_{\text{c}}}{l_{\text{f}}}\right)\mathcal{X} - 72d_{\text{cr}}^{\text{e}2}\mathcal{Y}^2 + (24d_{\text{cr}}^{\text{e}} + 6)\frac{G_{\text{c}}}{l_{\text{f}}}\mathcal{Y} - \left(\frac{G_{\text{c}}}{l_{\text{f}}}\right)^2}{12(\mathcal{X} + \mathcal{Y})^2\sqrt{\mathcal{T}^{*2} - 4\mathcal{S}^*\mathcal{U}^*}}$$

Here, since $\mathcal{X} + \mathcal{Y} > 0$ and $\sqrt{\mathcal{T}^{*2} - 4\mathcal{S}^*\mathcal{U}^*} > 0$, let us derive $(\mathcal{X} + \mathcal{Y}) \sqrt{\mathcal{T}^{*2} - 4\mathcal{S}^*\mathcal{U}^*} \partial_{\mathcal{X}} \mathcal{K}_{22}^*$

$$\begin{aligned}
& (\mathcal{X} + \mathcal{Y}) \sqrt{\mathcal{T}^{*2} - 4\mathcal{S}^*\mathcal{U}^*} \frac{\partial \mathcal{K}_{22}^*}{\partial \mathcal{X}} \\
&= 36\mathcal{X}^2 + \left(-6\frac{G_c}{l_f} - 72\left(-\frac{1}{3}\frac{G_c}{l_f\mathcal{X}^*} + \frac{1}{36}\left(\frac{G_c}{l_f\mathcal{X}^*} \right)^2 \right) \mathcal{Y} \right) \mathcal{X} \\
&\quad - 72\left(-\frac{1}{3}\frac{G_c}{l_f\mathcal{X}^*} + \frac{1}{36}\left(\frac{G_c}{l_f\mathcal{X}^*} \right)^2 \right) \mathcal{Y}^2 - 6\frac{G_c}{l_f}\mathcal{Y} - 36\mathcal{Y}^2.
\end{aligned} \tag{A.10}$$

Note that Eq. (A.10) is a quadratic function of \mathcal{X} that is convex downward. Hence, it is sufficient to satisfy the second condition in Eq. (2.93) that Eq. (A.10) has zero or positive value for $\mathcal{X} = Q\mathcal{X}^* \geq \mathcal{X}^*$ with $Q \geq 1$. Also, given that d_{cr}^e is positive, we obtain an inequality $\mathcal{X}^* > \mathcal{X}_{cr}^* = G_c/6l_f$. Substituting $\mathcal{X} = Q\mathcal{X}^*$ and $\mathcal{X}^* = \mathcal{X}_{cr}^*$ into Eq. (A.10), we may confirm the second condition is satisfied:

$$\begin{aligned}
& 36Q^2\mathcal{X}^{*2} + \left(-6\frac{G_c}{l_f} - 72\left(-\frac{1}{3}\frac{G_c}{l_f\mathcal{X}^*} + \frac{1}{36}\left(\frac{G_c}{l_f\mathcal{X}^*} \right)^2 \right) \mathcal{Y} \right) Q\mathcal{X}^* \\
& - 72\left(-\frac{1}{3}\frac{G_c}{l_f\mathcal{X}^*} + \frac{1}{36}\left(\frac{G_c}{l_f\mathcal{X}^*} \right)^2 \right) \mathcal{Y}^2 - 6\frac{G_c}{l_f}\mathcal{Y} - 36\mathcal{Y}^2 \\
&= 36\mathcal{Y}^2 + (12Q - 6)\frac{G_c}{l_f}\mathcal{Y} + (Q^2 - Q)\left(\frac{G_c}{l_f} \right)^2 \\
&\quad \left\{ (12Q - 6)\frac{G_c}{l_f} \right\}^2 - 144(Q^2 - Q)\left(\frac{G_c}{l_f} \right)^2 = 36\left(\frac{G_c}{l_f} \right)^2 > 0 \\
&\Rightarrow \mathcal{K}_{22}^* > 0 \quad \text{and} \quad \mathcal{K}_{22} > 0.
\end{aligned} \tag{A.11}$$

A.3 Components accounting for global tangent matrix

The component in Eq. (2.124) is written as

$$\frac{\partial \boldsymbol{\tau}}{\partial \mathbf{F}} = \begin{cases} g(d^e) \frac{\partial \boldsymbol{\tau}_{0,\text{vol}}}{\partial \mathbf{F}} + g(d^e) \frac{\partial \boldsymbol{\tau}_{0,\text{dev}}}{\partial \mathbf{F}} & \text{for } J^e \geq 1 \\ \frac{\partial \boldsymbol{\tau}_{0,\text{vol}}}{\partial \mathbf{F}} + g(d^e) \frac{\partial \boldsymbol{\tau}_{0,\text{dev}}}{\partial \mathbf{F}} & \text{for } J^e < 1 \end{cases} \tag{A.12}$$

with

$$\frac{\partial \boldsymbol{\tau}_0}{\partial \mathbf{F}} = \left\{ \frac{\partial \boldsymbol{\tau}_{0,\text{vol}}}{\partial \mathbf{b}^e} + \frac{\partial \boldsymbol{\tau}_{0,\text{dev}}}{\partial \mathbf{b}^e} \right\} : \frac{\partial \mathbf{b}^e}{\partial \mathbf{F}} = \left\{ \frac{1}{2} \kappa J^{e2} \mathbf{1} \otimes \mathbf{b}^{e-1} + \mu J^{e-2/3} \left(\mathbf{1}_{\text{dev}} - \frac{1}{3} \mathbf{b}_{\text{dev}}^e \otimes \mathbf{b}^{e-1} \right) \right\} : \frac{\partial \mathbf{b}^e}{\partial \mathbf{F}}, \tag{A.13}$$

where $\mathbf{1}$ and $\underline{\mathbf{1}}_{\text{dev}}$ denote the second-order identity tensor and the fourth-order deviatoric identity tensor, respectively. Using the total differential, the last term in Eq. (A.13) yields

$$\frac{\partial \mathbf{b}^e}{\partial \mathbf{F}} = \left. \frac{\partial \mathbf{b}^e}{\partial \mathbf{F}} \right|_{\lambda^p, \mathbf{n}=\text{const.}} + \left. \frac{\partial \mathbf{b}^e}{\partial \lambda^p} \right|_{\mathbf{n}, \mathbf{F}=\text{const.}} \otimes \frac{\partial \lambda^p}{\partial \mathbf{F}} + \left. \frac{\partial \mathbf{b}^e}{\partial \mathbf{n}} \right|_{\mathbf{F}, \lambda^p=\text{const.}} : \frac{\partial \mathbf{n}}{\partial \mathbf{F}} \quad (\text{A.14})$$

with

$$\left. \frac{\partial \mathbf{b}^e}{\partial \mathbf{F}} \right|_{\lambda^p, \mathbf{n}=\text{const.}} = \exp \left(-2 \frac{\lambda^p}{g(d^e)} \Delta t \mathbf{n} \right) \otimes \left(\mathbf{C}^{p-1}_n \cdot \mathbf{F}^T \right)^T + \left\{ \exp \left(-2 \frac{\lambda^p}{g(d^e)} \Delta t \mathbf{n} \right) \cdot \mathbf{F} \cdot \mathbf{C}^{p-1}_n \right\} \otimes \mathbf{1}, \quad (\text{A.15})$$

$$\left. \frac{\partial \mathbf{b}^e}{\partial \lambda^p} \right|_{\mathbf{n}, \mathbf{F}=\text{const.}} = \left\{ \mathbf{D} \exp \left(-2 \frac{\lambda^p}{g(d^e)} \Delta t \mathbf{n} \right) : \left(-2 \frac{1}{g(d^e)} \Delta t \mathbf{n} \right) \right\} \cdot \mathbf{b}^{e, \text{tr}}, \quad (\text{A.16})$$

$$\left. \frac{\partial \mathbf{b}^e}{\partial \mathbf{n}} \right|_{\mathbf{F}, \lambda^p=\text{const.}} = \underbrace{\left\{ \mathbf{D} \exp \left(-2 \frac{\lambda^p}{g(d^e)} \Delta t \mathbf{n} \right) : \left(-2 \frac{\lambda^p}{g(d^e)} \Delta t \underline{\mathbf{1}}_{\text{sym}} \right) \right\}}_{i a k l} * \underbrace{\mathbf{b}^{e, \text{tr}}}_{a j}. \quad (\text{A.17})$$

Then, $\frac{\partial \lambda^p}{\partial \mathbf{F}}$ and $\frac{\partial \mathbf{n}}{\partial \mathbf{F}}$ are obtained from the total differential of two local residuals

$$-\frac{\partial \|\boldsymbol{\tau}_{0, \text{dev}}\|}{\partial \mathbf{F}} - \mathbf{k}_{\lambda^p, \lambda^p} \frac{\partial \lambda^p}{\partial \mathbf{F}} - \mathbf{k}_{\lambda^p, \mathbf{n}} : \frac{\partial \mathbf{n}}{\partial \mathbf{F}} = \mathbf{0} \quad (\text{A.18})$$

and

$$-\frac{\partial}{\partial \mathbf{F}} \frac{\boldsymbol{\tau}_{0, \text{dev}}}{\|\boldsymbol{\tau}_{0, \text{dev}}\|} - \mathbf{k}_{\mathbf{n}, \lambda^p} \otimes \frac{\partial \lambda^p}{\partial \mathbf{F}} - \mathbf{k}_{\mathbf{n}, \mathbf{n}} : \frac{\partial \mathbf{n}}{\partial \mathbf{F}} = \underline{\mathbf{0}}. \quad (\text{A.19})$$

Taking into account the symmetry of the flow tensor, an equation in Vogit notation for Eqs. (A.18) and (A.19) is obtained

$$\mathbf{k} \cdot \begin{bmatrix} \frac{\partial \lambda^p}{\partial \mathbf{F}} \\ \frac{\partial \mathbf{F}}{\partial n_{11}} \\ \frac{\partial \mathbf{F}}{\partial n_{22}} \\ \frac{\partial \mathbf{F}}{\partial n_{33}} \\ \frac{\partial \mathbf{F}}{\partial n_{23}} \\ \frac{\partial \mathbf{F}}{\partial n_{13}} \\ \frac{\partial \mathbf{F}}{\partial n_{12}} \end{bmatrix} = - \begin{bmatrix} \frac{\partial \|\boldsymbol{\tau}_{0,\text{dev}}\|}{\partial \mathbf{F}} \\ \frac{\partial}{\partial \mathbf{F}} \frac{\tau_{0,\text{dev},11}}{\|\boldsymbol{\tau}_{0,\text{dev}}\|} \\ \frac{\partial}{\partial \mathbf{F}} \frac{\tau_{0,\text{dev},22}}{\|\boldsymbol{\tau}_{0,\text{dev}}\|} \\ \frac{\partial}{\partial \mathbf{F}} \frac{\tau_{0,\text{dev},33}}{\|\boldsymbol{\tau}_{0,\text{dev}}\|} \\ 2 \frac{\partial}{\partial \mathbf{F}} \frac{\tau_{0,\text{dev},23}}{\|\boldsymbol{\tau}_{0,\text{dev}}\|} \\ 2 \frac{\partial}{\partial \mathbf{F}} \frac{\tau_{0,\text{dev},13}}{\|\boldsymbol{\tau}_{0,\text{dev}}\|} \\ 2 \frac{\partial}{\partial \mathbf{F}} \frac{\tau_{0,\text{dev},12}}{\|\boldsymbol{\tau}_{0,\text{dev}}\|} \end{bmatrix} \quad (\text{A.20})$$

$$\text{with } \mathbf{k} = \begin{bmatrix} k_{\lambda^p, \lambda^p} & k_{\lambda^p, n_{11}} & k_{\lambda^p, n_{22}} & k_{\lambda^p, n_{33}} & 2k_{\lambda^p, n_{23}} & 2k_{\lambda^p, n_{13}} & 2k_{\lambda^p, n_{12}} \\ k_{n_{11}, \lambda^p} & k_{n_{11}, n_{11}} & k_{n_{11}, n_{22}} & k_{n_{11}, n_{33}} & 2k_{n_{11}, n_{23}} & 2k_{n_{11}, n_{13}} & 2k_{n_{11}, n_{12}} \\ k_{n_{22}, \lambda^p} & k_{n_{22}, n_{11}} & k_{n_{22}, n_{22}} & k_{n_{22}, n_{33}} & 2k_{n_{22}, n_{23}} & 2k_{n_{22}, n_{13}} & 2k_{n_{22}, n_{12}} \\ k_{n_{33}, \lambda^p} & k_{n_{33}, n_{11}} & k_{n_{33}, n_{22}} & k_{n_{33}, n_{33}} & 2k_{n_{33}, n_{23}} & 2k_{n_{33}, n_{13}} & 2k_{n_{33}, n_{12}} \\ 2k_{n_{23}, \lambda^p} & 2k_{n_{23}, n_{11}} & 2k_{n_{23}, n_{22}} & 2k_{n_{23}, n_{33}} & 4k_{n_{23}, n_{23}} & 4k_{n_{23}, n_{13}} & 4k_{n_{23}, n_{12}} \\ 2k_{n_{13}, \lambda^p} & 2k_{n_{13}, n_{11}} & 2k_{n_{13}, n_{22}} & 2k_{n_{13}, n_{33}} & 4k_{n_{13}, n_{23}} & 4k_{n_{13}, n_{13}} & 4k_{n_{13}, n_{12}} \\ 2k_{n_{12}, \lambda^p} & 2k_{n_{12}, n_{11}} & 2k_{n_{12}, n_{22}} & 2k_{n_{12}, n_{33}} & 4k_{n_{12}, n_{23}} & 4k_{n_{12}, n_{13}} & 4k_{n_{12}, n_{12}} \end{bmatrix},$$

where

$$\begin{aligned} \frac{\partial \|\boldsymbol{\tau}_{0,\text{dev}}\|}{\partial \mathbf{F}} &= \frac{\partial \|\boldsymbol{\tau}_{0,\text{dev}}\|}{\partial \mathbf{b}^e} : \left\{ \exp\left(-2 \frac{\lambda^p}{g(d^e)} \Delta \mathbf{m}\right) \bar{\otimes} (\mathbf{C}_n^{p-1} \cdot \mathbf{F}^T)^T \right. \\ &\quad \left. + \left\{ \exp\left(-2 \frac{\lambda^p}{g(d^e)} \Delta \mathbf{m}\right) \cdot \mathbf{F} \cdot \mathbf{C}_n^{p-1} \right\} \otimes \mathbf{1} \right\}, \\ \frac{\partial}{\partial \mathbf{F}} \frac{\tau_{0,\text{dev}}}{\|\boldsymbol{\tau}_{0,\text{dev}}\|} &= \left(\frac{1}{\|\boldsymbol{\tau}_{0,\text{dev}}\|} \frac{\partial \tau_{0,\text{dev}}}{\partial \mathbf{b}^e} - \frac{\tau_{0,\text{dev}}}{\|\boldsymbol{\tau}_{0,\text{dev}}\|^2} \otimes \frac{\partial \|\boldsymbol{\tau}_{0,\text{dev}}\|}{\partial \mathbf{b}^e} \right) \\ &\quad : \left\{ \exp\left(-2 \frac{\lambda^p}{g(d^e)} \Delta \mathbf{m}\right) \bar{\otimes} (\mathbf{C}_n^{p-1} \cdot \mathbf{F}^T)^T \right. \\ &\quad \left. + \left\{ \exp\left(-2 \frac{\lambda^p}{g(d^e)} \Delta \mathbf{m}\right) \cdot \mathbf{F} \cdot \mathbf{C}_n^{p-1} \right\} \otimes \mathbf{1} \right\}. \end{aligned} \quad (\text{A.21})$$

In a same manner, $\frac{\partial \mathbf{F}^e}{\partial \alpha}$ yields

$$\frac{\partial \mathbf{F}^e}{\partial \alpha} = \frac{\partial \mathbf{F}^e}{\partial \lambda^p} \bigg|_{\mathbf{n}=\text{const.}} \frac{\partial \lambda^p}{\partial \alpha} + \frac{\partial \mathbf{F}^e}{\partial \mathbf{n}} \bigg|_{\lambda^p=\text{const.}} : \frac{\partial \mathbf{n}}{\partial \alpha} \quad (\text{A.22})$$

with

$$\sqrt{\frac{2}{3}} \frac{\partial r_0^p}{\partial \alpha} - k_{\lambda^p \lambda^p} \frac{\partial \lambda^p}{\partial \alpha} - k_{\lambda^p \mathbf{n}} : \frac{\partial \mathbf{n}}{\partial \alpha} = 0 \quad (\text{A.23})$$

and

$$-k_{\mathbf{n} \lambda^p} \frac{\partial \lambda^p}{\partial \alpha} - k_{\mathbf{n} \mathbf{n}} : \frac{\partial \mathbf{n}}{\partial \alpha} = 0, \quad (\text{A.24})$$

Taking into account the symmetry of the flow tensor, an equation in Vogit notation for Eqs. (A.23) and (A.24) is obtained

$$\mathbf{k} \cdot \begin{bmatrix} \frac{\partial \lambda^p}{\partial \alpha} \\ \frac{\partial \lambda^p}{\partial n_{11}} \\ \frac{\partial \lambda^p}{\partial n_{22}} \\ \frac{\partial \lambda^p}{\partial n_{33}} \\ \frac{\partial \lambda^p}{\partial n_{23}} \\ \frac{\partial \lambda^p}{\partial n_{13}} \\ \frac{\partial \lambda^p}{\partial n_{12}} \\ \frac{\partial \lambda^p}{\partial \alpha} \end{bmatrix} = \begin{bmatrix} \sqrt{\frac{2}{3}} \frac{\partial r_0^p}{\partial \alpha} \\ 0 \\ 0 \\ 0 \\ 0 \\ 0 \\ 0 \\ 0 \end{bmatrix}, \quad (\text{A.25})$$

where

$$\frac{\partial r_0^p}{\partial \alpha} = \frac{\partial}{\partial \alpha} \left\{ \hat{y}(\bar{\alpha}) + p_p (\bar{\alpha} - \alpha) \right\} = -p_p. \quad (\text{A.26})$$

In addition, $\frac{\partial \bar{\alpha}}{\partial \alpha}$ and $\frac{\partial \bar{\alpha}}{\partial \mathbf{F}}$ are obtained as

$$\frac{\partial \bar{\alpha}}{\partial \alpha} = \frac{\partial}{\partial \alpha} \left(\bar{\alpha}_n + \sqrt{\frac{2}{3}} \frac{\lambda_{n+1}^p}{g(d^p)} \Delta t_{n+1} \right) = \sqrt{\frac{2}{3}} \frac{1}{g(d^p)} \frac{\partial \lambda^p}{\partial \alpha} \Delta t_{n+1} \quad (\text{A.27})$$

and

$$\frac{\partial \bar{\alpha}}{\partial \mathbf{F}} = \frac{\partial}{\partial \mathbf{F}} \left(\bar{\alpha}_n + \sqrt{\frac{2}{3}} \frac{\lambda_{n+1}^p}{g(d^p)} \Delta t_{n+1} \right) = \sqrt{\frac{2}{3}} \frac{1}{g(d^p)} \frac{\partial \lambda^p}{\partial \mathbf{F}} \Delta t_{n+1}. \quad (\text{A.28})$$

Appendix B Supplements for CPFFCM

B.1 Numerical error caused by rearrangement of finite covers

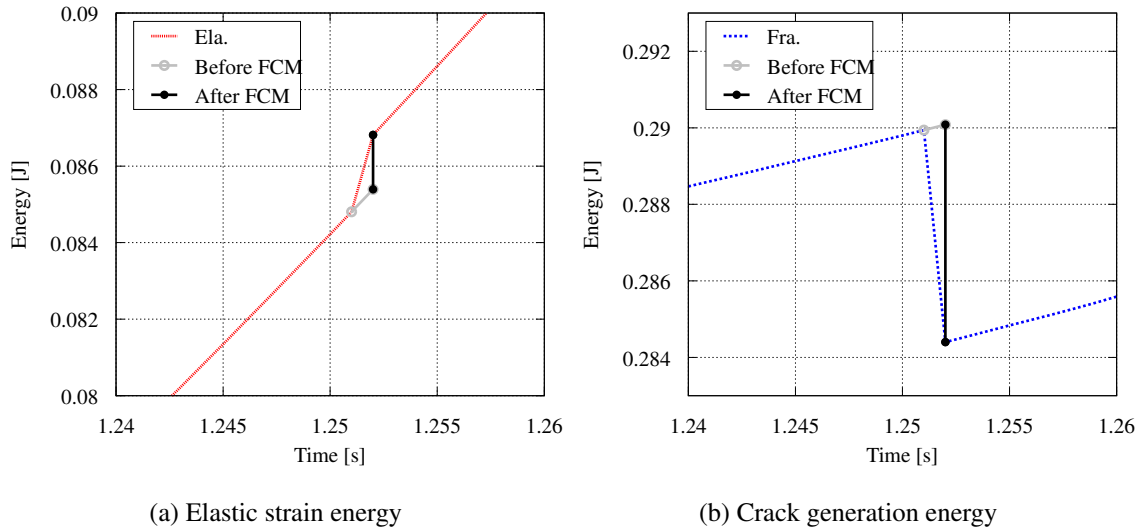


Fig. B.1: Enlarged views of Fig. 5.31(b) along with data plots of FC-based staggered iterations.

A demonstration of the numerical error caused by the rearrangement of finite covers is presented here. For the sake of demonstration, the numerical setup “Case hs2” in Section 5.2.2 is again used here.

Fig. B.1 shows the enlarged views of Fig. 5.31(b) along with data plots of FC-based staggered iterations. Here, the gray-colored and black-colored plots correspond to the solutions

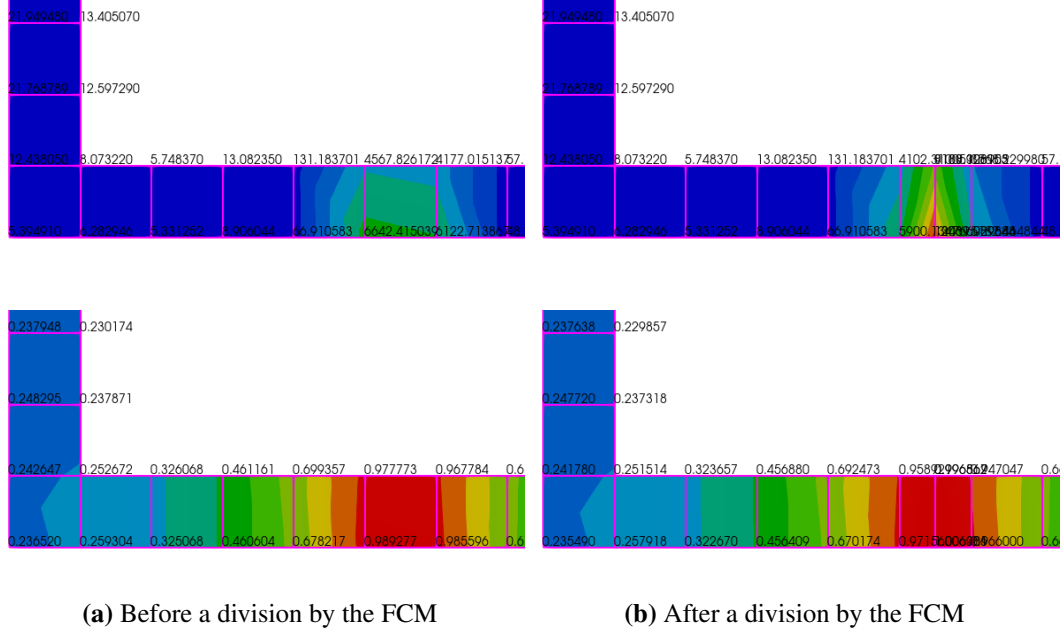


Fig. B.2: Distributions of the history variable \mathcal{H}^e and damage variable d in order from the top in the initial configuration.

obtained in FC-based staggered iterations before and after the execution of the FCM. As shown in the figure, the variations of the elastic strain and crack generation energies are relatively large compared to the nearby plots. This is because the positions of Gaussian points are redefined when the FCM is executed. Accordingly, the geometry around the severely damaged region is updated, and another Newton-Raphson loop is needed to find a new stationary condition for the updated geometry during the loading step.

For a better visual understanding, the distributions of the history variable \mathcal{H}^e and damage variable d are presented in Fig. B.2; specifically, see the third and sixth elements from the left at the bottom edge. The upper left node of the sixth element has the value $\mathcal{H}^e \approx 4568 \text{ [N/mm}^2\text{]}$ before a division by the FCM. Once the FCM is performed, the upper left node of the sixth element no more has the original value for the history variable, and a new value $\mathcal{H}^e \approx 4102 \text{ [N/mm}^2\text{]}$ is given due to the redefinition of the positions for new Gaussian points. Subsequently, new damage variables are computed for the sixth element, and in the meantime, damage variables on other nodes are also updated due to the spatial gradient term

∇d . Hence, the upper left node of the third element has a new value $d \approx 0.323$ from the original one $d \approx 0.326$, whereas its history variable has the same value $\mathcal{H}^e \approx 5.74 \text{ [N/mm}^2\text{]}$ before and after performing the FCM.

It is worth remarking that this numerical error becomes more apparent when the crack is sufficiently large compared to the whole geometry of a simulation model, such as Example 2 in Section 5.2.2. In contrast, this issue is neglectable in Example 3 and Example 4, as presented in Section 5.2.3 and Section 5.2.4, respectively, since the crack is small.

REFERENCES

- 1) Watson JT, Gayer M, Connolly MA. Epidemics after natural disasters. *Emerging Infectious Diseases* 2007; 13(1): 1–5. doi: 10.3201/eid1301.060779
- 2) Kouadio IK, Aljunid S, Kamigaki T, Hammad K, Oshitani H. Infectious diseases following natural disasters: Prevention and control measures. *Expert Review of Anti-Infective Therapy* 2012; 10(1): 95–104. doi: 10.1586/eri.11.155
- 3) Özdamar L, Ekinci E, Küçükyazıcı B. Emergency logistics planning in natural disasters. *Annals of Operations Research* 2004; 129(1-4): 217–245. doi: 10.1023/B:ANOR.0000030690.27939.39
- 4) Sheu JB. An emergency logistics distribution approach for quick response to urgent relief demand in disasters. *Transportation Research Part E: Logistics and Transportation Review* 2007; 43(6): 687–709. doi: 10.1016/j.tre.2006.04.004
- 5) Yasunari TJ, Stohl A, Hayano RS, Burkhart JF, Eckhardt S, Yasunari T. Cesium-137 deposition and contamination of Japanese soils due to the Fukushima nuclear accident. *Proceedings of the National Academy of Sciences of the United States of America* 2011; 108(49): 19530–19534. doi: 10.1073/pnas.1112058108
- 6) Griffith AA. VI. The phenomena of rupture and flow in solids. *Philosophical Transactions of the Royal Society of London. Series A, Containing Papers of a Mathematical or Physical Character* 1921; 221(582-593): 163–198. doi: 10.1098/rsta.1921.0006
- 7) Irwin GR. Analysis of Stresses and Strains Near the End of a Crack Traversing a Plate. *Journal of Applied Mechanics* 1957; 24(3): 361–364. doi: 10.1115/1.4011547

- 8) Orowan E. Fracture and strength of solids. *Reports on Progress in Physics* 1949; 12(1): 185–232. doi: 10.1088/0034-4885/12/1/309
- 9) Abaqus Finite Element Analysis for Mechanical Engineering and Civil Engineering, <https://www.3ds.com/products-services/simulia/products/abaqus/>.
- 10) Ansys Mechanical Finite Element Analysis (FEA) Software for Structural Engineering, <https://www.ansys.com/products/structures/ansys-mechanical>.
- 11) COMSOL Multiphysics Structural Mechanics Module, <https://www.comsol.com/structural-mechanics-module>.
- 12) DYANA FEA Structural Design, <https://dianafea.com/sectors/structural-design/>.
- 13) MSC Nastran Structural Analysis, <https://hexagon.com/solutions/structural-analysis>.
- 14) Chaboche JL. Continuum damage mechanics: Part I-general concepts. *Journal of Applied Mechanics, Transactions ASME* 1988; 55(1): 59–64. doi: 10.1115/1.3173661
- 15) de Borst R. Fracture in quasi-brittle materials: A review of continuum damage-based approaches. *Engineering Fracture Mechanics* 2001; 69(2): 95–112. doi: 10.1016/S0013-7944(01)00082-0
- 16) Besson J. Continuum models of ductile fracture: A review. *International Journal of Damage Mechanics* 2010; 19(1): 3–52. doi: 10.1177/1056789509103482
- 17) Murakami S. *Continuum Damage Mechanics*. 185 of *Solid Mechanics and Its Applications*. Dordrecht: Springer Netherlands . 2012
- 18) Gurson AL. Continuum theory of ductile rupture by void nucleation and growth: Part 1 - yield criteria and flow rules for porous ductile media. *Journal of Engineering Materials and Technology, Transactions of the ASME* 1977; 99(1): 2–15. doi: 10.1115/1.3443401

- 19) Tvergaard V, Needleman A. Analysis of the cup-cone fracture in a round tensile bar. *Acta Metallurgica* 1984; 32(1): 157–169. doi: 10.1016/0001-6160(84)90213-X
- 20) Lemaitre J. A continuous damage mechanics model for ductile fracture. *Journal of Engineering Materials and Technology, Transactions of the ASME* 1985; 107(1): 83–89. doi: 10.1115/1.3225775
- 21) Bažant ZP, Prat PC. Microplane Model for Brittle-Plastic Material: I. Theory. *Journal of Engineering Mechanics* 1988; 114(10): 1672–1688. doi: 10.1061/(asce)0733-9399(1988)114:10(1672)
- 22) Bažant ZP, Belytschko TB, Chang TP. Continuum Theory for Strain-Softening. *Journal of Engineering Mechanics* 1984; 110(12): 1666–1692. doi: 10.1061/(asce)0733-9399(1984)110:12(1666)
- 23) Pijaudier-Cabot G, Bažant ZP. Nonlocal Damage Theory. *Journal of Engineering Mechanics* 1987; 113(10): 1512–1533. doi: 10.1061/(ASCE)0733-9399(1987)113:10(1512)
- 24) Peerlings RHJ, de Borst R, Brekelmans WAM, De Vree JHP. Gradient enhanced damage for quasi-brittle materials. *International Journal for Numerical Methods in Engineering* 1996; 39(19): 3391–3403. doi: 10.1002/(SICI)1097-0207(19961015)39:19<3391::AID-NME7>3.0.CO;2-D
- 25) Bažant ZP, Ožbolt J. Nonlocal Microplane Model for Fracture, Damage, and Size Effect in Structures. *Journal of Engineering Mechanics* 1990; 116(11): 2485–2505. doi: 10.1061/(asce)0733-9399(1990)116:11(2485)
- 26) Peerlings RHJ, de Borst R, Brekelmans WAM, Geers MGD. Gradient-enhanced damage modelling of concrete fracture. *Mechanics of Cohesive-Frictional Materials* 1998; 3(4): 323–342. doi: 10.1002/(SICI)1099-1484(1998100)3:4<323::AID-CFM51>3.0.CO;2-Z

- 27) Reusch F, Svendsen B, Klingbeil D. Local and non-local Gurson-based ductile damage and failure modelling at large deformation. *European Journal of Mechanics, A/Solids* 2003; 22(6): 779–792. doi: 10.1016/S0997-7538(03)00070-6
- 28) Geers MGD. Finite strain logarithmic hyperelasto-plasticity with softening: A strongly non-local implicit gradient framework. *Computer Methods in Applied Mechanics and Engineering* 2004; 193(30-32): 3377–3401. doi: 10.1016/j.cma.2003.07.014
- 29) Golshani A, Okui Y, Oda M, Takemura T. A micromechanical model for brittle failure of rock and its relation to crack growth observed in triaxial compression tests of granite. *Mechanics of Materials* 2006; 38(4): 287–303. doi: 10.1016/j.mechmat.2005.07.003
- 30) Lyakhovsky V, Hamiel Y, Ben-Zion Y. A non-local visco-elastic damage model and dynamic fracturing. *Journal of the Mechanics and Physics of Solids* 2011; 59(9): 1752–1776. doi: 10.1016/j.jmps.2011.05.016
- 31) Waffenschmidt T, Polindara C, Menzel A, Blanco S. A gradient-enhanced large-deformation continuum damage model for fibre-reinforced materials. *Computer Methods in Applied Mechanics and Engineering* 2014; 268: 801–842. doi: 10.1016/j.cma.2013.10.013
- 32) Thai TQ, Rabczuk T, Bazilevs Y, Meschke G. A higher-order stress-based gradient-enhanced damage model based on isogeometric analysis. *Computer Methods in Applied Mechanics and Engineering* 2016; 304: 584–604. doi: 10.1016/j.cma.2016.02.031
- 33) Poh LH, Sun G. Localizing gradient damage model with decreasing interactions. *International Journal for Numerical Methods in Engineering* 2017; 110(6): 503–522. doi: 10.1002/nme.5364
- 34) Kurumatani M, Soma Y, Terada K. Simulations of cohesive fracture behavior of reinforced concrete by a fracture-mechanics-based damage model. *Engineering Fracture Mechanics* 2019; 206: 392–407. doi: 10.1016/j.engfracmech.2018.12.006

- 35) Francfort GA, Marigo JJ. Revisiting brittle fracture as an energy minimization problem. *Journal of the Mechanics and Physics of Solids* 1998; 46(8): 1319–1342. doi: 10.1016/S0022-5096(98)00034-9
- 36) Mumford D, Shah J. Optimal approximations by piecewise smooth functions and associated variational problems. *Communications on Pure and Applied Mathematics* 1989; 42(5): 577–685. doi: 10.1002/cpa.3160420503
- 37) Ambrosio L, Tortorelli VM. Approximation of functional depending on jumps by elliptic functional via t-convergence. *Communications on Pure and Applied Mathematics* 1990; 43(8): 999–1036. doi: 10.1002/cpa.3160430805
- 38) Bourdin B, Francfort GA, Marigo JJ. Numerical experiments in revisited brittle fracture. *Journal of the Mechanics and Physics of Solids* 2000; 48(4): 797–826. doi: 10.1016/S0022-5096(99)00028-9
- 39) Miehe C, Welschinger F, Hofacker M. Thermodynamically consistent phase-field models of fracture: Variational principles and multi-field FE implementations. *International Journal for Numerical Methods in Engineering* 2010; 83(10): 1273–1311. doi: 10.1002/nme.2861
- 40) Miehe C, Hofacker M, Welschinger F. A phase field model for rate-independent crack propagation: Robust algorithmic implementation based on operator splits. *Computer Methods in Applied Mechanics and Engineering* 2010; 199(45-48): 2765–2778. doi: 10.1016/j.cma.2010.04.011
- 41) Larsen CJ, Ortner C, Süli E. Existence of solutions to a regularized model of dynamic fracture. *Mathematical Models and Methods in Applied Sciences* 2010; 20(7): 1021–1048. doi: 10.1142/S0218202510004520
- 42) Bourdin B, Larsen CJ, Richardson CL. A time-discrete model for dynamic fracture based on crack regularization. *International Journal of Fracture* 2011; 168(2): 133–143. doi: 10.1007/s10704-010-9562-x

- 43) Borden MJ, Verhoosel CV, Scott MA, Hughes TJR, Landis CM. A phase-field description of dynamic brittle fracture. *Computer Methods in Applied Mechanics and Engineering* 2012; 217-220: 77–95. doi: 10.1016/j.cma.2012.01.008
- 44) Hofacker M, Miehe C. Continuum phase field modeling of dynamic fracture: Variational principles and staggered FE implementation. *International Journal of Fracture* 2012; 178(1-2): 113–129. doi: 10.1007/s10704-012-9753-8
- 45) Hesch C, Weinberg K. Thermodynamically consistent algorithms for a finite-deformation phase-field approach to fracture. *International Journal for Numerical Methods in Engineering* 2014; 99(12): 906–924. doi: 10.1002/nme.4709
- 46) Nguyen VP, Wu JY. Modeling dynamic fracture of solids with a phase-field regularized cohesive zone model. *Computer Methods in Applied Mechanics and Engineering* 2018; 340: 1000–1022. doi: 10.1016/j.cma.2018.06.015
- 47) Bourdin B, Francfort GA, Marigo JJ. The Variational Approach to Fracture. *Journal of Elasticity* 2008; 91(1-3): 5–148. doi: 10.1007/s10659-007-9107-3
- 48) Lorentz E, Godard V. Gradient damage models: Toward full-scale computations. *Computer Methods in Applied Mechanics and Engineering* 2011; 200(21-22): 1927–1944. doi: 10.1016/j.cma.2010.06.025
- 49) Lorentz E, Cuvilliez S, Kazymyrenko K. Convergence of a gradient damage model toward a cohesive zone model. *Comptes Rendus - Mecanique* 2011; 339(1): 20–26. doi: 10.1016/j.crme.2010.10.010
- 50) Verhoosel CV, de Borst R. A phase-field model for cohesive fracture. *International Journal for Numerical Methods in Engineering* 2013; 96(1): 43–62. doi: 10.1002/nme.4553
- 51) Vignollet J, May S, de Borst R, Verhoosel CV. Phase-field models for brittle and cohesive fracture. *Meccanica* 2014; 49(11): 2587–2601. doi: 10.1007/s11012-013-9862-0

- 52) May S, Vignollet J, de Borst R. A numerical assessment of phase-field models for brittle and cohesive fracture: Γ -Convergence and stress oscillations. *European Journal of Mechanics - A/Solids* 2015; 52: 72–84. doi: 10.1016/j.euromechsol.2015.02.002
- 53) Wu JY. A unified phase-field theory for the mechanics of damage and quasi-brittle failure. *Journal of the Mechanics and Physics of Solids* 2017; 103: 72–99. doi: 10.1016/j.jmps.2017.03.015
- 54) Wu JY, Nguyen VP. A length scale insensitive phase-field damage model for brittle fracture. *Journal of the Mechanics and Physics of Solids* 2018; 119: 20–42. doi: 10.1016/j.jmps.2018.06.006
- 55) Geelen RJM, Liu Y, Hu T, Tupek MR, Dolbow JE. A phase-field formulation for dynamic cohesive fracture. *Computer Methods in Applied Mechanics and Engineering* 2019; 348: 680–711. doi: 10.1016/j.cma.2019.01.026
- 56) Alessi R, Vidoli S, De Lorenzis L. A phenomenological approach to fatigue with a variational phase-field model: The one-dimensional case. *Engineering Fracture Mechanics* 2018; 190: 53–73. doi: 10.1016/j.engfracmech.2017.11.036
- 57) Lo YS, Borden MJ, Ravi-Chandar K, Landis CM. A phase-field model for fatigue crack growth. *Journal of the Mechanics and Physics of Solids* 2019; 132: 103684. doi: 10.1016/j.jmps.2019.103684
- 58) Carrara P, Ambati M, Alessi R, De Lorenzis L. A framework to model the fatigue behavior of brittle materials based on a variational phase-field approach. *Computer Methods in Applied Mechanics and Engineering* 2020; 361: 112731. doi: 10.1016/j.cma.2019.112731
- 59) Seiler M, Linse T, Hantschke P, Kästner M. An efficient phase-field model for fatigue fracture in ductile materials. *Engineering Fracture Mechanics* 2020; 224: 106807. doi: 10.1016/j.engfracmech.2019.106807

- 60) Schreiber C, Kuhn C, Müller R, Zohdi T. A phase field modeling approach of cyclic fatigue crack growth. *International Journal of Fracture* 2020; 225(1): 89–100. doi: 10.1007/s10704-020-00468-w
- 61) Seleš K, Aldakheel F, Tonković Z, Sorić J, Wriggers P. A general phase-field model for fatigue failure in brittle and ductile solids. *Computational Mechanics* 2021; 67(5): 1431–1452. doi: 10.1007/s00466-021-01996-5
- 62) Ulloa J, Wambacq J, Alessi R, Degrande G, François S. Phase-field modeling of fatigue coupled to cyclic plasticity in an energetic formulation. *Computer Methods in Applied Mechanics and Engineering* 2021; 373: 113473. doi: 10.1016/j.cma.2020.113473
- 63) Abdollahi A, Arias I. Phase-field modeling of crack propagation in piezoelectric and ferroelectric materials with different electromechanical crack conditions. *Journal of the Mechanics and Physics of Solids* 2012; 60(12): 2100–2126. doi: 10.1016/j.jmps.2012.06.014
- 64) Bourdin B, Marigo JJ, Maurini C, Sicsic P. Morphogenesis and propagation of complex cracks induced by thermal shocks. *Physical Review Letters* 2014; 112(1): 14301. doi: 10.1103/PhysRevLett.112.014301
- 65) Miehe C, Schänzel LM, Ulmer H. Phase field modeling of fracture in multi-physics problems. Part I. Balance of crack surface and failure criteria for brittle crack propagation in thermo-elastic solids. *Computer Methods in Applied Mechanics and Engineering* 2015; 294: 449–485. doi: 10.1016/j.cma.2014.11.016
- 66) Wu T, De Lorenzis L. A phase-field approach to fracture coupled with diffusion. *Computer Methods in Applied Mechanics and Engineering* 2016; 312: 196–223. doi: 10.1016/j.cma.2016.05.024
- 67) Lee S, Wheeler MF, Wick T. Iterative coupling of flow, geomechanics and adaptive phase-field fracture including level-set crack width approaches. *Journal of Computational and Applied Mathematics* 2017; 314: 40–60. doi: 10.1016/j.cam.2016.10.022

- 68) Wu JY, Chen WX. Phase-field modeling of electromechanical fracture in piezoelectric solids: Analytical results and numerical simulations. *Computer Methods in Applied Mechanics and Engineering* 2021; 387: 114125. doi: 10.1016/j.cma.2021.114125
- 69) Ambati M, Gerasimov T, De Lorenzis L. A review on phase-field models of brittle fracture and a new fast hybrid formulation. *Computational Mechanics* 2015; 55(2): 383–405. doi: 10.1007/s00466-014-1109-y
- 70) Wu JY, Nguyen VP, Nguyen CT, Sutula D, Sinaie S, Bordas SPA. Phase-field modeling of fracture. In: Bordas SPA, Balint DS., eds. *Advances in Applied Mechanics*. 53. Elsevier. 2020 (pp. 1–183)
- 71) Henry H, Levine H. Dynamic instabilities of fracture under biaxial strain using a phase field model. *Physical Review Letters* 2004; 93(10): 105504. doi: 10.1103/PhysRevLett.93.105504
- 72) Amor H, Marigo JJ, Maurini C. Regularized formulation of the variational brittle fracture with unilateral contact: Numerical experiments. *Journal of the Mechanics and Physics of Solids* 2009; 57(8): 1209–1229. doi: 10.1016/j.jmps.2009.04.011
- 73) Steinke C, Kaliske M. A phase-field crack model based on directional stress decomposition. *Computational Mechanics* 2019; 63(5): 1019–1046. doi: 10.1007/s00466-018-1635-0
- 74) Storm J, Supriatna D, Kaliske M. The concept of representative crack elements for phase-field fracture: Anisotropic elasticity and thermo-elasticity. *International Journal for Numerical Methods in Engineering* 2020; 121(5): 779–805. doi: 10.1002/nme.6244
- 75) Alessi R, Marigo JJ, Vidoli S. Gradient Damage Models Coupled with Plasticity and Nucleation of Cohesive Cracks. *Archive for Rational Mechanics and Analysis* 2014; 214(2): 575–615. doi: 10.1007/s00205-014-0763-8

- 76) Alessi R, Marigo JJ, Vidoli S. Gradient damage models coupled with plasticity: Variational formulation and main properties. *Mechanics of Materials* 2015; 80(PB): 351–367. doi: 10.1016/j.mechmat.2013.12.005
- 77) Ambati M, Gerasimov T, De Lorenzis L. Phase-field modeling of ductile fracture. *Computational Mechanics* 2015; 55(5): 1017–1040. doi: 10.1007/s00466-015-1151-4
- 78) Ambati M, Kruse R, De Lorenzis L. A phase-field model for ductile fracture at finite strains and its experimental verification. *Computational Mechanics* 2016; 57(1): 149–167. doi: 10.1007/s00466-015-1225-3
- 79) Miehe C, Hofacker M, Schänzel LM, Aldakheel F. Phase field modeling of fracture in multi-physics problems. Part II. Coupled brittle-to-ductile failure criteria and crack propagation in thermo-elastic-plastic solids. *Computer Methods in Applied Mechanics and Engineering* 2015; 294: 486–522. doi: 10.1016/j.cma.2014.11.017
- 80) Miehe C, Aldakheel F, Raina A. Phase field modeling of ductile fracture at finite strains: A variational gradient-extended plasticity-damage theory. *International Journal of Plasticity* 2016; 84: 1–32. doi: 10.1016/j.ijplas.2016.04.011
- 81) Miehe C. Variational gradient plasticity at finite strains. Part I: Mixed potentials for the evolution and update problems of gradient-extended dissipative solids. *Computer Methods in Applied Mechanics and Engineering* 2014; 268: 677–703. doi: 10.1016/j.cma.2013.03.014
- 82) Miehe C, Welschinger F, Aldakheel F. Variational gradient plasticity at finite strains. Part II: Local-global updates and mixed finite elements for additive plasticity in the logarithmic strain space. *Computer Methods in Applied Mechanics and Engineering* 2014; 268: 704–734. doi: 10.1016/j.cma.2013.07.015
- 83) Borden MJ, Hughes TJR, Landis CM, Anvari A, Lee IJ. A phase-field formulation for fracture in ductile materials: Finite deformation balance law derivation, plastic

- degradation, and stress triaxiality effects. *Computer Methods in Applied Mechanics and Engineering* 2016; 312: 130–166. doi: 10.1016/j.cma.2016.09.005
- 84) Dittmann M, Aldakheel F, Schulte J, Wriggers P, Hesch C. Variational phase-field formulation of non-linear ductile fracture. *Computer Methods in Applied Mechanics and Engineering* 2018; 342: 71–94. doi: 10.1016/j.cma.2018.07.029
- 85) Yin B, Kaliske M. A ductile phase-field model based on degrading the fracture toughness: Theory and implementation at small strain. *Computer Methods in Applied Mechanics and Engineering* 2020; 366: 113068. doi: 10.1016/j.cma.2020.113068
- 86) Dal Maso G, Orlando G, Toader R. Fracture models for elasto-plastic materials as limits of gradient damage models coupled with plasticity: the antiplane case. *Calculus of Variations and Partial Differential Equations* 2016; 55(3): 45. doi: 10.1007/s00526-016-0981-z
- 87) Kuhn C, Noll T, Müller R. On phase field modeling of ductile fracture. *GAMM Mitteilungen* 2016; 39(1): 35–54. doi: 10.1002/gamm.201610003
- 88) Alessi R, Marigo JJ, Maurini C, Vidoli S. Coupling damage and plasticity for a phase-field regularisation of brittle, cohesive and ductile fracture: One-dimensional examples. *International Journal of Mechanical Sciences* 2018; 149: 559–576. doi: 10.1016/j.ijmecsci.2017.05.047
- 89) Aldakheel F, Wriggers P, Miehe C. A modified Gurson-type plasticity model at finite strains: formulation, numerical analysis and phase-field coupling. *Computational Mechanics* 2018; 62(4): 815–833. doi: 10.1007/s00466-017-1530-0
- 90) Dittmann M, Aldakheel F, Schulte J, Schmidt F, Krüger M, Wriggers P, Hesch C. Phase-field modeling of porous-ductile fracture in non-linear thermo-elasto-plastic solids. *Computer Methods in Applied Mechanics and Engineering* 2020; 361: 112730. doi: 10.1016/j.cma.2019.112730

- 91) Han J, Matsubara S, Moriguchi S, Kaliske M, Terada K. Crack phase-field model equipped with plastic driving force and degrading fracture toughness for ductile fracture simulation. *Computational Mechanics* 2022; 69(1): 151–175. doi: 10.1007/s00466-021-02087-1
- 92) Alessi R, Ambati M, Gerasimov T, Vidoli S, De Lorenzis L. Comparison of Phase-Field Models of Fracture Coupled with Plasticity. In: Oñate E, Peric D, Souza Neto dE, Chiumenti M., eds. *Advances in Computational Plasticity: A Book in Honour of D. Roger J. Owen* Cham: Springer International Publishing. 2018 (pp. 1–21)
- 93) Huang C, Gao X. Development of a phase field method for modeling brittle and ductile fracture. *Computational Materials Science* 2019; 169: 109089. doi: 10.1016/j.commatsci.2019.109089
- 94) Azinpour E, Cruz DJ, Sa dJM, Santos A. Phase-field approach in elastoplastic solids: application of an iterative staggered scheme and its experimental validation. *Computational Mechanics* 2021; 68(2): 255–269. doi: 10.1007/s00466-021-02029-x
- 95) Ngo D, Scordelis AC. Finite element analysis of reinforced concrete beams. In: . 64. *ACI Journal Proceedings*. ; 1967: 152–163.
- 96) Ingraffea AR, Saouma V. Numerical Modeling of Discrete Crack Propagation in Reinforced and Plain Concrete.. In: Sih GC, DiTommaso A., eds. *Fract Mech of Concr, Struct Appl and Numer Calc* Dordrecht: Springer Netherlands. 1985 (pp. 171–225)
- 97) Belytschko T, Lu YY, Gu L. Element-free Galerkin methods. *International Journal for Numerical Methods in Engineering* 1994; 37(2): 229–256. doi: 10.1002/nme.1620370205
- 98) Lu YY, Belytschko T, Gu L. A new implementation of the element free Galerkin method. *Computer Methods in Applied Mechanics and Engineering* 1994; 113(3-4): 397–414. doi: 10.1016/0045-7825(94)90056-6

- 99) Jirásek M. Comparative study on finite elements with embedded discontinuities. *Computer Methods in Applied Mechanics and Engineering* 2000; 188(1): 307–330. doi: 10.1016/S0045-7825(99)00154-1
- 100) Melenk JM, Babuška I. The partition of unity finite element method: Basic theory and applications. *Computer Methods in Applied Mechanics and Engineering* 1996; 139(1-4): 289–314. doi: 10.1016/S0045-7825(96)01087-0
- 101) Babuška I, Melenk JM. The partition of unity method. *International Journal for Numerical Methods in Engineering* 1997; 40(4): 727–758. doi: 10.1002/(SICI)1097-0207(19970228)40:4<727::AID-NME86>3.0.CO;2-N
- 102) Wells GN, Sluys LJ. A new method for modelling cohesive cracks using finite elements. *International Journal for Numerical Methods in Engineering* 2001; 50(12): 2667–2682. doi: 10.1002/nme.143
- 103) Strouboulis T, Babuška I, Copps K. The design and analysis of the Generalized Finite Element Method. *Computer Methods in Applied Mechanics and Engineering* 2000; 181(1-3): 43–69. doi: 10.1016/S0045-7825(99)00072-9
- 104) Strouboulis T, Copps K, Babuška I. Computational mechanics advances. The generalized finite element method. *Computer Methods in Applied Mechanics and Engineering* 2001; 190(32-33): 4081–4193. doi: 10.1016/S0045-7825(01)00188-8
- 105) Moës N, Dolbow J, Belytschko T. A finite element method for crack growth without remeshing. *International Journal for Numerical Methods in Engineering* 1999; 46(1): 131–150. doi: 10.1002/(SICI)1097-0207(19990910)46:1<131::AID-NME726>3.0.CO;2-J
- 106) Dolbow J, Moës N, Belytschko T. Discontinuous enrichment in finite elements with a partition of unity method. *Finite elements in analysis and design* 2000; 36(3): 235–260. doi: 10.1016/S0168-874X(00)00035-4

- 107) Shi GH. Manifold Method of Material Analysis. tech. rep., Army Research Office Research Triangle Park NC; <https://apps.dtic.mil/sti/citations/ADP006591>: 1991.
- 108) Terada K, Asai M, Yamagishi M. Finite cover method for linear and non-linear analyses of heterogeneous solids. *International Journal for Numerical Methods in Engineering* 2003; 58(9): 1321–1346. doi: 10.1002/nme.820
- 109) Kurumatani M, Terada K. Finite cover method with mortar elements for elastoplasticity problems. *Computational Mechanics* 2005; 36(1): 45–61. doi: 10.1007/s00466-004-0641-6
- 110) Murakami Y. Analysis of stress intensity factors of modes I, II and III for inclined surface cracks of arbitrary shape. *Engineering Fracture Mechanics* 1985; 22(1): 101–114. doi: 10.1016/0013-7944(85)90163-8
- 111) Rice JR. A path independent integral and the approximate analysis of strain concentration by notches and cracks. *Journal of Applied Mechanics, Transactions ASME* 1968; 35(2): 379–388. doi: 10.1115/1.3601206
- 112) Fleming M, Chu YA, Moran B, Belytschko T. Enriched element-free galerkin methods for crack tip fields. *International Journal for Numerical Methods in Engineering* 1997; 40(8): 1483–1504. doi: 10.1002/(SICI)1097-0207(19970430)40:8<1483::AID-NME123>3.0.CO;2-6
- 113) Rao BN, Rahman S. Efficient meshless method for fracture analysis of cracks. *Computational Mechanics* 2000; 26(4): 398–408. doi: 10.1007/s004660000189
- 114) Liu XY, Xiao QZ, Karihaloo BL. XFEM for direct evaluation of mixed mode SIFs in homogeneous and bi-materials. *International Journal for Numerical Methods in Engineering* 2004; 59(8): 1103–1118. doi: 10.1002/nme.906
- 115) Laborde P, Pommier J, Renard Y, Salaün M. High-order extended finite element

- method for cracked domains. *International Journal for Numerical Methods in Engineering* 2005; 64(3): 354–381. doi: 10.1002/nme.1370
- 116) Ghorashi SS, Valizadeh N, Mohammadi S. Extended isogeometric analysis for simulation of stationary and propagating cracks. *International Journal for Numerical Methods in Engineering* 2012; 89(9): 1069–1101. doi: 10.1002/nme.3277
- 117) Rao BN, Rahman S. Mesh-free analysis of cracks in isotropic functionally graded materials. *Engineering Fracture Mechanics* 2003; 70(1): 1–27. doi: 10.1016/S0013-7944(02)00038-3
- 118) Béchet E, Minnebo H, Moës N, Burgardt B. Improved implementation and robustness study of the X-FEM for stress analysis around cracks. *International Journal for Numerical Methods in Engineering* 2005; 64(8): 1033–1056. doi: 10.1002/nme.1386
- 119) Belytschko T, Gracie R. On XFEM applications to dislocations and interfaces. *International Journal of Plasticity* 2007; 23(10-11): 1721–1738. doi: 10.1016/j.ijplas.2007.03.003
- 120) Duflot M. A study of the representation of cracks with level sets. *International Journal for Numerical Methods in Engineering* 2007; 70(11): 1261–1302. doi: 10.1002/nme.1915
- 121) Simone A, Wells GN, Sluys LJ. From continuous to discontinuous failure in a gradient-enhanced continuum damage model. *Computer Methods in Applied Mechanics and Engineering* 2003; 192(41-42): 4581–4607. doi: 10.1016/S0045-7825(03)00428-6
- 122) Areias PMA, Belytschko T. Analysis of three-dimensional crack initiation and propagation using the extended finite element method. *International Journal for Numerical Methods in Engineering* 2005; 63(5): 760–788. doi: 10.1002/nme.1305
- 123) Mediavilla J, Peerlings RHJ, Geers MGD. Discrete crack modelling of ductile fracture

- driven by non-local softening plasticity. *International Journal for Numerical Methods in Engineering* 2006; 66(4): 661–688. doi: 10.1002/nme.1572
- 124) Comi C, Mariani S, Perego U. An extended FE strategy for transition from continuum damage to mode I cohesive crack propagation. *International Journal for Numerical and Analytical Methods in Geomechanics* 2007; 31(2): 213–238. doi: 10.1002/nag.537
 - 125) Moës N, Stolz C, Bernard PE, Chevaugeon N. A level set based model for damage growth: The thick level set approach. *International Journal for Numerical Methods in Engineering* 2011; 86(3): 358–380. doi: 10.1002/nme.3069
 - 126) Roth SN, Léger P, Soulaïmani A. A combined XFEM-damage mechanics approach for concrete crack propagation. *Computer Methods in Applied Mechanics and Engineering* 2015; 283: 923–955. doi: 10.1016/j.cma.2014.10.043
 - 127) Wang Y, Waisman H. From diffuse damage to sharp cohesive cracks: A coupled XFEM framework for failure analysis of quasi-brittle materials. *Computer Methods in Applied Mechanics and Engineering* 2016; 299: 57–89. doi: 10.1016/j.cma.2015.10.019
 - 128) Wu Z, Fan L, Liu Q, Ma G. Micro-mechanical modeling of the macro-mechanical response and fracture behavior of rock using the numerical manifold method. *Engineering Geology* 2017; 225: 49–60. doi: 10.1016/j.enggeo.2016.08.018
 - 129) Giovanardi B, Scotti A, Formaggia L. A hybrid XFEM-Phase field (Xfield) method for crack propagation in brittle elastic materials. *Computer Methods in Applied Mechanics and Engineering* 2017; 320: 396–420. doi: 10.1016/j.cma.2017.03.039
 - 130) Geelen RJM, Liu Y, Dolbow JE, Rodríguez-Ferran A. An optimization-based phase-field method for continuous-discontinuous crack propagation. *International Journal for Numerical Methods in Engineering* 2018; 116(1): 1–20. doi: 10.1002/nme.5911
 - 131) Muixí A, Marco O, Rodríguez-Ferran A, Fernández-Méndez S. A combined XFEM

- phase-field computational model for crack growth without remeshing. *Computational Mechanics* 2021; 67(1): 231–249. doi: 10.1007/s00466-020-01929-8
- 132) Sun Y, Liu Z, Tang X. A hybrid FEMM-Phase field method for fluid-driven fracture propagation in three dimension. *Engineering Analysis with Boundary Elements* 2020; 113: 40–54. doi: 10.1016/j.enganabound.2019.12.018
- 133) Hussein A, Hudobivnik B, Wriggers P. A combined adaptive phase field and discrete cutting method for the prediction of crack paths. *Computer Methods in Applied Mechanics and Engineering* 2020; 372: 113329. doi: 10.1016/j.cma.2020.113329
- 134) Yang L, Yang Y, Zheng H, Wu Z. An explicit representation of cracks in the variational phase field method for brittle fractures. *Computer Methods in Applied Mechanics and Engineering* 2021; 387: 114127. doi: 10.1016/j.cma.2021.114127
- 135) Rajendran S, Zhang BR. A "FE-meshfree" QUAD4 element based on partition of unity. *Computer Methods in Applied Mechanics and Engineering* 2007; 197(1-4): 128–147. doi: 10.1016/j.cma.2007.07.010
- 136) Brezzi F, Falk RS, Donatella Marini L. Basic principles of mixed virtual element methods. *ESAIM: Mathematical Modelling and Numerical Analysis* 2014; 48(4): 1227–1240. doi: 10.1051/m2an/2013138
- 137) Da Veiga LB, Brezzi F, Marini LD, Russo A. The Hitchhiker's guide to the virtual element method. *Mathematical Models and Methods in Applied Sciences* 2014; 24(8): 1541–1573. doi: 10.1142/S021820251440003X
- 138) Yang L, Yang Y, Zheng H. A phase field numerical manifold method for crack propagation in quasi-brittle materials. *Engineering Fracture Mechanics* 2021; 241: 107427. doi: 10.1016/j.engfracmech.2020.107427
- 139) Tamayo-Mas E, Rodríguez-Ferran A. A medial-axis-based model for propagating

- cracks in a regularised bulk. *International Journal for Numerical Methods in Engineering* 2014; 101(7): 489–520. doi: 10.1002/nme.4757
- 140) Cottrell JA, Hughes TJR, Bazilevs Y. *Isogeometric Analysis: Toward Integration of CAD and FEA*. John Wiley & Sons . 2009
- 141) Forest S. Micromorphic Approach for Gradient Elasticity, Viscoplasticity, and Damage. *Journal of Engineering Mechanics* 2009; 135(3): 117–131. doi: 10.1061/(asce)0733-9399(2009)135:3(117)
- 142) Miehe C, Aldakheel F, Teichtmeister S. Phase-field modeling of ductile fracture at finite strains: A robust variational-based numerical implementation of a gradient-extended theory by micromorphic regularization. *International Journal for Numerical Methods in Engineering* 2017; 111(9): 816–863. doi: 10.1002/nme.5484
- 143) Borden MJ, Hughes TJR, Landis CM, Verhoosel CV. A higher-order phase-field model for brittle fracture: Formulation and analysis within the isogeometric analysis framework. *Computer Methods in Applied Mechanics and Engineering* 2014; 273: 100–118. doi: 10.1016/j.cma.2014.01.016
- 144) Duda FP, Ciarbonetti A, Sánchez PJ, Huespe AE. A phase-field/gradient damage model for brittle fracture in elastic-plastic solids. *International Journal of Plasticity* 2014; 65: 269–296. doi: 10.1016/j.ijplas.2014.09.005
- 145) Choo J, Sun WC. Coupled phase-field and plasticity modeling of geological materials: From brittle fracture to ductile flow. *Computer Methods in Applied Mechanics and Engineering* 2018; 330: 1–32. doi: 10.1016/j.cma.2017.10.009
- 146) Rodriguez P, Ulloa J, Samaniego C, Samaniego E. A variational approach to the phase field modeling of brittle and ductile fracture. *International Journal of Mechanical Sciences* 2018; 144: 502–517. doi: 10.1016/j.ijmecsci.2018.05.009

- 147) Huang C, Gao X. Development of a phase field method for modeling brittle and ductile fracture. *Computational Materials Science* 2019; 169: 109089. doi: 10.1016/j.commatsci.2019.109089
- 148) Fang J, Wu C, Li J, Liu Q, Wu C, Sun G, Li Q. Phase field fracture in elasto-plastic solids: Variational formulation for multi-surface plasticity and effects of plastic yield surfaces and hardening. *International Journal of Mechanical Sciences* 2019; 156: 382–396. doi: 10.1016/j.ijmecsci.2019.03.012
- 149) Zhao Z, Huang K, Li C, Wang C, Qin H. A Novel Plastic Phase-Field Method for Ductile Fracture with GPU Optimization. *Computer Graphics Forum* 2020; 39(7): 105–117. doi: 10.1111/cgf.14130
- 150) Hu T, Talamini B, Stershic AJ, Tupek MR, Dolbow JE. A variational phase-field model For ductile fracture with coalescence dissipation. *Computational Mechanics* 2021; 68(2): 311–335. doi: 10.1007/s00466-021-02033-1
- 151) Omiya M, Arakawa S, Yao Z, Muramatsu M, Nishi S, Takada K, Murata M, Okato K, Ogawa K, Oide K, Kobayashi T, Han J, Terada K. Influence of strength and notch shape on crack initiation and propagation behavior of advanced high strength steel sheets. *Engineering Fracture Mechanics* 2022; 271: 108573. doi: 10.1016/j.engfracmech.2022.108573
- 152) Han J, Matsubara S, Nishi S, Takada K, Muramatsu M, Omiya M, Ogawa K, Oide K, Kobayashi T, Murata M, Moriguchi S, Terada K. Gradient damage model for ductile fracture introducing degradation of damage hardening modulus: implementation and experimental investigations. *International Journal of Fracture* 2023; 240(2): 183–208. doi: 10.1007/s10704-022-00681-9
- 153) Grassl P, Jirásek M. Damage-plastic model for concrete failure. *International Journal of Solids and Structures* 2006; 43(22-23): 7166–7196. doi: 10.1016/j.ijsolstr.2006.06.032

- 154) Eaves BC. The Linear Complementarity Problem. *Management Science* 1971; 17(9): 612–634. doi: 10.1287/mnsc.17.9.612
- 155) Cottle RW, Pang JS, Stone RE. *The Linear Complementarity Problem*. Society for Industrial and Applied Mathematics . 2009
- 156) Cottle RW, Pang JS, Stone RE. *The Linear Complementarity Problem*. Society for Industrial and Applied Mathematics . 2009
- 157) Han J, Matsubara S, Moriguchi S, Terada K. Variational crack phase-field model for ductile fracture with elastic and plastic damage variables. *Computer Methods in Applied Mechanics and Engineering* 2022; 400: 115577. doi: 10.1016/j.cma.2022.115577
- 158) Simo JC, Hughes TJR. *Computational Inelasticity*. Interdisciplinary Applied Mathematics New York: Springer-Verlag . 1998
- 159) Bonet J, Gil AJ, Wood RD. *Nonlinear Solid Mechanics for Finite Element Analysis: Statics*. Cambridge University Press . 2016
- 160) Coleman BD, Gurtin ME. Thermodynamics with internal state variables. *The Journal of Chemical Physics* 1967; 47(2): 597–613. doi: 10.1063/1.1711937
- 161) Han W, Reddy BD. *Plasticity*. Interdisciplinary Applied Mathematics New York, NY: Springer New York . 2013
- 162) Kachanov LM. On rupture time under condition of creep. *Nank S. S. R. Otd Tech Nauk* 1958; 8: 26–31.
- 163) Rabotnov YN. Creep Rupture. In: Springer. 1968 (pp. 342–349).
- 164) Borden MJ. *Isogeometric Analysis of Phase-field Models for Dynamic Brittle and Ductile Fracture*. PhD thesis. University of Texas at Austin, <http://repositories.tdl.org/tdl-ir/handle/2152/ETD-UT-2012-08-6113>; 2012.

- 165) Brepols T, Wulfinghoff S, Reese S. Gradient-extended two-surface damage-plasticity: Micromorphic formulation and numerical aspects. *International Journal of Plasticity* 2017; 97: 64–106. doi: 10.1016/j.ijplas.2017.05.010
- 166) Brepols T, Wulfinghoff S, Reese S. A gradient-extended two-surface damage-plasticity model for large deformations. *International Journal of Plasticity* 2020; 129: 102635. doi: 10.1016/j.ijplas.2019.11.014
- 167) Eldahshan H, Bouchard PO, Alves J, Perchat E, Munoz DP. Phase field modeling of ductile fracture at large plastic strains using adaptive isotropic remeshing. *Computational Mechanics* 2021; 67(3): 763–783. doi: 10.1007/s00466-020-01962-7
- 168) Grassl P, Jirásek M. Damage-plastic model for concrete failure. *International Journal of Solids and Structures* 2006; 43(22-23): 7166–7196. doi: 10.1016/j.ijsolstr.2006.06.032
- 169) Li H, Fu MW, Lu J, Yang H. Ductile fracture: Experiments and computations. *International Journal of Plasticity* 2011; 27(2): 147–180. doi: 10.1016/j.ijplas.2010.04.001
- 170) Anderson TL. *Fracture Mechanics*. CRC Press . 2017
- 171) Lawn B. *Fracture of Brittle Solids*. Cambridge Solid State Science Series Cambridge University Press . 1993
- 172) Mott NF. Fracture of metals: Theoretical considerations. *Engineering* 1948; 165: 16–18.
- 173) Yoffe EH. LXXV. The moving griffith crack. *The London, Edinburgh, and Dublin Philosophical Magazine and Journal of Science* 1951; 42(330): 739-750. doi: 10.1080/14786445108561302
- 174) Broberg KB. The propagation of a brittle crack. *Arkiv för Fysik* 1960; 18(2): 159–192.
- 175) Freund LB. *Dynamic Fracture Mechanics*. Cambridge University Press . 1990

- 176) Newmark NM. A Method of Computation for Structural Dynamics. *Journal of the Engineering Mechanics Division* 1959; 85(3): 67–94. doi: 10.1061/JMCEA3.00000098
- 177) Han J, Shintaku Y, Moriguchi S, Terada K. A transition scheme from diffusive to discrete crack topologies at finite strain during the course of a staggered iterative procedure. *International Journal for Numerical Methods in Engineering* 2023; 124(6): 1405–1433. doi: 10.1002/nme.7169
- 178) Mediavilla J, Peerlings RHJ, Geers MGD. A robust and consistent remeshing-transfer operator for ductile fracture simulations. *Computers and Structures* 2006; 84(8-9): 604–623. doi: 10.1016/j.compstruc.2005.10.007
- 179) Ramulu M, Kobayashi AS. Mechanics of crack curving and branching — a dynamic fracture analysis. In: Williams ML, Knauss WG. , eds. *Dynamic fracture* Dordrecht: Springer Netherlands. 1985 (pp. 61–75)
- 180) Sharon E, Fineberg J. Microbranching instability and the dynamic fracture of brittle materials. *Physical Review B - Condensed Matter and Materials Physics* 1996; 54(10): 7128–7139. doi: 10.1103/PhysRevB.54.7128
- 181) Kalthoff JF, Winkler S. Failure mode transition at high rates of shear loading. *Impact Loading and Dynamic Behavior of Materials* 1988; 1: 185–195.
- 182) Han J. Movies for "Crack phase-field enhanced finite cover method for dynamic fracture at finite strain". doi: 10.17632/zn8d8rtmyw.2
- 183) Bonet J, Gil AJ, Wood RD. *Nonlinear Solid Mechanics for Finite Element Analysis: Dynamics*. Cambridge University Press . 2021
- 184) John R, Shah SP. Mixed-Mode Fracture of Concrete Subjected to Impact Loading. *Journal of Structural Engineering* 1990; 116(3): 585–602. doi: 10.1061/(asce)0733-9445(1990)116:3(585)

- 185) Borden MJ, Hughes TJR, Landis CM, Verhoosel CV. A higher-order phase-field model for brittle fracture: Formulation and analysis within the isogeometric analysis framework. *Computer Methods in Applied Mechanics and Engineering* 2014; 273: 100–118. doi: 10.1016/j.cma.2014.01.016
- 186) Han J, Yin B, Kaliske M, Tarada K. Incorporation of gradient-enhanced microplane damage model into isogeometric analysis. *Engineering Computations (Swansea, Wales)* 2021; 38(8): 3388–3415. doi: 10.1108/EC-08-2020-0455
- 187) Guo J, Zhao S, Murakami RI, Zang S. Experimental and numerical investigation for ductile fracture of Al-alloy 5052 using modified Rousselier model. *Computational Materials Science* 2013; 71: 115–123. doi: 10.1016/j.commatsci.2013.01.011
- 188) Guo J. *An Experimental and Numerical Investigation on Damage Evolution and Ductile Fracture Mechanism of Aluminum Alloy*. PhD thesis. The University of Tokushima, <https://repo.lib.tokushima-u.ac.jp/en/list/niitype/Thesis2013>.